Steady state properties of discrete and continuous models of nonequilibrium phenomena

A Dissertation
submitted in partial fulfillment
of the requirements for the award of the
degree of
Doctor of Philosophy

by
Dipankar Roy

Under the supervision of
Prof. Arvind Ayyer and Prof. Rahul Pandit

Department of Mathematics
Indian Institute of Science
Bangalore - 560012

Declaration

I hereby declare that the work reported in this thesis is entirely original and has been carried out by me under the supervision of Prof. Arvind Ayyer at the Department of Mathematics, and Prof. Rahul Pandit at the Department of Physics, Indian Institute of Science, Bangalore. I further declare that this work has not been the basis for the award of any degree, diploma, fellowship, associateship or similar title of any University or Institution.

Dipankar Roy
S.R. No. : 12626

Indian Institute of Science,
Bangalore,
16 October 2020.

Prof. Arvind Ayyer
(Research advisor)
and
Prof. Rahul Pandit
(Research advisor)

Dedication

Dedicated to

my PhD advisors,
Prof. Arvind Ayyer,
and
Prof. Rahul Pandit,

and my parents,
Mrs. Iva Roy,
and
Mr. Satyendra Nath Roy.

Acknowledgement

It is a great pleasure to thank my PhD advisors, Prof. Arvind Ayyer and Prof. Rahul Pandit, for their valuable guidance throughout the last five years. Both of them have been very patient in advising me. Every discussion with them have taught me something new. I have learnt from my advisors about not only the subject of my current research, but also writing research papers, presenting results or ideas precisely, and asking insightful questions. In particular, I am grateful to Prof. Ayyer for introducing me to the asymmetric exclusion processes right at the early stage of my PhD. The early training by Prof. Ayyer has been very beneficial to all of my projects undertaken later for my PhD thesis. Prof. Pandit encouraged me to work in simple models of turbulence. I am thankful to him because the projects with him introduced me to a variety of research topics and helped me develop numerical skills. In addition to working on two types projects, my advisors have always inspired me to explore new ideas or pursue other topics of research. Their timely advices, positive outlook, and constant support regarding academic and non-academic matters have been essential to my personal growth for the last five years. I extend deep gratitude to my PhD advisors for such an impact on my life.

I would like to thank Dr. Caley Finn and Prof. Uriel Frish as well for collaborations. Discussions with them have been informative and stimulating.

I am also grateful to my friends: Amit, Bhawana, Indrajit, Mahesh, Priyanka, Ratan, Subhajit, Tushar, and Vikas. Academic and non-academic conversations with them have enriched my knowledge, experience, and viewpoints. Meetings with them over tea, lunch or dinner have always been refreshing breaks from mundane routine. I am indebted to them for their cordial and enthusiastic friendship over the last few years.

Other friends have also been very helpful. Friendly advices and suggestions from Arnab, Arun, Biswapriyo, Debarghya, Gobindo, Priyo, Rahul, Riya, Sanyukta, Shubhadeep, Soubhik, Srishti, and Subhadip are highly appreciated. I am thankful to all of them.

Also, I thank the present and past members of Prof. Rahul Pandit's group. I learnt many things about numerical simulations from discussions with them.

The help from the staff of National Mathematics Initiative, Department of Mathematics, and Department of Physics is also acknowledged.

I am also happy to thank my teachers who taught me in the past. Besides, I learnt a lot from my friends, especially my undergraduate batchmates. So I owe them a debt of gratitude.

Lastly, I am grateful to my parents and sister as well as other family members for their unconditional support. They stood by me through thick and thin. Particularly, no words of gratitude are enough to thank my parents for the countless sacrifices which they have been making for me for almost three decades. Their motivating words and unwavering faith in me have been the driving force for my endeavours. It gives me immense joy to acknowledge their blessings.

Abstract

The understanding of nonequilibrium phenomena, of fundamental importance in statistical physics, has great implications for many physical, chemical, and biological systems. Such phenomena are observed almost everywhere in the natural world. These phenomena are characterized by complicated spatiotemporal evolution. To explore nonequilibrium phenomena we often study simple model systems that embody their essential characteristics. In this thesis, we report the results of our investigations of the statistically steady state properties of three one-dimensional models: multispecies asymmetric simple exclusion processes, the Kuramoto-Sivashinsky equation, and the Burgers equation. The thesis is divided into two parts: Part I and Part II.

In Chapters 2–5 of Part I, we present our results for multispecies exclusion models, principally the phase diagrams and statistical properties of their nonequilibrium steady state (NESS). We list below abstracts of these chapters.

- In Chapter 2, we consider a multispecies ASEP (mASEP) on a one-dimensional lattice with semipermeable boundaries in contact with particle reservoirs. The mASEP involves $(2r+1)$ species of particles: r species of positive charges and their negative counterparts as well as vacancies. At the boundaries, a species can replace or be replaced by its negative counterpart. We derive the exact nonequilibrium phase diagram for the system in the long time limit. We find two new phenomena in certain regions of the phase diagram: *dynamical expulsion* when the density of a species becomes zero throughout the system, and *dynamical localization* when the density of a species is nonzero only within an interval far from the boundaries. We give a complete explanation of the macroscopic features of the phase diagram using what we call *nested fat shocks*.

- In Chapter 3, we study an asymmetric exclusion process with two species and vacancies on an open one-dimensional lattice called the left-permeable ASEP (LPASEP). The left boundary is permeable for the vacancies but the right boundary is not. We find a matrix product solution for the stationary state and the exact stationary phase diagram for the densities and currents. By calculating the density of each species at the boundaries, we find further structure in the stationary phases. In particular, we find that the slower species can reach and accumulate at the far boundary, even in phases where the bulk density of these particles approaches zero.

- In Chapter 4, we study a multispecies generalization of the model in Chapter 3. We determine all phases in the phase diagram using an exact projection to the LPASEP solved earlier. In most phases, we observe the phenomenon of dynamical expulsion of

one or more species. We explain the density profiles in each phase using interacting shocks. This explanation is corroborated by simulations.

- In Chapter 5, we investigate a multispecies generalization of the single-species asymmetric simple exclusion process defined on an open one-dimensional, finite lattice connected to particle reservoirs. At the boundaries, a species can be replaced with any other species. We devise an exact projection scheme to find the phase diagram in terms of densities and currents of all species. In most of the phases, one or more species are absent in the system due to dynamical expulsion. We observe shocks as well in some regions of the phase diagram. We explain the density profiles using a generalized shock structure that is substantiated by numerical simulations.

In Chapters 7 and 8 of Part II, we study the statistical properties of turbulent, but statistically steady, states of the Kuramoto-Sivashinsky and the Burgers equations in one dimension. Our main results are summarized below.

- In Chapter 7, we investigate the long time and large system size properties of the one-dimensional Kuramoto-Sivashinsky equation. Tracy-Widom and Baik-Rains distributions appear as universal limit distributions for height fluctuations in the one-dimensional Kardar-Parisi-Zhang (KPZ) stochastic partial differential equation (PDE). We obtain the same universal distributions in the spatiotemporally chaotic, nonequilibrium, but statistically steady state of KS deterministic PDE, by carrying out extensive pseudospectral direct numerical simulations to obtain the spatiotemporal evolution of the KS height profile $h(x,t)$ for different initial conditions. We establish, therefore, that the statistical properties of the one-dimensional (1D) KS PDE in this state are in the 1D KPZ universality class.

- In Chapter 8, we study the statistical properties of decaying turbulence in the one-dimensional Burgers equation, in the vanishing-viscosity limit; we start with random initial conditions, whose energy spectra have simple functional dependences on the wavenumber k:

$$E_0(k) = A\,\mathcal{E}(k)\,\exp\left[-2k^2/k_c^2\right]\ ,$$

  where A is a positive real number, and k_c is a cutoff wavenumber. The simplest case is the single-power law $\mathcal{E}(k) = |k|^n$. We focus here on the case of the Gaussian laws which are characterized by $\mathcal{E}(k) = \exp\left[-(k-k_c)^2/2k_c + 2k^2/k_c^2\right]$; in addition, we consider initial spectra which are combinations of either two or four single-power law spectral regions. For all these initial conditions, we systematize (a) the temporal decay of the total energy, (b) the rich temporal evolution of the energy spectrum, and (c) the spatiotemporal evolution of the velocity field. We present our results in the context of earlier studies of this problem.

Contents

List of Figures

List of Tables

List of papers or preprints

The present thesis is based on

1 A Ayyer and D Roy, *The exact phase diagram for a class of open multispecies asymmetric exclusion processes* Sci. Rep. 7, 13555 (2017)

2 A Ayyer, C Finn and D Roy, *Matrix product solution of a left-permeable two-species asymmetric exclusion process*, Phys. Rev. E 97, 012151 (2018)

3 A Ayyer, C Finn and D Roy, *The phase diagram for a multispecies left-permeable asymmetric exclusion process*, J. Stat. Phys. 174: 605 (2019)

4 D Roy and R Pandit, *The one-dimensional Kardar-Parisi-Zhang and Kuramoto-Sivashinsky universality class: limit distributions*, Phys. Rev. E 101, 030103(R) (2020)

5 D Roy, *The phase diagram for a class of multispecies permissive asymmetric exclusion processes*, J. Stat. Mech. 013201 (2021)

Part I

Multispecies exclusion processes: Phase diagrams

Chapter 1

Introduction to exclusion processes

Nature is full of systems which are collections of large number of simple entities. We are familiar with such systems in our everyday life. Take the example of a simple substance, say water. What we observe as water, is a collection of H_2O molecules in the liquid state. To quantify, the number of molecules per mililiter at room temperature is of the order 10^{23}. In a first attempt to study this system we might assume these water molecules to be classical particles interacting via some potential. Inspite of this crude approximation, the total number of degrees of freedom is huge and increases with the number of molecules. In principle, one can still apply the Newton's laws for such systems with large number of particles. But then, a huge number of coupled differential equations needs to be solved. This is clearly an impossible task. Thus we run into problems if we seek detailed information about each and every microscopic particle in a macroscopic system. This naturally raises the question: How can we study such systems which has a large number of interacting particles?

The discipline of statistical physics offers an interesting approach as follows. On a macroscopic level, the collective behaviour of an enormous number of microscopic constituents can be characterized by a small number of relevant parameters that depend on the nature of microscopic interactions. Indeed, we might need only few parameters to describe a macroscopic system. For example, one can know whether water in thermal equilibrium is in liquid state or not from the knowledge of the macroscopic quantities, such as pressure and temperature. This remains true even though we do not know the precise number of water molecules in a macroscopic volume. So it is sufficient, in order to describe the physical properties of a macroscopic system, to find the suitable macroscopic observables by taking into account only the essential aspects of interactions between the microscopic constituents. Adopting this approach, statistical physics has achieved great success in the case of systems in equilibrium. In particular, there has been tremendous progress in the understanding of critical phenomena in equilibrium systems. A very well-known model of equilibrium statistical physics is the Ising model which was exactly solved [123, 168]. As a result, the model has been so crucial to our understanding of critical phenomena that it is recognized as paradigmatic.

There is a well-known, general framework for equilibrium systems in statistical physics. The probability that a system is in configuration C is related to the energy E corresponding to the

configuration as

$$P(C) \propto \exp\left[-\beta E\right] , \tag{1.0.1}$$

where β is the inverse temperature. Based on this mathematical prescription, one can compute the partition function for a system in equilibrium and thus compute other thermodynamic variables. However, there is no such general principle for nonequilibrium statistical physics. Nonequilibrium systems which are only slightly away from equilibrium can still be handled with linear response theory. But a deep theory that is also applicable to systems very far from equilibrium is still unknown.

Nonequilibrium systems differ significantly from equilibrium ones. Although the probability of an allowed configuration does not change with time both for systems in the equilibrium, and for nonequilibrium systems in the *steady* (or *stationary*) state. One important difference lies in the transport properties. In equilibrium, there is no current. However, there is generally a nonzero current in *nonequilibrium steady state* (NESS). Moreover, the condition of detailed balance is generally not satisfied by the steady state probabilities of the configurations in the NESS unlike in equilibrium.

A few examples of nonequilibrium phenomena are driven diffusion of interacting particles [40], interface growth [113], reaction-diffusion phenomena [70, 71, 98], and turbulence [103, 29, 152]. There are many quantities of interest in the study of these problems. Of course, one is interested in the steady state distributions as well as phase diagrams. Besides, correlation functions, nonequilibrium fluctuations, relaxation properties, and transport coefficients, e.g. diffusion constant, show extremely non-trivial and intriguing characteristics.

Nonequilibrium phenomena are generally very difficult to analyze exactly. So we study various toy models of nonequilibrium phenomena. An interesting model must be simple enough so that it is mathematically tractable. But at the same time, the model must retain important features of the physical phenomena so that it should not be physically trivial. In particular, exactly solvable models are of great value. Since we can compute physical quantities exactly, such models offer insight into the nontrivial and novel aspects of nonequilibrium phenomena. We hope to arrive at a general framework for nonequilibrium phenomena based on our understanding of these models subject to experimental verification. In addition, the study of these models often requires very sophisticated mathematical techniques. Thus they are important from the point of view of pure and applied mathematics. In fact, this is true for most of the models discussed in this thesis.

We shall consider asymmetric simple exclusion processes, which model driven diffusion phenomena, in one dimension in this part of the thesis. In this chapter, we provide an overview for asymmetric simple exclusion processes on finite lattices along with a literature survey on multispecies models. In the rest of the chapters, we consider multispecies models. Our main interest will be phase diagrams for these models and the macroscopic properties in the phases.

1.1 Exclusion processes

Exclusion processes are prototypical models of driven diffusion phenomena. In these models, particles move on a lattice interacting via hard-core interaction. The hops between the lattice sites follow stochastic dynamics. There are different types of exclusion processes based on the kind of lattice and dynamics. The simplest type of the exclusion process is when the hops occur between the neighbouring sites. Then the model is referred to as simple exclusion process (SEP). If the particles prefer to hop towards a particular direction we call the model *asymmetric simple exclusion process* or *ASEP* [40]. When there is extreme asymmetry, i.e. the particles are biased to move only in one direction we refer to the model as *totally asymmetric simple exclusion process* or *TASEP* [79, 40]. The most basic exclusion processes are considered in one-dimensional lattices. If the lattice is finite, one can distinguish two cases: periodic and open ASEPs. The number of particles in the periodic ASEP are conserved because the lattice is closed. For the open ASEP, the lattice is in contact with particle reservoirs at the ends. Thus particles can be exchanged between the lattice and the reservoirs at the boundaries. Moreover, there are different types of update schemes, namely, *random sequential update*, *parallel update*, *sublattice parallel update* and *ordered sequential update* [180]. We shall consider only random sequential update where only one hop is allowed at a particular point of time.

Exclusion process was first studied in the modelling of biopolymerization kinetics [155, 154]. The term 'exclusion', however, was introduced in the mathematical literature in a study of interacting Markov processes in [203]. Since then, exclusion processes found application in modelling many biological and physical transport phenomena. For example, fast ionic conductors were modelled as stochastic lattice gas with excluded volume interaction in [132]. Moreover, exclusion processes were used for modelling traffic flow [194, 191, 192], DNA reptation [194], molecular motors [137], random sequences in computational biology [48], cellular automata [190, 17], growth processes [113, 62] to name but a few. To get a physical picture, one might take the example of the traffic flow on a one-way, single-lane road. One can discretize the path and imagine the motor vehicles to be moving on it without overtaking another vehicles. Thus a vehicle is allowed to move forward only when the space in front of it is vacant. Assuming that the time taken by the vehicles to move to the next allowed position is exponentially distributed, one can consider the TASEP as a simple model for the traffic flow on a one-way road.

Aside from modelling diffusive systems, the exclusion process has received attention in the physics literature as an important nonequilibrium model [40]. This is largely because not only exact mathematical analysis can be pursued in the exclusion models, but also the physical properties of these models are often very interesting. A striking feature of the open ASEP is boundary induced phase transitions in 1D as shown in [145]. Such one-dimensional phase transitions are impossible in equilibrium systems. Moreover, the open TASEP was exactly solved by Derrida, Evans, Hakim, and Pasquier [79]. This was a remarkable study because the authors introduced a novel technique, namely the *matrix product ansatz* that allowed computation of the stationary distribution and physical quantities in terms of the boundary parameters exactly. Thus the nonequilibrium phase diagram for the TASEP was determined in terms of the boundary parameters. Since then, the matrix ansatz was used in the partially asymmetric variants of the open TASEP [185, 187, 4, 188, 212]. However, the method was

far more demanding for partially asymmetric cases. In fact, a representation involving q-orthogonal polynomial was used to compute the phase diagram for these cases in most of the studies. Appropriate representations relevant to the matrix product ansatz for these variants were also studied in [90].

Besides boundary induced phase transitions in the TASEP, other physical properties were investigated as well. For example, the diffusion constant [82], non-equal-time correlations and fluctuations in current [150] were studied. The diffusion constant was also investigated in [77] for the periodic ASEP. The exact large deviation function for current was determined in [87] for the periodic ASEP using the technique of Bethe ansatz. In [76], a universal large deviation function for the particle displacements was computed for the ASEP with ring geometry using Bethe ansatz. It was conjectured there that the same scaling function for the ASEP should hold for models described by one-dimensional Kardar-Parisi-Zhang equation. Later, the large deviation functional for the density in the open ASEP was studied in [84, 86]. In [85], it was shown that the non-Gaussian density fluctuations in open ASEP are related to the statistical properties of Brownian excursions. These computations was helpful in formulating general principles for driven diffusive models: the additivity principle [41] and the macroscopic fluctuation theory [33]. Moreover, the theory of Lee-Yang zeroes for equilibrium statistical physics was extended to the open ASEP in [39]. Finally, Bethe ansatz was applied to the open ASEP in [72] to compute the spectral gap that controls the approach to the stationary state. The dynamical phase diagram was also derived there revealing parts of the phase diagram where dynamical phase transition takes place. Numerical evidence was provided in support of this later using density matrix renormalization techniques in [175]. Thus, the single species ASEP, both periodic and open, has become a paradigmatic model for nonequilibrium statistical physics because of tractability and its intriguing characteristics in broader theoretical investigations.

We shall now discuss the single species ASEP on finite lattices in a more detailed manner in this introductory chapter. We recall significant results related to the open ASEP in Section 1.1.1. There we shall discuss the main ideas of the matrix product ansatz which has been very useful in computing the phase diagram for the open ASEPs. Following this, we shall discuss the multispecies variants of the ASEP in Section 1.1.2 setting the direction for the theme of rest of the chapters in Part I. Finally, we shall briefly summarize in Section 1.2 the results in the Chapters 3 to 5.

1.1.1 Open ASEP

In the open ASEP, one considers a 1D lattice of size L as well. But, now, the lattice is coupled with two reservoirs of particles at the first and the last site. Particles can be injected into the lattice from reservoirs or be removed from the system at the first or the last site. One is interested in studying the stationary state of the system under the effect of such boundary interactions. In particular, we will discuss here phase transitions induced by boundary interactions in such open systems in details.

Let us define the boundary and bulk interactions in the open ASEP more precisely. At the left boundary, a particle can either come with rate α from the left reservoir to the first site if it is empty, or leave the system with rate γ from site 1 if it is occupied. These left boundary

interactions are succinctly expressed as

$$i \to j \text{ with rate } \begin{cases} \alpha & \text{if } i < j, \\ \gamma & \text{if } i > j, \end{cases} \tag{1.1.1}$$

where $i, j \in \mathbb{L}_b$. Similarly, if the last site is occupied then the particle can leave the system, and if the last site is empty, the particle can come to it from the right reservoir. These interactions happen with rates given by

$$i \to j \text{ with rate } \begin{cases} \beta & \text{if } i > j, \\ \delta & \text{if } i < j, \end{cases} \tag{1.1.2}$$

We shall always assume that $\alpha, \beta \in \mathbb{R}_+$. The bulk dynamics is same as in the periodic ASEP with the preferred direction being from left to right. If $\tau_k = i$ and $\tau_{k+1} = j$, then the rates are

$$ij \to ji \text{ with rate } \begin{cases} p & \text{if } i > j, \\ q & \text{if } i < j. \end{cases} \tag{1.1.3}$$

We again assume $q \leq p$. An illustrative diagram is shown in Figure 1.1.

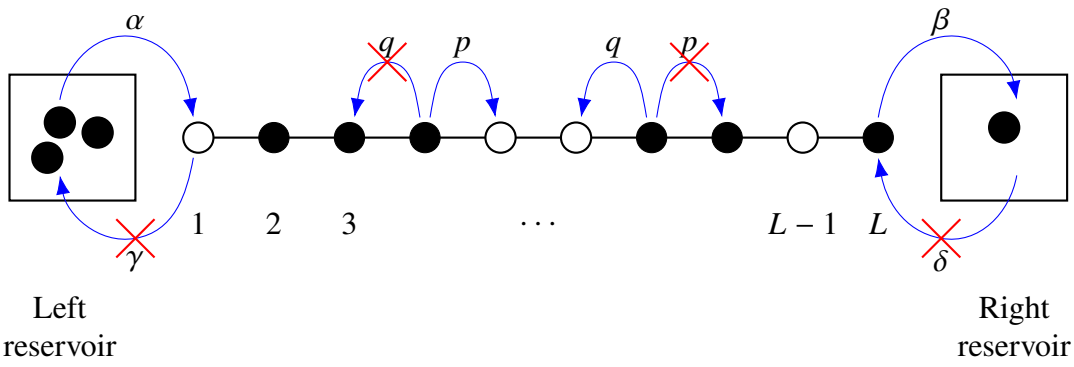

Figure 1.1: Schematic diagram of the open ASEP. The red crosses indicate the interactions which are not allowed.

Without loss of generality, we set $p = 1$. There are two important variants of the open ASEP. If we have $0 < q < 1$, then the model is often referred to as *partially asymmetric simple exclusion process* or *PASEP*. The totally asymmetric version where we set $\gamma = \delta = q = 0$ is called *totally asymmetric simple exclusion process* or *TASEP*. Moreover, we shall fix $0 \leq \alpha, \beta \leq 1$ in the TASEP. In doing so, we do not loose any generality because we can always rescale time t. Clearly, the ASEP is a more general version of the TASEP. For simplicity, we shall focus on the TASEP and discuss it in details in Sections 1.1.1.1-1.1.1.4. We shall recall the results for the ASEP briefly in Section 1.1.1.5.

1.1.1.1 Matrix product approach for TASEP

The TASEP can be exactly solved using a matrix product formulation [79]. In this section, we shall discuss the marix product approach in the context of the TASEP. We recount here only

the main idea that will be useful later in Chapter 3.

First, we fix some notations to describe concisely the time evolution of the probabilities of the system configurations. We recall that the lattice has L sites with each site being empty or occupied by a particle. Let us denote the former local state by $|0\rangle$ and the latter by $|1\rangle$. We identify these local states with the standard basis of $\mathbb{C}^2$:

$$|0\rangle = \begin{pmatrix} 1 \\ 0 \end{pmatrix}, \qquad |1\rangle = \begin{pmatrix} 0 \\ 1 \end{pmatrix}. \tag{1.1.4}$$

Thus a typical configuration $\boldsymbol{\tau} = (\tau_1, \ldots, \tau_L)$ is represented by a basis vector $|\boldsymbol{\tau}\rangle \in (\mathbb{C}^2)^{\otimes L}$, which is L-fold tensor product of the local states

$$|\boldsymbol{\tau}\rangle = |\tau_1\rangle \otimes \cdots \otimes |\tau_L\rangle. \tag{1.1.5}$$

We denote the probability of the configuration $\boldsymbol{\tau}$ at time t with $P_{\boldsymbol{\tau}}(t)$. To describe the evolution of the probabilities compactly, we write the vector

$$|P(t)\rangle = \sum_{\tau} P_{\boldsymbol{\tau}}(t)|\boldsymbol{\tau}\rangle. \tag{1.1.6}$$

Then the evolution is determined by the master equation which is given by

$$\frac{\mathrm{d}}{\mathrm{d}t}|P(t)\rangle = M|P(t)\rangle, \tag{1.1.7}$$

where the matrix M is the Markov matrix for the TASEP.

The system is *ergodic*, i.e. starting from any configuration the system can visit any other configuration. For $t \to \infty$, the process converges to the stationary distribution $|P_{\mathrm{stat}}\rangle$. Let $|\psi\rangle$ be the unnormalized eigenvector of M with eigenvalue 0, i.e.

$$M|\psi\rangle = 0, \tag{1.1.8}$$

where the vector $|\psi\rangle$ is expressed as

$$|\psi\rangle = \sum_{\tau} \psi_{\boldsymbol{\tau}}|\boldsymbol{\tau}\rangle. \tag{1.1.9}$$

The scalars ψ_{τ} are called *stationary weights*. By our choice of basis, $|\psi\rangle$ is a column vector and the stationary weights are its entries. The stationary distribution $|P_{\mathrm{stat}}\rangle$ is obtained by normalizing $|\psi\rangle$ with the normalization Z_L given by

$$Z_L = \sum_{\tau} \psi_{\boldsymbol{\tau}}. \tag{1.1.10}$$

Thus $P_{\boldsymbol{\tau}}$, the stationary probability of the configuration $\boldsymbol{\tau}$ is the ratio of the stationary weight

corresponding to $\boldsymbol{\tau}$ and the normalization Z_L

$$P_{\boldsymbol{\tau}} = \frac{\psi_{\boldsymbol{\tau}}}{Z_L}. \tag{1.1.11}$$

The existence of a unique stationary distribution and convergence to it are guaranteed for an ergodic continuous time Markov chain. So, it suffices to find the eigenvector of M corresponding to zero eigenvalue. Then it is easy to evaluate the stationary distribution and relevant macroscopic observables. For small L, this might be possible by brute-force computation. However, it is nontrivial to find the stationary distribution for general L. The approach of Derrida, *et al.* [79], often referred to as matrix product ansatz, is very useful in computing an explicit expression for the stationary distribution in terms of the parameters.

The matrix ansatz begins with an ansatz for the stationary weights written as a product of matrices. The first step is to assume that there exists matrices X_1 and X_0 as well as vectors $\langle W|$ and $|V\rangle$ satisfying certain conditions. The stationary weight $\psi_{\boldsymbol{\tau}}$ corresponding to the configuration $\boldsymbol{\tau}$ is then expressed in terms of a product in the following manner

$$\psi_{\boldsymbol{\tau}} = \langle W|X_{\tau_1}X_{\tau_2}\cdots X_{\tau_k}\cdots X_{\tau_{L-1}}X_{\tau_L}|V\rangle = \langle W|\prod_{k=1}^{L} X_{\tau_k}|V\rangle. \tag{1.1.12}$$

Thus if there is a particle (resp. vacancy) at site k for the configuration $\boldsymbol{\tau}$, then X_1 (resp. X_0) is the k-th matrix from the left in the product $\prod_{k=1}^{L} X_{\tau_k}$. It is a common practice to use the symbols D and E for X_1 and X_0 respectively. Here, we shall use them interchangeably for the TASEP.

The vector $|\psi\rangle$ is then given by

$$|\psi\rangle = \begin{pmatrix} \langle W|X_0X_0\cdots X_0X_0|V\rangle \\ \langle W|X_0X_0\cdots X_0X_1|V\rangle \\ \vdots \\ \langle W|X_1X_1\cdots X_1X_1|V\rangle \end{pmatrix} = \begin{pmatrix} \langle W|EE\cdots EE|V\rangle \\ \langle W|EE\cdots ED|V\rangle \\ \vdots \\ \langle W|DD\cdots DD|V\rangle \end{pmatrix}. \tag{1.1.13}$$

To write this succinctly, we define the vector

$$X := \begin{pmatrix} X_0 \\ X_1 \end{pmatrix} = \begin{pmatrix} E \\ D \end{pmatrix} \tag{1.1.14}$$

and adopt the notation

$$\langle\langle W|H := \begin{pmatrix} \langle W|h_1 \\ \vdots \\ \langle W|h_n \end{pmatrix}, \qquad H|V\rangle\rangle := \begin{pmatrix} h_1|V\rangle \\ \vdots \\ h_n|V\rangle \end{pmatrix}, \tag{1.1.15}$$

where $H = (h_1, \ldots, h_n)^T$. The entries, h_i, can be scalars or matrices. Thus the vector $|\psi\rangle$ can

be written as

$$|\psi\rangle = \langle\langle W|X^{\otimes L}|V\rangle\rangle = \langle\langle W|X \otimes X \otimes \cdots \otimes X|V\rangle\rangle. \tag{1.1.16}$$

The Markov matrix M encodes all interactions in the system - the exchange of particles in the bulk as well as injection and removal of particles at the boundaries. Thus M can be expressed as a sum of $(L+1)$ matrices each representing the local interactions

$$M = B_l \otimes I_2^{\otimes L-1} + \sum_{k=1}^{L-1} I_2^{\otimes(k-1)} \otimes w \otimes I_2^{\otimes(L-k-1)} + I_2^{\otimes L-1} \otimes B_r. \tag{1.1.17}$$

Here I_2 is the identity matrix in $\mathbb{C}^{2\times 2}$ while B_l and B_r are 2×2 matrices given by

$$B_l = \begin{pmatrix} -\alpha & 0 \\ \alpha & 0 \end{pmatrix}, \qquad B_r = \begin{pmatrix} 0 & \beta \\ 0 & -\beta \end{pmatrix}. \tag{1.1.18}$$

Also, w is a matrix in $(\mathbb{C}^{2\times 2})^{\otimes 2}$ with

$$w = \begin{pmatrix} 0 & 0 & 0 & 0 \\ 0 & 0 & 1 & 0 \\ 0 & 0 & -1 & 0 \\ 0 & 0 & 0 & 0 \end{pmatrix}. \tag{1.1.19}$$

The matrix w corresponds to the local interaction of exchange of particles between a pair of neighbouring sites in the bulk. Since there are $(L-1)$ such pairs of sites, same number of terms involving w appear in (1.1.17).

It can be checked that $|\psi\rangle$ expressed in the product form as in (1.1.16) satisfies (1.1.8) provided that

$$\begin{aligned} B_l\langle\langle W|X &= \langle\langle W|\widehat{x} \\ w(X \otimes X) &= -\widehat{x} \otimes X + X \otimes \widehat{x} \\ B_r X|V\rangle\rangle &= \widehat{x}\,|V\rangle\rangle, \end{aligned} \tag{1.1.20}$$

where $\widehat{x} = (-1, 1)^T$. It might not be immediately clear why this should work. A detailed discussion can be found in [40].

The equations in (1.1.20) can be further simplified. After simplification, we obtain two boundary relations involving boundary and bulk matrices

$$\begin{aligned} \langle W|E &= \frac{1}{\alpha}\langle W|, \\ D|V\rangle &= \frac{1}{\beta}|V\rangle, \end{aligned} \tag{1.1.21}$$

and another involving bulk matrices

$$DE = D + E. \tag{1.1.22}$$

This is the well-known reduction equation for the TASEP and related exclusion models.

One possible choice for the matrices D and E is given by

$$D = \begin{pmatrix} \frac{1}{\beta} & \frac{1}{\beta} & \frac{1}{\beta} & \frac{1}{\beta} & \cdots \\ 0 & 1 & 1 & 1 & \\ 0 & 0 & 1 & 1 & \vdots \\ 0 & 0 & 0 & 1 & \\ \vdots & & \cdots & & \ddots \end{pmatrix}, \quad E = \begin{pmatrix} 0 & 0 & 0 & 0 & \cdots \\ 1 & 0 & 0 & 0 & \\ 0 & 1 & 0 & 0 & \vdots \\ 0 & 0 & 1 & 0 & \\ \vdots & & \cdots & & \ddots \end{pmatrix}. \tag{1.1.23}$$

(Derrida, *et al.* [79])

The boundary matrices are

$$\langle W| = \left(1, \frac{1}{\alpha}, \frac{1}{\alpha^2}, \cdots\right), \qquad |V\rangle = \begin{pmatrix} 1 \\ 0 \\ 0 \\ \vdots \end{pmatrix}. \tag{1.1.24}$$

(Derrida, *et al.* [79])

For this example the product $\langle W|V\rangle$ equals 1. We shall assume this to be so from now on even though we shall not use the explicit representation. More examples of representations can be found in [79].

1.1.1.2 Computing normalization Z_L

The normalization Z_L is an important quantity that appears in computing the physical quantities. Using (1.1.10) and (1.1.12), one observes that

$$Z_L = \langle W|F^L|V\rangle, \qquad F = D + E. \tag{1.1.25}$$

The product F^L can be simplified to the following form

$$F^L = \sum_{n=0}^{L} B_{L,n} \sum_{m=0}^{n} E^m D^{n-m}, \tag{1.1.26}$$

where the factor $B_{L,n}$ (see [79], [40]) is defined by

$$B_{L,n} = \begin{cases} \frac{n(2L-1-n)!}{L!(L-n)!} & \text{for } 0 \le n \le L, \\ 0 & \text{otherwise .} \end{cases} \tag{1.1.27}$$

These numbers are known as ballot numbers in combinatorics. Using this expression the normalization is computed to be

$$Z_L = \sum_{n=0}^{L} B_{L,n} \frac{\beta^{-n-1} - \alpha^{-n-1}}{\beta^{-1} - \alpha^{-1}}. \tag{1.1.28}$$

As a simple example we consider $L = 2$. We use the bulk and boundary relations to find

$$\begin{aligned} Z_2 &= \langle W|(D+E)^2|V\rangle, \\ &= \langle W|(DD + DE + ED + EE)|V\rangle, \\ &= \langle W|(DD + ED + EE + D + E)|V\rangle, \\ &= \frac{1}{\beta^2} + \frac{1}{\alpha\beta} + \frac{1}{\alpha^2} + \frac{1}{\beta} + \frac{1}{\alpha}. \end{aligned}$$

We arrive at the same result using the expression for Z_L for $L = 2$.

1.1.1.3 Physical quantities

The physical quantities which are of prime interest here are density and current. The density (of positively charges particles) at site k is given by

$$\rho(k) = \frac{1}{Z_L}\langle W|F^{k-1}DF^{L-k}|V\rangle. \tag{1.1.29}$$

This is easy to check using the definition of (sitewise) density and the matrix ansatz for the stationary distribution.

The key to evaluating the expression on the right hand side of (1.1.29) is to simplify the product of the form of DF^N using the bulk reduction relation (1.1.22). The simplified expression is

$$DF^N = \sum_{k=0}^{N-1} C_k F^{N-k} + \sum_{j=2}^{N+1} B_{N,j} D^j, \tag{1.1.30}$$

where C_k is defined by

$$C_k = \frac{1}{k+1}\binom{2k}{k}. \tag{1.1.31}$$

These are known as Catalan numbers. Then the exact expression for the density is found to be

$$\rho(k) = \sum_{i=0}^{L-k-1} C_i \frac{Z_{L-1-i}}{Z_L} + \frac{Z_{k-1}}{Z_L} \sum_{j=2}^{N+1} B_{N,j}\beta^{-j}. \tag{1.1.32}$$

We can also compute J the current of particles. It is easy to check that

$$J = \frac{1}{Z_L}\langle W|F^{k-1}DEF^{L-k-1}|V\rangle = \frac{Z_{L-1}}{Z_L} \qquad \text{for } 1 \le k < L. \tag{1.1.33}$$

Finally, we compute the current and density in the thermodynamic limit $L \to \infty$ to find the phase diagram. We describe these in the next section.

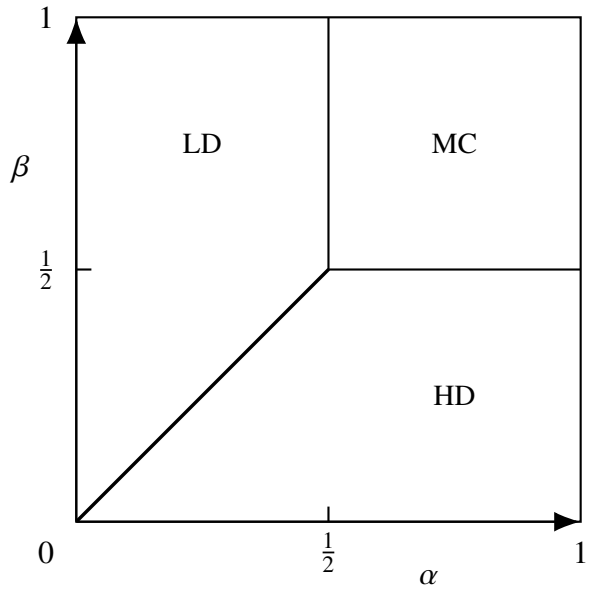

Figure 1.2: Phase diagram for the TASEP. The coexistence line (CL) is the line segment $\alpha = \beta < 1/2$ (indicated as a thick line).

1.1.1.4 Phase diagram of the TASEP

There are three phases for the TASEP in the steady state in the thermodyanmic limit. The phase diagram is the $\alpha - \beta$ plane which is divided into three regions each with different asymptotic forms of current and density. The three phases along with the corresponding current are

- *maximal current* or *MC* phase $(\min\{\alpha, \beta\} > 1/2)$, $J = 1/4$,
- *high density* or *HD* phase $(\min\{\beta, 1/2\} < \alpha)$, $J = \beta(1 - \beta)$,
- *low density* or *LD* phase : $(\min\{\alpha, 1/2\} < \beta)$, $J = \alpha(1 - \alpha)$.

The boundary between HD and LD phase is known as the *coexistence line* or *CL*. The exact steady state phase diagram is given in Figure 1.2. In different parts of the phase diagram, density takes the following forms

- MC phase: $\rho(Lx) \simeq 1/2$,
- HD phase: $\rho(Lx) \simeq 1 - \beta$,
- LD phase: $\rho(Lx) \simeq \alpha$,
- CL: $\rho(Lx) \simeq \alpha + x(1 - 2\alpha)$.

Here, $x = k/L$ is the normalized site position in the thermodynamic limit.

The naming of the phase regions is self-explanatory except probably the CL. On this line, both phases coexist, i.e. both high density and low density regions coexist in the system. Thus

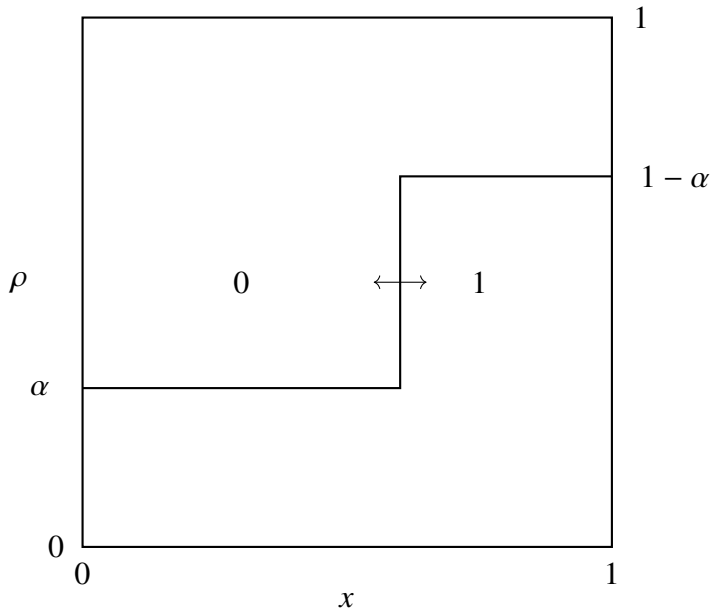

Figure 1.3: Shock picture for the TASEP on the coexistence line $\alpha = \beta < 1/2$. The normalized site position x equals i/L.

a discontinuity appears in the density profile. This is referred to as a *shock*. The boundary between the high and low density region is sometimes also called the *shock front*. The position of the shock is random, and uniformly distributed over the whole system. A shock can be observed in the simulations if we take a snapshot of the system for a phase point on the CL in the steady state with sufficiently large L. The shock picture is shown in Figure 1.3.

On the CL, the shock formed between 1's and 0's perform symmetric random walk with zero net drift in the system leading to a linear density profile. In the HD phase, the shock acquires negative drift. Thus the shock gets pinned to the left and high density of 1's prevail on the system. In the LD phase, the shock is pinned to the right because it has positive drift. As a result, the system assumes low density. However, as one approaches the MC phase along the coexistence line, the height of the shock becomes zero with both particles and vacancies attaining equal bulk density.

We can take the current J as the order parameter here. Since we know different functional forms of the order parameter in the three phases, we might ask what kind of phase transition happens along the boundary between these phases. J assumes the maximum value $1/4$ in the MC phase. Clearly, it is continuous across the MC-HD and MC-LD boundaries. In fact, even the first order derivatives of J are continuous along these boundaries. The second order derivatives, however, are discontinuous there. So, in analogy with equilibrium statistical physics, the phase transition at the MC-HD and MC-LD boundary is of the second order. On the other hand, first order phase transition occurs across the coexistence line. The first order derivatives of J are discontinuous on this line.

1.1.1.5 Phases of the ASEP

The phase diagram of the ASEP is similar to that of the TASEP. We discuss the phases of the ASEP here because it will be useful to us later. In the thermodynamic limit $L \to \infty$ [212], the ASEP also exhibits three phases - *high density* or HD, *low density* or LD and *maximal current* or MC, as well as HD-LD *coexistence line*. The phase regions as well as bulk density and current in each phase region are listed in the Table 1.1 in terms of the boundary parameters $a = \kappa_{\alpha,\gamma}$ and $b = \kappa_{\beta,\delta}$, where

$$\kappa_{u,v} := \frac{1 - q - u + v + \sqrt{(1 - q - u + v)^2 + 4uv}}{2u}. \tag{1.1.34}$$

To summarize, the 1's have high density ($> 1/2$) in HD phase, low density ($< 1/2$) in LD phase, and density of $1/2$ in MC phase. On the coexistence line, the density has a linear profile. J_1 is $(1 - q)/4$ in MC phase, and depends on a (resp. b) in LD (resp. HD) phase as given in Table 1.1. Figure 1.4 shows the structure of the phase diagram which is drawn using a and b. The macroscopic features of the density profiles in different phases can be understood by appealing to the shock picture on the coexistence line $1 < a = b$ in the phase diagram. This explanation for ASEP is similar to the case of the TASEP as discussed in Section 1.1.1.4.

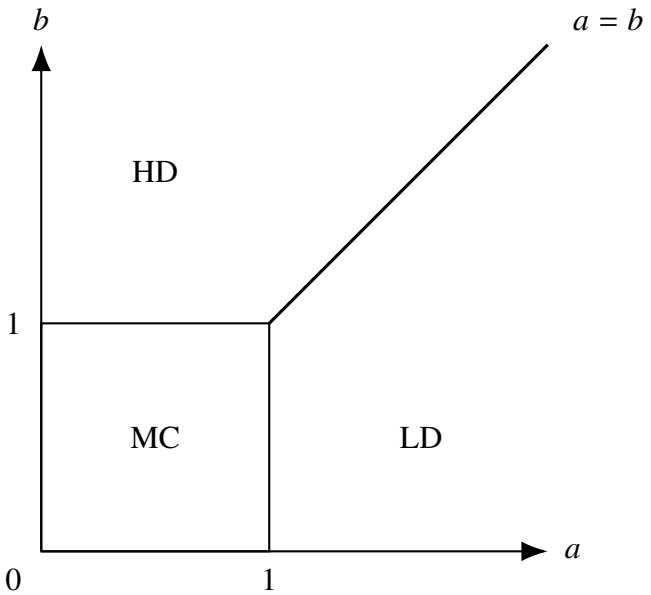

Figure 1.4: Phase diagram for the ASEP. The HD-LD coexistence region is the semi-infinite line $1 < a = b$.

1.1.2 Multispecies exclusion processes

The study of generalized versions of ASEPs is an important and interesting topic. From the point of view of modelling nonequilibrium phenomena, it might be desirable to drop some of the simplifying assumptions which made the one-dimensional single species ASEP suitable. It can be exemplified with the traffic flow. Earlier, we assumed traffic movement for an single-lane road with each vehicle being identical (i.e. having same speed or mobility).

Phase	Phase Region	ρ_1	J_1
HD (High Density)	$\max\{a,1\} < b$	$\frac{b}{1+b}$	$(1-q)\frac{b}{(1+b)^2}$
LD (Low Density)	$\max\{b,1\} < a$	$\frac{1}{1+a}$	$(1-q)\frac{a}{(1+a)^2}$
MC (Maximal Current)	$\max\{a,b\} < 1$	$\frac{1}{2}$	$\frac{1}{4}(1-q)$
HD-LD coexistence line	$1 < a = b$	$\frac{1-x+xb}{1+b}$	$(1-q)\frac{b}{(1+b)^2}$

Table 1.1: Currents and densities for the ASEP. We note here that $\rho_0 + \rho_1 = 1$, and $J_0 = -J_1$.

One possibility is to consider different types or classes of vehicles on a (single-lane) road. This is indeed the case in traffic where both fast vehicles (e.g. cars, ambulances) and slow vehicles (e.g. trucks, carts) might be moving. In order to model traffic flow with various types of vehicles, we can consider *multispecies* ASEP models, i.e. ASEPs with more than one species of particles. Indeed, multispecies ASEPs were used in the modelling of traffic flow in [151, 129, 100, 58], motility mechanism in [198, 170], dense colloidal suspensions in [118] and biological systems in [10, 36, 57, 136]. Moreover, such models can be considered as discrete models for multispecies diffusion in chemical physics [47].

The simplest nontrivial multispecies ASEP model involves two species of particles (and vacancies which may be considered as a different species as well). The two-species models exhibit very interesting physical phenomenology like the single species case [80, 81]. For example, a class of two-species models manifests boundary-induced phase transitions, spontaneous symmetry breaking as well as condensation as observed in [91, 18, 19]. Among the open models, different types of boundaries were considered in a number of studies. In the semipermeable ASEP, the boundaries are semipermeable i.e. one species is not allowed to pass through both the boundaries. The TASEP version was exactly solved in [14, 13]. Later, the phase diagram for a more general version of the semipermeable ASEP was derived with the help of matrix ansatz and using appropriate representation in term of the q-orthogonal polynomials in [211]. The same model was investigated and understood using Koornwinder polynomials in [52]. Nonequilibrium properties in the steady state were understood for the semi-permeable TASEP in [22]. Moreover, open two-species totally asymmetric models with general bulk and boundary rates were studied in [23]. Boundaries in the semipermeable ASEP had a special mathematical property called *integrability*. This mathematical structure played a crucial role in the application of matrix ansatz technique. Such integrable boundary conditions for two-species ASEPs were completely classified in [66]. Finally, phase diagrams were also investigated for a couple of totally asymmetric two-species models in [68] where an explicit representation for matrix ansatz was studied in details.

One might wonder what happens when more than two species are present in the system. Is it possible to find the nonequilibrium properties when arbitrary number of species are interacting? Obviously, we can expect more complicated physical properties and phase diagram for models with the increase of number of species. Moreover, sophisticated mathematical techniques become essential in the analysis to extract the nonequilibrium behaviour in these models. Indeed, there has been some studies related to such models as follows. For periodic boundary

conditions, the matrix ansatz was developed for both the multispecies TASEP [92, 15] and the multispecies ASEP [176, 16]. The NESS for the multispecies TASEP was obtained using queueing-theoretic techniques in [96, 97]. Correlations in the multispecies TASEP was computed for periodic boundary conditions in [20]. The structure of the phase diagram was gleaned for an open multispecies model where rates were chosen from a continuous or discrete distribution [135]. Matrix ansatz was used to understand multispecies models with ordered sequential and sub-lattice parallel update schemes in [100], and a multispecies generalization in the context of traffic flow in [129]. The semi-permeable two-species models were generalized by defining a multispecies ASEP model known as *mASEP* in [53]. There, important results related to its NESS were rigorously proved. In [69], integrable boundary conditions were discussed for a class of multispecies models with arbitrary number of species.

1.2 Plan of Part I

We report the results of our investigation in Chapters 3-5. The content of the chapters are summarized below.

In Chapter 2, we study the phase diagram of the *multispecies ASEP* or *mASEP* [53] with $(2r+1)$ species. In our terminology, there are r positive charges and equal number of negative charges as well as vacancies. The boundaries are impermeable to the vacancies. We use a *colouring argument* to compute the phase diagram via projections on the (two-species) semipermeable ASEP. There are $(2r+1)$ phases in total. In some of the phases, we observe *dynamical expulsion* where one or more species are expelled from the system. Moreover, a species can be localized in a certain region of the system in some phases. We refer to this phenomena as *dynamical localization*. We explain these features using a structure called *nested fat shock* which is the generalized version of *fat shock* studied in the context of the (two-species) semipermeable ASEP [22].

In Chapter 3, we investigate the phase diagram of a model called *left-permeable ASEP* or *LPASEP*. The LPASEP involves two species and vacancies as well as a combination of permeable and semi-permeable boundaries [24]. We apply the matrix ansatz and derive the matrix algebra for the LPASEP. The integrability structure of the LPASEP allows for a representation in terms of continuous big q-Hermite polynomials. We compute the densities and current of the fastest species using asymptotic analysis in the thermodynamic limit. Based on these results, we find there are three bulk phases. We obtain a much richer structure of the phase diagram when we compute the boundary densities.

In Chapter 4, we introduce a model called *multispecies left-permeable ASEP* or *mLPASEP* to generalize the LPASEP. The model can have either $(2r+1)$ or $2r$ species. For the former case, the model involves one species for which the right boundary is impermeable. The model can be projected onto the LPASEP for both the cases using the colouring argument. We determine the phase diagram computing the densities and currents for all species. In this model too, we observe dynamical expulsion in most of the phases. We observe interesting shock structure which can be used for explaining coarse features of the density profiles and the phenomena of dynamical expulsion.

In Chapter 5, we investigate another model, namely *multispecies permissive ASEP* or *mpASEP*

which is a generalized version of the single-species ASEP. The boundaries are permeable to all species. The dynamical rules of particle exchange at the boundaries are such that the mpASEP can be mapped onto the single-species ASEP. Again we apply the colouring argument to compute the phase diagram. We observe dynamical expulsion in most of the phases. However, each species can exhibit high density in one of the phases. Again, we find the generalized shock picture that can be used to understand the density profiles in all the phases.

Chapter 2

The exact phase diagram for a class of open multispecies asymmetric exclusion processes

2.1 Introduction

In this chapter, we study a multispecies exclusion process on a finite one-dimensional lattice with vacancies and r species of charges called the mASEP introduced recently [53]. The hopping rates in the bulk are asymmetric and those in the boundary are defined in such a way that there are $r + 1$ conserved particle numbers. The main results are the following. We obtain the complete $(r + 2)$-dimensional phase diagram and present formulas for all densities and currents in the thermodynamic limit in all regions of the phase diagram. It will turn out that all the macroscopic features can be explained by a new structure which we call a nested fat shock. We review the features for the semipermeable ASEP in Appendix A. We will prove our results by using projections to the semipermeable ASEP.

The chapter is organized as follows. We describe the model in Section 2.2. Then we discuss the colouring argument in Section 2.3. We describe the phases as well as provide proofs for currents and density profiles in Section 2.4. Finally, we discuss the macroscopic properties of the phases in Section 2.5.

2.2 Model

We precisely define the mASEP in Section 2.2.1. We also show in Section 2.2.2 that there is a unique nonequilibrium steady state (NESS) for the mASEP.

2.2.1 Definition

The mASEP is defined on a one-dimensional lattice of size n, where each site is occupied by exactly one particle of type $\{\overline{r}, \ldots, \overline{1}, 0, 1, \ldots, r\}$. The barred particles are negative charges,

the unbarred ones are positive charges, and 0's are vacancies. There are r species of charges, with the total number of particles of charge j being fixed to be n_j for $1 \leq j \leq r$. As a consequence, the number n_0 of vacancies is also fixed, with $n_0 + \ldots + n_r = n$. More precisely, fix an $(r+1)$-tuple of positive integers $\underline{n} = (n_0, \ldots, n_r)$. The state space $\Omega_{\underline{n}}$ consists of all words of length n in the alphabet $\{\overline{r}, \ldots, \overline{1}, 0, 1, \ldots, r\}$ such that the total number of j's and $\overline{j}$'s is equal to n_j for $1 \leq j \leq r$ and the total number of 0's is n_0. The dynamics is the effect of a rightward-pointing electric field. In the bulk, we have the asymmetric hopping rule

$$ij \to ji \quad \text{with rate} \quad \begin{cases} 1 & \text{if } i > j \\ q & \text{if } i < j \end{cases} \tag{2.2.1}$$

where we think of the barred particles as negative numbers, and set $q < 1$. On the left and right boundaries, positive charges can only replace and be replaced by their negatively charged partners with rates given by

$$\underline{\text{Left}}: \quad \begin{cases} \bar{i} \to i & \text{with rate } \alpha \\ i \to \bar{i} & \text{with rate } \gamma \end{cases}$$

$$\underline{\text{Right}}: \quad \begin{cases} i \to \bar{i} & \text{with rate } \beta \\ \bar{i} \to i & \text{with rate } \delta. \end{cases}$$

The mASEP possesses charge-conjugation symmetry in the following sense: interchanging positively and negatively charged particles as well as the rates 1 and q, α and β, and γ and δ, and changing the direction of motion leaves the mASEP invariant. The model with $r = 1$ and $n_0 = 0$ is the single-species open ASEP [79, 212]; for arbitrary n_0, this is the semipermeable ASEP [211]. Furthermore, if $q = \gamma = \delta = 0$, this is the semipermeable TASEP [14, 13, 22] (see Appendix A). We thus denote the mASEP with $q = \gamma = \delta = 0$ as the mTASEP.

2.2.2 Uniqueness of NESS

The mASEP possesses a unique nonequilibrium steady state because it is ergodic; see [153, Theorem 20.1], for example. We will prove below the ergodicity of the mASEP with conserved charges $\underline{n} = (n_0, \ldots, n_r)$.

Proposition 1. *The mASEP is ergodic.*

Proof. It will suffice to prove that the mTASEP with conserved charges $\underline{n} = (n_0, \ldots, n_r)$ is ergodic. This follows from abstract considerations in the theory of affine Coxeter groups [37], but we will prove the ergodicity from first principles.

Define the configurations

$$\begin{aligned}\delta^{\uparrow} = &\quad (\underbrace{0,\ldots,0}_{n_0},\ldots,\underbrace{r,\ldots,r}_{n_r})\\ \delta^{\downarrow} = &\quad (\underbrace{0,\ldots,0}_{n_0},\ldots,\underbrace{\overline{r},\ldots,\overline{r}}_{n_r}),\end{aligned} \tag{2.2.2}$$

both of which belong to the state space. Let $m_j(\tau)$ be the number of j's in τ for $j \in \{\overline{r},\ldots,0,\ldots,r\}$ and $\underline{m} = (m_{\overline{r}},\ldots,m_0,\ldots,m_r)$. Define

$$\begin{aligned}\delta^{\uparrow}_{\underline{m}} = &\quad (\underbrace{\overline{r},\ldots,\overline{r}}_{m_{\overline{r}}},\ldots,\underbrace{0,\ldots,0}_{m_0},\ldots,\underbrace{r,\ldots,r}_{m_r})\\ \delta^{\downarrow}_{\underline{m}} = &\quad (\underbrace{r,\ldots,r}_{m_r},\ldots,\underbrace{0,\ldots,0}_{m_0},\ldots,\underbrace{\overline{r},\ldots,\overline{r}}_{m_{\overline{r}}}).\end{aligned} \tag{2.2.3}$$

We will first show that the following sequence can be obtained

$$\delta^{\downarrow} \to \delta^{\downarrow}_{\underline{m}} \to \tau \to \delta^{\uparrow}_{\underline{m}} \to \delta^{\uparrow}. \tag{2.2.4}$$

First of all, it is clear that τ can be obtained starting from $\delta^{\downarrow}_{\underline{m}}$ and $\delta^{\downarrow}_{\underline{m}}$ can be obtained from τ by making purely bulk transitions. To make transitions from $\delta^{\downarrow}$ to $\delta^{\downarrow}_{\underline{m}}$, first move m_1 of the $\overline{1}$'s to the left by bulk transitions and convert them to 1's. Repeat this procedure for m_2 of the 2's, and so on, all the way till m_r of the r's. We then end up with $\delta^{\downarrow}_{\underline{m}}$. Finally, starting with $\delta^{\uparrow}_{\underline{m}}$, convert all $m_{\overline{r}}$ $\overline{r}$'s to r's on the left boundary and move them to the right. Continue this way for $(\overline{r-1})$'s and so on, all the way till $\overline{1}$'s, ending up with $\delta^{\uparrow}$.

We will now construct a sequence of moves taking $\delta^{\uparrow}$ to $\delta^{\downarrow}$, which is the difficult part of the proof. We will do this in r stages, where the end of the j'th stage will be the configuration given by

$$\sigma_j = (\underbrace{\overline{r},\ldots,\overline{r}}_{n_r},\ldots,\underbrace{\overline{j+1},\ldots,\overline{j+1}}_{n_{j+1}},\underbrace{0,\ldots,0}_{n_0},\underbrace{\overline{1},\ldots,\overline{1}}_{n_1},\ldots,\underbrace{\overline{j},\ldots,\overline{j}}_{n_j}) \tag{2.2.5}$$

Starting from $\delta^{\uparrow}$, convert all r's to $\overline{r}$'s and move them to the left. Repeat this procedure for $\overline{r-1}$'s continuing up to $\overline{2}$'s. Now convert all 1's to $\overline{1}$'s to end up with σ_1. We now show how to reach σ_{j+1} from σ_j. First, convert all $\overline{r}$'s to r's, move them to the right, and convert them back to $\overline{r}$'s. Repeat this procedure for $\overline{r-1}$'s continuing up to $\overline{j+1}$'s. Now move all $\overline{r},\ldots,\overline{j+2}$'s to the left using bulk transitions to end up with σ_{j+1}. Once we have repeated this argument r times, we end up with $\sigma_r = \delta^{\uparrow}$.

We have thus shown how to reach $\delta^{\uparrow}$ from τ and vice versa for every configuration τ, thus completing the proof.

□

As an illustration of Proposition 1, we give the following example.

Example 1. The transition graph of the mTASEP with $r = 2$ and $\underline{n} = (1, 1, 1)$ is given in Figure 2.1.

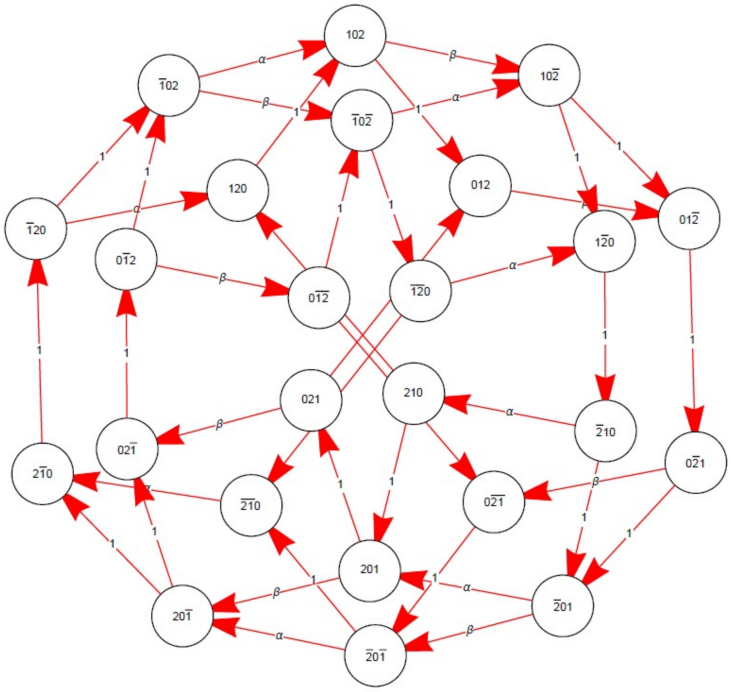

Figure 2.1: The transition graph of the mTASEP with $\underline{n} = (1, 1, 1)$. The rates associated to each transition are marked on the arrows.

2.3 Colouring argument for mASEP

The colouring argument is reviewed in the context of the semipermeable TASEP in Appendix A. For mASEP, we will use a colouring scheme called *k-colouring* which is the following. We label species $\{\overline{k-1}, \ldots, 0, \ldots, k-1\}$ with 0_k, species $\{\overline{r}, \ldots, \overline{k}\}$ with $\overline{1}_k$, and species $\{r, \ldots, k\}$ with 1_k. Then the new species $\overline{1}_k$, 0_k and 1_k follow exactly the dynamics of the two-species semipermeable ASEP both in the bulk and at the boundaries. We describe these ideas more precisely below.

The colouring argument is known as *projection* or *lumping* in the mathematical literature. For completeness, we define here a general notion of lumping of Markov processes, which plays the key role in the proof of our results.

Definition 1 ([153, Section 2.3])**.** *Let (X_t) be a Markov process on a state space Ω with Markov matrix M. Let $\mathcal{S}$ be a set partition of Ω (i.e. a collection of pairwise disjoint subsets of Ω whose union is Ω). If, for all $S, T \in \mathcal{S}$, and $x, x' \in S$,*

$$\sum_{y \in T} M(y, x) = \sum_{y \in T} M(y, x') \tag{2.3.1}$$

then the stochastic process (Y_t) on $\mathcal{S}$ which is obtained from (X_t) by keeping track of the subset of is itself a Markov process, with Markov matrix M' given by $M'(T,S) = \sum_{y\in T} M(y,x)$. The process (Y_t) is then said to be a lumping of (X_t).

Recall that the mASEP is defined by the conserved charges $\underline{n} = (n_0, \ldots, n_r)$ with state space $\Omega_{\underline{n}}$.

Definition 2. *For k such that $1 \leq k \leq r$, set $\underline{n}' = (n_0 + \ldots + n_{k-1}, n_k + \ldots + n_r)$. Define the map $\lambda_k : \Omega_{\underline{n}} \to \Omega_{\underline{n}'}$ as follows:*

$$\lambda_k(\tau_i) = \begin{cases} 0 & \text{if } \tau_i \text{ has charge } j \text{ or } \overline{j} \text{ and } 0 \leq j < k, \\ 1 & \text{if } \tau_i \text{ has charge } j \text{ or } j \geq k, \\ \overline{1} & \text{if } \tau_i \text{ has charge } \overline{j} \text{ or } j \geq k. \end{cases} \tag{2.3.2}$$

Then the k-colouring of the mASEP with conserved charges $\underline{n}$ is the set partition of $\Omega_{\underline{n}}$ obtained by λ_k^{-1}.

Proposition 2. *Let $\underline{n} = (n_0, \ldots, n_r)$ and $1 \geq k \geq r$. The k-colouring leads to a lumping of the mASEP with conserved charges $\underline{n}$ onto the semipermeable ASEP with $n_0 + \ldots + n_{k-1}$ particles of species 0.*

Proof. One can check that the transitions in the bulk, as well as those in the left and right boundary, commute with the map λ_k. □

As a consequence of Proposition 2, we will call the lumping of the mASEP via the k-colouring as the *k-coloured semipermeable ASEP*.

2.4 Phase diagram

We discuss the phase diagram in this section. First, we describe the phases as well as densities and currents in these phases. Then we provide the proofs of the relations which determine density profiles and currents.

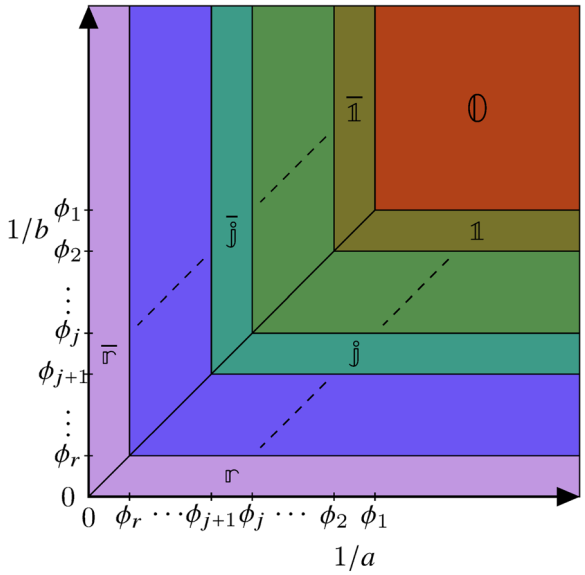

Figure 2.2: The nonequilibrium phase diagram of the mASEP with r species of charges. There are $2r+1$ different regions, which are labelled $\mathbb{0}, \mathbb{1}, \ldots, \mathbb{r}, \bar{\mathbb{1}}, \ldots, \bar{\mathbb{r}}$. Each region is characterized by different bulk densities of all particles. The explanation for the nomenclature of the phases is given below. See Tables 2.1 and 2.2 for the densities and currents respectively in the NESS in these $2r+1$ regions.

2.4.1 Phases

We define following parameters in order to describe the phase diagram. For each integer j between 0 and r, let $\theta_j = n_j/n$ be the total density of (both positively and negatively charged) particles of species j. We consider the behaviour of the mASEP in the limit $n \to \infty$ and $n_j \to \infty$ for each j such that the total density of species j particles converges to $\theta_j > 0$. Define the quantities

$$a = \frac{1-q-\alpha+\gamma+\sqrt{(1-q-\alpha+\gamma)^2+4\gamma\alpha}}{2\alpha}$$
$$b = \frac{1-q-\beta+\delta+\sqrt{(1-q-\beta+\delta)^2+4\beta\delta}}{2\beta} \tag{2.4.1}$$

and the function $f(x) = 1/(1+x)$. Set $\Theta_k = (\theta_k + \ldots + \theta_r)/2$ and $\phi_k = \Theta_k/(1-\Theta_k)$ for $1 \le k \le r$. Then the exact phase diagram is given in Figure 2.2.

The nonequilibrium phase diagram of the r-species mASEP in Figure 2.2 comprises $2r+1$ phases, $\bar{\mathbb{r}}, \ldots, \bar{\mathbb{1}}, \mathbb{0}, \mathbb{1}, \ldots, \mathbb{r}$, each one of which is characterised by the bulk densities ρ_j for $j \in \{\bar{r}, \ldots, 0, \ldots, r\}$, as well as the currents J_j for $j \in 1, \ldots, r$ of all types of particles; we tabulate these in Tables 2.1 and 2.2 respectively. Note that there is no current of 0's and the current of $\bar{j}$'s to the left is the same as that of j's to the right. The mean densities of the j and $\bar{j}$ jump discontinuously across the $\mathbb{j} - \bar{\mathbb{j}}$ boundary. By contrast, the mean densities vary continuously along the $\mathbb{j} - (\mathbb{j}+\mathbb{1})$ (and $\bar{\mathbb{j}} - (\overline{\mathbb{j}+\mathbb{1}})$) boundary. All currents J_j change continuously across all phase boundaries in Figure 2.2. In all phases except $\mathbb{0}$, the system

shows phase coexistence with a sharp interface separating intervals of different density for some particle type, as we show by the illustrative density profiles in Figure 2.3 for the mTASEP with $r = 2$ and Figure A.2 in Appendix A for the mASEP with $r = 1$. The proofs of the density profiles in Table 2.1 and currents in Table 2.2, which explain the phase diagram in Figure 2.2, are given below.

Phase	Densities in the bulk	
	Species	Density ρ
$\mathbb{0}$	$k = 0$	$\rho_0 = \theta_0$
	$1 \le k \le r$	$\rho_k = \rho_{\overline{k}} = \theta_k/2$
$\mathbb{j}$	$k = 0$	ρ_0 piecewise constant
	$1 \le k \le j-1$	$\rho_{\overline{k}} = 0$ ρ_k piecewise constant
	$k = j$	$\rho_{\overline{j}} = f(b) - \Theta_{j+1}$ ρ_j piecewise constant
	$j+1 \le k \le r$	$\rho_k = \rho_{\overline{k}} = \theta_k/2$
$\overline{\mathbb{j}}$	$k = 0$	ρ_0 piecewise constant
	$1 \le k \le j-1$	$\rho_k = 0$ $\rho_{\overline{k}}$ piecewise constant
	$k = j$	$\rho_j = f(b) - \Theta_{j+1}$ $\rho_{\overline{j}}$ piecewise constant
	$j+1 \le k \le r$	$\rho_k = \rho_{\overline{k}} = \theta_k/2$
$\mathbb{j} - \overline{\mathbb{j}}$ boundary	$k = 0$	ρ_0 piecewise linear
	$1 \le k \le j-1$	$\rho_k, \rho_{\overline{k}}$ piecewise linear
	$j+1 \le k \le r$	$\rho_k = \rho_{\overline{k}} = \theta_k/2$

Table 2.1: The densities of all species of particles in phase $\mathbb{0}$, as well as phases $\mathbb{j}$ and $\overline{\mathbb{j}}$, and the $\mathbb{j} - \overline{\mathbb{j}}$ boundary for $1 \le j \le r$. Piecewise constant densities correspond to phase separation and piecewise linear profiles correspond to averaging over shocks. The exact formulas can be calculated from the schematic plots in the top row of Figure 2.6.

2.4.2 Proofs for currents and density profiles

First, we obtain the densities of species r and $\overline{r}$ in the mASEP.

Proposition 3. *The densities at site i of species r and $\overline{r}$ (resp. current J_r of species r) in the mASEP with conserved charges $(n_0, \ldots, n_r)$ are the same as those of the densities at site i of species 1 and $\overline{1}$ respectively (resp. current J_1 of species 1) in the semipermeable ASEP with size $n_0 + \ldots + n_r$ with $n_0 + \ldots + n_{r-1}$ particles of species 0.*

Proof. This follows immediately from Proposition 2 using the r-colouring. □

To arrive at the main result, we take the limit of the mASEP with r species of charges with $n_0, \ldots, n_r \to \infty$ such that $n_j/n \to \theta_j$ for all $1 \le j \le r$.

Theorem 1. *The densities and currents of particles of all species in all phases in the mASEP with r species of charges are given in Table 2.1 and Table 2.2 respectively.*

Proof. We will simultaneously use all possible k-colourings in the proof. First, we fix some notation. For the k-coloured ASEP, we denote the species by 1_k, 0_k and $\overline{1}_k$. The (fixed) number of particles of species 0_k is $n_{0_k} = n_0 + \ldots + n_{k-1}$ and hence $\theta_{0_k} = \theta_0 + \cdots + \theta_{k-1}$ and similarly for θ_{1_k} and $\theta_{\overline{1}_k}$. The single-site densities and currents of the k-coloured species are related to those of the original mASEP as follows:

$$\begin{aligned} \rho_{1_k} &= \rho_k + \ldots + \rho_r, \\ \rho_{\overline{1}_k} &= \rho_{\overline{k}} + \ldots + \rho_{\overline{r}}, \\ \rho_{0_k} &= \rho_{\overline{k-1}} + \ldots + \rho_{k-1}, \\ J_{1_k} &= J_k + \ldots + J_r. \end{aligned} \tag{2.4.2}$$

We give the proof of the densities and currents in phase $\mathbb{j}$. The argument for the other phases and phase-boundaries is similar. Recall that the phase $\mathbb{j}$ is defined by the constraints

$$\frac{1+\theta_0+\ldots+\theta_{j-1}}{1-(\theta_0+\ldots+\theta_{j-1})} < b < \frac{1+\theta_0+\ldots+\theta_j}{1-(\theta_0+\ldots+\theta_j)} \text{ and } b > a, \tag{2.4.3}$$

according to the phase diagram in Figure 2.2. Now, consider the k-colouring of the mASEP for $k \le j$. In that case, we see that $b > (1+\theta_{0_k})/(1-\theta_{0_k})$ and hence, the k-coloured semipermeable ASEP is in phase $\mathbb{1} = \mathrm{B}$. Thus $\rho_{\overline{1}_k}$ equals $1/(b+1)$ in the bulk (from Table A.1) for each $1 \le k \le j$.

$$\rho_{\overline{1}} + \cdots + \rho_{\overline{r}} = \rho_{\overline{2}} + \cdots + \rho_{\overline{r}} = \cdots = \rho_{\overline{j}} + \cdots + \rho_{\overline{r}} = \frac{1}{1+b}, \tag{2.4.4}$$

from which it follows that $\rho_{\overline{1}} = \rho_{\overline{2}} = \cdots = \rho_{\overline{j-1}} = 0$. Now, consider the k-colouring of the mASEP for $j < k \le r$. In that case,

$$\frac{1+\theta_{0_k}}{1-\theta_{0_k}} > \frac{1+\theta_0+\ldots+\theta_j}{1-(\theta_0+\ldots+\theta_j)} > b \tag{2.4.5}$$

and the k-coloured semipermeable ASEP is in $\mathbb{0} = \mathrm{C}$. From Table A.1, we see that

$$\rho_{\overline{1}_k} = \frac{1-\theta_{0_k}}{2} = \frac{\theta_k + \cdots + \theta_r}{2}, \tag{2.4.6}$$

and hence $\rho_k = \theta_k/2$ for each $j+1 \le k \le r$. Now, using (2.4.4), we can calculate the density of j. We have thus obtained the densities of all negatively charged species of particles. See the top row of Figure 2.4(a) for comparison. Similar computations yield the densities of positively charged species and 0, as well as the currents. □

Remark 1. In [53, Corollary 2], it is shown that the nonequilibrium partition function $Z_{\underline{n}}$ is given by the following explicit product formula

$$Z_{\underline{n}} = \prod_{k=1}^{r} Z_{(n_0+\cdots+n_{k-1},\, n_k+\cdots+n_r)} \tag{2.4.7}$$

where $Z_{(n_0,\, n_1)}$ is the partition function for the semipermeable ASEP [211, Equation (5.6)], where the notation $L = n_0 + n_1$ and $N = n_0$ is used for the system size and the number of 0's respectively. Theorem 1 provides a justification (although not a proof) of why the factorization of the partition function in (2.4.7) is to be expected. The k'th term on the right is precisely the partition function of the k-coloured semipermeable ASEP explained in Proposition 2.

Phase	Currents	
	Species	Values of J_k
$\mathbb{0}$	$1 \le k < r$	$(1-q)(\Theta_k - \Theta_{k+1})(1 - \Theta_k - \Theta_{k+1})$
	$k = r$	$(1-q)\Theta_r(1-\Theta_r)$
$\mathbb{j}$	$1 \le k \le j-1$	0
	$k = j$	$(1-q)(f(b)(1-f(b)) - \Theta_{j+1}(1-\Theta_{j+1}))$
	$j+1 \le k < r$	$(1-q)(\Theta_k - \Theta_{k+1})(1 - \Theta_k - \Theta_{k+1})$
	$k = r$	$(1-q)\Theta_r(1-\Theta_r)$
$\bar{\mathbb{j}}$	$1 \le k \le j-1$	0
	$k = j$	$(1-q)(f(a)(1-f(a)) - \Theta_{j+1}(1-\Theta_{j+1}))$
	$j+1 \le k < r$	$(1-q)(\Theta_k - \Theta_{k+1})(1 - \Theta_k - \Theta_{k+1})$
	$k = r$	$(1-q)\Theta_r(1-\Theta_r)$

Table 2.2: The currents of all species of particles in phase $\mathbb{0}$, as well as phases $\mathbb{j}$ and $\bar{\mathbb{j}}$ for $1 \le j \le r$. All currents are seen to be continuous across the $\mathbb{j} - \bar{\mathbb{j}}$ boundary. For the special cases of $\mathbb{r}$ and $\bar{\mathbb{r}}$, take $\Theta_{r+1} = 0$. Note that $J_0 = 0$ and $J_{\overline{k}} = -J_k$.

2.5 Macroscopic properties of the phases

We discuss the macroscopic properties of the phases in this section. We start with the simpler case of $r = 2$ in Section 2.5.1. Then we develop the nested fat shock in Section 2.5.2. Using this construction, we understand the macroscopic features of the mASEP.

2.5.1 Example of $r = 2$

We illustrate the density profiles for various regions in the phase diagram for the example of the 2-species mTASEP (i.e. $q = \gamma = \delta = 0$) in Figure 2.3. Therefore, $a = (1-\alpha)/\alpha$ and $b = (1-\beta)/\beta$ from (2.4.1), and $f(a) = \alpha$, $f(b) = \beta$. There are five phases for this system, corresponding to $r = 2$, and two relevant phase-boundaries. The currents can be calculated

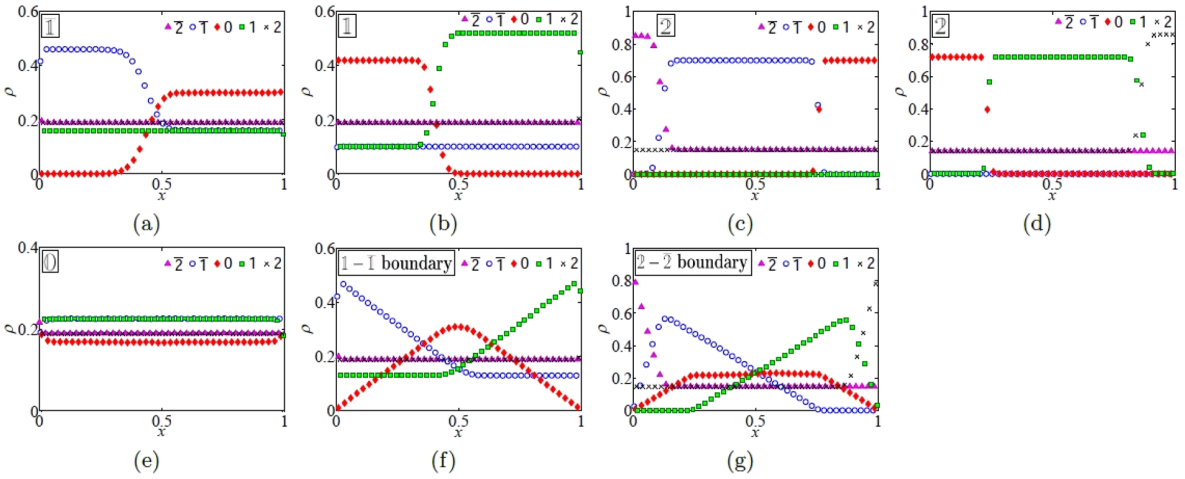

Figure 2.3: Plots of the densities of particles 2 (black crosses), 1 (green squares), 0 (red diamonds), 1 (blue circles), and 2 (pink triangles), versus the scaled position $x = m/n$ for the mTASEP with $r = 2$ where $n = 1000$, $\theta_0 = 0.17, \theta_1 = 0.45$ and $\theta_2 = 0.38$ in the regions (a) $\overline{\mathbb{1}}$ ($\alpha = 0.35, \beta = 0.83$), (b) $\mathbb{1}$ ($\alpha = 0.73, \beta = 0.29$), (c) $\overline{\mathbb{2}}$ ($\alpha = 0.15, \beta = 0.81$), (d) $\mathbb{2}$ ($\alpha = 0.73, \beta = 0.14$), (e) $\mathbb{0}$($\alpha = 0.71, \beta = 0.87$), (f) the $\mathbb{1} - \overline{\mathbb{1}}$ shock line ($\alpha = \beta = 0.32$), and (g) the $\mathbb{2} - \overline{\mathbb{2}}$ shock line ($\alpha = \beta = 0.15$).

by mean-field type calculations from the densities in each of the regions. More precisely, $J_2 = \rho_2(1 - \rho_2) = \rho_{\overline{2}}(1 - \rho_{\overline{2}})$ and $J_1 = \rho_1(1 - \rho_1 - 2\rho_2) = \rho_{\overline{1}}(1 - \rho_{\overline{1}} - 2\rho_{\overline{2}})$. When there is phase-separation, the densities of all species conspire to ensure that the currents are constant across the system (because of particle conservation in the bulk). The value of the currents in each phase can be compared with Table 2.2.

In phase $\mathbb{0}$, all densities are constant, and the densities of oppositely charged particles are equal. Therefore, $\rho_0 = \theta_0$, and $\rho_k = \rho_{\overline{k}} = \theta_k/2$ for $k = 1, 2$. This is seen in Figure 2.3(e) and matches with the first row of Table 2.1.

In phase $\mathbb{1}$, the densities of 2's, 2 and 1's are constant, whereas those of 1's and 0's undergo phase separation. As in phase $\mathbb{0}$, $\rho_2 = \rho_{\overline{2}} = \theta_2/2$. Moreover, $\rho_{\overline{1}} = \beta - \theta_2/2$ is also constant throughout the system. In the phase-separated regions, either $\rho_1 + \rho_{\overline{1}} = 1 - \beta_2$ (forcing $\rho_0 = 0$), or $\rho_1 = \rho_{\overline{1}}$ from which ρ_0 can be calculated. The density plots can be seen in Figure 2.3(b) and match the calculation of the densities in the second row of Table 2.1 with $\mathbb{j} = \mathbb{1}$. The density profiles in $\overline{\mathbb{1}}$ can be calculated analogously using charge-conjugation symmetry.

In phase $\mathbb{2}$, the only constant densities are given by $\rho_{\overline{2}} = \beta$ and $\rho_{\overline{1}} = 0$. It is not immediately obvious why 1's are excluded from the system, and we give an explanation for this phenomenon of dynamical expulsion in the next section. Particles of species 0, 1 and 2 are phase segregated in three distinct parts. The density of 2's, ρ_2, is given by $1 - \beta$ in the rightmost part and $\rho_{\overline{2}}$ in the other two parts. Particles of species 0 exist only in the leftmost part with density $1 - 2\beta$, and those of species 1 exist only in the middle part with the same density. In the thermodynamic limit, the middle part is infinitely far away from both boundaries and it is not immediately clear how 1's can be localized in the bulk. We call this phenomenon *dynamical localization* and explain how this occurs in the next section. The densities can be seen in Figure 2.3(d) and

match the calculation of the densities in the second row of Table 2.1 with $\mathbb{j} = \mathbb{2}$. Again, the profiles in $\overline{\mathbb{2}}$ can be calculated using charge-conjugation symmetry.

The nomenclature for the phases can now be explained. Each phase is denoted by the phase-segregated species with largest absolute value. For example, 0's and 1's are segregated in phase $\mathbb{1}$, 0's and $\overline{1}$'s are segregated in phase $\overline{\mathbb{1}}$, 0's, 1's and 2's are segregated in phase $\mathbb{2}$, and 0's, 1's and 2's are segregated in phase $\overline{\mathbb{2}}$. The sole exception is phase $\mathbb{0}$, where all species have constant density.

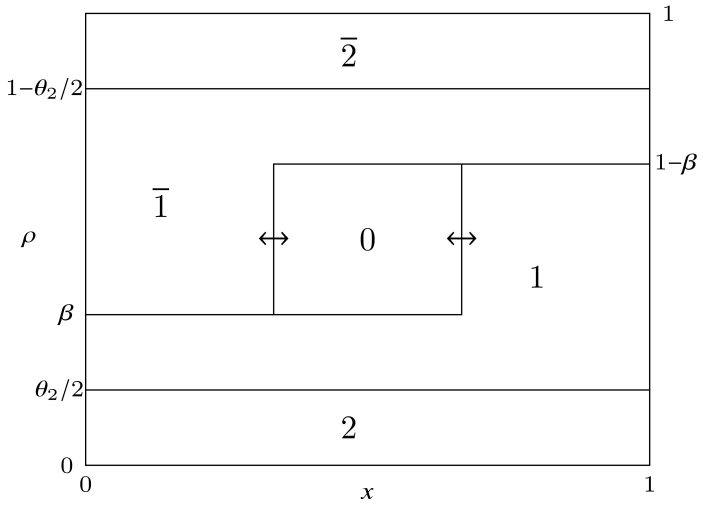

Figure 2.4: Instantaneous picture of the nested fat shock in the $\mathbb{1} - \overline{\mathbb{1}}$ boundary in the rescaled mTASEP with $r = 2$. Each connected region is labelled with the species of a particle and the height of a region at a given location represents the density of that species at that point.

To understand the density profiles in the $\mathbb{1} - \overline{\mathbb{1}}$ and $\mathbb{2} - \overline{\mathbb{2}}$ boundaries, we appeal to the nested fat shock construction, which we explain below. Recall that the phase diagram is calculated in the limit where the system size, $n \to \infty$. We rescale the system by a factor of $1/n$ so that the locations lie in the interval $[0, 1]$. In the $\mathbb{1} - \overline{\mathbb{1}}$ boundary, as shown in Figure 2.4, the densities of particles 2 and $\overline{2}$ are constant and equal to $\theta_2/2$. All the particles of type 0 form a 'bound state' of fixed width. We call this the nested fat shock (the nesting is of order 1 here). Both ends of the bound state execute a synchronised symmetric random walk with reflecting boundary conditions. As a consequence, $\rho_{\overline{1}}$, ρ_0 and ρ_1 are piecewise linear after averaging. In particular, ρ_1 is constant towards the left, since the right end of the bound state cannot move all the way to the left, and similarly for $\rho_{\overline{1}}$. This is shown in Figure 2.3(f).

In the $\mathbb{2} - \overline{\mathbb{2}}$ boundary as shown in Figure 2.5, none of the densities are constant, and the picture is more complicated. The nested fat shock here consists of the regions containing $\overline{1}$'s, 0's and 1's, in that order from left to right. The nesting is of order 2 here. There are four boundaries between the regions $\overline{2} - \overline{1}$, $\overline{1} - 0$, $0 - 1$ and $1 - 2$, and all of them perform synchronised symmetric random walks in the bulk so that the widths of the regions containing $\overline{1}$, 0 and 1 is fixed. When one of them touches the boundary the widths of either 1 or 1 can decrease, causing the oppositely charged region to increase in size so that the sum of the widths of these two remains constant. The width of the region containing 0 never changes. This behaviour results in the piecewise linear profile shown in Figure 2.3(g).

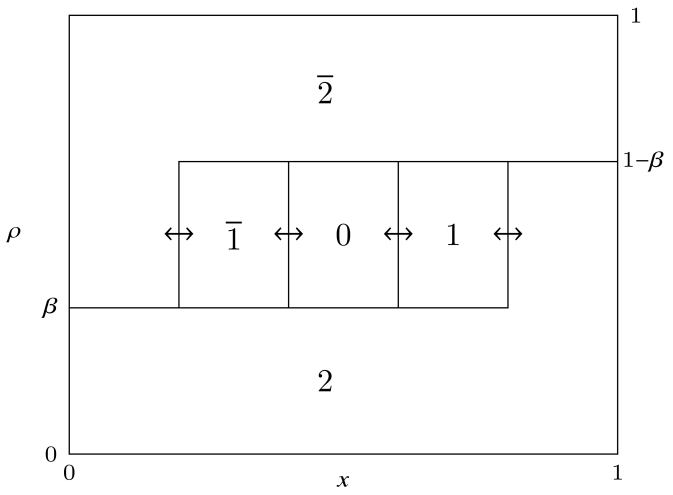

Figure 2.5: Instantaneous picture of the nested fat shock in the $2 - \overline{2}$ boundary in the rescaled mTASEP with $r = 2$. Each connected region is labelled with the species of a particle and the height of a region at a given location represents the density of that species at that point.

One can now derive the density profiles in regions $\mathbb{1}, \mathbb{2}, \overline{\mathbb{1}}$ and $\overline{\mathbb{2}}$ from these nested fat shocks. For example, in $\mathbb{1}$, one has the same nested fat shock structure as in Figure 2.4, but the ends of the bound state containing 0 execute a random walk with negative drift, which ensures that the nested fat shock is pinned to the left. Similarly, the nested fat shock is pinned to the right in $\overline{\mathbb{1}}$. Similarly, the density profiles in $\mathbb{2}$ and $\overline{\mathbb{2}}$ can be calculated by forcing the nested fat shock in Figure 2.5 to be pinned to the left and right respectively.

The general structure of the nested fat shock is explained in the next section.

2.5.2 Nested fat shock

All coarse features of the phase diagram in Figure 2.2 are explained by the nested fat shock construction. This is a generalisation of the fat shock construction, which explains the phase diagram for the semipermeable TASEP [22] (i.e. the mTASEP with $r = 1$). Roughly speaking, the fat shock consists of a macroscopic interval of the system, where all the 0's are localized. The 0's form two simultaneous shocks with the 1's and $\overline{1}$'s, with a constant macroscopic width. For more details on the fat shock, see Appendix A.

The nested fat shock is a macroscopic interval of the system where, for some $j = 0$, particles of species $\overline{j}, \ldots, 0, \ldots, j$ are localized in a very specific way.

Particles of species 0 have a nonzero constant density in a subinterval of fixed width inside this interval. Particles of species 1 (resp. $\overline{1}$) have a nonzero constant density in a subinterval to the right (resp. left) of the 0's. Although the widths of the 1 and $\overline{1}$ subintervals may vary, the sum of their widths is fixed. This pattern continues until species j on the right and species $\overline{j}$ on the left. The boundary between any two adjacent subintervals is a shock-front. Depending on which part of the phase diagram the system finds itself in, the nested fat shock can have either negative, positive or zero drift. If the drift is negative, the negatively charged subintervals containing $\overline{1}, \ldots, \overline{j}$ will not exist, and similarly if there is positive drift, the positively charged

subintervals $1, \ldots, j$ will vanish. If there is zero drift, all subintervals will exist and move in a synchronized fashion.

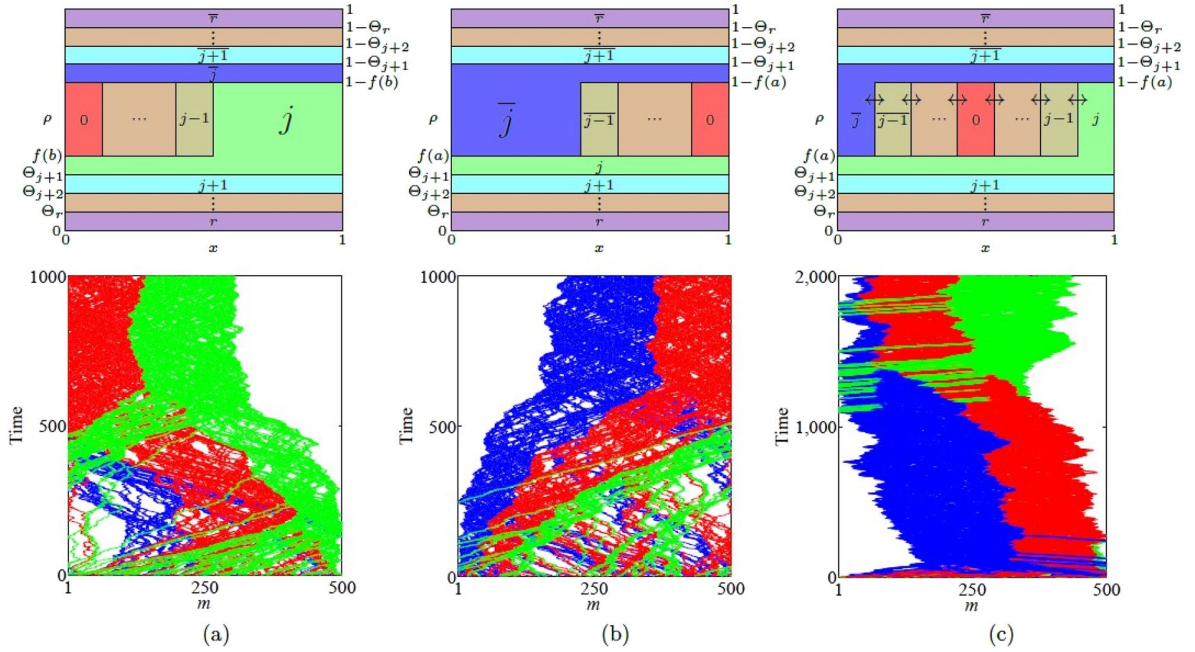

Figure 2.6: The top row shows schematic plots of the densities ρ_j and $\rho_{\overline{j}}$, for all j, versus the normalised position x illustrating the nested fat shock (a) pinned to the left in region $\mathbb{j}$, (b) pinned to the right in region $\overline{\mathbb{j}}$ and (c) unpinned in the $\mathbb{j} - \overline{\mathbb{j}}$ boundary in (c). The densities $\rho_a(x)$ are plotted against the rescaled location x. The value of $\rho_a(x)$ is the height of the region containing particle a at x. The bottom row shows simulation results in multiples of 2000 steps as spatiotemporal plots for the mTASEP with $r = 2$ and $n_0 = 70, n_1 = 100, n_2 = 330$ in (a) region $\mathbb{2}(\alpha = 0.79, \beta = 0.23)$, (b) region $\overline{\mathbb{2}}(\alpha = 0.25, \beta = 0.73)$, and (c) the $\mathbb{2} - \overline{\mathbb{2}}$ boundary $(\alpha = \beta = 0.28)$. The blue, red and green colours represent $\overline{1}$, 0 and 1 particles respectively. The particles of type 2 and $\overline{2}$ are shown in white.

The top row of Figure 2.6 shows the structure of the nested fat shock in these three cases in the most general scenario. We give a concrete example of a simulation run of the mTASEP with $r = 2$ in the bottom row of the figure, which shows the results for phases (a) $\mathbb{2}$ (negative drift), (b) $\overline{\mathbb{2}}$ (positive drift), and (c) the $\mathbb{2} - \overline{\mathbb{2}}$ boundary (zero drift). The simulations show the densities of particles of species $\overline{1}$, 0 and 1 only. If the nested fat shock has nonzero drift, it gets pinned to one of the boundaries; it is pinned on the left in (a) and on the right in (b). When the nested fat shock is pinned to the left, it consists of species 0 and 1, and particles of species $\overline{1}$ exit the system from the left. Similarly, when pinned to the right, it consists of species $\overline{1}$ and 0, and particles of species 1 vacate the system from the right. When the nested fat shock has zero drift as in (c), blocks of $\overline{1}$, 0 and 1 are present, with all shock fronts performing lockstep symmetric random walks.

2.5.3 General case: mASEP with arbitrary r

The precise details for the macroscopic features of each phase with reference to the nested fat shock are given below.

2.5.3.1 Region $\mathbb{0}$

Here, only the particles of species 0 participate in the nested fat shock and the width of the shock is larger than the system size. As a result, all densities are constant throughout the system. This explains the densities and currents in region $\mathbb{0}$. See the density plot in Figure 2.3(e) for the result of simulations.

2.5.3.2 Regions $\mathbb{j}$ and $\bar{\mathbb{j}}$

We give details only for region $\mathbb{j}$, since those of $\bar{\mathbb{j}}$ can be obtained by analogous arguments.

In region $\mathbb{j}$, particles of species $\overline{j-1}, \ldots, 0, \ldots, j-1$ participate in the nested fat shock. The velocity of this shock is negative and it gets pinned to the left boundary. However, this is not a stable situation. Initially, particles of species $\overline{j-1}$ will be replaced by those of species $j-1$, which will then move rightwards in the bulk, until they join the subinterval of the nested fat shock occupied by the particles of species $j-1$. Once that process is completed, a similar phenomenon will happen with particles of species $\overline{j-2}$. This process will continue until all negatively charged particles in the nested fat shock have been replaced by their positive counterparts. In the steady state, we will only see particles of species $0, \ldots, j-1$ participating in the shock, which will be pinned to the left.

We point out two new nonequilibrium features of this phase which can be seen in the top row of Figure 2.6(a). First, note that species 0 through $j-1$ are localised in the interior of the system. Each of these species has undergone phase separation, with one region of non-zero density and the remaining of zero density. The precise locations of the region with non-zero density can be calculated from the values of $\theta_0, \ldots, \theta_{j-1}$. What is more interesting is that species 1 through $j-1$ are localized away from the boundary. This is somewhat counterintuitive since we have taken the thermodynamic limit and these particles are infinitely far away from the boundary. We call this phenomenon dynamical localization. Such a phenomenon cannot occur in an equilibrium system. The second new feature is the complete absence of particles of species $\overline{1}, \ldots, \overline{j-1}$ in the system, i.e. $\rho_{\overline{1}} = \cdots = \rho_{\overline{j-1}} = 0$. This is related to the previous phenomenon since these particles can only enter at the expense of the dynamically localised particles. We call this phenomenon dynamical expulsion. In the extreme case of the $\mathbb{r}$ phase, all the barred particles except r are expelled.

The picture in the $\bar{\mathbb{j}}$ phase can be derived analogously. See the density plots in Regions $\overline{\mathbb{1}}, \mathbb{1}, \overline{\mathbb{2}}$ and $\mathbb{2}$ of Figure 2.3 (a), (b), (c) and (d) respectively for the results of simulations. See Figure 2.6(a) (resp. (b)) for an illustration of the nested fat shock pinned on the left (resp. right) in the top row and the result of a simulation for $r = 2$ and $\mathbb{2}$ (resp. $\overline{\mathbb{2}}$) in the bottom row.

2.5.3.3 Boundary of the $\mathbb{j} - \bar{\mathbb{j}}$ region

In the $\mathbb{j} - \bar{\mathbb{j}}$ boundary, particles of species $\overline{j-1}, \ldots, 0, \ldots, j-1$ participate in the nested fat shock. The velocity of the shock fronts are now zero. Therefore, all these fronts perform a lockstep symmetric random walk in the bulk of the system. All subinterval widths will remain constant until the nested fat shock hits the boundary. When one of the extreme fronts gets pinned to the boundary, the widths of the subinterval containing $j-1$'s and $j-1$'s can change, but the sum of their widths will remain constant. The other subinterval widths will remain the same. While this front is pinned, the other fronts continue to move synchronously until either another one gets pinned or the one stuck to the boundary gets unpinned. If one more (either $j-2$ or $\overline{j-2}$) gets pinned, the same phenomenon will repeat for that species. Note that, for instance, if the nested fat shock gets (temporarily) pinned to the right and then the next shock front also gets pinned, the density of $j-2$'s becomes zero. More and more shock fronts can get pinned until the fat shock containing 0's touches the boundary, at which point the latest front to get pinned can only get unpinned. We thus end up with an instantaneous profile whose schematic is given in the top row of Figure 2.6(c). A simulation of the movement of the shock fronts can be seen in the spatiotemporal plot in the bottom row of Figure 2.6(c). The steady state density profile can be obtained by averaging over the uniform shock locations and gives rise to piecewise linear profiles for species $\bar{j}, \ldots, 0, \ldots, j$. The calculation of these profiles is not difficult, but is tedious and is skipped. The currents have the same values as those in regions $\mathbb{j}$ and $\bar{\mathbb{j}}$ with $a = b$.

Chapter 3

Left-permeable asymmetric simple exclusion process

3.1 Introduction

In this chapter, we focus on one of the integrable classes of exclusion processes with two species of particles and vacancies. The vacancies are considered here as a separate species of particles. The vacancies can only enter and exit from the left boundary. We call this the *left-permeable two-species ASEP* (or *LPASEP* in short). We begin with the preliminaries in Section 3.2. We derive the matrix product solution for the stationary distribution in Section 3.3 and find a representation of the matrix algebra in Section 3.4. We find the phase diagram of the model in the thermodynamic limit and derive formulas for the densities and current in all phases in Section 3.5. We end by computing the enriched phase diagrams for two different order parameters in Section 3.5.2: the density of the vacancies at the last site, and the difference of bulk and boundary densities for both species. We note that a large part of these calculations are generalizations of Uchiyama's techniques [211].

3.2 Preliminaries

3.2.1 Definition of the model

The two-species ASEP describes particles hopping on a one dimensional lattice. We consider a finite lattice of length L where each lattice site is either empty, or occupied by a single particle of species $\overline{1}$ or 1. Particles move along the lattice by exchanging places with their immediate neighbours. We can consider an empty site as a particle of species 0 (with $\overline{1} < 0 < 1$), and then specify a lattice configuration by the tuple $\boldsymbol{\tau} = (\tau_1, \ldots, \tau_L)$, $\tau_i \in \{\overline{1}, 0, 1\}$. In the bulk, exchanges between neighbouring particles occur with rates

$$\tau_i \tau_{i+1} \longrightarrow \tau_{i+1} \tau_i \text{ with rate } \begin{cases} p, & \tau_i > \tau_{i+1}, \\ q, & \tau_i < \tau_{i+1}. \end{cases} \tag{3.2.1}$$

We will take $p > q$ so that a particle of species j moves preferentially to the right ahead of all species $i < j$.

At the boundaries, we allow particles to enter and exit with the following rates:

- Left boundary:

$$\begin{aligned} &\overline{1} \to 0 \text{ with rate } \gamma, \\ &\overline{1}, 0 \to 1 \text{ with rate } \alpha, \\ &1 \to 0 \text{ with rate } \widetilde{\gamma}. \end{aligned} \tag{3.2.2}$$

- Right boundary:

$$\begin{aligned} &\overline{1} \to 1 \text{ with rate } \delta, \\ &1 \to \overline{1} \text{ with rate } \beta. \end{aligned} \tag{3.2.3}$$

The rate $\widetilde{\gamma}$ is fixed as

$$\widetilde{\gamma} = \frac{\alpha + \gamma + q - p}{\alpha + \gamma}\gamma. \tag{3.2.4}$$

The other rates $p, q, \alpha, \gamma, \beta, \delta$ can be arbitrary positive real numbers, subject to the constraint

$$\alpha + \gamma + q - p \geq 0, \tag{3.2.5}$$

so that $\widetilde{\gamma}$ is not negative. With this choice of rates, the model is integrable [66, 67]. Although we will not make direct use of the machinery of integrability, we will see that the constraint in equation (3.2.4) also arises directly from the matrix product algebra approach.

The boundary rates (equation (3.2.2) and (3.2.3)) allow species 1 to enter and exit at both boundaries. With $q < p$ there will be a non-zero current of these particles from left to right, and so the system is out of equilibrium. In contrast, species 0 can only enter exit at the left boundary, and so although this species is driven in the bulk, its net current will be zero. Because species 0 is blocked by the right boundary but not by the left, we say that this model is *left-permeable*.

If instead of the left boundary rates (equation (3.2.2)), we take

$$\begin{aligned} &\overline{1} \to 1 \text{ with rate } \alpha, \\ &1 \to \overline{1} \text{ with rate } \gamma, \end{aligned}$$

(keeping the right-boundary rates in equation (3.2.3)), species 0 is trapped on the lattice. We call this the semipermeable ASEP. Again, the net current of species 0 is zero, but in addition the *number* of particles of species 0 is fixed. Thus the system decomposes into sectors according to the number of particles of species 0 on the lattice. The stationary state for this semipermeable model was found in matrix product form first for $q = \gamma = \delta = 0$ [13] and then in general [211]. Later it was also studied through a Koornwinder polynomial approach [52]. In this work we

will follow the approach of [211] and show that it can also be applied to the left-permeable model.

3.2.2 Markov process formulation

The models we have described are in fact continuous time Markov processes, which can be specified formally by giving the transition matrix. To do so, we must specify a basis. To a site i, with state given by τ_i, we associate the standard basis vector $|\tau_i\rangle \in \mathbb{C}^3$, that is

$$|\overline{1}\rangle = \begin{pmatrix}1\\0\\0\end{pmatrix}, \qquad |0\rangle = \begin{pmatrix}0\\1\\0\end{pmatrix}, \qquad |1\rangle = \begin{pmatrix}0\\0\\1\end{pmatrix}.$$

Then the lattice configuration is given by a vector $|\boldsymbol{\tau}\rangle \in (\mathbb{C}^3)^{\otimes L}$,

$$|\boldsymbol{\tau}\rangle = |\tau_1, \ldots, \tau_L\rangle = |\tau_1\rangle \otimes \ldots \otimes |\tau_L\rangle.$$

The rates at which neighbouring particles exchange places (equation (3.2.1)) are encoded in the local transition matrix $w \in \mathbb{C}^3 \otimes \mathbb{C}^3$,

$$w = \begin{pmatrix}
0 & 0 & 0 & 0 & 0 & 0 & 0 & 0 & 0\\
0 & -q & 0 & p & 0 & 0 & 0 & 0 & 0\\
0 & 0 & -q & 0 & 0 & 0 & p & 0 & 0\\
0 & q & 0 & -p & 0 & 0 & 0 & 0 & 0\\
0 & 0 & 0 & 0 & 0 & 0 & 0 & 0 & 0\\
0 & 0 & 0 & 0 & 0 & -q & 0 & p & 0\\
0 & 0 & q & 0 & 0 & 0 & -p & 0 & 0\\
0 & 0 & 0 & 0 & 0 & q & 0 & -p & 0\\
0 & 0 & 0 & 0 & 0 & 0 & 0 & 0 & 0
\end{pmatrix}, \tag{3.2.6}$$

acting on the ordered basis,

$$\{|\overline{1},\overline{1}\rangle, |\overline{1},0\rangle, |\overline{1},1\rangle, |0,\overline{1}\rangle, |0,0\rangle, |0,1\rangle, |1,\overline{1}\rangle, |1,0\rangle, |1,1\rangle\}.$$

The boundary rates (equation (3.2.2) and (3.2.3)) are encoded (respectively) by matrices B, $\overline{B} \in \mathbb{C}^3$:

$$B = \begin{pmatrix}-\alpha-\gamma & 0 & 0\\ \gamma & -\alpha & \widetilde{\gamma}\\ \alpha & \alpha & -\widetilde{\gamma}\end{pmatrix}, \ \overline{B} = \begin{pmatrix}-\delta & 0 & \beta\\ 0 & 0 & 0\\ \delta & 0 & -\beta\end{pmatrix}. \tag{3.2.7}$$

The complete transition matrix is then given by the sum of local matrices

$$M = B_1 + \sum_{i=1}^{L-1} w_{i,i+1} + \overline{B}_L. \tag{3.2.8}$$

The subscripts indicate the sites on which each matrix acts. That is,

$$\begin{aligned} B_1 &= B \otimes I^{(L-1)}, \\ w_{i,i+1} &= I^{(i-1)} \otimes w \otimes I^{(L-i-1)}, \\ \overline{B}_L &= I^{(L-1)} \otimes \overline{B}, \end{aligned}$$

where $I^{(k)}$ is the identity matrix on the k-fold tensor product of $\mathbb{C}^3$.

Writing $P_{\boldsymbol{\tau}}(t)$ for the probability of a configuration $\boldsymbol{\tau}$ at time t, the time evolution is determined by the master equation

$$\begin{aligned} \frac{\mathrm{d}}{\mathrm{d}t}|P(t)\rangle &= M|P(t)\rangle, \\ \text{where} \qquad |P(t)\rangle &= \sum_{\boldsymbol{\tau}} P_{\boldsymbol{\tau}}(t)|\boldsymbol{\tau}\rangle. \end{aligned}$$

At late times, the system converges to the stationary distribution of the process given by the normalized eigenvector of M with eigenvalue 0. That is, with

$$|\Psi\rangle = \sum_{\boldsymbol{\tau}} \psi_{\boldsymbol{\tau}}|\boldsymbol{\tau}\rangle, \qquad M|\Psi\rangle = 0,$$

the stationary distribution is

$$|P_{\mathrm{stat}}\rangle = \frac{1}{Z_L}|\Psi\rangle, \qquad Z_L = \sum_{\boldsymbol{\tau}} \psi_{\boldsymbol{\tau}}.$$

We will see later that the normalisation Z_L plays a role analogous to that of the partition function in equilibrium statistical mechanics. We will, with some abuse of terminology, refer to Z_L as the partition function throughout the paper.

From the stationary distribution we can compute the density of species $k = 0, 1$ at site i

$$\rho_k(i) = \frac{1}{Z_L} \sum_{\substack{\boldsymbol{\tau} \\ \tau_i = k}} \psi_{\boldsymbol{\tau}},$$

and we write ρ_k for the density averaged across the lattice. We can also compute the current J_1, of species 1: the probability per unit time that a particle of species 1 crosses a fixed point on the lattice (see equation (3.3.12)). Recall that the net current of species 0 is zero.

There is also a *right-permeable* two-species model analogous to the left-permeable model, with boundary matrices

$$B = \begin{pmatrix} -\alpha & 0 & \gamma \\ 0 & 0 & 0 \\ \alpha & 0 & -\gamma \end{pmatrix}, \qquad \overline{B} = \begin{pmatrix} -\widetilde{\delta} & \beta & \beta \\ \widetilde{\delta} & -\beta & \delta \\ 0 & 0 & -\beta - \delta \end{pmatrix},$$

with

$$\widetilde{\delta} = \frac{\beta + \delta + p - q}{\beta + \delta}\delta,$$

and the same bulk matrix (equation (3.2.6)). If we write the unnormalized stationary state vector for the left-permeable model as

$$|\Psi^{\text{left}}(\alpha, \beta, \gamma, \delta; p, q)\rangle = \sum_{\tau} \psi_{\tau}^{\text{left}}(\alpha, \beta, \gamma, \delta; p, q)|\boldsymbol{\tau}\rangle,$$

the weights for the right-permeable model are given by

$$\psi_{\tau}^{\text{right}}(\alpha, \beta, \gamma, \delta; p, q) = \psi_{\widetilde{\tau}}^{\text{left}}(\beta, \alpha, \delta, \gamma; q, p), \quad \widetilde{\tau}_i = -\tau_{L-i+1}.$$

Note for the right-permeable model, we take $q > p$. Taking $q < p$ would correspond to a reverse-biased regime, where the boundary rates oppose the preferred direction of flow in the bulk [4, 73].

3.3 Stationary state for the left-permeable two-species ASEP

In this section we give a matrix product algebra and representation for the left-permeable two-species ASEP with boundary matrices (equation (3.2.7)). From this point on, we fix the rightwards hopping rate to $p = 1$. We can do this without loss of generality, as it corresponds to rescaling the unit of time.

3.3.1 Matrix product algebra

To write the stationary probabilities in matrix product form, define two vectors,

$$X = \begin{pmatrix} E \\ A \\ D \end{pmatrix}, \qquad x = \begin{pmatrix} -1 \\ 0 \\ 1 \end{pmatrix}.$$

The entries of X (E, A, D) are matrices in some auxilliary space. We take $\langle W|$, $|V\rangle$ as left and right vectors in this space that contract the matrices to give scalar values. We write the unnormalized stationary vector as

$$|\Psi\rangle = \langle\langle W|X \otimes \ldots \otimes X|V\rangle\rangle, \tag{3.3.1}$$

so that

$$\psi_{\boldsymbol{\tau}} = \langle W|X_{\tau_1} \ldots X_{\tau_L}|V\rangle. \tag{3.3.2}$$

That is to say, in every configuration, the occurence of $\overline{1}$ is represented by E, 0 by A, and 1 by D. In order for this construction to give the stationary state, it is sufficient to find matrices

E, A, D and vectors $\langle W|, |V\rangle$ for which the following conditions hold:

$$\begin{aligned} B\langle\langle W|X &= \langle\langle W|x, \\ wX \otimes X &= -x \otimes X + X \otimes x, \\ \overline{B}X|V\rangle\rangle &= -x|V\rangle\rangle. \end{aligned} \tag{3.3.3}$$

If we apply the transition matrix M of form equation (3.2.8) to $|\Psi\rangle$ given by equation (3.3.1), these relations cause the bulk sum to telescope to two terms, which are cancelled by the left and right boundary terms (see [79, 40, 65] where this is discussed in more detail). It is important to note that we must also show that relations (equation (3.3.3)) are consistent. We will do this, in the usual manner, by giving explicit matrices E, D, A, and boundary vectors $\langle W|$, $|V\rangle$ that satisfy the relations in equation (3.3.3). In fact, we will see that all we require is a representation of same algebra as used for the semipermeable model in [211], and we review that representation in Section 3.4.

With w given by equation (3.2.6), the bulk relations implied by equation (3.3.3) are

$$\begin{aligned} DE - qED &= D + E, \\ AE - qEA &= A, \\ DA - qAD &= A. \end{aligned} \tag{3.3.4}$$

And with boundary matrices (equation (3.2.7)), the boundary relations are

$$\begin{aligned} (\alpha + \gamma)\langle W|E &= \langle W|, \\ \gamma\langle W|E - \alpha\langle W|A + \widetilde{\gamma}\langle W|D &= 0, \\ -\delta E|V\rangle + \beta D|V\rangle &= |V\rangle. \end{aligned} \tag{3.3.5}$$

Using these relations, any expression of the form of equation (3.3.2) can be reduced to a scalar multiple of $\langle W|V\rangle$. For small system sizes, we can compute the stationary weights in this way. Checking that the computed vector is in fact the eigenvector of the transition matrix in equation (3.2.8) with eigenvalue zero, we find that it is *necessary* that $\widetilde{\gamma}$ takes on its integrable value (equation (3.2.4)). We will show that this constraint on the parameters is also sufficient by giving an explicit representation of this algebra.

The bulk relations (equation (3.3.4)) are the same as those from [211] for the semipermeable ASEP. Following [211], we express the bulk relations in terms of matrices $\mathbf{e}$, $\mathbf{d}$, satisfying the q-deformed oscillator algebra [185],

$$\mathbf{de} - q\mathbf{ed} = 1 - q. \tag{3.3.6}$$

Then

$$\begin{aligned} D &= \frac{1}{1-q}(1 + \mathbf{d}), \qquad E = \frac{1}{1-q}(1 + \mathbf{e}), \\ A &= \lambda(DE - ED) = \frac{\lambda}{1-q}(1 - \mathbf{ed}), \end{aligned}$$

satisfy the bulk algebra, with λ a free parameter. We will write the boundary relations as

$$\begin{aligned} &\langle W|\mathbf{e} + ac\langle W|\mathbf{d} = (a+c)\langle W|, \\ &\mathbf{d}|V\rangle + bd\mathbf{e}|V\rangle = (b+d)|V\rangle, \end{aligned} \tag{3.3.7}$$

where the parameters a, b, c, d are

$$a = \kappa^{+}_{\alpha,\gamma}, \;\; c = \kappa^{-}_{\alpha,\gamma}, \;\; b = \kappa^{+}_{\beta,\delta}, \;\; d = \kappa^{-}_{\beta,\delta}, \tag{3.3.8}$$

with

$$\kappa^{\pm}_{u,v} = \frac{1}{2u}\left(1 - q - u + v \pm \sqrt{(1-q-u+v)^2 + 4uv}\right).$$

This parameterization satisfies $a, b \geq 0$, and with $q < 1$, $-1 < c, d \leq 0$. The same form of the boundary relations as in (3.3.7) is used for the semipermeable ASEP [211], and also the single species ASEP [212].

The *three* boundary relations (equation (3.3.5)) for the left-permeable two-species ASEP reduce to *two* relations of the form in equation (3.3.7) if we fix $\lambda = \gamma/\alpha$ and $\widetilde{\gamma}$ at the value given in equation (3.2.4). The parameters a, b, c, d are given by

$$a = 0, \;\; c = \frac{1 - q - \alpha - \gamma}{\alpha + \gamma}, \;\; b = \kappa^{+}_{\beta,\delta}, \;\; d = \kappa^{-}_{\beta,\delta}. \tag{3.3.9}$$

With the constraint equation (3.2.5), we can write

$$a = \kappa^{+}_{\alpha+\gamma,0}, \;\; c = \kappa^{-}_{\alpha+\gamma,0}, \text{ and } -1 < c \leq 0, \tag{3.3.10}$$

where the lower bound assumes that $q < 1$.

Representations of the algebra (equation (3.3.6) and (3.3.7)) are well known, and in Section 3.4.2 we will give the explicit form of the representation used in [211]. Since we know that a representation exists, the matrix product relations for the left-permeable two-species ASEP are consistent, and can be used to calculate the stationary state. But first, we describe the main physical quantities of interest, and how they are calculated.

3.3.2 Physical quantities

The stationary probabilities are obtained by normalising the stationary weights (equation (3.3.2)). Thus

$$\begin{aligned} P_{\boldsymbol{\tau}} &= \frac{1}{Z_L}\langle W|X_{\tau_1}\ldots X_{\tau_L}|V\rangle, \\ \text{with } Z_L &= \langle W|C^L|V\rangle, \quad C = E + D + A. \end{aligned} \tag{3.3.11}$$

The current of type 1 particles is given by

$$\begin{aligned} J_1 &= \frac{1}{Z_L}\langle W|C^{i-1}\left(DE - qED + DA - qAD\right)C^{L-i-1}|V\rangle \\ &= \frac{Z_{L-1}}{Z_L}, \end{aligned} \tag{3.3.12}$$

which is independent of position, i. The net current of type 1 particles must be zero as they can only enter at the left boundary. Indeed, computing with the matrix product algebra, we find

$$\begin{aligned} J_0 =& \frac{1}{Z_L}\langle W|C^{i-1}\left(AE - qEA + qAD - DA\right)C^{L-i-1}|V\rangle \\ =& 0. \end{aligned}$$

We would also like to compute the average density of species $k = 0, 1$, which is given by

$$\rho_k = \frac{1}{L}\frac{1}{Z_L}\sum_{i=1}^{L}\langle W|C^{i-1}X_kC^{L-i}|V\rangle. \tag{3.3.13}$$

To achieve this, we define

$$Z_L(\xi^2,\zeta) = \langle W|\left(E + \xi^2 D + \zeta A\right)^L|V\rangle, \tag{3.3.14}$$

which plays the role of a partition function with fugacities ξ^2, ζ for type 0 and 1 particles respectively. Then

$$\begin{aligned} \rho_0 &= \frac{1}{L}\frac{\partial}{\partial\zeta}\ln Z_L(\xi^2,\zeta)\big|_{\xi^2=\zeta=1}, \\ \rho_1 &= \frac{1}{L}\frac{\partial}{\partial\xi^2}\ln Z_L(\xi^2,\zeta)\big|_{\xi^2=\zeta=1}. \end{aligned} \tag{3.3.15}$$

In order to compute the partition function defined in equation (3.3.14), it will be convenient to rewrite it as

$$Z_L(\xi^2,\zeta) = \left(\frac{\xi}{1-q}\right)^L \times \langle W|\left(\xi^{-1} + \xi + \bar{\mathbf{e}} + \bar{\mathbf{d}} + (1-q)\bar{\zeta}A\right)^L|V\rangle, \tag{3.3.16}$$

with

$$\bar{\mathbf{e}} = \xi^{-1}\mathbf{e}, \qquad \bar{\mathbf{d}} = \xi\mathbf{d}, \qquad \bar{\zeta} = \zeta\xi^{-1}.$$

The rescaled generators $\bar{\mathbf{e}}$, $\bar{\mathbf{d}}$ satisfy the same q-oscillator algebra (equation (3.3.6)). Defining also

$$\bar{a} = \xi^{-1}a, \quad \bar{c} = \xi^{-1}c, \quad \bar{b} = \xi b, \quad \bar{d} = \xi d,$$

the boundary relations for the rescaled generators are obtained by putting bars over the boundary parameters a, b, c, d in equation (3.3.7). Thus, given a representation of the original algebra, we obtain a representation of the scaled algebra, simply by replacing the boundary parameters by their barred versions.

3.4 Representation of the algebra and the partition function

For the representation of the algebra we use exactly that from [211], but with parameters specialized differently. We then review how this is used to find an integral form for the partition function.

3.4.1 Continuous big q-Hermite polynomials

To give the representation of the algebra, we must first introduce certain notation from the 'q-calculus' [105, 138]. The q-shifted factorial is given by

$$(a_1, \ldots, a_s; q)_n = \prod_{r=1}^{s} (a_r; q)_n,$$

where

$$(a; q)_n = \prod_{k=0}^{n-1} (1 - aq^k) = (1 - a)(1 - aq) \cdots (1 - aq^{n-1}),$$

valid also for $n \to \infty$ when $q < 1$. The basic hypergeometric series is given by

$${}_r\phi_s \left[\begin{matrix} a_1, \ldots, a_r \\ b_1, \ldots, b_s \end{matrix} \middle| q, z \right] = \sum_{k=0}^{\infty} \frac{(a_1, \ldots, a_r; q)_k}{(q, b_1, \ldots, b_s; q)_k} \left((-1)^k q^{\binom{k}{2}} \right)^{1+s-r} z^k.$$

Following [211], we define

$$F_n(u, v; \lambda) = \sum_{k=0}^{n} \frac{(q; q)_n}{(q; q)_k (q; q)_{n-k}} (\lambda u; q)_k v^k u^{n-k},$$

which satisfies the recurrence relation

$$F_{n+1}(u, v; \lambda) + \lambda uvq^n F_n(u, v; \lambda) + (1 - q^n) uv F_{n-1}(u, v; \lambda) = (u + v) F_n(u, v; \lambda),$$

with $F_{-1} = 0$ and $F_0 = 1$. Specialization of the parameters u, v gives the *continuous big q-Hermite polynomial* [138],

$$H_n(\cos\theta; \lambda | q) = F_n(\mathrm{e}^{\mathrm{i}\theta}, \mathrm{e}^{-\mathrm{i}\theta}; \lambda).$$

For λ real and $|\lambda| < 1$, $H_n(\cos\theta; \lambda | q)$ satisfies the orthogonality relation

$$\int_0^{\pi} \frac{\mathrm{d}\theta}{2\pi} w(\cos\theta; \lambda)\, H_m(\cos\theta; \lambda | q)\, H_n(\cos\theta; \lambda | q) = (q; q)_n \delta_{mn}, \tag{3.4.1}$$

with

$$w(\cos\theta; \lambda) = w(\mathrm{e}^{\mathrm{i}\theta}, \mathrm{e}^{-\mathrm{i}\theta}; \lambda) = \frac{(q, \mathrm{e}^{2\mathrm{i}\theta}, \mathrm{e}^{-2\mathrm{i}\theta}; q)_\infty}{(\lambda \mathrm{e}^{\mathrm{i}\theta}, \lambda \mathrm{e}^{-\mathrm{i}\theta}; q)_\infty}. \tag{3.4.2}$$

Alternatively, we can write equation (3.4.1) as the contour integral

$$\oint \frac{\mathrm{d}z}{4\pi \mathrm{i} z} w(z, z^{-1}; \lambda)\, H_m\left(\frac{z+z^{-1}}{2}; \lambda|q\right) H_n\left(\frac{z+z^{-1}}{2}; \lambda|q\right) = (q;q)_n \delta_{mn}, \tag{3.4.3}$$

where the contour of integration is the unit circle. The orthogonality condition for $\lambda > 1$ is obtained from equation (3.4.3) by deforming the contour of integration: such that the origin and all poles at λq^k are included, and all poles at $\lambda^{-1} q^{-k}$ are excluded, with $k = 0, 1, 2, \ldots$.

We will need the q-Mehler-type sum formula given in [211] (see also [46]) for $|\tau u|, |\tau v| < 1$:

$$\sum_{n=0}^{\infty} \frac{\tau^n}{(q;q)n} H_n(\cos\theta; \lambda|q)\, F_n(u, v; 0) = \Theta(\cos\theta; \tau u, \tau v|\lambda), \tag{3.4.4}$$

where

$$\begin{aligned} \Theta(\cos\theta; u, v|\lambda) &\equiv \Theta(\mathrm{e}^{\mathrm{i}\theta}, \mathrm{e}^{-\mathrm{i}\theta}; u, v|\lambda) \\ &= \frac{(\lambda u, \lambda v; q)_\infty}{(u\mathrm{e}^{\mathrm{i}\theta}, u\mathrm{e}^{-\mathrm{i}\theta}, v\mathrm{e}^{\mathrm{i}\theta}, v\mathrm{e}^{-\mathrm{i}\theta}; q)_\infty} {}_2\phi_2 \left[\begin{matrix} \lambda\mathrm{e}^{\mathrm{i}\theta}, \lambda\mathrm{e}^{-\mathrm{i}\theta} \\ \lambda u, \lambda v \end{matrix} \middle| q, uv \right]. \end{aligned} \tag{3.4.5}$$

For the model we consider, we will need to take $u = 0$ (or equivalently $v = 0$), and can do this by taking the limit $u \to 0$. For convenience, we will write

$$\begin{aligned} &F_n(0, v; \lambda) = \lim_{u\to 0} F_n(u, v; \lambda) = v^n, \quad \text{and} \\ &{}_2\phi_2 \left[\begin{matrix} \lambda\mathrm{e}^{\mathrm{i}\theta}, \lambda\mathrm{e}^{-\mathrm{i}\theta} \\ 0, \lambda v \end{matrix} \middle| q, 0 \right] = \lim_{u\to 0} {}_2\phi_2 \left[\begin{matrix} \lambda\mathrm{e}^{\mathrm{i}\theta}, \lambda\mathrm{e}^{-\mathrm{i}\theta} \\ \lambda u, \lambda v \end{matrix} \middle| q, uv \right] = 1. \end{aligned}$$

Note also that if $|\tau u| > 1$ or $|\tau v| > 1$, the sum in equation (3.4.4) is divergent as, for example, if $|u| > |v|$, $F_n(u, v; 0) \sim u^n$ for large n.

3.4.2 Representation

The q-oscillator algebra (equation (3.3.6)) has a Fock space representation

$$\begin{aligned} \mathbf{d} &= \sum_{n=1}^{\infty} \sqrt{1-q^n}\, |n-1\rangle\langle n|, \\ \mathbf{e} &= \sum_{n=0}^{\infty} \sqrt{1-q^{n+1}}\, |n+1\rangle\langle n|, \end{aligned} \tag{3.4.6}$$

and therefore

$$A = \frac{\lambda}{1-q} \sum_{n=0}^{\infty} q^n |n\rangle\langle n|.$$

Writing the boundary vectors as

$$\langle W| = \sum_{n=0}^{\infty} w_n \langle n|, \qquad |V\rangle = \sum_{n=0}^{\infty} v_n |n\rangle, \tag{3.4.7}$$

then from the boundary relations (equation (3.3.7)), the coefficients must satisfy

$$\sqrt{(q;q)_{n+1}}\, w_{n+1} - (a+c)\sqrt{(q;q)_n}\, w_n + ac(1-q^n)\sqrt{(q;q)_{n-1}}\, w_{n-1} = 0,$$
$$\sqrt{(q;q)_{n+1}}\, v_{n+1} - (b+d)\sqrt{(q;q)_n}\, v_n + bd(1-q^n)\sqrt{(q;q)_{n-1}}\, v_{n-1} = 0.$$

These recurrences are solved by taking

$$w_n = \frac{F_n(a,c;0)}{\sqrt{(q;q)_n}}, \qquad v_n = \frac{F_n(b,d;0)}{\sqrt{(q;q)_n}}. \tag{3.4.8}$$

Note that as we have $a = 0$, w_n has the simpler form

$$w_n = \frac{c^n}{\sqrt{(q;q)_n}}.$$

With Eqs. (3.4.6), (3.4.7) and (3.4.8), we have a representation of the algebra in Eqs. (3.3.6) and (3.3.7).

In order to compute the partition function $Z(\xi^2, \zeta)$, we start from the form equation (3.3.16). The trick is to find a solution of the eigenvalue equation

$$(\bar{\mathbf{e}} + \bar{\mathbf{d}} + (1-q)\bar{\zeta}A)|h(\cos\theta)\rangle = 2\cos\theta |h(\cos\theta)\rangle. \tag{3.4.9}$$

Using the representation in equation (3.4.6) (which also gives a representation of the barred algebra), we find

$$|h(\cos\theta)\rangle = \sum_{n=0}^{\infty} \frac{H_n(\cos\theta; \lambda\zeta\xi^{-1}|q)}{\sqrt{(q;q)_n}} |n\rangle.$$

As $(\bar{\mathbf{e}}+\bar{\mathbf{d}}+(1-q)\bar{\zeta}A)$ is a symmetric matrix, it has the transpose $\langle\langle h\cos\theta|$ as a right eigenvector with the same eigenvalue. From the orthogonality condition (equation (3.4.1)), we then obtain

$$\int_0^{\pi} \frac{\mathrm{d}\theta}{2\pi} w(\cos\theta; \lambda\zeta\xi^{-1})\, |h(\cos\theta)\rangle\langle h(\cos\theta)| = 1, \tag{3.4.10}$$

for $|\lambda\zeta\xi^{-1}| < 1$. For the case $|\lambda\zeta\xi^{-1}| > 1$, we use the contour integral form of the orthogonality condition, with the contour deformed as described below (equation (3.4.3)).

3.4.3 Partition function

Following [211, 212], we write the partition function in integral form. Starting from the partition function as given in equation (3.3.16), use equation (3.4.10) to insert the identity, then the eigenvalue equation equation (3.4.9), then finally the sum formula equation (3.4.4). This

gives the integral form

$$Z_L(\xi^2,\zeta) = \int_0^\pi \frac{\mathrm{d}\theta}{2\pi}\Bigg[w(\cos\theta;\lambda\zeta\xi^{-1})\,\Theta(\cos\theta;0,\xi^{-1}c|\lambda\zeta\xi^{-1}) \times \Theta(\cos\theta;\xi b,\xi d|\lambda\zeta\xi^{-1})\left(\frac{1+\xi^2+2\xi\cos\theta}{1-q}\right)^L\Bigg]. \tag{3.4.11}$$

We have used the boundary vectors of the 'barred' algebra to obtain this expression. The form equation (3.4.11) is valid for $|\zeta\xi^{-1}\lambda|, |\xi b|, |\xi^{-1}c|, |\xi d| < 1$. Recall also that for the left-permeable model we have $a = 0$.

In fact, in our model $|c|, |d| < 1$, and we can take ζ, ξ arbitrarily close to 1. Thus we need only be concerned with the cases where $\lambda > 1$ or $b > 1$. For these cases, we write the partition function in equation (3.4.11) by changing to the variable $z = e^{\mathrm{i}\theta}$ as

$$Z_L(\xi^2,\zeta) = \oint \frac{\mathrm{d}z}{4\pi\mathrm{i}z}\Bigg[w(z,z^{-1};\lambda\zeta\xi^{-1})\Theta(z,z^{-1};0,\xi^{-1}c|\lambda\zeta\xi^{-1}) \times \Theta(z,z^{-1};\xi b,\xi d|\lambda\zeta\xi^{-1})\left(\frac{(1+\xi z)(1+\xi z^{-1})}{1-q}\right)^L\Bigg], \tag{3.4.12}$$

where for the contour of integration we take the unit circle deformed to include all poles at $z = \lambda\zeta\xi^{-1}q^k$, $z = \xi b q^k$, and exclude all poles at $z = 1/(\lambda\zeta\xi^{-1}q^k)$, $z = 1/(\xi b q^k)$, with $k = 0, 1, 2, \ldots$.

The deformation to include or exclude the λ poles follows from the orthogonality condition (equation (3.4.3)). The case with $b > 1$ is less straightforward. With $b > 1$, the product $\langle h(\cos\theta)|V\rangle$, which appears when we compute the partition function, is in fact a divergent sum. A representation without this problem is known for the single species ASEP [212], but not in the multispecies case. However, the deformation of the contour for the $b > 1$ case can be justified as the analytic continuation of the partition function [79, 4].

3.5 Stationary properties in the thermodynamic limit

For finite sizes, the integral form of the partition function $Z_L(\xi^2,\zeta)$ is difficult to work with. However, it is possible to extract its asymptotic behaviour when L is large, allowing the computation of stationary currents and densities.

3.5.1 Phase diagram

To find the phase diagram of the model, we need to find an asymptotic form of the partition function. And the key to the asymptotics of the partition function are the poles due to λ, b in the integral form. For $\lambda, b < 1$, the asymptotic form can be obtained from the form equation (3.4.11) following the method in [187], or by a saddle-point analysis of the complex integral (equation (3.4.12)) [4]. For $\lambda > 1$ (or similarly $b > 1$) we must subtract the contribution

of the poles at $z = 1/(\lambda\zeta\xi^{-1}q^k)$ from this result, and add the contribution of the poles at $z = \lambda\zeta\xi^{-1}q^k$ (see [40] for a detailed explanation). The contribution from the poles with $k = 0$ give the dominant asymptotic behaviour.

From the asymptotic form of the partition function we can compute the species 1 current through equation (3.3.12), and the averaged densities of species 0 and 1 through equation (3.3.15). We find three phases, as in the model with semipermeable boundaries (see Figure A.3), which we name according to the behaviour of the species 1.

- Maximum current phase (MC): For $\lambda < 1$ and $b < 1$, the asymptotic form of the partition function is

$$Z_L(\xi^2,\zeta) \simeq \frac{(q;q)_\infty^3(\zeta\lambda b, \zeta\xi^{-2}\lambda c, \zeta\lambda d; q)_\infty}{(\zeta\xi^{-1}\lambda, \xi b, \xi^{-1}c, \xi d; q)_\infty^2}\, {}_2\phi_2\left[\begin{matrix}\zeta\xi^{-1}\lambda, \zeta\xi^{-1}\lambda \\ \zeta\lambda b, \zeta\lambda d\end{matrix}\middle| q, \xi^2 bd\right] \times \frac{[(1+\xi)(1+\xi^{-1})]^{3/2}}{2\sqrt{\pi}L^{3/2}}\left[\frac{(1+\xi)^2}{1-q}\right]^L.$$

  From this we obtain the currents and average densities

$$J_1 = \frac{1-q}{4}, \quad \rho_0 = O(1/L), \quad \rho_1 = \frac{1}{2}.$$

  The complete leading order term of the density ρ_0 can be computed through equation (3.3.15), but we have not found a simple expression for it.

- Low density phase (LD): For $\lambda > 1$, $\lambda > b$, the leading term comes from adding (subtracting) the contribution of the pole at $z = \zeta\xi^{-1}\lambda$ ($z = 1/(\zeta\xi^{-1}\lambda)$), and gives

$$Z_L(\xi^2,\zeta) \simeq \frac{(\zeta^{-2}\xi^2\lambda^{-2};q)_\infty}{(\zeta^{-1}\xi^2 b/\lambda, \zeta^{-1}c/\lambda, \zeta^{-1}\xi^2 d/\lambda; q)_\infty}\left(\frac{(1+\zeta\lambda)(1+\zeta^{-1}\xi^2\lambda^{-1})}{1-q}\right)^L.$$

  From this we obtain

$$J_1 = \frac{(1-q)\lambda}{(1+\lambda)^2}, \quad \rho_0 = \frac{\lambda-1}{1+\lambda}, \quad \rho_1 = \frac{1}{1+\lambda}.$$

- High density phase (HD): For $b > 1$, $b > \lambda$, the leading term comes from adding (subtracting) the contribution of the pole at $z = \xi b$ ($z = 1/(\xi b)$), and gives

$$Z_L(\xi^2,\zeta) \simeq \frac{(\zeta\xi^{-2}\lambda c, \zeta\lambda d, \xi^{-2}b^{-2}; q)_\infty}{(\zeta\xi^{-2}\lambda/b, bc, \xi^{-2}c/b, \xi^2 bd, d/b; q)_\infty}\, {}_1\phi_1\left[\begin{matrix}\zeta\xi^{-2}\lambda/b \\ \zeta\lambda d\end{matrix}\middle| q, \xi^2 bd\right] \times \left(\frac{(1+\xi^2 b)(1+b^{-1})}{1-q}\right)^L.$$

From this we obtain

$$J_1 = \frac{(1-q)b}{(1+b)^2}, \quad \rho_0 = O(1/L), \quad \rho_1 = \frac{b}{1+b}.$$

Again, we have not found a simple expression for the density ρ_0.

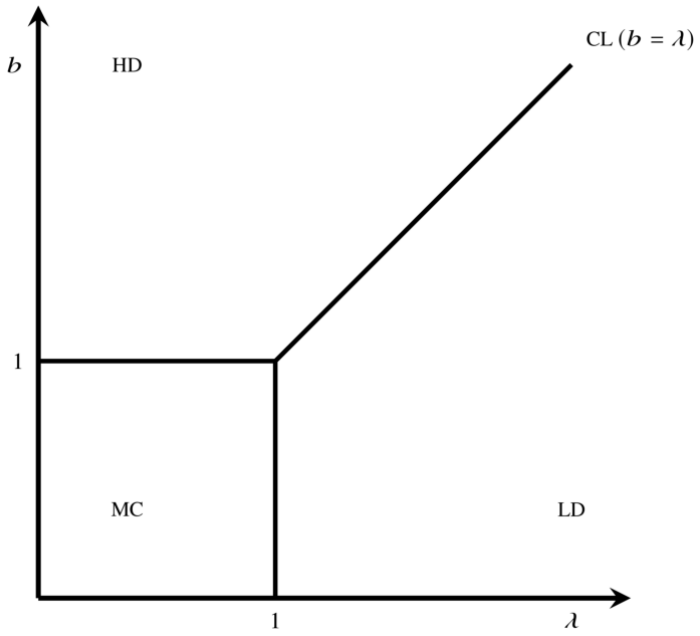

Figure 3.1: Phase diagram for lattice average current and density with $\lambda = \gamma/\alpha$.

The phase diagram is shown in Figure 3.1. Simulation results showing typical density profiles for each of the phases are shown in Figure 3.2. The sub-phases identified in those figures will be discussed in Section 3.5.2. In each phase, the current can be expressed in the mean-field form, $J_1 = (1-q)\rho_1(1-\rho_1)$. This is not obvious from the definition of the model because although 1's cannot distinguish between 0's and $\overline{1}$'s in the bulk or at the left boundary, they can be distinguished at the right boundary.

As in the ASEP, there is a first order phase transition along the coexistence line (CL): that is, the line $\lambda = b > 1$ separating the high and low density phases. On this line, high and low density domains coexist on the lattice. The left boundary attempts to impose a region characteristic of the low density phase, while the right boundary attempts to impose a region as in the high density phase. These two domains are separated by a moving shock, or domain wall [143, 172]. The linear profiles shown in Figure 3.3(a) are characteristic of this situation when the position of the shock is averaged across the lattice. In Figure 3.3(b), we show an instantaneous density profile in this phase, with the shock captured at around $0.6L$. Figure 3.3(b) was obtained by taking a very large lattice length ($L = 2500$), then computing a coarse-grained spatial density by averaging over windows of 50 sites.

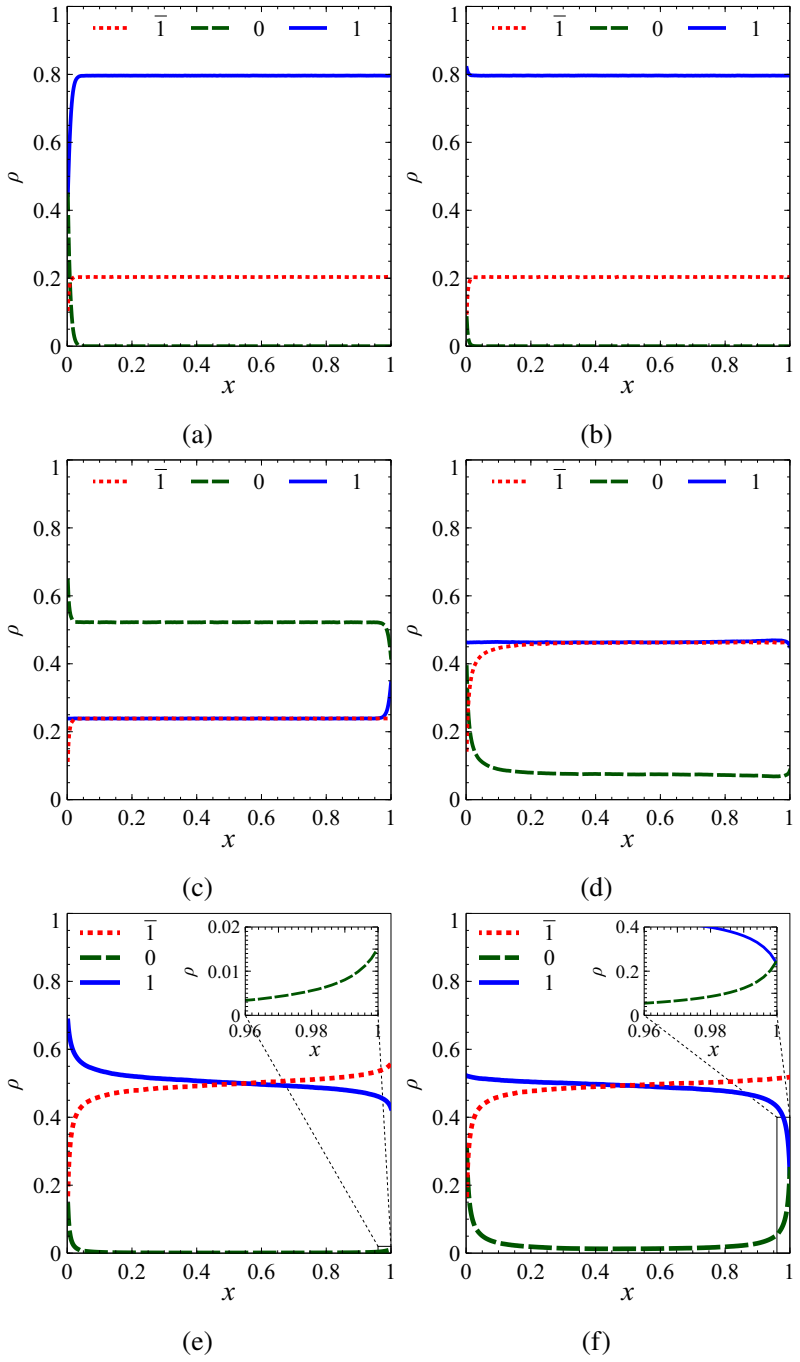

Figure 3.2: (Color online) Density profiles in the HD, LD and MC phases. Plots show densities of species $\bar{1}$ (red dotted line), 0 (green dashed line) and 1 (blue solid line) versus normalized site position $x = i/L$ for $L = 500$ in (a) sub-phase HD1 for $\lambda = 1.75, b = 3.91$, and $d = -0.66$ ($\alpha = 0.32, \gamma = 0.56, \beta = 0.35, \delta = 0.9, q = 0.41$), (b) sub-phase HD2 for $\lambda = 0.20, b = 3.91$, and $d = -0.66$ ($\alpha = 0.81, \gamma = 0.16, \beta = 0.35, \delta = 0.9, q = 0.41$), (c) sub-phase LD1 for $\lambda = 3.18, b = 1.25$, and $d = -0.59$ ($\alpha = 0.22, \gamma = 0.7, \beta = 0.64, \delta = 0.47, q = 0.41$), (d) sub-phase LD2 for $\lambda = 1.16, b = 0.94$, and $d = -0.68$ ($\alpha = 0.5, \gamma = 0.58, \beta = 0.95, \delta = 0.61, q = 0.41$), (e) MC-phase for $\lambda = 0.37, b = 0.75$, and $d = -0.59$ ($\alpha = 0.62, \gamma = 0.23, \beta = 0.83, \delta = 0.37, q = 0.41$), and (f) MC-phase for $\lambda = 0.91, b = 0.26$, and $d = -0.45$ ($\alpha = 0.45, \gamma = 0.41, \beta = 0.85, \delta = 0.1, q = 0.41$). The sub-phases LD1, LD2, HD1 and HD2 will be described in Section 3.5.2.

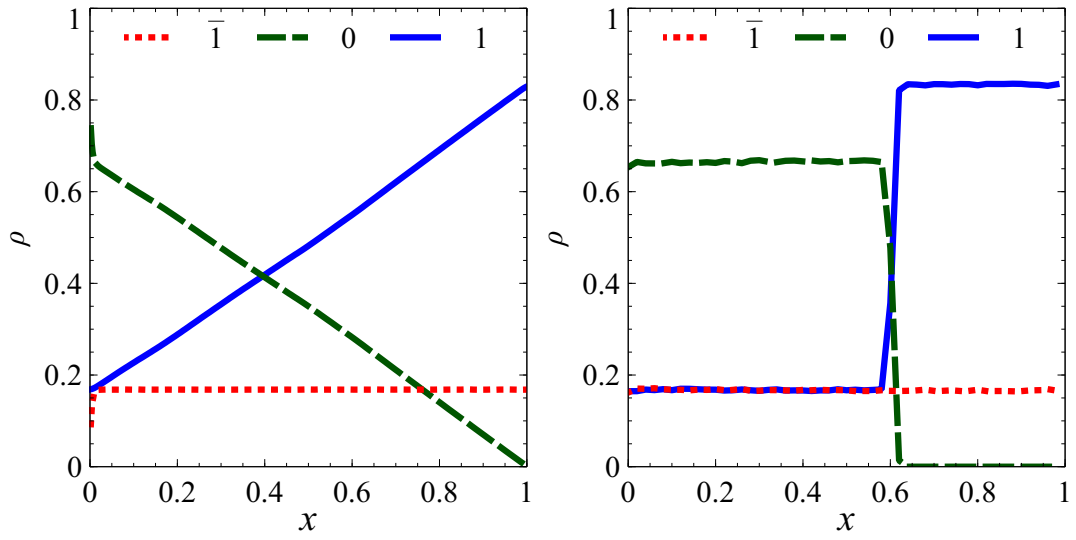

Figure 3.3: (Color online) Plots of (a) time-averaged densities for $L = 500$ and (b) instantaneous density profiles for $L = 2500$, coarse-grained over 50 sites, on the coexistence line for $\lambda = b = 4.93$ and $d = -0.59$ ($\alpha = 0.15, \gamma = 0.74, \beta = 0.28, \delta = 0.89, q = 0.41$). Each plot shows densities of species $\bar{1}$ (red dotted line), 0 (green dashed line) and 1 (blue solid line) versus normalized site position $x = i/L$.

3.5.2 Boundary densities

The simulation results show that the per-site density differs from the value averaged across the lattice. We can get some indication of this behaviour by computing the site densities

$$\rho_k(i) = \frac{1}{Z_L}\langle W|C^{i-1}X_kC^{L-i}|V\rangle, \tag{3.5.1}$$

for species $k = 0, 1$ at the first and last sites. We can use the boundary algebra relations (equation (3.3.5)) to express the density at site 1 in terms of the current J_1 (equation (3.3.12)). We obtain

$$\begin{aligned}\rho_0(1) &= \frac{-c\lambda(1-q)+\lambda(1+c)^2J_1}{(1-q)(1-c\lambda)},\\ \rho_1(1) &= \frac{1-q-(1+\lambda)(1+c)J_1}{(1-q)(1-c\lambda)}.\end{aligned} \tag{3.5.2}$$

Taking the value of J_1 for each phase gives the density at the left boundary (see Table 3.1). At the right boundary we find

$$\rho_1(L) = \frac{(1+b)(1+d)J_1-(1-q)bd}{(1-q)(1-bd)} + \frac{bd}{1-bd}\rho_0(L), \tag{3.5.3}$$

but the algebraic relations alone are not enough to give $\rho_0(L)$. Instead we must return to the

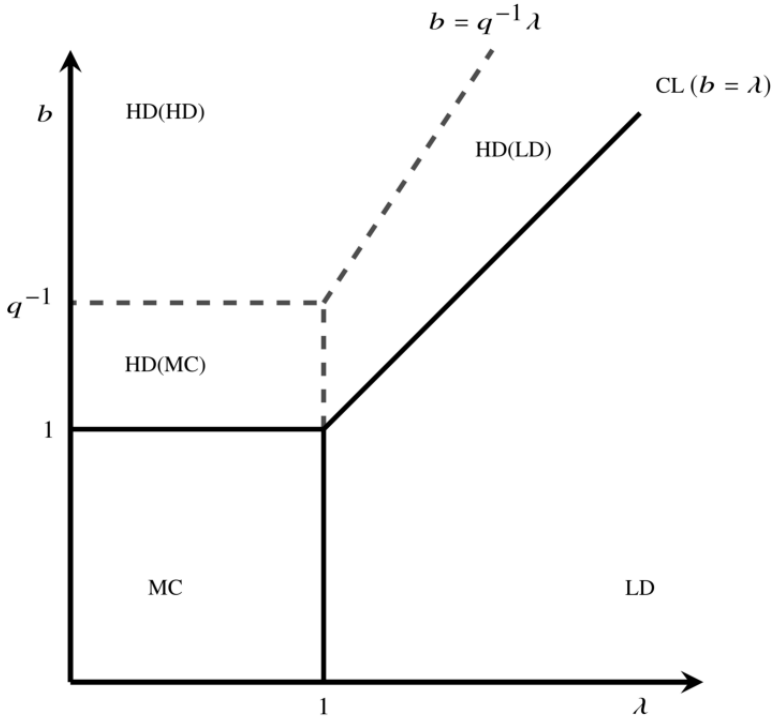

Figure 3.4: Division of the HD phase according to the scaling of $\rho_0(L)$, as given in equation (3.5.6) – equation (3.5.8).

representation of the algebra. Again, we will use the trick of inserting the identity operator (equation (3.4.10)), but now we take $\zeta = \xi = 1$, and write

$$I_{L,k} = \langle W|C^{L-k}A^k|V\rangle = \int_0^\pi \frac{\mathrm{d}\theta}{2\pi} w(\cos\theta;\lambda)\langle W|C^{L-k}|h(\cos\theta)\rangle\langle h(\cos\theta)|A^k|V\rangle,$$

which will allow us to compute the probability that the k rightmost sites are occupied by particles of species 0. Using the representation of the algebra, and the sum formula (equation (3.4.4)), we find

$$\begin{aligned}\langle h(\cos\theta)|A^k|V\rangle &= \frac{\lambda^k}{(1-q)^k}\sum_{n=0}^{\infty}\frac{q^{kn}}{(q;q)_n}H_n(\cos\theta;\lambda|q)F_n(b,d;0)\\ &= \frac{\lambda^k}{(1-q)^k}\Theta(\cos\theta;q^k b,q^k d|\lambda).\end{aligned}$$

Thus we find that the integral expression for $I_{L,k}$ is (up to an overall factor) simply that of the partition function at length $L-k$ with $b \to q^k b$, $d \to q^k d$. That is,

$$I_{L,k} = \frac{\lambda^k}{(1-q)^k} Z_{L-k}\Big|_{\substack{b\to q^k b\\ d\to q^k d}},$$

where $Z_L = Z_L(\xi^2 = 1, \zeta = 1)$.

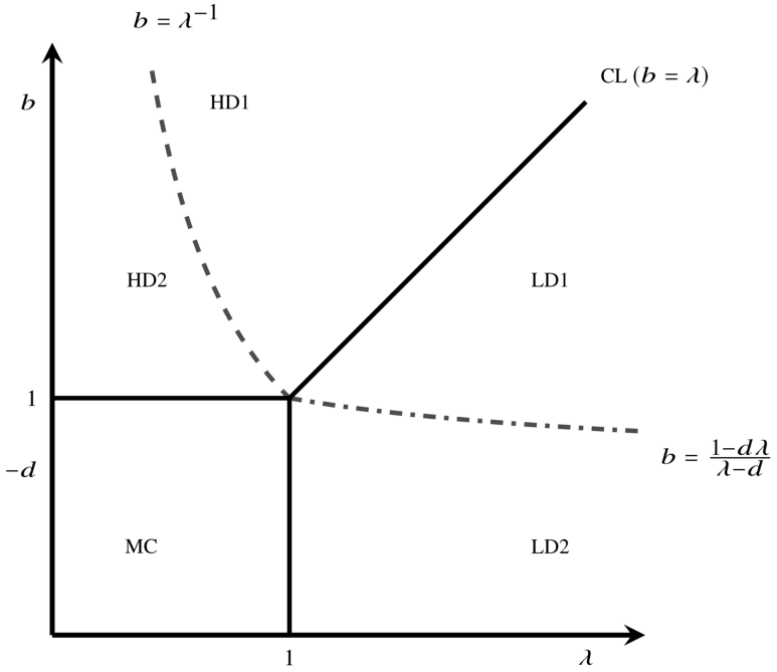

Figure 3.5: Division of phases according to the difference between bulk and boundary densities for a fixed value of d.

The asymptotic behaviour of $I_{L,k}$ is the same as that for the partition function, except that the phase boundaries now depend on $q^k b$ instead of on b. We will write Z_L^{LD}, Z_L^{HD}, Z_L^{MC}, to indicate the expression for the partition function in the low density, high density, or maximum current phases respectively. Then we write $I_{L,k}^{\mathrm{XX}}$ for the corresponding value of $I_{L,k}$, but with the phase boundaries determined by $q^k b$.

Now, the probability of having the k rightmost sites occupied by particles of type 0 is

$$P_0^{\mathrm{jam}}(k) = P(\tau_{L-k+1} = \ldots \tau_L = 0) = \frac{I_{L,k}^{\mathrm{YY}}}{Z_L^{\mathrm{XX}}}. \tag{3.5.4}$$

Here XX, YY indicates the appropriate phase for each part of the expression: the XX phase boundaries are determined by (λ, b), and the YY boundaries are determined by $(\lambda, q^k b)$. The density $\rho_0(L)$ is given by equation (3.5.4) with $k = 1$. We compute $\rho_0(L)$ for each possible phase combination, indicating these by the shorthand XX(YY):

- MC(MC) phase, $\lambda, b < 1$:

$$\rho_0(L) = \frac{\lambda}{4}\frac{(1-b)^2(1-d)^2}{(1-\lambda b)(1-\lambda d)}\left(\frac{L}{L-1}\right)^{3/2}\left(\frac{{}_2\phi_2\left[\begin{matrix}\lambda,\lambda\\ q\lambda b, q\lambda d\end{matrix}\middle| q, q^2 bd\right]}{{}_2\phi_2\left[\begin{matrix}\lambda,\lambda\\ \lambda b, \lambda d\end{matrix}\middle| q, bd\right]}\right). \tag{3.5.5}$$

Note that $\rho_0(L)$ approaches a constant value for large L. Note also that for $q, |bd| \ll 1$, the ${}_2\phi_2$ series in this expression are close to 1, and we can approximate

$$\rho_0(L) \simeq \frac{\lambda}{4}\frac{(1-b)^2(1-d)^2}{(1-\lambda b)(1-\lambda d)}.$$

- HD(MC) phase, $\lambda < 1$, $1 < b < q^{-1}$:

$$\rho_0(L) \sim \frac{1}{(L-1)^{3/2}}\left(\frac{4}{(1+b)(1+b^{-1})}\right)^L. \tag{3.5.6}$$

By '$\sim$' we mean the scaling behaviour with L. We do not write out the full expression, only because we have not found a simple form for it.

- HD(HD) phase, $b > q^{-1}$, $b > q^{-1}\lambda$:

$$\rho_0(L) \sim \left(\frac{(1+qb)(1+q^{-1}b^{-1})}{(1+b)(1+b^{-1})}\right)^L. \tag{3.5.7}$$

- HD(LD) phase, $\lambda > 1$, $\lambda < b < q^{-1}\lambda$:

$$\rho_0(L) \sim \left(\frac{(1+\lambda)(1+\lambda^{-1})}{(1+b)(1+b^{-1})}\right)^L. \tag{3.5.8}$$

- LD(LD) phase, $\lambda > 1$, $\lambda > b$:

$$\rho_0(L) \simeq \frac{(\lambda-b)(\lambda-d)}{(1+\lambda)^2}. \tag{3.5.9}$$

Taking $\rho_0(L)$ as the order parameter, the high density phase splits into sub-phases according to the scaling behaviour. However across all these high density sub-phases, the density $\rho_0(L)$ scales as z^L or $z^L/L^{3/2}$ with $z < 1$. These sub-phases are depicted in Figure 3.4.

The maximum current and low density phases do not split into sub-phases, and the leading order behaviour is constant in L. The expressions for $P_0^{\text{jam}}(k)$ in these phases are non-vanishing (with L):

- MC(MC) phase, $\lambda, b < 1$:

$$P_0^{\text{jam}}(k) = \left(\frac{\lambda}{4}\right)^k \frac{(b,d;q)_k^2}{(\lambda b, \lambda d; q)_k}\left(\frac{L}{L-k}\right)^{3/2}\left(\frac{{}_2\phi_2\left[\begin{matrix}\lambda,\lambda\\ q^k\lambda b, q^k\lambda d\end{matrix}\middle| q, q^{2k}bd\right]}{{}_2\phi_2\left[\begin{matrix}\lambda,\lambda\\ \lambda b,\lambda d\end{matrix}\middle| q, bd\right]}\right).$$

- LD(LD) phase, $\lambda > 1, \lambda > b$:

$$P_0^{\text{jam}}(k) \simeq \frac{\lambda^k(\lambda^{-1}b, \lambda^{-1}d; q)_k}{(1+\lambda)^{2k}}.$$

Phase	$\rho_0(1) - \rho_0$	$\rho_1(1) - \rho_1$	$\rho_0(L) - \rho_0$	$\rho_1(L) - \rho_1$
MC ($\lambda, b < 1$)	$\frac{(1-c)^2}{4(1-c\lambda)}$	$\frac{(1-c)(1-\lambda)}{4(1-c\lambda)}$	$\rho_0(L)$	$-\frac{(1-b)(1-d)}{4(1-bd)} + \frac{bd}{1-bd}\rho_0(L)$
LD ($\lambda > 1, \lambda > b$)	$\frac{1-c\lambda}{(1+\lambda)^2}$	0	$-\frac{b(\lambda-d)-(1-d\lambda)}{(1+\lambda)^2}$	$\frac{b(\lambda-d)-(1-d\lambda)}{(1+\lambda)^2}$
HD ($b > 1, b > \lambda$)	$\frac{(b-c)(1-bc)\lambda}{(1+b)^2(1-c\lambda)}$	$\frac{(b-c)(1-b\lambda)}{(1+b)^2(1-c\lambda)}$	0	0

Table 3.1: Difference between boundary density and average bulk density in each phase. The value $\rho_0(L)$ in the MC phase is given in equation (3.5.5). Recall that $-1 < c, d \leq 0$ in all phases.

It might seem surprising at first glance to find that in the MC phase, species 0 has a fixed finite density at the right boundary for large L, even as the bulk density vanishes as $1/L$ (see equation (3.5.5)). However, this can be understood from the mean field-like behaviour of the system. There are only isolated 0's in the bulk, which perform independent asymmetric random walks with forward hopping rate $\rho_{\bar{1}} + q\rho_1$ and reverse hopping rate $\rho_1 + q\rho_{\bar{1}}$. In the bulk, these are equal, but on the right boundary, $\rho_{\bar{1}} > \rho_1$, which causes a drift towards the right leading to a buildup of 0's. The insets in Fig.3.2(e), 3.2(f) show close-ups of such density profiles. The simulation results and analytically calculated values are in good agreement.

In Table 3.1 we give the densities of species 0 and 1 at the first and last sites. We present these as the difference from the bulk density, i.e. $\rho_j(i) - \rho_j$. Of note is that this density difference can change signs for both species at the right boundary in the LD phase, and for species 1 at the left boundary in the HD phase. We identify the following subphases:

- HD1, $b > \lambda^{-1}, b > \lambda$: Here $\rho_1(1) < \rho_1$. A typical profile is shown in Figure 3.2(a).
- HD2, $1 < b < \lambda^{-1}$: Here $\rho_1(1) > \rho_1$. A typical profile is shown in Figure 3.2(b).
- LD1, $\frac{1-d\lambda}{\lambda-d} < b < \lambda$: Here $\rho_0(L) < \rho_0$ and $\rho_1(L) > \rho_1$. A typical profile is shown in Figure 3.2(c).
- LD2, $\lambda > 1, b < \frac{1-d\lambda}{\lambda-d}$: Here $\rho_0(L) > \rho_0$ and $\rho_1(L) < \rho_1$. A typical profile is shown in Figure 3.2(d).

These subdivisions are depicted in Figure 3.5.

Beyond the density difference at the boundary, it would be interesting to calculate the correlation

lengths, that is the form of the decay to the bulk density values. For the single species ASEP, this has been studied through a variety of different approaches [145, 78, 193, 79, 90, 187, 143].

We also note that the phase diagrams in Fig.3.4 and 3.5 resemble those that have appeared in other contexts in connection with the single species ASEP. The subdivisions of the high density phase in Figure 3.4 (related to the scaling of the density $\rho_0(L)$) appear in the phase diagram for the correlation lengths of the ASEP [187]. And the subdivisions in Figure 3.5 are similar (but not identical) to the parameter constraints for which there are finite dimensional representations of the matrix product algebra [157]. It would be interesting to know if any deeper connection exists in these cases.

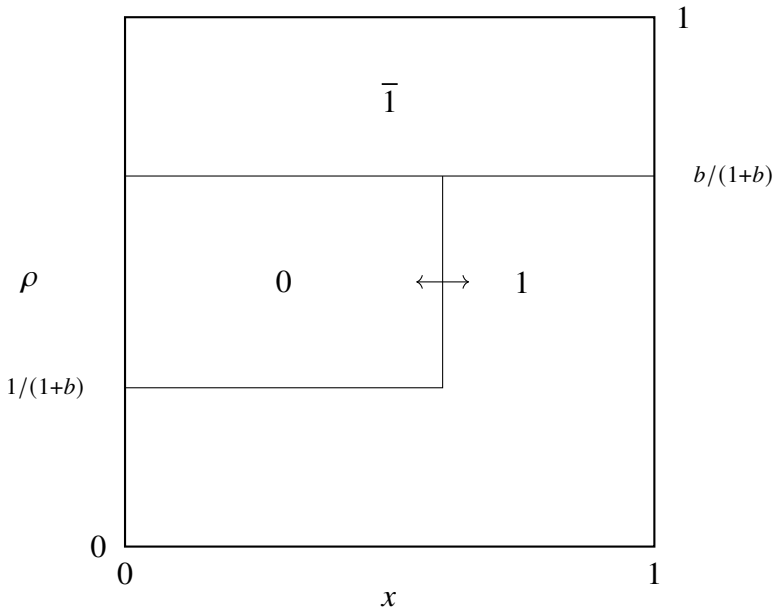

Figure 3.6: Shock picture for the LPASEP on the coexistence line $b = \lambda > 1$. At each normalized position $x = i/L$, the height of a region equals bulk density of the species which the region is labelled with.

3.6 Shock picture

The coarse features of the density profiles in the steady state in all phases can be explained by a shock picture, just as for the semipermeable ASEP [22] (also see Appendix A), which we now explain. In the absence of correlations (which we expect in the thermodynamic limit), the current of 1's is given by $J_1 = (1-q)\rho_1(1-\rho_1)$, whereas that of $\overline{1}$'s is $J_{\overline{1}} = (1-q)\rho_{\overline{1}}(1-\rho_{\overline{1}})$ in the opposite direction. Equating these two, we find two solutions:

(3.6.1) either $\rho_1 = \rho_{\overline{1}}$ and $\rho_0 = 1 - 2\rho_1$, or $\rho_1 = 1 - \rho_{\overline{1}}$ and $\rho_0 = 0$.

We therefore expect to find this property at all normalized site positions $x = i/L$ in the thermodynamic limit.

In the LPASEP, a shock is formed between particles of species 0 and species 1, and particles

of species $\overline{1}$ act as spectators. This is easiest to explain on the $\mathbb{1} - \mathbb{0}$ boundary and is shown in Figure 3.6. Particles of species 0 and species 1 have discontinuous densities across the shock. The shock has zero drift and performs a symmetric random walk within the system, leading to linear density profiles for 0 and 1.

In HD phase, the shock has negative drift and gets pinned to the left of the system. Therefore, the 0's have zero density in the system leading to a high density of 1's in the system. This phenomenon is known as *dynamical expulsion* [21], where the boundary parameters cause a species to be absent in the bulk of the system only in certain phases. In LD phase, the shock has positive drift and gets pinned to the right of the system. In that case, the densities of 1's and $\overline{1}$'s become equal and constant and the density of 0's is non-zero. In MC phase, the height of the shock becomes zero and 0's are again dynamically expelled from the system. Here, the density of 1's and $\overline{1}$'s become $1/2$, leading to the maximum possible current.

Chapter 4

The exact phase diagram of a multispecies left-permeable asymmetric exclusion process

4.1 Introduction

In the present chapter, we derive the exact phase diagram for a model with arbitrary number of species generalizing the LPASEP. By analogy with the mASEP, we call the model the mLPASEP. We use exact colourings of the mLPASEP to the LPASEP to determine the multidimensional phase diagram. We also give physical explanations for the currents and densities in each phase by appealing to the shock picture. We observe the phenomenon of *dynamical expulsion* here too just as in the mASEP [21]. There are two kinds of colourings depending on the parity of the number of species. We focus on the technically easier case of the odd mLPASEP for the most part. The differences for the even mLPASEP are highlighted in Section 4.5.

The plan of the chapter is as follows. We define the models in Section 4.2. Since the understanding of the phase diagram of the odd mLPASEP depends crucially on the LPASEP studied in Chapter 3. In Section 4.3, we discuss the colouring approach and derive the exact phase diagram of the odd mLPASEP in the thermodynamic limit. We also give formulas for the currents and densities in all phases. To illustrate the ideas, we explain the three dimensional phase diagram of the odd mLPASEP with 5 species in Section 4.3.3. We also perform simulations of the NESS for this case in Figure 4.2. We explain the coarse features of the density profiles in Section 4.4 by appealing to the generalized shock picture. Here, we simulate the shocks on certain phase boundaries in Figure 4.5 and study the spatiotemporal evolution of the shock in Figure 4.6 for the odd mLPASEP with 5 species. Finally, we discuss the even mLPASEP in Section 4.5.

4.2 Model definitions

The *multispecies left-permeable ASEP* or mLPASEP is a variant of the ASEP where there are several different types or *species* of particles. Each site of the lattice is occupied by exactly one particle of a certain species. In our convention, the vacancies too are considered as a species of particles. The model with odd (resp. even) number of species is referred to as the *odd mLPASEP* (resp. *even mLPASEP*). We now give the precise definitions of the models.

4.2.1 The odd mLPASEP: mLPASEP with $(2r+1)$-species

Each species in the odd mLPASEP is labelled by an element of $\mathbb{L} := \left\{\overline{r}, \ldots, \overline{1}, 0, 1, \ldots, r\right\}$. The barred labels should be regarded as negative integers with the natural order relation : $\overline{r} < \cdots < 0 < \cdots < r$. The dynamics is as follows. In the bulk, the rules for exchange of particles i and j $(i, j \in \mathbb{L})$ between two neighbouring sites are given by

$$ij \to ji \quad \text{with rate} \begin{cases} 1 & \text{if } i > j, \\ q & \text{if } i < j, \end{cases} \tag{4.2.1}$$

where we impose $q < 1$. At the left boundary, either of the two type of transitions are permissible: (i) a species can replace a smaller species, or (ii) a species whose label is nonnegative can replace a higher order species. These transitions and corresponding rates are summarized as

$$i \to j \quad \text{with rate} \begin{cases} \alpha_j & \text{if } \overline{r} \le i < j, \\ \gamma_j & \text{if } i > j \ge 0. \end{cases} \tag{4.2.2}$$

The rates α_i are independent positive parameters, whereas the γ_i's are defined in terms of the α_i's and q. To write the relation concisely, we define the quantities $\theta_k = \sum_{i=k}^{r} \alpha_i$, and $\phi_k = \sum_{i=\overline{k-1}}^{k-1} \alpha_i$ for $k \in [r]$. Then

$$\gamma_k = \begin{cases} \dfrac{\phi_1\,(\phi_1 + \theta_1 - 1 + q)}{\phi_1 + \theta_1} & \text{if } k = 0, \\ \alpha_k + \alpha_{\overline{k}} - \dfrac{(1-q)\left(\alpha_k \phi_k + \alpha_k \theta_k + \alpha_{\overline{k}} \theta_k\right)}{(\theta_k + \phi_k)(\theta_{k+1} + \phi_{k+1})} & \text{if } k > 0. \end{cases} \tag{4.2.3}$$

In order that γ_k's are positive, we impose the restriction $\theta_0 > 1 - q$. This specific choice of γ_k's allows us to map mLPASEP onto LPASEP by colouring as explained later in Section 4.3. At the right boundary, an unbarred species i can replace or be replaced by its barred counterpart with the following rates

$$\begin{cases} i \to \bar{i} & \text{with rate } \beta, \\ \bar{i} \to i & \text{with rate } \delta, \end{cases} \tag{4.2.4}$$

where β and δ are positive parameters. Thus, species 0 can neither enter nor exit from the right boundary.

4.2.2 The even mLPASEP: mLPASEP with $(2r)$-species

The label set for all species in even mLPASEP is $\mathbb{L}_0 \equiv \mathbb{L} \setminus \{0\}$. The bulk and right boundary transitions given by (4.2.1) and (4.2.4) are unaltered. The left boundary transitions resemble those in the odd mLPASEP, except that species $\overline{1}$ can also replace a higher species. More precisely,

$$i \to j \quad \text{with rate} \begin{cases} \alpha_j & \text{if } \overline{r} \le i < j, \\ \gamma'_j & \text{if } i > j \ge 1, \\ \gamma'_0 & \text{if } i > j = \overline{1}. \end{cases} \tag{4.2.5}$$

As before, the rates α_i are independent positive parameters and the γ'_i's are defined in terms of the α_i's and q. Define θ_k's as for the odd mLPASEP and $\phi'_k = \sum_{i=1}^{k-1}(\alpha_i + \alpha_{\bar{i}})$ for $2 \le k \le r$. Then

$$\gamma'_k = \begin{cases} \dfrac{\phi'_1(\phi'_1 + \theta_1 - 1 + q)}{\phi'_1 + \theta_1} - \gamma'_0 & \text{if } k = 1, \\ \alpha_k + \alpha_{\overline{k}} - \dfrac{(1-q)\left(\alpha_k \phi'_k + \alpha_k \theta_k + \alpha_{\overline{k}} \theta_k\right)}{(\theta_k + \phi'_k)(\theta_{k+1} + \phi'_{k+1})} & \text{if } k > 1, \end{cases} \tag{4.2.6}$$

where the rates are chosen so that $\phi'_1 + \theta_1 > 1 - q$ and $\gamma'_0 < \phi'_1(\phi'_1 + \theta_1 - 1 + q)/(\phi'_1 + \theta_1)$. Again, the way in which γ'_k's are defined above is crucial to the application of colouring technique.

As mentioned above, we will focus on the odd mLPASEP throughout the article. The treatment of the even mLPASEP follows very similar lines and we relegate that discussion to Section 4.5.

4.3 Exact Phase diagram for odd mLPASEP

To derive the phase diagram, we will construct a series of exact projections from the odd mLPASEP to the LPASEP. This strategy was successfully used to derive the exact phase diagram for the mASEP [21]. The projection is called the *k-colouring* and is explained below. We will use it to calculate densities and currents for all species of particles in all phases. Then these results are illustrated by considering the case $r = 2$. The idea of colouring is that some species of particles will be indistinguishable and the dynamics will be the same as that of an odd mLPASEP with fewer number of species. We emphasize that the colouring is exact in the sense that the projection respects the dynamics both in the bulk and on the boundaries.

To be precise, we fix k between 1 and r. We then identify species $\overline{r}, \ldots, \overline{k}$, as a new species which we label $\overline{1}_k$. Similarly, species $k, \ldots, r$, are identified as 1_k, and species $\overline{k-1}, \ldots, k-1$, are called 0_k. Each k-colouring maps odd mLPASEP onto the LPASEP with the boundary rates given by:

$$\underline{\text{Left}}: \quad \begin{cases} \overline{1}_k, 0_k \to 1_k & \text{with rate } \theta_k, \\ \overline{1}_k \to 0_k & \text{with rate } \phi_k, \\ 1_k \to 0_k & \text{with rate } \zeta_k, \end{cases}$$

$$\underline{\text{Right}}: \quad \begin{cases} 1_k \to \overline{1}_k & \text{with rate } \beta, \\ \overline{1}_k \to 1_k & \text{with rate } \delta, \end{cases}$$

where $\zeta_k = \sum_{i=0}^{k-1} \gamma_i$. It can be easily checked using the definition of γ_i's that $\zeta_k = \phi_k(\theta_k + \phi_k - 1 + q)/(\theta_k + \phi_k)$. The left boundary parameter $\lambda_k = \theta_k/\phi_k$ and the right boundary parameter $b = \kappa_{\beta,\delta}$ (which is independent of k), where

$$\kappa_{u,v} := \frac{1 - q - u + v + \sqrt{(1 - q - u + v)^2 + 4uv}}{2u}, \tag{4.3.1}$$

determine part of the phase diagram of the odd mLPASEP. Since there are such r possible colourings, the overall phase diagram of the generalized model depends on the following $r + 1$ parameters: $\lambda_1, \ldots, \lambda_r$ and b. Note that $\lambda_1 < \cdots < \lambda_r$ by definition.

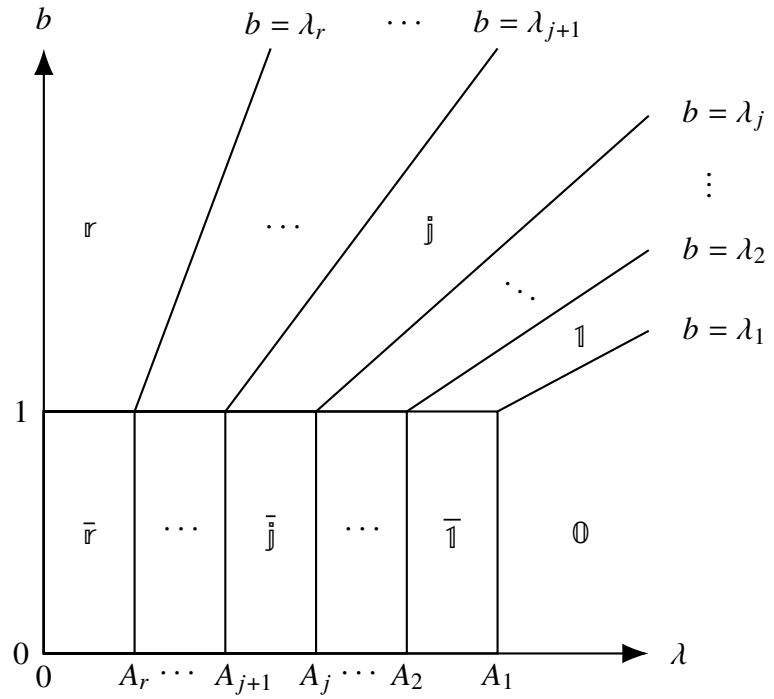

Figure 4.1: A slice of the phase diagram for the odd mLPASEP determined by parameters $(s_1, \ldots, s_{r-1})$.

4.3.1 Phase diagram

We obtain the phase diagram of the odd mLPASEP by dividing the $(r + 1)$-dimensional phase space appropriately. In order to find all phases, we consider the phase diagram for the model

obtained by k-colouring for all k simultaneously. The three phase regions in the LPASEP phase diagram in Figure 3.1 lead to a total of $2r + 1$ phase regions as follows.

- Phase $\bar{\mathbb{r}}$: $\max\{\lambda_r, b\} < 1$.
- For $1 \le j \le r-1$, phase $\bar{\mathbb{j}}$: $\max\{\lambda_j, b\} < 1 < \lambda_{j+1}$.
- Phase $\mathbb{0}$: $\max\{1, b\} < \lambda_1$.
- For $1 \le j \le r-1$, phase $\mathbb{j}$: $\max\{1, \lambda_j\} < b < \lambda_{j+1}$.
- Phase $\mathbb{r}$: $\max\{1, \lambda_r\} < b$.

In order to visualize the phases, we fix real constants $(s_1, \ldots, s_{r-1})$ such that $s_1 > \cdots > s_{r-1} > 1$. Consider the two-dimensional plane determined by $\lambda_r = s_{r-1}\lambda_{r-1} = \cdots = s_1\lambda_1$. On this plane, $\lambda = \left(\sum_{i=1}^{r} \lambda_i^2\right)^{1/2}$ measures the radial distance from origin in the $(\lambda_1, \ldots, \lambda_r)$-subspace. Let A_i be the point on this plane at which the hyperplanes $b = 0$ and $\lambda_i = 1$ intersect. Then A_i has coordinates given by

$$\begin{cases} (s_i/s_1, \ldots, s_i/s_{i-1}, 1, s_i/s_{i+1}, \ldots, s_i/s_{r-1}, s_i, 0) & 1 \le i < r, \\ (1/s_1, \ldots, 1/s_{r-1}, 1, 0) & i = r. \end{cases}$$

We draw the two-dimensional phase diagram in terms of A_i's and the parameters λ and b. The phase regions are as illustrated in Figure 4.1. The line $b = \lambda_j$ is the boundary between phases $\mathbb{j} - \mathbb{1}$ and $\mathbb{j}$ for $1 \le j \le r$. We now describe the currents and densities in each phase.

4.3.2 Currents and Densities

We explain how to calculate densities and currents using k-colouring for the odd mLPASEP. We will give all the details only for phase $\mathbb{0}$ and sketch the argument for other phases. To describe the densities and currents succinctly, we define $f(x) = 1/(1+x)$, $\overline{f}(x) = 1 - f(x)$, and $g(x, y) = (1-q)\left(f(x)\overline{f}(x) - f(y)\overline{f}(y)\right)$. The results are tabulated in Table 4.1 and summarized below.

Before we go on to the calculation, we make a couple of remarks about the currents. The currents of barred species are determined completely by their unbarred partners; specifically $J_{\bar{i}} = -J_i$. This is because every species i can enter and exit the right boundary only at the expense of its barred partner. Moreover, since 0's can neither enter or leave from the right boundary, there is no current of species 0, i.e. $J_0 = 0$.

Phase $\mathbb{0}$

In phase $\mathbb{0}$, the odd mLPASEP is projected onto the LD phase of the LPASEP by all colourings. Hence, we have from

$$\rho_0 = 1 - 2f(\lambda_1), \quad \sum_{i=1}^{r} \rho_i = \sum_{i=\bar{r}}^{\bar{1}} \rho_i = f(\lambda_1),$$

and $\sum_{i=1}^{r} J_i = g(\lambda_1, 0)$ by the 1-colouring. Similarly, $2 \le k \le r$, one obtains

$$\sum_{i=\overline{k-1}}^{k-1} \rho_i = 1 - 2f(\lambda_k), \quad \sum_{i=k}^{r} \rho_i = \sum_{i=\overline{r}}^{\overline{k}} \rho_i = f(\lambda_k)$$

and $\sum_{i=k}^{r} J_i = g(\lambda_k, 0)$ by k-colouring. Comparing the k and $(k+1)$-colouring, we find that $\rho_k = \rho_{\overline{k}} = f(\lambda_k) - f(\lambda_{k+1})$ and $J_k = g(\lambda_k, \lambda_{k+1})$ for $1 \le k < r$. Finally, by the r-colouring, one obtains $\rho_r = \rho_{\overline{r}} = f(\lambda_r)$, and $J_r = g(\lambda_r, 0)$. See Figure 4.2(c) for the densities in phase $\mathbb{0}$ of the odd mLPASEP with $r = 2$.

Phase	Species	Density ρ	Current J
$\bar{\mathbb{r}}$	$\overline{r}$	$f(1)$	
	$\overline{r} < i < r$	0	0
	r	$f(1)$	$g(1,0)$
$\bar{\mathbb{j}}$	$\overline{r}$	$f(\lambda_r)$	
	$i < \overline{j}$	$f(\lambda_{\lvert i\rvert}) - f(\lambda_{\lvert i\rvert+1})$	
	$\overline{j}$	$f(1) - f(\lambda_{j+1})$	
	$\overline{j} < i < j$	0	
	j	$f(1) - f(\lambda_{j+1})$	
	$i > j$	$f(\lambda_i) - f(\lambda_{i+1})$	$g(\lambda_i, \lambda_{i+1})$
	r	$f(\lambda_r)$	$g(\lambda_r, 0)$
$\mathbb{0}$	$\overline{r}$	$f(\lambda_r)$	
	$\overline{r} < i < 0$	$f(\lambda_{\lvert i\rvert}) - f(\lambda_{\lvert i\rvert+1})$	
	0	$1 - 2f(\lambda_1)$	0
	$0 < i < r$	$f(\lambda_i) - f(\lambda_{i+1})$	$g(\lambda_i, \lambda_{i+1})$
	r	$f(\lambda_r)$	$g(\lambda_r, 0)$
$\mathbb{j}$	$\overline{r}$	$f(\lambda_r)$	
	$i < \overline{j}$	$f(\lambda_{\lvert i\rvert}) - f(\lambda_{\lvert i\rvert+1})$	
	$\overline{j}$	$f(b) - f(\lambda_{j+1})$	
	$\overline{j} < i < j$	0	0
	j	$\overline{f}(b) - f(\lambda_{j+1})$	$g(b, \lambda_{j+1})$
	$i > j$	$f(\lambda_i) - f(\lambda_{i+1})$	$g(\lambda_i, \lambda_{i+1})$
	r	$f(\lambda_r)$	$g(\lambda_r, 0)$
$\mathbb{r}$	$\overline{r}$	$f(b)$	
	$\overline{r} < i < r$	0	0
	r	$\overline{f}(b)$	$g(b, 0)$

Table 4.1: Bulk densities and currents in each phase for odd mLPASEP. We do not write the currents for barred species since $J_{\bar{i}} = -J_i$.

Phases $\mathbb{j}$ and $\bar{\mathbb{j}}$

Here, the k-colouring maps phase $\mathbb{j}$ to the LD (resp. HD) phase of the LPASEP and phase $\bar{\mathbb{j}}$ to the LD (resp. MC) phase of an LPASEP for $k \geq j$ (resp. $k < j$). In these phases, we have (i) $\rho_i = \rho_{\bar{i}}$ for all $i > j$, and (ii) all species i with $\bar{j} < i < j$ are dynamically expelled, i.e. $\rho_i = 0$. See Figures 4.2(b) and (d) for the densities in phases $\bar{\mathbb{1}}$ and $\mathbb{1}$ of the odd mLPASEP with $r = 2$.

Phases $\mathbb{r}$ and $\bar{\mathbb{r}}$

All k-colourings now map phase $\mathbb{r}$ and $\bar{\mathbb{r}}$ onto HD and MC phases respectively of the LPASEP. Thus all species i satisfying $\bar{r} < i < r$ are dynamically expelled. The density and current of species r are then given by the r-colouring. See Figures 4.2(a) and (e) for the densities in phases $\bar{\mathbb{2}}$ and $\mathbb{2}$ of the odd mLPASEP with $r = 2$.

$(\mathbb{j} - \mathbb{1}) - \mathbb{j}$ coexistence line

The k-colouring maps the $(\mathbb{j} - \mathbb{1}) - \mathbb{j}$ boundary to the HD-LD coexistence line of the LPASEP for $k = j$, and to the LD (resp. HD) phase of the LPASEP for $k > j$ (resp. $k < j$). All species i with $\bar{j} < i < j - 1$ are dynamically expelled. Moreover, species $j - 1$ and j have linear densities on these lines. See Figures 4.2(f) and (g) for the densities on the $\mathbb{1} - \mathbb{2}$ and $\mathbb{0} - \mathbb{1}$ coexistence lines of the odd mLPASEP with $r = 2$.

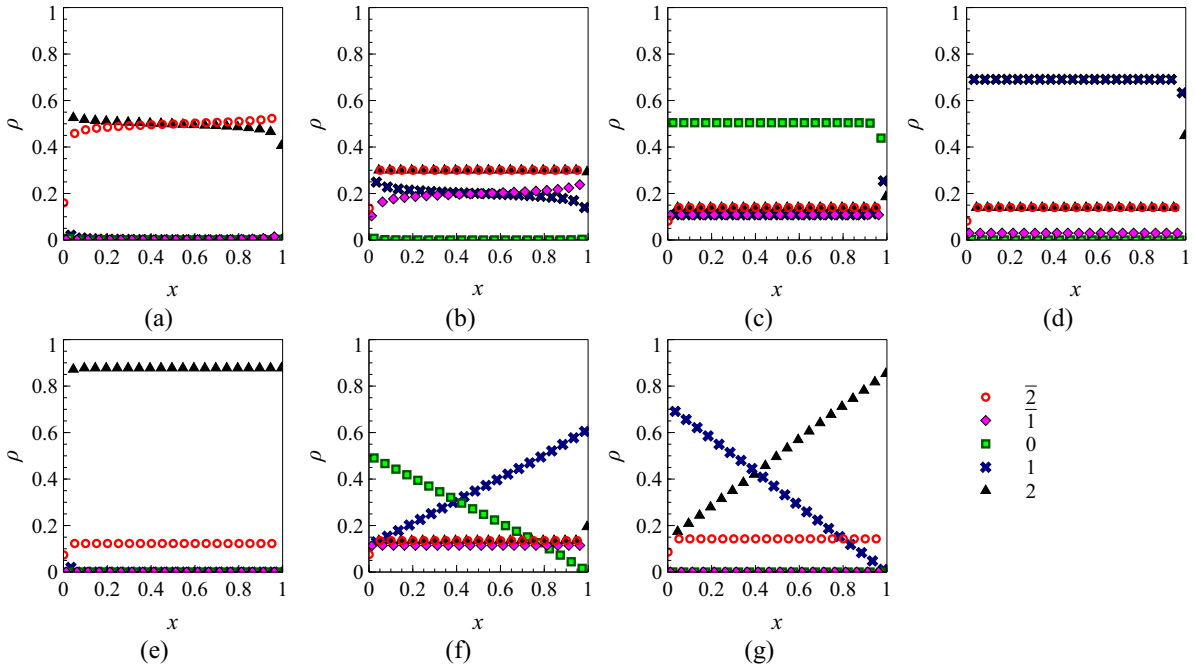

Figure 4.2: Time-average densities in 5-species odd mLPASEP for species $\bar{2}$ (red circles), $\bar{1}$ (magenta diamonds), 0 (green boxes), 1 (blue crosses) and 2 (black triangles) for (a) phase $\bar{\mathbb{2}}$ ($\lambda_1 \simeq 0.36, \lambda_2 \simeq 0.8, b \simeq 0.59$), (b) phase $\bar{\mathbb{1}}$ ($\lambda_1 \simeq 0.37, \lambda_2 \simeq 2.33, b \simeq 0.59$), (c) phase $\mathbb{0}$ ($\lambda_1 \simeq 3.04, \lambda_2 \simeq 6.16, b \simeq 2.61$), (d) phase $\mathbb{1}$ ($\lambda_1 \simeq 3.04, \lambda_2 \simeq 6.16, b \simeq 4.91$), (e) phase $\mathbb{2}$ ($\lambda_1 \simeq 3.02, \lambda_2 \simeq 6.09, b \simeq 7.15$), (f) $\mathbb{0} - \mathbb{1}$ coexistence line ($\lambda_1 = 3, \lambda_2 \simeq 6.41, b = 3$), and (g) $\mathbb{1} - \mathbb{2}$ coexistence line ($\lambda_1 \simeq 3.05, \lambda_2 = 6, b = 6$). The lattice size is 1000 for all cases.

4.3.3 Example of $r = 2$

The simplest nontrivial odd mLPASEP is the one with five species. The boundary transitions are given by

$$\underline{\text{Left}}: \quad \begin{cases} \overline{2}, \overline{1}, 0, 1 \to 2 & \text{with rate } \alpha_2, \\ \overline{2}, \overline{1}, 0 \to 1 & \text{with rate } \alpha_1, \\ \overline{2}, \overline{1} \to 0 & \text{with rate } \alpha_0, \\ 1, 2 \to 0 & \text{with rate } \gamma_0, \\ 2 \to 1 & \text{with rate } \gamma_1, \end{cases}$$

$$\underline{\text{Right}}: \quad \begin{cases} 2 \to \overline{2} & \text{with rate } \beta, \\ 1 \to \overline{1} & \text{with rate } \beta, \\ \overline{1} \to 1 & \text{with rate } \delta, \\ \overline{2} \to 2 & \text{with rate } \delta. \end{cases}$$

In the 1-colouring, we identify species 1's and 2's as 1_1, $\overline{1}$'s and $\overline{2}$'s as $\overline{1}_1$, and 0's as 0_1, such that the rates for boundary transitions are given by

$$\underline{\text{Left}}: \quad \begin{cases} \overline{1}_1, 0_1 \to 1_1 & \text{with rate } \theta_1, \\ \overline{1}_1 \to 0_1 & \text{with rate } \phi_1, \\ 1_1 \to 0_1 & \text{with rate } \zeta_1, \end{cases}$$

$$\underline{\text{Right}}: \quad \begin{cases} 1_1 \to \overline{1}_1 & \text{with rate } \beta, \\ \overline{1}_1 \to 1_1 & \text{with rate } \delta. \end{cases}$$

The relevant left and right boundary parameters are λ_1 and $b = \kappa_{\beta,\delta}$ respectively. On the other hand, we label $\overline{1}$'s,0's and 1's with 0_2, 2's with 1_2, and $\overline{2}$'s with $\overline{1}_2$ in 2-colouring. Now, we have the following boundary rates

$$\underline{\text{Left}}: \quad \begin{cases} \overline{1}_2, 0_2 \to 1_2 & \text{with rate } \theta_2, \\ \overline{1}_2 \to 0_2 & \text{with rate } \phi_2, \\ 1_2 \to 0_2 & \text{with rate } \zeta_2, \end{cases}$$

$$\underline{\text{Right}}: \quad \begin{cases} 1_2 \to \overline{1}_2 & \text{with rate } \beta, \\ \overline{1}_2 \to 1_2 & \text{with rate } \delta. \end{cases}$$

The relevant parameters λ_2 and $b = \kappa_{\beta,\delta}$ correspond to the left and right boundary respectively.

The phase diagram is the three-dimensional space of the parameters λ_1, λ_2 and b. The region $\lambda_1 > \lambda_2$ is excluded. We fix a constant $s_1 > 1$ and consider the two dimensional plane $\lambda_2 = s_1\lambda_1$. In this plane, λ is the distance along the $b = 0$ plane. This plane passes through all the phases and, as a result, allows us to visualize all phases on a two-dimensional phase diagram as shown in Figure 4.3. Using the colouring ideas as outlined in Section 4.3, we find that there are five phases in the phase diagram:

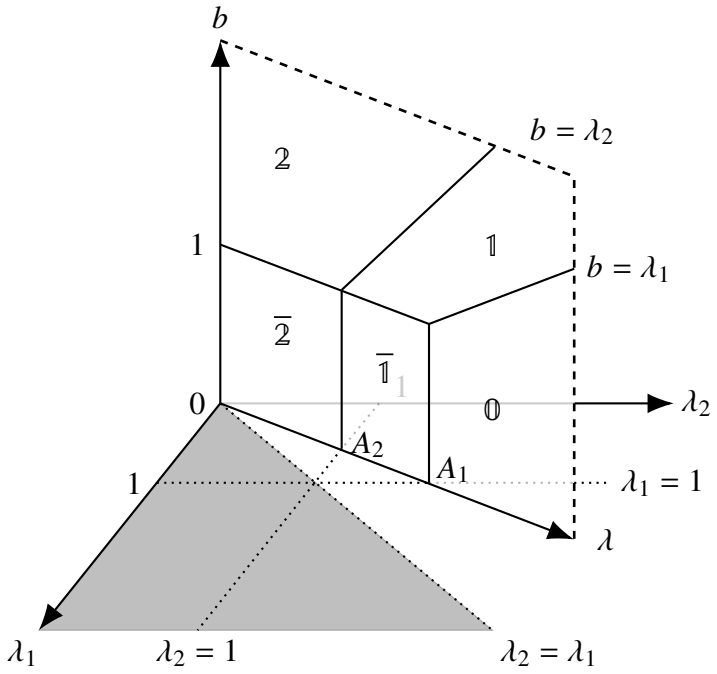

Figure 4.3: Phase diagram for mLPASEP with $r = 2$. The shaded region ($\lambda_1 > \lambda_2$) is forbidden. The plane in focus is given by $\lambda_2 = s_1\lambda_1$.

- phase $\overline{2}$: $\max\{b, \lambda_2\} < 1$,
- phase $\overline{1}$: $\max\{b, \lambda_1\} < 1 < \lambda_2$,
- phase $\mathbb{0}$: $\max\{1, b\} < \lambda_1$,
- phase $\mathbb{1}$: $\max\{1, \lambda_1\} < b < \lambda_2$,
- phase $\mathbb{2}$: $\max\{1, \lambda_2\} < b$.

In addition, the two coexistence planes, the $\mathbb{0} - \mathbb{1}$ phase boundary: $1 < b = \lambda_1$, and the $\mathbb{1} - \mathbb{2}$ phase boundary: $1 < b = \lambda_2$, appear as lines. On the $b = 0$ plane, the plane $\lambda_i = 1$ and the plane $\lambda_2 = s_1\lambda_1$ intersect at the point denoted by A_i for $i = 1, 2$. A_1 and A_2 have locations $(1, s_1, 0)$ and $(1/s_1, 1, 0)$.

4.4 Shock picture in the odd mLPASEP

We now use the shock picture in the LPASEP to understand the density profiles as well as the phenomenon of dynamical expulsion in the odd mLPASEP. We will explain this picture in each phase and phase-boundary. This picture is best understood by looking at the coexistence lines first.

The $(\mathbb{j} - \mathbb{1}) - \mathbb{j}$ coexistence line for $1 \leq j \leq r$: From the k-colouring argument, we see that species $j - 1$ and j are phase-segregated and other species have constant densities on this coexistence line. In other words, only species $j - 1$ and j take part in the shock on this coexistence line. This is illustrated in the schematic plot in Figure 4.4. The shock performs a

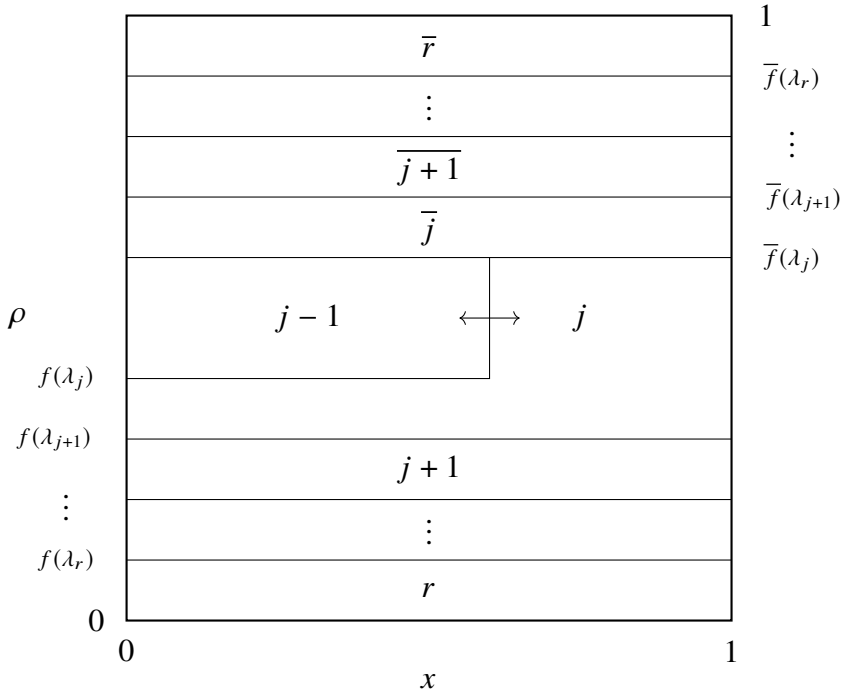

Figure 4.4: The shock picture for mLPASEP: The schematic plot shows the shock on the coexistence line $b = \lambda_j > 1$ for the odd mLPASEP where $1 \leq j \leq r$. At each point x, the densities of the k-coloured species 1_k and $\overline{1}_k$ satisfy (3.6.1) for each k.

random walk with no net drift. Moreover, species $\overline{j-1}, \ldots, j-2$ are dynamically expelled. See Figure 4.2(f) and (g) for simulations of the odd mLPASEP with $r = 2$ on the $\mathbb{0} - \mathbb{1}$ and $\mathbb{1} - \mathbb{2}$ coexistence lines respectively. See also Figures 4.5 (a) and (b) for instantaneous profiles of the shock in these lines.

Phases $\bar{\mathbb{j}}$ and $\mathbb{j}$ for $1 \leq j \leq r$: In phase $\mathbb{j}$, the shock front is pinned to the left causing the dynamical expulsion of species $j-1$ and higher density of j's compared to $\overline{j}$'s. In phase $\bar{\mathbb{j}}$, the $j-1$'s are again dynamically expelled because the height of the shock vanishes. See Figure 4.2(a), (b), (d) and (e) for simulations of the odd mLPASEP with $r = 2$ in phases $\overline{\mathbb{2}}$, $\overline{\mathbb{1}}$, $\mathbb{1}$ and $\mathbb{2}$.

Phase $\mathbb{0}$: The shock picture on the $\mathbb{0} - \mathbb{1}$ coexistence line is Figure 4.4 with $j = 1$. The shock front has positive drift in phase $\mathbb{0}$ and consequently gets pinned to the right boundary resulting in non-zero bulk density of species 0. Hence, all species have non-zero densities in phase $\mathbb{0}$. See Figure 4.2(c) for simulations of the odd mLPASEP with $r = 2$ in phase $\mathbb{0}$.

In addition, we note the following on the $(\mathbb{j} - \mathbb{1}) - \mathbb{j}$ coexistence line. Species $\overline{j-1}$ is dynamically expelled on this line, although species $j-1$ has non-zero bulk density. This might seem counterintuitive because (3.6.1) suggests that either a species and its barred partner are both present or both absent. The resolution of this apparent contradiction is the fact that (3.6.1) only applies to the k-coloured species $\overline{1}_k$ and 1_k for each k.

To illustrate this point further, we perform a spatiotemporal simulation of the odd mLPASEP with $r = 2$ on the $\mathbb{1} - \mathbb{2}$ coexistence line. The results of the simulation are shown in Figure 4.6.

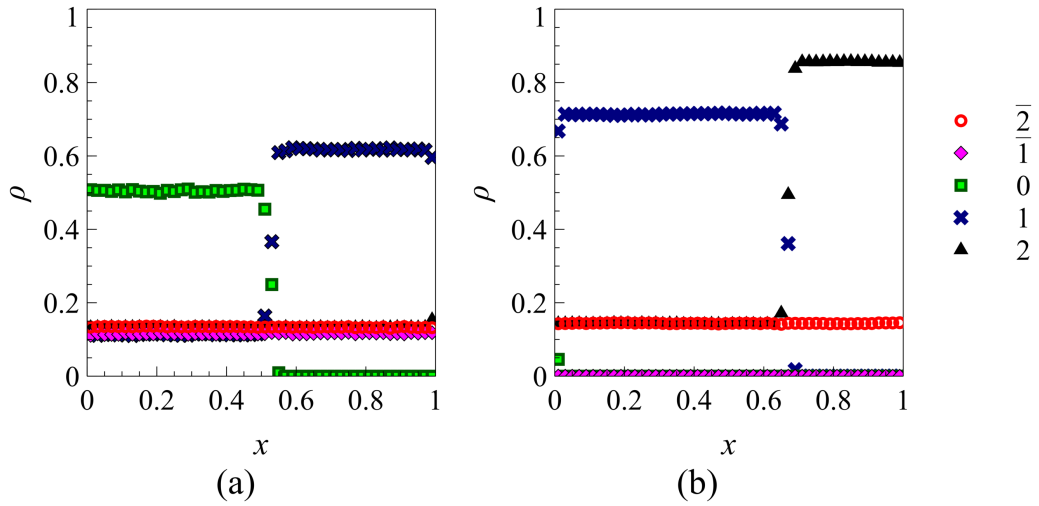

Figure 4.5: Instantaneous shock profiles in the 5-species odd mLPASEP : Density profiles for species $\overline{2}$ (red circles), $\overline{1}$ (magenta diamonds), 0 (green boxes), 1 (blue crosses) and 2 (black triangles) on (a) $\mathbb{0} - \mathbb{1}$ coexistence line ($\lambda_1 = 3, \lambda_2 \simeq 6.41, b = 3$), and (b) $\mathbb{1} - \mathbb{2}$ coexistence line ($\lambda_1 \simeq 3.05, \lambda_2 = 6, b = 6$), where the lattice size is 2500.

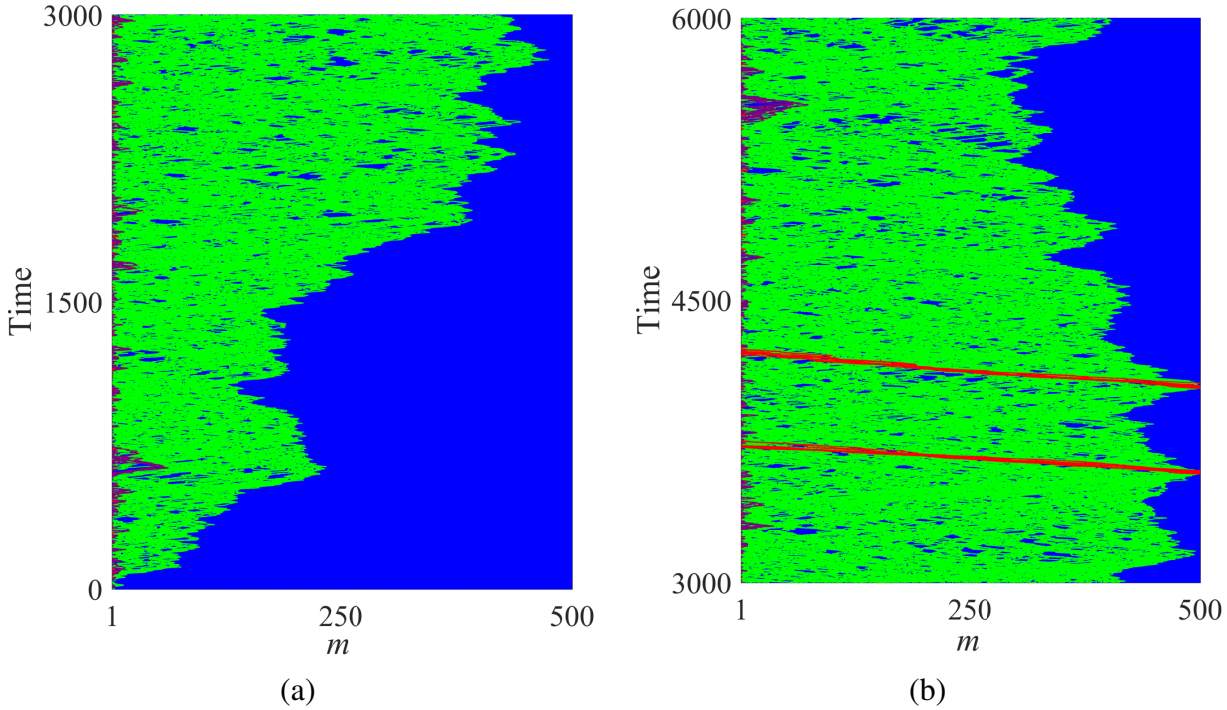

Figure 4.6: The spatiotemporal evolution of the shock on the $\mathbb{1}-\mathbb{2}$ coexistence line for 5-species odd mLPASEP for 6000 time steps. Each time step equals 4000 random sequential updates in the simulation. The plots show trajectories of species $\overline{1}$ (red), 0 (violet), 1 (green) and 2 (blue) versus site position after the system reaches steady state. Particles of species $\overline{2}$ are not shown. The parameters are as follows: $\alpha_{\overline{1}} = 0.08, \alpha_0 = 0.45, \alpha_1 = 0.13, \alpha_2 = 0.33, \gamma_0 \simeq 0.005, \gamma_1 \simeq 0.06, q = 0.1, \beta = 0.475,$ and $\delta = 0.35$ ($b = \lambda_2 = 2, \lambda_1 \simeq 0.98$), and the lattice size is 500.

The shock there is formed between species 1 and 2 and has zero mean velocity. Species $\overline{0}$ and $\overline{1}$ are dynamically expelled. As one can see from the simulation, particles of species $\overline{1}$ can enter either on the left or the right boundary, but they eventually leave from the left boundary because of the high density of 1's and 2's. They can only enter at the right boundary when the $1-2$ shock touches the right boundary.

4.5 The even mLPASEP

We explain the salient features of the phase diagram of the even mLPASEP focusing on the aspects that make the analysis more complicated than that for the odd mLPASEP.

The phase diagrams for the even mLPASEP with $2r$ species and the odd mLPASEP with $(2r+1)$ species have identical structure as depicted in Figure 4.1. The main difference between the two is that the 1-colouring projects the even mLPASEP to the (single-species) ASEP (see Section 1.1.1.5) so that the boundary parameters are $\lambda_1 = \kappa_{\theta_1,\gamma_0'}$ and $b = \kappa_{\beta,\delta}$. All other k-colourings continue to project the even mLPASEP to the LPASEP with boundary parameters $\lambda_k = \theta_k/\phi_k'$ and $b = \kappa_{\beta,\delta}$, where $\theta_k = \sum_{i=k}^{r} \alpha_i$ and $\phi_i' = \sum_{i=1}^{k-1} \left(\alpha_i + \alpha_{\bar{i}}\right)$ were defined in Section 4.2.2.

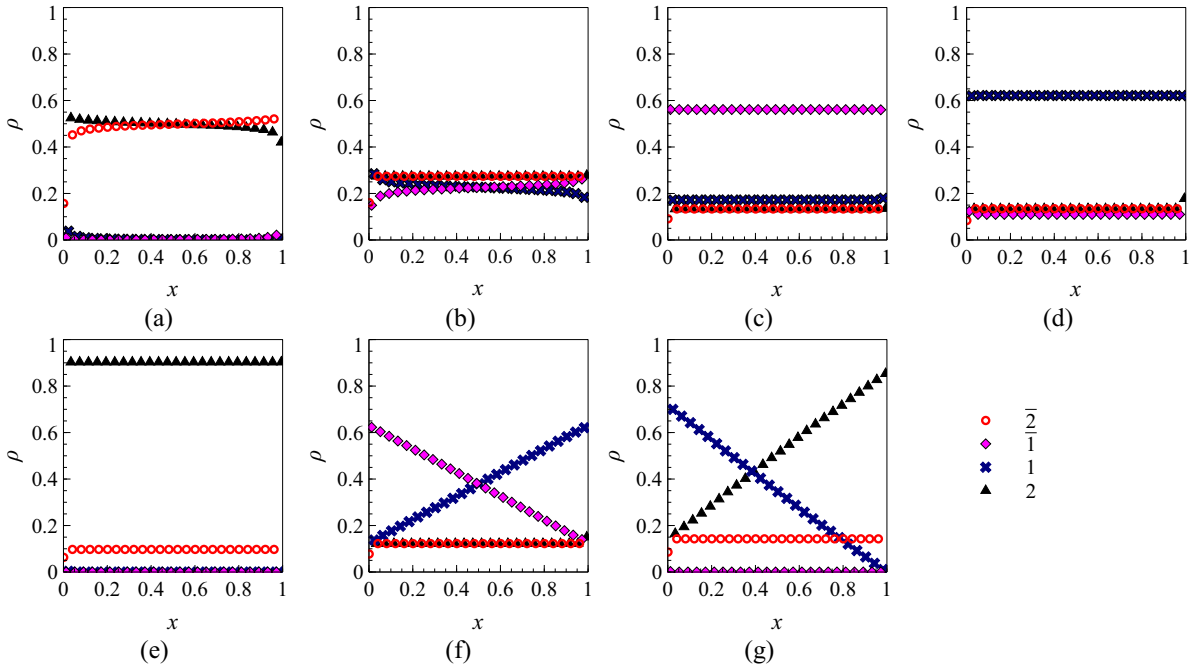

Figure 4.7: Time-average densities in 4-species mLPASEP for species $\overline{2}$ (red circles), $\overline{1}$ (magenta diamonds), 0 (green boxes), 1 (blue crosses) and 2 (black triangles) for (a) phase $\overline{\mathbb{2}}$ ($\lambda_1 \simeq 0.23, \lambda_2 \simeq 0.84, b \simeq 0.65$), (b) phase $\overline{\mathbb{1}}$ ($\lambda_1 \simeq 0.44, \lambda_2 \simeq 2.65, b \simeq 0.75$), (c) phase 0 ($\lambda_1 \simeq 2.27, \lambda_2 \simeq 6.5, b \simeq 0.92$), (d) phase $\mathbb{1}$ ($\lambda_1 \simeq 1.17, \lambda_2 \simeq 6.45, b \simeq 3.09$), (e) phase $\mathbb{2}$ ($\lambda_1 \simeq 1.17, \lambda_2 \simeq 6.45, b \simeq 9.28$), (f) $\mathbb{0}-\mathbb{1}$ coexistence line ($\lambda_1 = 3, \lambda_2 \simeq 7.18, b = 3$), and (g) $\mathbb{1}-\mathbb{2}$ coexistence line ($\lambda_1 \simeq 1.34, \lambda_2 = 6, b = 6$). For all simulations, we fix the lattice size to be 1000.

Taking into account all possible colourings, there are $r+1$ relevant boundary parameters,

namely, $\lambda_1, \ldots, \lambda_r$ and b. Again, the inequalities $\lambda_1 < \lambda_2 < \ldots < \lambda_r$ are satisfied. Because of these relations among λ_i's, we arrive at the same phase diagram in Figure 4.1 which shows all $2r + 1$ phases in the even mLPASEP. In all phases except phase $\mathbb{0}$, the densities of all species have the same expression in the even mLPASEP as given in Table 4.1. In phase $\mathbb{0}$, the densities of 1 and $\overline{1}$ are $(f(\lambda_1) - f(\lambda_2))$ and $(\overline{f}(\lambda_1) - f(\lambda_2))$ respectively. We illustrate the density profiles with simulations for the 4-species even mLPASEP in Figure 4.7.

The shock picture in the even mLPASEP is identical to that in the odd mLPASEP in all coexistence lines except the $\mathbb{0} - \mathbb{1}$ boundary. On this coexistence line, 1's and $\overline{1}$'s form a shock with zero drift as shown in Figure 4.8. The shock is pinned to the right (resp. left) boundary in phase $\mathbb{0}$ (resp. $\mathbb{1}$). In phase $\overline{\mathbb{1}}$, the density of these two species become equal and the height of the shock goes to zero as the system approaches this phase along the $\mathbb{0} - \mathbb{1}$ coexistence line. We have performed simulations showing instantaneous density profiles for the even mLPASEP with 4 species on the $\mathbb{0} - \mathbb{1}$ boundary and the results exactly match with the theoretical prediction.

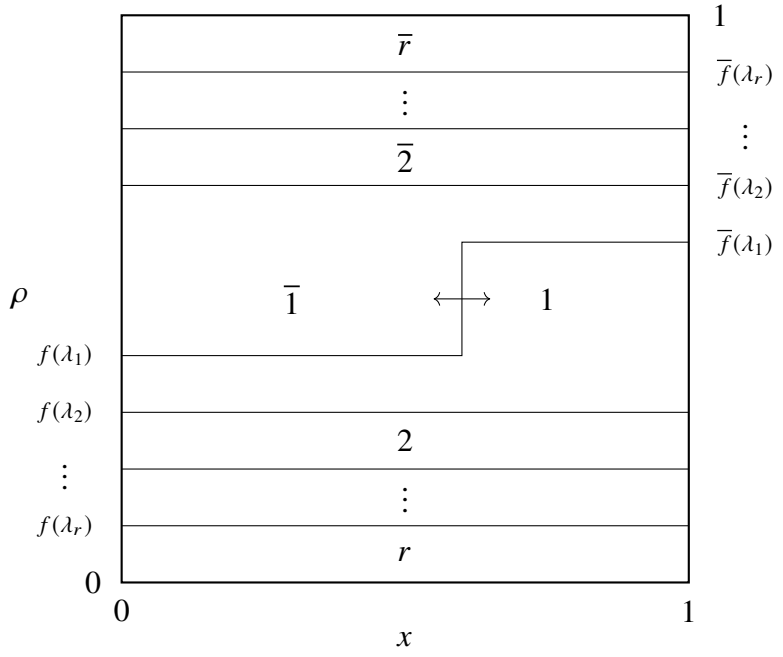

Figure 4.8: The shock picture for the even mLPASEP on the $\mathbb{0} - \mathbb{1}$ coexistence line.

Chapter 5

The phase diagram for a class of multispecies permissive asymmetric exclusion processes

5.1 Introduction

In the present chapter, we study the phase diagram of a multispecies partially asymmetric exclusion process with arbitrary number of species and permeable boundaries. We shall call our model multispecies *permissive* ASEP (or *mpASEP* in short) because both the boundaries permit a species to be replaced with any other species. We construct a colouring scheme that projects the mpASEP onto the open single-species ASEP model. We identify all phases as well as the coexistence regions in the multi-dimensional phase diagram. In the majority of the phases, we observe interesting physical phenomena such as *dynamical expulsion* when particles of one or more species are expelled from the lattice. Nevertheless, corresponding to each species, we find a phase where high density of that particular species can be adopted in the system. We provide explanation to the coarse features of density profiles by means of the generalized shock picture. We note here that we use only colouring argument to compute the macroscopic quantities and the phase diagram without any matrix ansatz.

The present chapter is organized in the following way. First, we define the mpASEP in Section 5.2. In Section 5.3, we present the phase diagram and all densities and currents in each phase. The penultimate section, i.e. Section 5.4, contains discussion regarding the generalized shock picture.

5.2 Model definition

Below, we define a multispecies model which has completely permeable boundaries. Indeed, the boundary interactions make this model distinct from other multispecies models such as mASEP [53, 21] and mLPASEP [25] where passage of particles is far more restricted at the boundaries.

The precise definition of multispecies permissive ASEP or mpASEP is as follows. Similar to the open ASEP, the mpASEP is defined on an open one-dimensional lattice of size L. There are total of $(r+1)$ species of particles in the mpASEP. Each species is identified with an element of the label set $\mathbb{L} := \{0, 1, \ldots, r\}$. The preference of rightwards hopping is determined by the natural order relation among the species: $0 < 1 < \cdots < r$. One can think of 0's as vacancies or the slowest species, r's as the fastest species, and any intermediate species i $(0 < i < r)$ being faster or slower than another species j according to where $i > j$ or $i < j$ respectively. The left boundary interactions are given by

$$i \to j \text{ with rate } \begin{cases} \alpha_j \text{ if } i < j, \\ \gamma_j \text{ if } i > j, \end{cases} \tag{5.2.1}$$

where $(\alpha_1, \ldots, \alpha_r)$ and $(\gamma_0, \ldots, \gamma_{r-1})$ are sets of fixed positive parameters. In the bulk exchange of particles between neighbouring sites follows the rule

$$ij \to ji \text{ with rate } \begin{cases} 1 \text{ if } i > j, \\ q \text{ if } i < j, \end{cases} \tag{5.2.2}$$

where we impose the condition $0 < q < 1$. On the right boundary particles can be replaced with the following rates

$$i \to j \text{ with rate } \begin{cases} \beta_j \text{ if } i > j, \\ \delta_j \text{ if } i < j, \end{cases} \tag{5.2.3}$$

where the parameters $(\beta_0, \ldots, \beta_{r-1})$ and $(\delta_1, \ldots, \delta_r)$ are again fixed and positive. Finally, it is useful to introduce $A_k := \sum_{i=k}^{r} \alpha_i$, and $G_k := \sum_{i=0}^{k-1} \gamma_i$. Also, we define $B_k := \sum_{i=0}^{k-1} \beta_i$, and $D_k := \sum_{i=k}^{r} \delta_i$ in terms of the right boundary parameters. These quantities will appear as boundary parameters when we apply the colouring technique.

Remark 1

We can define a totally asymmetric variant of the mpASEP with r species in the following manner. We allow $q = 0$ as well as $\gamma_i = \delta_j = 0$ for $0 \le i < r$ and $1 \le j \le r$. Moreover, we put restrictions on the nonzero boundary rates such that $\sum_{i=1}^{r} \alpha_i \le 1$ and $\sum_{i=0}^{r-1} \beta_i \le 1$. As an example, one checks that the model becomes the single-species TASEP for $r = 1$.

5.3 The exact phase diagram for the mpASEP

We derive the phase diagram for the mpASEP by constructing projections onto the single-species ASEP (see Section 1.1.1.5). We will refer to this projection procedure as *k-colouring*. The colouring technique was used earlier to study two-species TASEP models in [22, 23, 68] as well as to obtain the phase diagrams for mASEP in Chapter 2 and mLPASEP in Chapter 4.

The essence of the colouring argument is that a set of particles might appear indistinguishable from the perspective of another set of particles because of the dynamical rules of the process.

Thus an appropriate colouring, i.e. identifying particles of different species as a single species, can project the original model onto another model with fewer number of species. We refer to the colouring as exact if it is valid both in the bulk and the boundaries. For such a colouring procedure applicable to the mpASEP, we define k-colouring as follows. We label every species $i < k$ with 0_k, and all other species $i \geq k$ with 1_k. Consequently, mpASEP now resembles the ASEP where particles with label 1_k (resp. 0_k) play the role of particles (resp. vacancies). Before we go into more details for arbitrary r, let us first understand the colouring as well as the resulting phase diagram for the simplest nontrivial case, i.e. the case $r = 2$, in the next section. We postpone our discussion regarding the general case until Section 5.3.2.

5.3.1 Phase diagram of mpASEP with 2 species

If we set $r = 2$, then mpASEP involves only two types of particles (and vacancies). For the sake of completeness, we note all boundary interactions below:

$$\underline{\text{Left}}: \quad \begin{cases} 0, 1 \to 2 & \text{with rate } \alpha_2, \\ 0 \to 1 & \text{with rate } \alpha_1, \\ 1, 2 \to 0 & \text{with rate } \gamma_0, \\ 2 \to 1 & \text{with rate } \gamma_1, \end{cases}$$

$$\underline{\text{Right}}: \quad \begin{cases} 1, 2 \to 0 & \text{with rate } \beta_0, \\ 2 \to 1 & \text{with rate } \beta_1, \\ 0, 1 \to 2 & \text{with rate } \delta_2, \\ 0 \to 1 & \text{with rate } \delta_1. \end{cases}$$

There are two possible colourings. In the first colouring, which we call 1-colouring, we identify 1's and 2's as 1_1, and 0's as 0_1. Then the 2-species mpASEP behaves exactly as the ASEP with the boundary interaction rates given by

$$\underline{\text{Left}}: \quad \begin{cases} 0_1 \to 1_1 & \text{with rate } (\alpha_1 + \alpha_2), \\ 1_1 \to 0_1 & \text{with rate } \gamma_0, \end{cases}$$

$$\underline{\text{Right}}: \quad \begin{cases} 1_1 \to 0_1 & \text{with rate } \beta_0, \\ 0_1 \to 1_1 & \text{with rate } (\delta_1 + \delta_2). \end{cases}$$

The relevant left and right boundary parameters are $a_1 = \kappa_{\alpha_1+\alpha_2,\gamma_0}$ and $b_1 = \kappa_{\beta_0,\delta_1+\delta_2}$ respectively, where

$$\kappa_{u,v} := \frac{1 - q - u + v + \sqrt{(1 - q - u + v)^2 + 4uv}}{2u}. \tag{5.3.1}$$

The other possibility is 2-colouring in which we label species 2 with 1_2, and both species 0 and 1 with 0_2. Again the resulting model is the ASEP but with different boundary rates,

$$\underline{\text{Left}}: \quad \begin{cases} 0_2 \to 1_2 & \text{with rate } \alpha_2, \\ 1_2 \to 0_2 & \text{with rate } (\gamma_0 + \gamma_1), \end{cases}$$

$$\underline{\text{Right}}: \quad \begin{cases} 1_2 \to 0_2 & \text{with rate } (\beta_0 + \beta_1), \\ 0_2 \to 1_2 & \text{with rate } \delta_2. \end{cases}$$

The phase diagram for the model just described is determined by the left and right boundary parameters $a_2 = \kappa_{\alpha_2,\gamma_0+\gamma_1}$ and $b_2 = \kappa_{\beta_0+\beta_1,\delta_2}$ respectively.

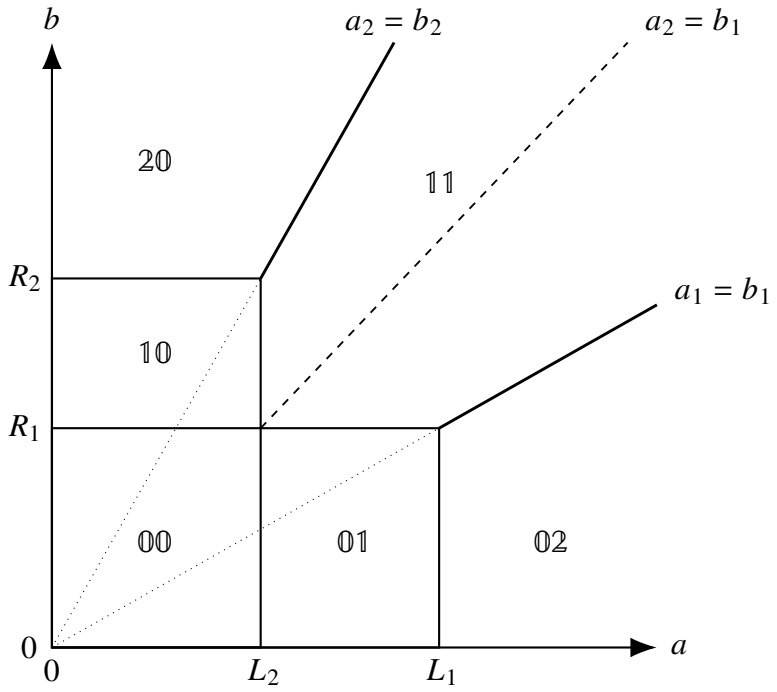

Figure 5.1: Phases of the mpASEP for $r = 2$ visualized on a two-dimensional plane that is embedded in the (a_1, a_2, b_1, b_2)-space and determined by parameters (μ_1, ν_1) as shown in (5.3.2). The coordinates of the points L_i and R_i are given by (5.3.4) in Section 5.3.2 for the general case.

All phases reside in the (a_1, a_2, b_1, b_2)-space. However, it is easy to check that the relevant boundary parameters obey the restrictions $a_1 < a_2$, and $b_2 < b_1$. These constraints allow us to visualize the phases on a two-dimensional plane that is fixed by

$$\begin{aligned} a_2 &= \mu_1 a_1, \\ b_1 &= \nu_1 b_2, \end{aligned} \tag{5.3.2}$$

where $\mu_1, \nu_1 > 1$. The parameter $a = \left(a_1^2 + a_2^2\right)^{1/2}$ gives the radial distance from the origin in the (a_1, a_2)-subspace. Similarly, we define $b = \left(b_1^2 + b_2^2\right)^{1/2}$ in the (b_1, b_2)-subspace.

We derive the phase diagram shown in Figure 5.1 taking into account all possible colourings. The phase diagram consists of the following phases.

- Phase $\mathbb{00}$: $\max\{a_1, a_2, b_1, b_2\} < 1$.
- Phase $\mathbb{01}$: $\max\{a_1, b_1\} < 1$, $\max\{1, b_2\} < a_2$.
- Phase $\mathbb{02}$: $\max\{1, b_1\} < a_1$.
- Phase $\mathbb{10}$: $\max\{a_1, 1\} < b_1$, $\max\{a_2, b_2\} < 1$.
- Phase $\mathbb{11}$: $\max\{1, a_1, b_2\} < \min\{a_2, b_1\}$.
- Phase $\mathbb{20}$: $\max\{a_2, 1\} < b_2$.

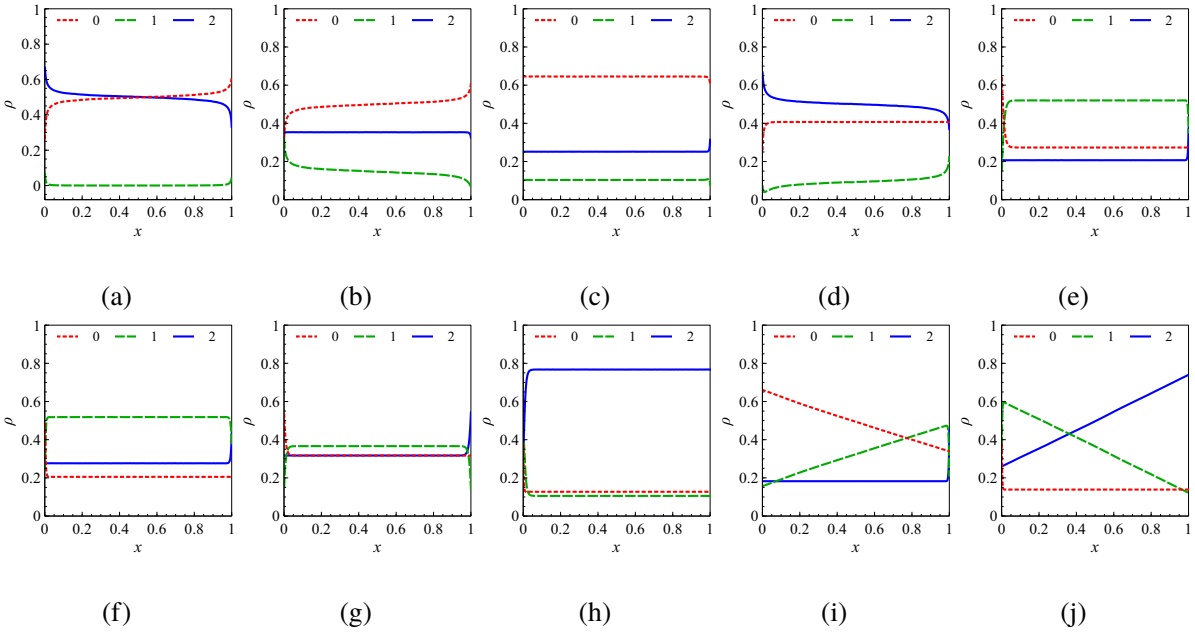

Figure 5.2: The time-average densities in the two-species mpASEP for species 2 (blue dotted line), 1 (green solid line), and 0 (red dashed line) for (a) phase $\mathbb{00}$ ($a_1 \simeq 0.29, a_2 \simeq 0.45, b_1 \simeq 0.61, b_2 \simeq 0.47$, (b) phase $\mathbb{01}$ ($a_1 \simeq 0.43, a_2 \simeq 1.83, b_1 \simeq 0.63, b_2 \simeq 0.48$), (c) phase $\mathbb{02}$ ($a_1 \simeq 1.82, a_2 \simeq 2.98, b_1 \simeq 0.66, b_2 \simeq 0.51$), (d) phase $\mathbb{10}$ ($a_1 \simeq 0.29, a_2 \simeq 0.45, b_1 \simeq 1.46, b_2 \simeq 0.56$), (e) phase $\mathbb{11}$ with $b_1 < a_2$ ($a_1 \simeq 2.04, a_2 \simeq 3.83, b_1 \simeq 2.66, b_2 \simeq 0.72$), (f) phase $\mathbb{11}$ with $a_2 < b_1$ ($a_1 \simeq 1.39, a_2 \simeq 2.62, b_1 \simeq 3.87, b_2 \simeq 0.86$), (g) phase $\mathbb{11}$ with $a_2 = b_1$ ($a_1 \simeq 1.27, a_2 = b_1 \simeq 2.15, b_2 \simeq 1.33$), (h) phase $\mathbb{20}$ ($a_1 \simeq 1.21, a_2 \simeq 2.46, b_1 \simeq 6.87, b_2 \simeq 3.3$), (i) $\mathbb{01} - \mathbb{11}$ coexistence region ($a_1 \simeq 1.95, a_2 \simeq 4.48, b_1 \simeq 1.95, b_2 \simeq 1.16$), and (j) $\mathbb{11} - \mathbb{20}$ coexistence region ($a_1 \simeq 1.1, a_2 \simeq 2.84, b_1 \simeq 6.21, b_2 \simeq 2.84$). The lattice size is 1000 in each case.

Here, we refer to each phase using a two-letter word of the form $\mathbb{ij}$. Our convention is such that the word $\mathbb{ij}$ signifies the following. The phase $\mathbb{ij}$ is mapped to the HD phase of the ASEP by k-colouring for $1 \leq k \leq i$. Moreover, k-colouring projects onto the LD phase for $2-j < k \leq 2$, and onto the MC phase for $i < k \leq 2-j$. For example, the phase $\mathbb{10}$ is projected onto the HD phase by 1-colouring, and onto the MC phase by 2-colouring. The word $\mathbb{10}$ indicates the same by our convention.

The currents in these phases are as follows. First, we note that the relation $J_2 = -J_1 - J_0$ is satisfied for all phases. This is true because the 2's can replace or be replaced by species 0

and 1 at the boundaries. Species 2 (resp. 0) has positive (resp. negative) current in all phases. Species 1 has zero current in phase $\mathbb{00}$ and on the semi-infinite line $1 < a_2 = b_1$. J_1 is positive or negative according to whether $a_2 < b_1$ or $a_2 > b_1$.

The densities can be easily computed as well. Here, we describe only the densities of species 2 and 1 because we have $\rho_0 + \rho_1 + \rho_2 = 1$ in each phase. The 2's have high density in phase $\mathbb{20}$, and low density in phases $\mathbb{11}$ and $\mathbb{02}$. But, ρ_2 remains constant at 1/2 throughout the phases $\mathbb{00}$ and $\mathbb{10}$. Species 1 is expelled from the lattice in phase $\mathbb{00}$ even though injection rates (α_1 and δ_1) of the 1's are positive. Such a phenomenon which was observed earlier for multispecies models like mASEP and mLPASEP is referred to as dynamical expulsion [21, 25]. Moreover, the 1's exhibit low density in all other phases except the phase $\mathbb{11}$. The 1's can assume either high or low density in phase $\mathbb{11}$. However, ρ_1 varies continuously in this phase. One observes linear density profiles for species 2 and 1 (resp. 1 and 0) on the coexistence line $1 < a_2 = b_2$ (resp. $1 < a_1 = b_1$) between the phases $\mathbb{20}$ and $\mathbb{11}$ (resp. $\mathbb{20}$ and $\mathbb{11}$).

For the exact expression for the densities and currents, the reader is referred to Table 5.1. The simulation results for densities are shown in Figure B.2.

Remark 2

We consider following specializations of the boundary parameters: (1) $\alpha_2 = \alpha = 1 - \alpha_1, \beta_0 = \beta = 1-\beta_1, \gamma_0 = \gamma_1 = \delta_2 = \delta_1 = 0$, and (2) $\alpha_2 = \alpha = 1-\alpha_1, \beta_0 = \beta, \gamma_0 = \gamma_1 = \delta_2 = \delta_1 = \beta_1 = 0$, with $\alpha, \beta < 1$. Then, if one permits $q = 0$, the 2-species mpASEP exactly corresponds to the couple of 2-species TASEP models discussed in [67]. There the models were referred to as P_1 and P_2 for specializations (1) and (2) respectively. One can easily check that in the limit $q \to 0$ the phase diagram in Figure 5.1 translates to the phase diagrams for P_1 and P_2 described in [67] for these specializations.

5.3.2 Phase diagram for mpASEP

The phase diagram for the mpASEP with r species is composed of total $r(r+1)/2$ phases in a $2r$-dimensional space. There are $2r$ independent parameters because of r possible k-colourings. On application of each k-colouring to the mpASEP, the boundary interactions become

$$\underline{\text{Left}}: \quad \begin{cases} 0_k \to 1_k & \text{with rate } A_k, \\ 1_k \to 0_k & \text{with rate } G_k, \end{cases}$$

$$\underline{\text{Right}}: \quad \begin{cases} 1_k \to 0_k & \text{with rate } B_k, \\ 0_k \to 1_k & \text{with rate } D_k. \end{cases}$$

In the bulk, 1_k's hop forward (resp. backward) with rate 1 (resp. q). Hence the relevant boundary parameters are $a_k := \kappa_{A_k,G_k}$, and $b_k := \kappa_{B_k,D_k}$. Since we need to consider all colourings at the same time, a typical point in the phase diagram for the mpASEP is described by the coordinates $(a_1, \ldots, a_r, b_1, \ldots, b_r)$.

In spite of a large number of parameters, finding the phases simplifies considerably because

$a_i < a_j$ and $b_j < b_i$ always hold true for $i < j$. In order to describe the phases, each phase is identified with a word consisting of two letters $\mathbb{i}, \mathbb{j} \in \{\mathbb{0}, \ldots, \mathbb{r}\}$ with $0 \le i + j \le r$. Further, it is convenient to use the shorthand notations $\bar{\mathbb{j}} = \mathbb{r} - \mathbb{j}$, and $\mathbb{j}_\pm = \mathbb{j} \pm \mathbb{1}$ such that $\mathbb{j}\bar{\mathbb{j}}$ stands for $\mathbb{j}(\mathbb{r} - \mathbb{j})$, $\mathbb{j}\overline{\mathbb{j}_\pm}$ means $\mathbb{j}(\mathbb{r} - \mathbb{j} \mp \mathbb{1})$, and so on. For example, $\mathbb{j}\bar{\mathbb{j}}$ stands for $\mathbb{1}\mathbb{1}$ for $j = 1$ and $r = 2$. Then the phases are as enlisted below.

- Phase $\mathbb{0}\ell$ $(0 \le l < r)$: $\max\{a_{r-l}, b_1\} < 1 < a_{r-l+1}$.
- Phase $\mathbb{0}\mathbb{r}$: $\max\{1, b_1\} < a_1$.
- Phase $\mathbb{j}\ell$ $(0 < j < r, 0 \le l < r - j)$: $\max\{a_{r-l}, b_{j+1}\} < 1 < \min\{a_{r-l+1}, b_j\}$.
- Phase $\mathbb{j}\bar{\mathbb{j}}$ $(0 < j < r)$: $\max\{1, a_{j-1}, b_j\} < \min\{a_j, b_{j-1}\}$.
- Phase $\mathbb{r}\mathbb{0}$: $\max\{a_r, 1\} < b_r$.

The notation is such that one can easily keep track of the effect of k-colouring on each phase. To be more specific, we consider phase $\mathbb{i}\mathbb{j}$. When we project the mpASEP onto the ASEP with the application of k-colouring, this phase maps to the HD phase for $1 \le k \le i$, to the LD phase for $r - j < k \le r$, and to the MC phase for $i < k \le r - j$.

We visualize all phases on a two-dimensional plane that passes through each phase. We focus on one such plane that is determined by

$$\begin{aligned} a_r &= \mu_{r-1} a_{r-1} = \cdots = \mu_1 a_1 \,, \\ b_1 &= \nu_1 b_2 = \cdots = \nu_{r-1} b_r \,, \end{aligned} \tag{5.3.3}$$

where we fix scalars $\mu_i, \nu_i > 1$ with $\mu_i > \mu_j$ and $\nu_j > \nu_i$ for $i, j \in [r-1]$ and $i < j$. On this plane, let L_i (resp. R_i) be the point where the hyperplanes $a_i = 1$ (resp. $b_i = 1$) and $b_i = 0$ (resp. $a_i = 0$) intersect. Thus the coordinates of L_i and R_i are given by

(5.3.4)

$$L_i \equiv \begin{cases} (\mu_i/\mu_1, \ldots, \mu_i/\mu_{i-1}, 1, \mu_i/\mu_{i+1}, \ldots, \mu_i/\mu_{r-1}, \mu_i, 0, \ldots, 0) & \text{if } 1 \le i < r \\ (1/\mu_1, \ldots, 1/\mu_{r-1}, 1, 0, \ldots, 0) & \text{if } i = r, \end{cases}$$

$$R_i \equiv \begin{cases} (0, \ldots, 0, 1, 1/\nu_1, \ldots, 1/\nu_{r-1}) & \text{if } i = 1, \\ (0, \ldots, 0, \nu_{i-1}, \nu_{i-1}/\nu_1, \ldots, \nu_{i-1}/\nu_{i-2}, 1, \nu_{i-1}/\nu_i, \ldots, \nu_{i-1}/\nu_{r-1}) & \text{if } 1 < i \le r \end{cases}$$

In the $(a_1, \ldots, a_r)$-subspace, we define $a := \left(\sum_{i=1}^r a_i^2\right)^{1/2}$ which is the radial distance from the origin; likewise, we have $b := \left(\sum_{i=1}^r b_i^2\right)^{1/2}$ for $(b_1, \ldots, b_r)$-subspace. We describe the structure of the phase diagram in Figure 5.3 in terms of the parameters a and b as well as L_i's and R_i's. The phases $\mathbb{j}\bar{\mathbb{j}}$ and $\mathbb{j}_-\overline{\mathbb{j}_-}$ coexist on the semi-infinite line $1 < a_j = b_j$ with $j \in [r]$. All coexistence lines appear as thick lines in the phase diagram in Figure 5.3. In addition, we show the semi-infinite lines $1 < a_i = b_j$ for $i > j$ as dashed lines. Unlike the coxistence lines, these lines do not separate different phases. The significance of these lines will be highlighted in the next subsection where we discuss densities and currents.

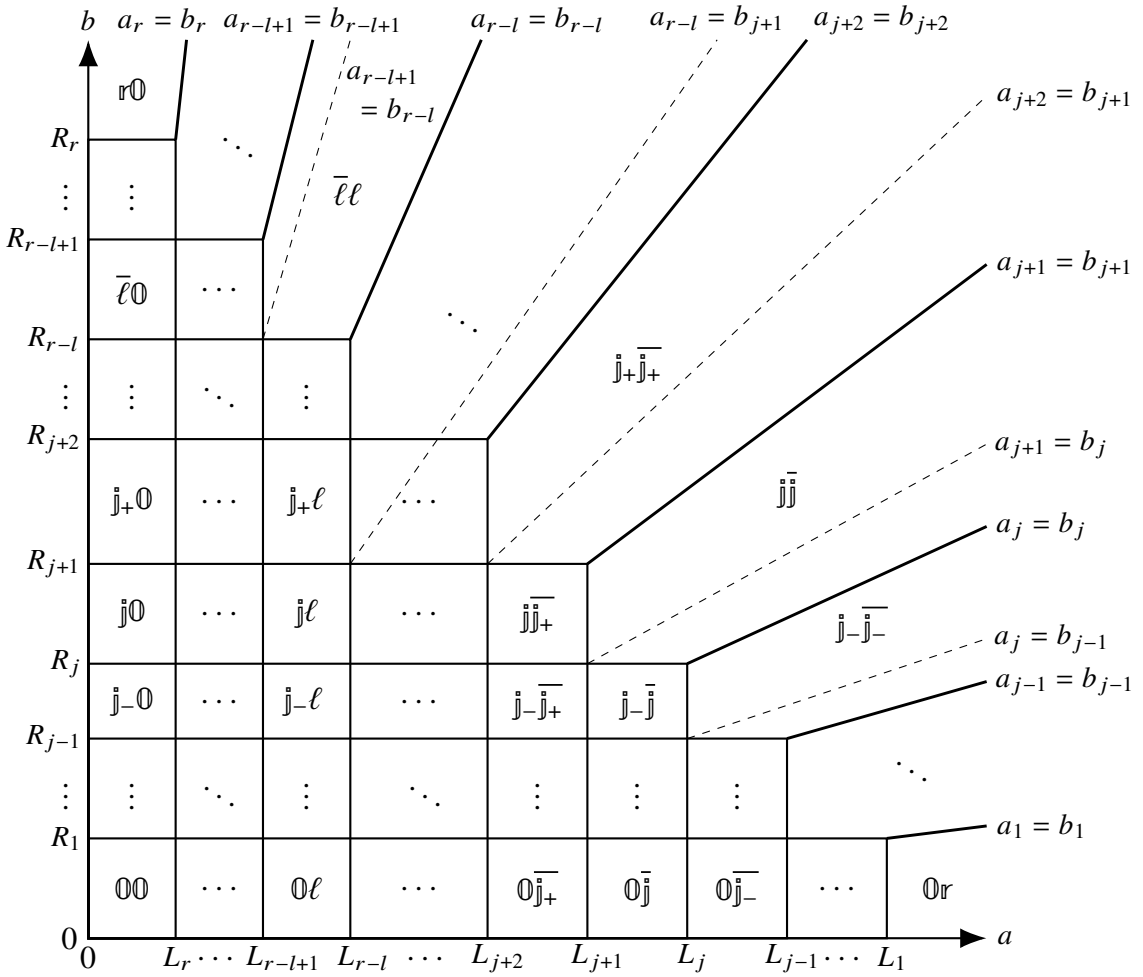

Figure 5.3: The schematic plot of a two-dimensional plane that shows all phases of the mpASEP. The plane is fixed by the scalars $(\mu_1, \ldots, \mu_{r-1}, \nu_1, \ldots, \nu_{r-1})$ in the $(a_1, \ldots, a_r, b_1, \ldots, b_r)$-space. We use the following shorthand notations: $\mathbb{j}_\pm \equiv \mathbb{j} \pm \mathbb{1}$, $\bar{\mathbb{j}} \equiv \mathbb{r} - \mathbb{j}$, and $\overline{\mathbb{j}_\pm} \equiv \mathbb{r} - \mathbb{j}_\pm$. We also explain the notations in Section 5.3.2.

5.3.3 Currents and densities

All densities and currents can be computed using the k-colouring. We discuss the calculations in details for phase $\mathbb{0}\mathbb{j}$, and mention only the results for rest of the phase regions below. For our convenience, we define $f(x) = 1/(1+x)$, $\overline{f}(x) = 1 - f(x)$, and $g(x,y) = (1-q)\left|f(x)\overline{f}(x) - f(y)\overline{f}(y)\right|$. We summarize the results in Table 5.1.

Phases $\mathbb{0}\ell$ and $\mathbb{0}\mathbb{r}$

The k-colourings project phase $\mathbb{0}\ell$ onto the MC phase for $k \leq r-l$ and LD phase for $k > r-l$. Therefore densities satisfy

$$\begin{aligned} &\sum_{i=0}^{k-1} \rho_i = \frac{1}{2} = \sum_{i=k}^{r} \rho_i, \quad 1 \leq k \leq r-l, \\ &\sum_{i=0}^{k-1} \rho_i = \overline{f}(a_k) = 1 - \sum_{i=k}^{r} \rho_i, \quad r-l < k \leq r. \end{aligned} \tag{5.3.5}$$

From these relations, we have $\rho_0 = 1/2$, and $\rho_i = 0$ for $0 < i < r-l$. Thus each species i greater than 0 and smaller than $(r-l)$ are dynamically expelled from the system. Other species have positive densities as listed in Table 5.1. Similarly, for the currents we have

$$\begin{aligned} &-\sum_{i=0}^{k-1} J_i = g(1,0) = \sum_{i=k}^{r} J_i, \quad 1 \leq k \leq r-l, \\ &-\sum_{i=0}^{k-1} J_i = g(a_k,0) = \sum_{i=k}^{r} J_i, \quad r-l < k \leq r. \end{aligned} \tag{5.3.6}$$

Straightforward calculation shows $J_0 = -g(1,0)$, $J_i = 0$ for $0 < i < r-l$, whereas all species $i \geq r-l$ have positive currents: $J_{r-l} = g(1, a_{r-l+1})$, $J_i = g(a_i, a_{i+1})$ for $r-l < i < r$, and $J_r = g(a_r, 0)$.

For the phase $\mathbb{0}\mathbb{r}$, all colourings map to LD phase. Each species have nonzero densities as well as currents. Except species r, every species has negative currents (see Table 5.1).

See Figure B.2 (a), (b) and (c) for density profiles obtained from numerical simulations in phases $\mathbb{0}\mathbb{0}$, $\mathbb{0}\mathbb{1}$ and $\mathbb{0}\mathbb{2}$ for the case $r = 2$.

Phases $\mathbb{j}\ell$ and $\mathbb{j}\bar{\mathbb{j}}$

Let us first consider the phase $\mathbb{j}\ell$ (with $\mathbb{j} > \mathbb{0}$ and $\ell < \bar{\mathbb{j}}$). All species i with $j < i < r-l$ are dynamically expelled in this phase. These species have vanishing densities and currents. All other species have low densities. Any species equal to or smaller (resp. greater) than j (resp. $r-l$) has negative (resp. positive) current.

The phase $\mathbb{j}\bar{\mathbb{j}}$ differs from other phases of the form $\mathbb{j}\ell$ because no k-colouring projects phase $\mathbb{j}\bar{\mathbb{j}}$ onto the MC phase. No species is dynamically expelled from the system. Every species

Phase	Species	Density ρ	Current J
$\mathbb{0}\ell$	0	$f(1)$	$-g(1,0)$
	$0 < i < r-l$	0	0
	$r-l$	$f(1) - f(a_{r-l+1})$	$g(1, a_{r-l+1})$
	$r-l < i < r$	$f(a_i) - f(a_{i+1})$	$g(a_i, a_{i+1})$
	r	$f(a_r)$	$g(a_r, 0)$
$\mathbb{0}\mathbb{r}$	0	$\overline{f}(a_1)$	$-g(a_1, 0)$
	$0 < i < r$	$f(a_i) - f(a_{i+1})$	$g(a_i, a_{i+1})$
	r	$f(a_r)$	$g(a_r, 0)$
$\mathbb{j}\ell$	0	$f(b_1)$	$-g(b_1, 0)$
	$0 < i < j$	$f(b_{i+1}) - f(b_i)$	$-g(b_{i+1}, b_i)$
	j	$f(1) - f(b_j)$	$-g(1, b_j)$
	$j < i < r-l$	0	0
	$r-l$	$f(1) - f(a_{r-l+1})$	$g(1, a_{r-l+1})$
	$r-l < i < r$	$f(a_i) - f(a_{i+1})$	$g(a_i, a_{i+1})$
	r	$f(a_r)$	$g(a_r, 0)$
$\mathbb{j}\bar{\mathbb{j}}$	0	$f(b_1)$	$-g(b_1, 0)$
	$0 < i < j$	$f(b_{i+1}) - f(b_i)$	$-g(b_{i+1}, b_i)$
	j	$\overline{f}(a_{j+1}) - f(b_j)$	$\text{sign}(a_{j+1} - b_j) g(a_{j+1}, b_j)$
	$j < i < r$	$f(a_i) - f(a_{i+1})$	$g(a_i, a_{i+1})$
	r	$f(a_r)$	$g(a_r, 0)$
$\mathbb{r}\mathbb{0}$	0	$f(b_1)$	$-g(b_1, 0)$
	$0 < i < r$	$f(b_{i+1}) - f(b_i)$	$-g(b_{i+1}, b_i)$
	r	$\overline{f}(b_r)$	$g(b_r, 0)$

Table 5.1: Densities and currents in each phase for the mpASEP. We use the convention that $J > 0$ (resp. $J < 0$) if flux of particles is directed towards the right (resp. left) boundary.

other than species j has low density everywhere in this phase. The species j assumes high density where a_{j+1} and b_j satisfies $f(a_{j+1}) + f(b_j) < 1/2$. Otherwise, density of the j's is low as well. It must be noted, nevertheless, that ρ_j varies continuously with the parameters a_{j+1} and b_j throughout phase $\mathbb{j}\bar{\mathbb{j}}$. The currents are nonzero for all species with the following exception. There is no current of species j on the part of the hyperplane $a_{j+1} = b_j$ contained in phase $\mathbb{j}\bar{\mathbb{j}}$. This part of the phase diagram is the semi-infinite line $1 < a_{j+1} = b_j$ shown as dashed line in Figure 5.3. To explain vanishing current of the j's on this line, we note that $\sum_{i=0}^{j-1} \rho_i = f(b_j)$ and $\sum_{i=j+1}^{r} \rho_i = f(a_{j+1})$ in phase $\mathbb{j}\bar{\mathbb{j}}$. Since correlations are expected to be absent in the theormodynamic limit, we have

$$J_j = (1-q)\rho_j \left(\sum_{i=0}^{j-1} \rho_i \right) - (1-q) \left(\sum_{l=j+1}^{r} \rho_l \right) \rho_j . \tag{5.3.7}$$

Thus J_j becomes zero for $a_{j+1} = b_j$. Furthermore, it immediately follows that J_j is positive (resp. negative) for $b_j < a_{j+1}$ (resp. $b_j > a_{j+1}$) in phase $\mathbb{j}\bar{\mathbb{j}}$.

The simulation results for density profiles in phases $\mathbb{10}$ and $\mathbb{11}$ related to the case $r = 2$ are recorded in Figure B.2 (d), (e), (f) and (g).

Phase $\mathbb{r0}$

Every colouring projects phase $\mathbb{r0}$ onto the HD phase. All species have nonzero densities, as well as currents. All but species 0 have positive currents.

The density profiles in phase $\mathbb{20}$ for $r = 2$ are plotted in Figure B.2 (h).

$\mathbb{j}_-\overline{\mathbb{j}_-} - \mathbb{j}\bar{\mathbb{j}}$ Coexistence Line and Other Semi-infinite Lines

The k-colouring maps $\mathbb{j}_-\overline{\mathbb{j}_-} - \mathbb{j}\bar{\mathbb{j}}$ coexistence line to the HD phase for $k < j-1$, to the LD phase for $k > j-1$, and to the coexistence line of the ASEP for $k = j-1$. All species have nonzero bulk densities, but the density profiles of species $(j-1)$ and j are phase-segregated. These two species have linear density profiles (see Figure B.2 (i) and (j) for simulation results related to the case $r = 2$).

It is interesting to note that, on the semi-infinite line $1 < a_i = b_j$ with $i > j$, the densities and currents always satisfy

$$\begin{aligned} &\sum_{m=j+1}^{i} \rho_m = 1 - 2f(a_i)\,, \qquad \sum_{m=0}^{j} \rho_m = \sum_{n=i+1}^{r} \rho_n = f(a_i)\,, \\ &\sum_{m=j+1}^{i} J_m = 0. \end{aligned} \tag{5.3.8}$$

We have already discussed the densities and currents for $i = j+1$. For $i > j+1$, the line $1 < a_i = b_j$ passes through more than one phase. Thus, the functional forms of the densities and currents for a point on this line will depend on the phase to which that point belongs.

5.4 The generalized shock picture in the mpASEP

We describe here the generalized shock picture that we use to explain density profiles in each phase for mpASEP. It is convenient to consider first the shock picture on the coexistence lines in the phase diagram. Below, we will start with the coexistence lines, and then go on to discuss other phases.

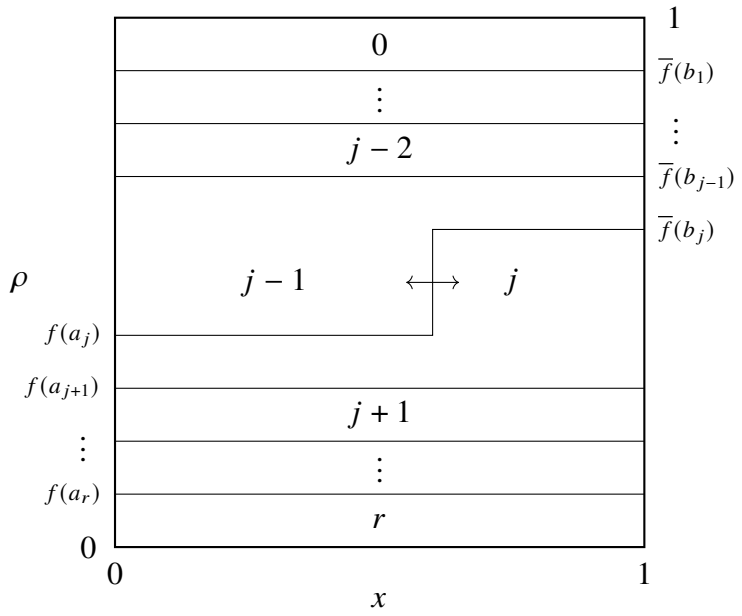

Figure 5.4: The generalized shock picture for the mpASEP on the $\mathbb{j}_-\overline{\mathbb{j}_-} - \mathbb{j}\bar{\mathbb{j}}$ coexistence line in the phase diagram in Figure 5.3. The schematic plot shows a shock formed between species $j-1$ and j. For $r = 1$, one recovers the shock picture for the ASEP shown in Figure 1.3 from the generalized shock picture.

$\mathbb{j}_-\overline{\mathbb{j}_-} - \mathbb{j}\bar{\mathbb{j}}$ Coexistence Line

A shock between species $(j-1)$ and j forms on the boundary of the phases $\mathbb{j}_-\overline{\mathbb{j}_-}$ and $\mathbb{j}\bar{\mathbb{j}}$ as shown in Figure 5.4. Particles of every other species play the role of spectators, and maintain constant density in the system. The shock undergoes a random walk with zero net drift. Thus, the density profiles for $(j-1)$ and j are linear, whereas ρ_i is constant for all other species. For $r = 1$, there is no other species except the 0's and 1's which take part in the shock. In this case, it is easy to verify that the generalized shock picture reduces to the one displayed in Figure 1.3.

In Figure 5.5 (a) and (b), we plot instantaneous density profiles for $r = 2$ obtained from numerical simulations pertaining to the coexistence regions $\mathbb{02} - \mathbb{11}$ and $\mathbb{11} - \mathbb{20}$ in the phase diagram. These simulations agree with the shock picture explained here.

Phase $\mathbb{j}_-\overline{\mathbb{j}_-}$ and $\mathbb{j}\bar{\mathbb{j}}$

As one moves away from $\mathbb{j}_-\overline{\mathbb{j}_-} - \mathbb{j}\bar{\mathbb{j}}$ coexistence line and approaches phase $\mathbb{j}\bar{\mathbb{j}}$, the $(j-1)-j$ shock acquires negative drift. Consequently, the shock gets pinned to the left boundary leading to the

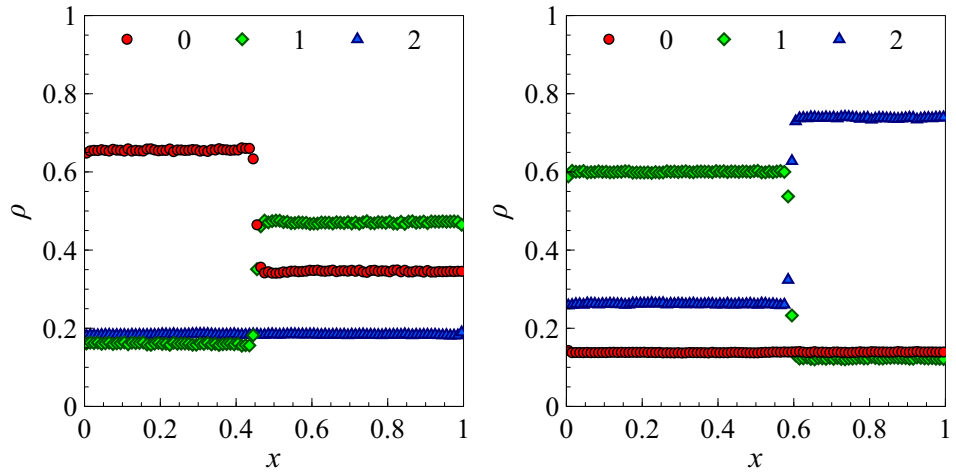

Figure 5.5: Densities on the phase coexistence regions in the mpASEP for $r = 2$: instantaneous density profiles for species 2 (blue triangles), 1 (green diamonds), and 0 (red circles) on (a) $\mathbb{01} - \mathbb{11}$ coexistence region ($a_1 \simeq 1.95, a_2 \simeq 4.48, b_1 \simeq 1.95, b_2 \simeq 1.16$), and (b) $\mathbb{11} - \mathbb{20}$ coexistence region ($a_1 \simeq 1.1, a_2 \simeq 2.84, b_1 \simeq 6.21, b_2 \simeq 2.84$), where we fixed the lattice size to be 10000.

bulk densities for phase $\mathbb{j}\bar{\mathbb{j}}$ listed in Table 5.1. The total density of all species $i \geq j$ is always higher than $1/2$ in phase $\mathbb{j}\bar{\mathbb{j}}$. However, in phase $\mathbb{j}_-\overline{\mathbb{j}_-}$, the $(j-1)-j$ shock has positive velocity which pins the shock to the right. Thus, densities are such that the inequality $\sum_{n=j}^{r} \rho_n < 1/2$ holds true in phase $\mathbb{j}_-\overline{\mathbb{j}_-}$.

Phase $\mathbb{j}\ell$

We consider all phases $\mathbb{j}\ell$ with $0 \leq j < r$ and $0 < l < r - j$. First, we consider the phase $\mathbb{j}\overline{\mathbb{j}_+}$. This phase can be accessed as we move along the $\mathbb{j}\bar{\mathbb{j}} - \mathbb{j}_+\overline{\mathbb{j}_+}$ coexistence line towards the origin. On this coexistence line, the shock is formed between species j and $j+1$. As one reaches phase $\mathbb{j}\overline{\mathbb{j}_+}$, the height of the shock reduces to zero along with $\sum_{m=0}^{j} \rho_m = 1/2 = \sum_{n=j+1}^{r} \rho_n$. All densities remain unchanged in this process except for species j and $j+1$. This is because k-colouring maps phase $\mathbb{j}\overline{\mathbb{j}_+}$ to the MC phase rather than the coexistence line of the ASEP for $k = j+1$, whereas the projections remain same for $k \neq j+1$.

Before we discuss density profiles in the rest of the phases, it is useful to understand the dynamical expulsion of every species greater than j and lower than $(r-l+1)$ in phase $\mathbb{j}\ell$ with $\ell < \overline{\mathbb{j}_+}$. Let us consider the simplest case $\ell = \overline{\mathbb{j}_{++}}$ where $\mathbb{j}_{++} = \mathbb{j}+\mathbb{2}$. We consider the semi-infinite line $1 < a_{j+2} = b_{j+1}$ on which we have $\rho_{j+1} = 1 - 2f(b_{j+1})$. As one moves along this part of the phase diagram towards the origin, ρ_{j+1} decreases as b_{j+1} decreases. Eventually, density of the $(j+1)$'s becomes zero for $b_{j+1} \leq 1$ when one enters the phase $\mathbb{j}\overline{\mathbb{j}_{++}}$ from phase $\mathbb{j}_+\overline{\mathbb{j}_+}$. Moreover, we observe that $\sum_{m=0}^{j} \rho_m = \sum_{n=j+2}^{r} \rho_n = 1/2$ is satisfied in phase $\mathbb{j}\overline{\mathbb{j}_{++}}$. Although ρ_{j+1} vanishes in phase $\mathbb{j}\overline{\mathbb{j}_{++}}$, it is possible that the $(j+1)$'s enter the lattice because of nonzero boundary rates. To see why such particles are driven out of the system, we must consider boundary effects near the left and right boundaries. The densities satisfy $\sum_{m=0}^{j} \rho_m(x) < 1/2 < \sum_{n=j+2}^{r} \rho_n(x)$ and

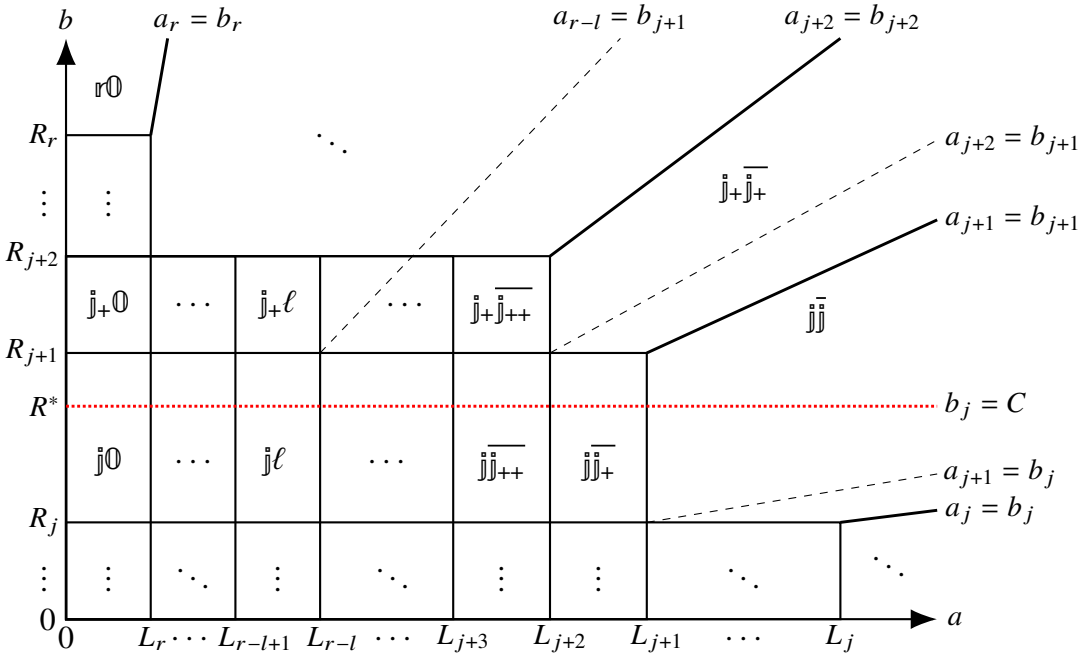

Figure 5.6: Schematic plot of the hyperplane $b_j = C$ (red dotted line) that passes through all phases of the form $\mathbb{j}\ell$. Here, we use the notation $\mathbb{j}_{++} = \mathbb{j}+2$. Some details of the phase diagram are omitted in this plot. We have included only the essential parts that make this illustration suitable to our discussion regarding phase $\mathbb{j}\ell$ in Section 5.4.

$\sum_{m=0}^{j} \rho_m(x) > 1/2 > \sum_{n=j+2}^{r} \rho_n(x)$ at the normalized site position x near the left and right boundary respectively due to boundary effects. Thus the $(j+1)$'s will be driven away from the bulk at both the boundaries. Similarly, we can understand dynamical expulsion in phase $\mathbb{j}\ell$ by considering the semi-infinite line $1 < a_{r-l} = b_{j+1}$. Indeed, one checks using (5.3.8) that $\sum_{n=j+1}^{r-l} \rho_n$ vanishes as one approaches phase $\mathbb{j}\ell$ along this line.

It suffices to understand density profiles in all phases $\mathbb{j}\ell$ for fixed $\mathbb{j}$. First, we fix a constant $C \in (1, \nu_j/\nu_{j-1})$, and the hyperplane $b_j = C$ on which $b_{j+1} < 1 < b_j$ is satisfied. One such hyperplane that passes through the phases under consideration here is indicated as the red dotted line in Figure 5.6. The coordinate of R^* where the hyperplanes $b_j = C$ and $a_r = 0$ intersect on the two-dimensional phase diagram is given by $R^* \equiv CR_j$.

Now, we explain the density profiles in phase $\mathbb{j}\overline{\mathbb{j}\mathbb{j}_{++}}$ starting with its adjacent phase $\mathbb{j}\overline{\mathbb{j}\mathbb{j}_{+}}$ for which we have already explained the density profiles using the shock picture. As one moves along the hyperplane $b_j = C$ from phase $\mathbb{j}\overline{\mathbb{j}\mathbb{j}_{+}}$ towards phase $\mathbb{j}\overline{\mathbb{j}\mathbb{j}_{++}}$, ρ_{j+2} increases to $(f(1) - \overline{f}(a_{j+3}))$ ($f(1)$ for $j+2 = r$) at the hyperplane $a_{j+2} = 1$ which is the boundary between these phases. The same expression for density of species $(j+2)$ remains unaltered throughout phase $\mathbb{j}\overline{\mathbb{j}\mathbb{j}_{++}}$. In constrast, the density of the $(j+1)$'s decreases to zero. The $(j+1)$'s stay dynamically expelled in phase $\mathbb{j}\overline{\mathbb{j}\mathbb{j}_{++}}$ as explained previously. However, other species retain their expressions for densites in this process.

In general, as we move further along $b_j = C$ towards phase $\mathbb{j}\mathbb{0}$, ρ_n vanishes and ρ_{n+1} becomes $(f(1) - f(a_{n+2}))$ ($f(1)$ for $n = r-1$) at the hyperplane $a_{n+1} = 1$ for $j+1 < n < r$. To reach

$\mathbb{j}\ell$ starting from $\mathbb{j}\overline{\mathbb{j}}_+$ along the line $b_j = C$, one must pass through the hyperplanes $a_n = 1$ for $j + 1 < n \leq r - l$. In this process, ρ_i declines to zero for $j < i < r - l$, and ρ_{r-l} becomes $(f(1) - f(a_{r-l+1})$ ($f(1)$ for $l = 0$), where functional forms of other densities remain the same as in phase $\mathbb{j}\overline{\mathbb{j}}_+$.

Part II

Simple models of turbulence: Statistical properties

Chapter 6

Introduction to Part II

In Part I we have studied multispecies asymmetric simple exclusion processes. In this part, we study two important nonequilibrium phenomena, namely, one-dimensional models for (a) nonlinear growth of interfaces and (b) turbulence. We first discuss the one-dimensional Kardar-Parisi-Zhang (KPZ) universality class: the KPZ *stochastic* partial differential equation shows universal statistical properties; a number of models for growth phenomena lie in this universality class. We next discuss the Kuramoto-Sivashinsky (KS) *deterministic* partial differential equation in 1D. We summarize earlier studies that turbulent but statistically steady state lies in the 1D KPZ universality class. Finally, we end this chapter with a brief discussion of the 1d Burgers equation with random initial conditions; evolution from such random conditions is often considered as a simple model for turbulence.

6.1 One-dimensional Kardar-Parisi-Zhang universality class

The models belonging to the one-dimensional Kardar-Parisi-Zhang universality class are characterized by the long-distance and long-time fluctuations of space and time dependent correlations of a height field $h(x,t)$. This universality class includes the following (to name but a few): (a) asymmetric simple exclusion process (for TASEP, $\alpha = \beta = 1/2$, see [169]), (b) Eden model [204, 186], (c) ballistic-deposition model [165, 133, 6], (d) direct polymers in random media [112], e)PNG (e) the KPZ stochastic partial differential equation of Kardar, Parisi, and Zhang [128] (KPZ). We focus on the 1D KPZ equation where the nonlinearly growing surface is kinetically roughened. Examples of such kinetically roughened surfaces include (a) slow combustion front in paper [163, 164], (b) a growing crystal, (c) surface morphology in the growth of bacterial colonies in agar gel, and flame-front propagation in combustible materials (such as a densely packed wheat field) [113] , liquid crystals (see) [113, 112, 206].

The quantity of interest in the KPZ equation is a scalar variable $h(x,t)$ that is interpreted as height of the growing surface (without overhanging segments). The 1D KPZ equation is the following equation

$$\partial_t h = \nu \partial_{xx} h + \frac{\lambda}{2} (\partial_x h)^2 + \eta \,, \tag{6.1.1}$$

where η is a Gaussian white noise in time and space:

$$\langle \eta(x,t)\eta(x',t')\rangle = 2D\delta(x'-x)\delta(t'-t); \tag{6.1.2}$$

ν being the diffusion constant (this term has a smoothening effect on the irregularities of the evolving surface); λ is the strength of the non-linear contribution to the velocity (see [128]), which originates from lateral growth (see Figure 6.1). For $\lambda = 0$, we obtain the Edwards-Wilkinson (EW) equation:

$$\partial_t h = \nu \partial_{xx} h + \eta \,, \tag{6.1.3}$$

where the non-linear term is absent. Here, the lateral growth effects are not taken into account with the surfacing growing only along the direction perpendicular to the lateral direction as illustrated in Figure 6.1 (also see [128]).

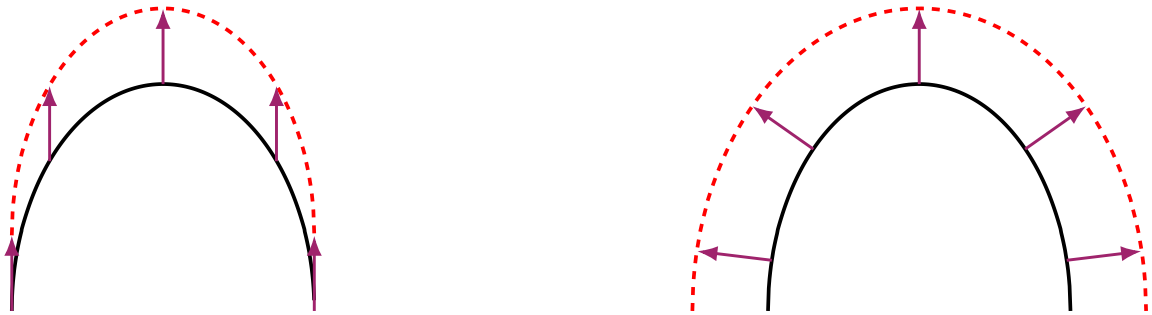

(a) EW growth (b) KPZ growth

Figure 6.1: Schematic illustration after [206] showing two types of growth in interfaces with EW growth in (a) and KPZ growth in (b).

The most basic universal behaviour is observed in the scaling properties of the width $w(l,t)$ which is defined as

$$w(l,t) := \sqrt{\left\langle \left(h(x,t) - h(x,0) - \langle h(x,t) - h(x,0)\rangle_l\right)^2 \right\rangle_l} \,, \tag{6.1.4}$$

where $\langle\cdot\rangle_l$ is the ensemble average over regions of spatial extent l. For example, we can extract the exponents α and β from the Family-Vicsek scaling [94] of $w(l,t)$, which determine the dynamical exponent $z = \alpha/\beta$. For the 1D KPZ universality class, these exponents are given by

$$\alpha = 1/2, \quad \beta = 1/3, \quad \text{and} \quad z = 3/2. \tag{6.1.5}$$

In contrast, the exponents for the EW universality class in the 1D case are given by

$$\alpha = 1/2, \quad \beta = 1/4, \quad \text{and} \quad z = 2. \tag{6.1.6}$$

In order to trace KPZ fluctuations clearly one needs to use careful analysis. Besides, there are various subclasses [62] of the KPZ universality class depending on the initial condition. For

flat initial conditions, the surface height at very large t behaves as

$$h \approx h_\infty t + (\Gamma t)^{1/3} \chi \,, \tag{6.1.7}$$

where χ is a random variable distributed according to the Tracy-Widom distribution for the Gaussian orthogonal ensemble (GOE). The Gaussian ensembles are well studied in random-matrix theory. Thus, for an experimental system or simulations we consider, whose distrubution for the quantity χ converges to the Tracy-Widom GOE distribution at large times

$$\chi \sim (h - h_\infty t)/(\Gamma t)^{1/3} \,. \tag{6.1.8}$$

For other initial conditions, we refer the reader to [62]. To summarize other prominent cases, for wedge initial conditions, we observe Tracy-Widom distribution for the Gaussian unitary ensemble (GUE), and for Browninian motion with initial data Baik-Rains distribution.

6.2 Kuramoto-Sivashinsky equation

The Kuramoto-Sivashinsky equation was studied in the context of various physical phenomena. For example, the equation was studied in the context of (a) persistant wave propagation in dissipative media under nonequilibrium conditions in [148], (b) the universal aspects in reaction-diffusion systems, in particular, near instability points in nonlinear chemical kinetics [147], (c) hydrodynamic instabilities in laminar flames in combustible media [201, 161, 199], (d) irregular flow of a viscous fluid down a vertical plane [200], (e) the instabilities in the flow of thin fluid films down inclined planes [197, 177], and (f) nonlinear saturation of thin flowing films [26, 177, 181]. In [146], the authors arrived at the following equation in the complex field $\psi(x,t)$, namely, the complex Ginzburg-Landau equation (CGLE) [12],

$$\partial_t \psi = (1 + i\alpha)\partial_{xx}\psi + (1 + i\beta)\psi - (1 - i\gamma)|\psi|^2\psi \,,\ \psi \in \mathbb{C} \,,\ \alpha, \beta, \gamma \in \mathbb{R} \,, \tag{6.2.1}$$

which describes the dynamical properties of spatiotemporal organization in such systems. In the parameter regime $\alpha\gamma > 1$, where phase turbulence is observed, the phase of $\psi(x,t)$ in the CGLE satisfies the Kuramoto-Sivashinsky equation. Below, we recall the derivation of the Kuramoto-Sivashinsky equation from the CGLE (equation (6.2.1)).

We write the complex field $\psi(x,t)$ in the polar form $\psi(x,t) = R(x,t)\exp[i\theta(x,t)]$. Considering the real and complex parts separately, we find that

$$\begin{aligned} R_t &= R - R^3 + \Big(R_{xx} - \theta_x^2 R\Big) - \alpha\Big(2\theta_x R_x + \theta_{xx} R\Big), \\ \theta_t &= \gamma R^2 + \left(2\theta_x \frac{R_x}{R} + \theta_{xx}\right) + \alpha\left(\frac{R_{xx}}{R} - \theta_x^2\right), \end{aligned} \tag{6.2.2}$$

where $R_t \equiv \partial_t R$, $\theta_t \equiv \partial_t \theta$, $R_x \equiv \partial_x R$, $\theta_x \equiv \partial_x \theta$, and so on. We assume that the fluctuations in R are negligible such that we can ignore all derivatives in our analysis [108]. Ignoring all

derivatives of R in the equation for R_t, we find the following set of equations

$$\begin{aligned} R^2 &\approx \left(1 - \theta_x^2 - \alpha\theta_{xx}\right), \\ \frac{R_x}{R} &\approx \frac{1}{2}\left(-2\theta_x\theta_{xx} - \alpha\theta_{xxx}\right), \\ \frac{R_{xx}}{R} &\approx \frac{-\alpha}{2}\theta_{xxxx}. \end{aligned}$$

Substituting these equations in the equation for θ_t, we have

$$\theta_t \approx \gamma + (1 - \alpha\gamma)\,\theta_{xx} - \frac{\alpha^2}{2}\theta_{xxxx} - (\alpha + \gamma)\,\theta_x^2 + \cdots . \tag{6.2.3}$$

This truncated equation is the KS equation. We rescale the parameters and the phase as

$$\begin{aligned} t' &= at, \\ x' &= bx, \\ \text{and} \qquad h &= c\theta + \gamma, \end{aligned}$$

with

$$\begin{aligned} a &= \frac{\alpha^2}{2(\alpha\gamma - 1)^2}, \\ b &= \frac{\alpha}{\sqrt{2(\alpha\gamma - 1)}}, \\ \text{and} \qquad c &= \frac{\alpha\gamma - 1}{2(\alpha + \gamma)}. \end{aligned}$$

Thus the KS equation in 1D is the following fourth-order partial differential equation (PDE):

$$\partial_t h + \partial_{xx} h + \partial_{xxxx} h + \tfrac{1}{2}\left[\partial_x h\right]^2 = 0\,; \tag{6.2.4}$$

here we omit the superscripts of t' and x' to simplify the notations. We can consider $h(x,t)$ as the height of a growing interface. The time and space variables are rescaled in such a way that all parameters have been removed. Then the only important parameter is the system size L, where the spatial domain of definition is $[-L/2, L/2]$. The equation in (6.2.4) can be written in terms of the velocity field $u(x,t)$ as

$$\partial_t u + \partial_{xx} u + \partial_{xxxx} u + u\partial_x u = 0\,, \tag{6.2.5}$$

where $u(x,t) = \partial_x h(x,t)$.

The Kuramoto-Sivashinsky equation exhibits interesting dynamical properties. It can be considered as a model with an infinite number of degrees of freedom with spatiotemporal chaos [171]. The global properties of the KS equation, such as nonlinear stability and attractors, were studied in [166]. The dynamical properties of the spatiotemporal chaos in Kuramoto-Sivashinsky equation were revealed in [119]. Moreover, the large-scale properties were studied

in [114] by considering this equation as a simple model for fully developed turbulence in 1D.

The large-size and large-time properties of the KS equation show spatiotemporal chaos. The system size L controls the number of degrees of freedom. The small modes of the KS equation are unstable and grow with time approximately as $\exp\left[(k^2 - k^4)t\right]$ (with $k \ll 1$); the growth is a maximal at $k_c = 1/\sqrt{2}$. The higher modes ($k > 1$) decay rapidly. The nonlinear term transfers energy from the unstable low k modes to the decaying high k modes. The nonlinear term in the equation for the velocity field $u(x,t)$ is the one-dimensional analog of the advection term in the Navier-stokes equation. The evolving height profile displays spatiotemporal chaos. Initially, it displays EW statistical properties; for sufficiently large system and simulation times, the system crosses over to a regime in which we observe KPZ statistical properties [202, 115].

6.3 Burgers equation

Hydrodynamic turbulence refers to the extremely chaotic motion of stirred fluids; shows extreme vortical structures and energy spectrum that spans a very large number of spatial and temporal scales. A complete understanding of turbulence is still elusive. Its various aspects continue to be a fascinating subject of study. The Navier-Stokes (NS) equation governs the flow of Newtonian fluids, including turbulent fluids. However, the dynamical properties of the NS PDE are extremely complicated. Given the computational difficulties, simple models of turbulence have been proposed, in particular, in low dimensions. These models are of great utility because they are sometimes amenable to exact analysis and compuationally less taxing than the 3D NS equation. Moreover, numerical experiments are less expensive in these models so that theoretical predictions can be accurately verified. One such model is the unforced Burgers equation in 1D.

The incompressible NS equation in the three-dimensional velocity field $\mathbf{u}(\mathbf{x},t)$ is

$$\begin{aligned} &\partial_t \mathbf{u} + \mathbf{u}\cdot\nabla\mathbf{u} - \nu\nabla^2\mathbf{u} = \frac{1}{\rho}\left(\mathbf{f} - \nabla p\right) \ , \\ &\nabla.\mathbf{u} = 0, \end{aligned} \tag{6.3.1}$$

where ν is kinematic viscosity of the fluid, $\mathbf{f}$ is the external force, p is pressure and ρ is the fluid density. In one dimension, the NS equation without the pressure term and any incompressibility condition is the (forced) Burgers equation:

$$\partial_t u + u\partial_x u = \nu\partial_{xx}u + \frac{1}{\rho}f \ . \tag{6.3.2}$$

The Burgers or Bateman-Burgers equation was originally introduced by Bateman in 1915 in the study of the surface of discontinuity in perfect fluids [30]. Later, the Burgers equation appeared as a simple mathematical model in the investigations by Burgers [49], Hopf [116, 117] and Cole [59].The Burgers equation was also studied for understanding (a) shocks in one dimension [144], (b) the formation of large-scale cosmological structures in the universe [195], (c) the mass distribution of such structures using the adhesion model in [213], and (d) shock phenomena in model driven diffusive systems, namely, the asymmetric simple exclusion process on an open

lattice [83].

This equation is actually same as the KPZ equation (6.1.1) with the identification $u(x,t) = -\partial_x h(x,t)$. The quantity $h(x,t)$ which is referred to as the height of an interface in the KPZ literature, is known as the potential in the Burgers literature and denoted by $\psi(x,t)$. In our discussion here, we adhere to the standard notations apt for the Burgers equation.

The unforced Burgers equation is integrable. Let us consider the case $f = 0$ and the spatial domain of definition to be the real line. Furthermore, we shall consider the variable $\theta(x,t)$ related to the potential $\psi(x,t)$ as

$$\psi(x,t) = 2\nu \ln \theta(x,t) \,, \qquad x \in \mathbb{R} \,. \tag{6.3.3}$$

This transformation of variables is often referred to as the *Hopf-Cole transformation*. Then the equation for θ is found to be

$$\partial_t \theta = \nu \partial_{xx} \theta \,, \tag{6.3.4}$$

which is nothing but the heat equation (or diffusion equation). The exact solution is given by

$$\psi(x,t) = 2\nu \ln \left\{ \frac{1}{\sqrt{4\pi\nu t}} \int_{\mathbb{R}} \exp\left[\frac{1}{2} \left(\psi_0(a) - \frac{(x-a)^2}{2t} \right) \right] da \right\} \,. \tag{6.3.5}$$

Here, $\psi_0(a)$ is the initial potential. We consider the solution in the limit $\nu \to 0$ (which is not the same as the case with $\nu = 0$). By using the steepest descent method, we obtain

$$\psi(x,t) = \max_a \left(\psi_0(a) - \frac{(x-a)^2}{2t} \right) \,. \tag{6.3.6}$$

Thus the solution at time t is determined from the initial condition via the maximization in the RHS of the last equation.

6.4 Plan of Part II

We report results in Chapters 7-8. We begin with a summary below.

In Chapter 7, we study the statistical properties of the height fluctuations in the Kuramoto-Sivashinsky (KS) equation. We perform extensive direct numerical simulations to solve numerically the KS equation for large system size L and long time. We use Family-Vicsek scaling to extract the KPZ exponents. Then we compute the probability distribution functions of height fluctuations for different initial conditions. We find the Tracy-Widom and Baik-Rains distributions.

In Chapter 8, we consider the unforced one-dimensional Burgers equation in the vanishing-viscosity limit and study the statistical properties of the energy decay. We start with random initial conditions, whose spectra have particular functional dependences on the wavenumber, including (a) the initial spectrum with sharp Gaussian peak, (b) spectra with two and four power laws. For all cases, we characterize the spectrum at different times, the energy decay and the

growth of the integral length scale. We also compute the histogram of the Lagrangian shock intervals at different times.

Chapter 7

The one-dimensional Kardar-Parisi-Zhang and Kuramoto-Sivashinsky universality class: limit distributions

7.1 Introduction

Fundamental investigations of the statistical properties of hydrodynamical turbulence often use *randomly forced* versions of the *deterministic* Navier-Stokes (NS) equations (3D NSE, in three dimensions); the latter use a non-random forcing term to produce a turbulent, but nonequilibrium, statistically steady state (NESS). A randomly forced 3D, incompressible NS equation (3D RFNSE), proposed first by Edwards [88] in 1964, has been studied extensively, via renormalization-group (RG) and other theoretical [99, 75, 101, 216, 162, 34, 7, 8] and numerical [184, 35] methods; these studies have shown that many statistical properties of turbulence in the 3D RFNSE are akin to their 3D NSE counterparts. In particular, the wave-number k dependence of the energy spectrum [141, 142, 102] $E(k)$, and even the mutiscaling corrections [102, 2, 32, 31, 160] to the Kolmogorov phenomenology [141, 142, 102] of 1941 are similar in both these models.

Can we find such similarity between the statistical properties of NESSs in *deterministic* and related *stochastic* partial differential equations (PDEs) that are simpler than their 3D hydrodynamical counterparts? It has been suggested, since the 1980s, that the Kuramoto-Sivashinsky (KS) PDE, a deterministic interface-growth model for a height field $h(\mathbf{x}, t)$, which is used in studies of chemical waves, flame fronts, and the surfaces of thin films flowing under gravity [149, 201, 200, 182, 3, 56, 108], is a simplified model for turbulence [3]. It has been conjectured [215], and subsequently shown by compelling numerical studies [121, 202, 115, 124, 42, 127], in both one dimension (1D) and two dimensions (2D), that the long-distance and long-time behaviors of correlation functions, in the spatiotemporally chaotic NESS of the KS PDE, exhibit the same power-law scaling as their counterparts in the Kardar-Parisi-Zhang (KPZ) equation [128, 113, 112, 178], a stochastic PDE (SPDE), in

which the height field $h(\mathbf{x}, t)$ is kinetically roughened. The elucidation of the statistics of $h(\mathbf{x}, t)$ in the KPZ SPDE has played a central role in nonequilibrium statistical mechanics, in general, and interface-growth phenomena, in particular. Early KPZ studies [128, 113] have concentrated on height-field correlations, the width $w(L, t)$ of the fluctuating KPZ interface, and their power-law dependences on the linear system size L and time t, for large L and t (see below); for the 1D case, several results can be obtained analytically. The universality of the power-law exponents has been demonstrated by explicit numerical calculations, e.g., in the poly-nuclear growth (PNG) model, directed polymers in random media (DPRM), and the asymmetric simple exclusion process (ASEP), and by experiments in turbulent liquid crystals [208, 207, 205], all of which lie (in suitable parameter regimes) in the KPZ universality class. The seminal work of Prähofer and Spohn work (recently referred to as "the 2^{nd} KPZ Revolution" [112]) on the PNG model [173] and the mathematical studies of Johansson [125] and Baik, Deift and Johansson [28] has led to a new set of studies of the 1D KPZ universality class [189, 51, 122, 62, 111, 178, 183], which have led to the remarkable result that, at a point x and at large times t,

$$h(x,t) - h(x,0) \approx v_\infty t + (\Gamma t)^{\beta_{\rm KPZ}} \chi_\beta + o(t^{\beta_{\rm KPZ}}) \ , \ \text{for } t \to \infty, \tag{7.1.1}$$

where v_∞ and Γ are model-dependent constants (see Appendix B), the exponent $\beta_{\rm KPZ} = 1/3$, and χ_β is a random variable distributed according to the Tracy-Widom (TW) distribution for the Gaussian Orthogonal Ensemble (GOE) ($\beta = 1$) and for the Gaussian Unitary Ensemble (GUE) ($\beta = 2$), familiar from the theory of random matrices [209, 43, 1], or the Baik-Rains (BR F_0) distribution [27] ($\beta = 0$); the value of β depends on the initial condition. We show, by extensive direct numerical simulations (DNSs), that the result (7.1.1) holds for the NESS of the 1D KS PDE. Thus, the correspondence between the statistical properties of these states, in the 1D KS (PDE) and their counterparts in the 1D KPZ (SPDE), does not stop at the simple correlation functions, investigated so far [121, 202, 115, 124]; we demonstrate that this correspondence includes the universal limit distributions obtained in "the 2^{nd} KPZ Revolution" [112]. Such a result has not been obtained hitherto for a spatiotemporally chaotic NESS of a deterministic PDE.

7.2 Model and Results

The KS PDE, which predates the KPZ SPDE, is

$$\partial_t h(\mathbf{x}, t) + \Delta h(\mathbf{x}, t) + \Delta^2 h(\mathbf{x}, t) + \frac{1}{2}(\nabla h(\mathbf{x}, t))^2 = 0, \tag{7.2.1}$$

where $\nabla \equiv \partial/\partial\mathbf{x}$, $\partial_t \equiv \partial/\partial t$, $\Delta \equiv \nabla^2$, and h, $\mathbf{x}$, and t have been scaled such that the linear system size L is the only control parameter. The dynamical and long-wavelength properties of the 1D KS PDE have been explored via DNSs in References [121, 202, 115, 120, 134]; several mathematical results have been obtained in References [60, 126, 61].

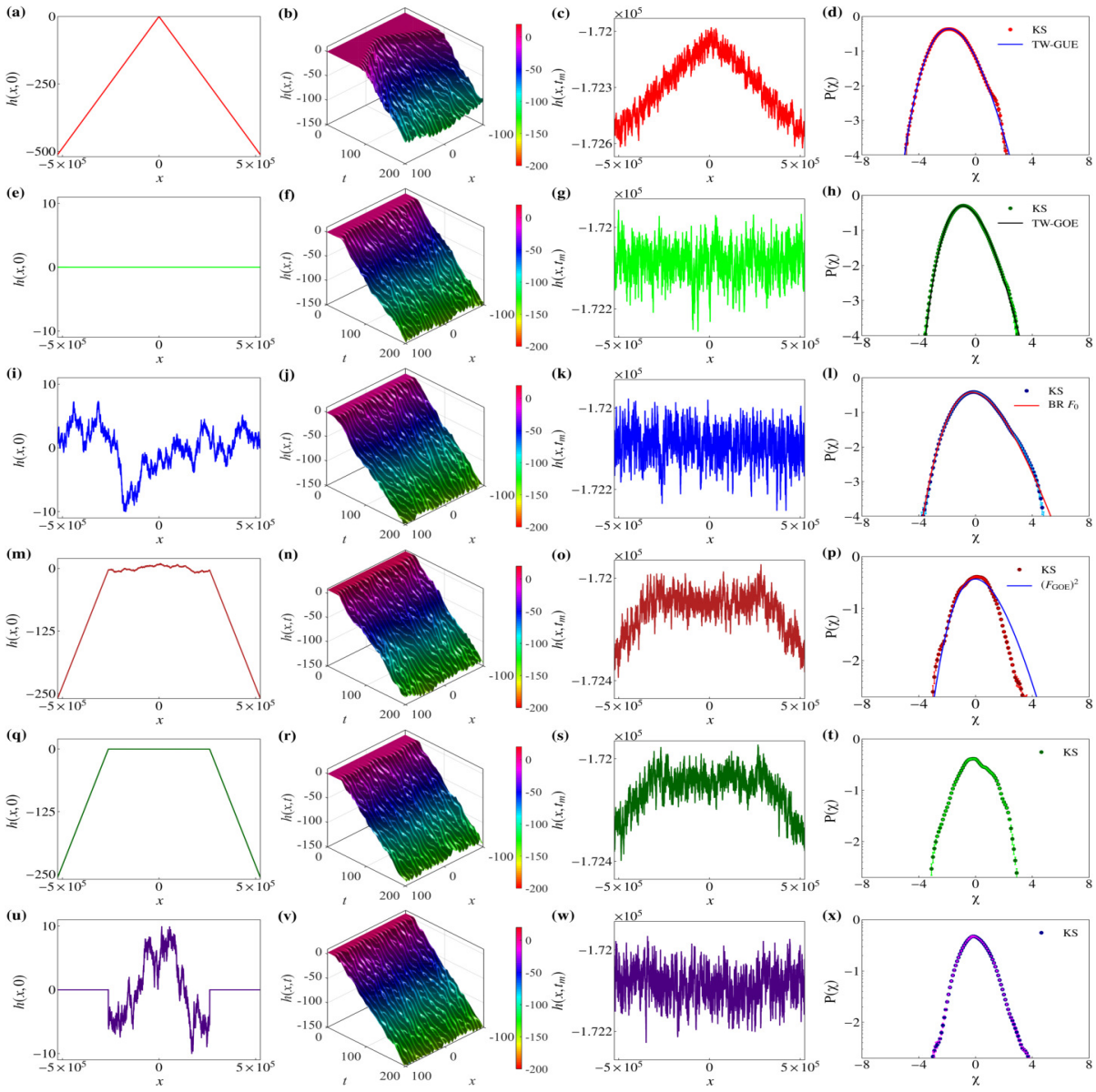

Figure 7.1: (Color online) Plots of $h(x,0)$ versus $x \in [-L/2, L/2]$, with $L = 2^{20}$, for the six different initial conditions, IC1, IC2, IC3, IC4, IC5, and IC6 in (a), (e), (i), (m), (q), and (u), respectively. The short-time spatiotemporal evolution of $h(x,t)$ is shown, in the interval $[-100, 100]$, for each one of IC1-IC6 in (b),(f),(j),(n),(r), and (v) (see the videos V1-V6 in Appendix B). The height profiles at time $t_m = 2 \times 10^5$ are plotted in (c), (g), (k), (o), (s), and (w) for IC1-IC6, respectively; and the plots (d), (h), (l), (p), (t), and (x) display corresponding limit distributions for χ (see text) in the NESSs; and in (d), (h), (l), and (x) we plot TW-GUE, TW-GOE, BR F_0, and $(F_{\rm GOE})^2$ distributions to compare them with data from our DNSs. The error bars on $\mathrm{P}(\chi)$ are smaller than the sizes of our symbols.

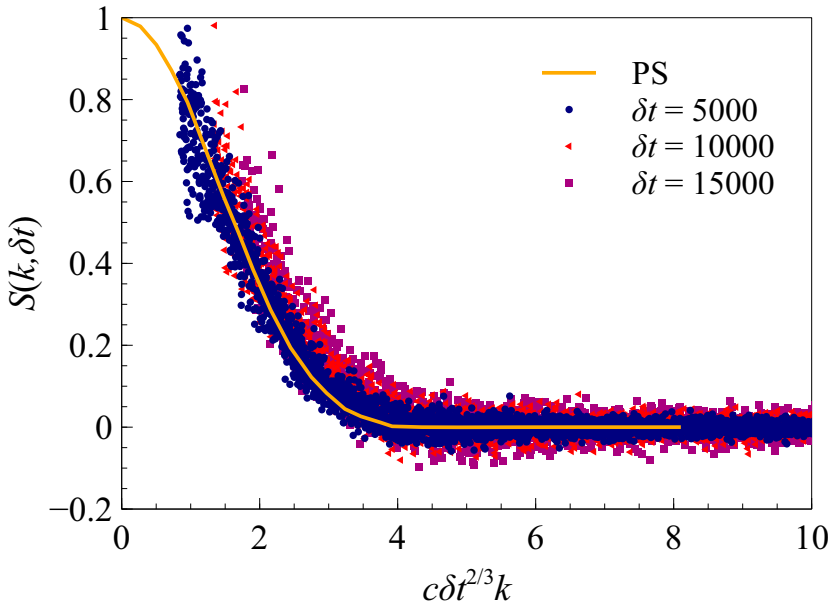

Figure 7.2: (Color online) Plot of the scaling form of the Fourier transform of the two-point time-dependent correlation function $S(k,\delta t)$ versus $c\delta t^{2/3}k$, with the nonuniversal $c = 1.6$, computed for IC3 (see Figure 7.1(i)). We plot $S(k,\delta t)$ for three different values of δt; we also show, for comparison, the theoretical result (orange curve PS) obtained by Prähofer and Spohn [174] for the 1D KPZ equation.

The 1D KPZ SPDE is

$$\begin{aligned} \partial_t h(x,t) &= \nu \Delta h(x,t) + \frac{\lambda}{2}(\nabla h(x,t))^2 + \eta \,, \\ \langle \eta(x,t)\eta(x',t')\rangle &= D\delta(x-x')\delta(t-t') \,, \end{aligned} \tag{7.2.2}$$

where ν, the diffusivity, and λ, the strength of the nonlinearity, are real parameters, and η is a zero-mean Gaussian white noise, with variance D.

We solve the 1D KS PDE (7.2.1), with periodic boundary conditions on a domain of size L, by using the pseudospectral method [54, 55, 210, 214, 106, 107] and the 2/3 dealiasing rule. For time marching we use the fourth-order, exponential time-differencing Runge-Kutta scheme ETDRK4 [130, 64]. For reliable statistics, it is important to carry out long simulations with large values of L; we report results with $L = 2^{20}$, by far the highest spatial resolution that has been used for a DNS of the 1D KS PDE (7.2.1); for this we have developed a CUDA C code that runs very efficiently on a GPU cluster with NVIDIA Tesla K80 accelerators.

From our DNSs we compute $h(x,t)$ for six different kinds of initial conditions, IC1-IC6, which we depict by plots of $h(x,0)$ versus x in Figures 7.1 (a), (e), (i), (m), (q), and (u); we show the short-time spatiotemporal evolution of $h(x,t)$, in the interval $x \in [-100,100]$, in Figures 7.1 (b), (f), (j), (n), (r), and (v) (see the videos V1-V6 in Appendix B). We choose these ICs to mimic the effect of wedge, flat, stationary, wedge-to-stationary, wedge-to-flat, and flat-to-stationary geometries in the ASEP model, which are listed in References [62, 44, 63] as initial conditions for six different sub-classes of the 1D KPZ universality class. Previous

numerical studies [115, 202] of the 1D KS PDE have shown that two-point, equal-time height-field correlations show the scaling behaviors of their 1D KPZ SPDE counterparts for times greater than a crossover time $t_c \simeq 18700$ and lengths larger than the crossover size $L_c \simeq 3600$. Therefore, we use a very large system size $L = 2^{20}$ and very long simulation times $t_{max} \geq 2\times10^5$ (see Appendix B).

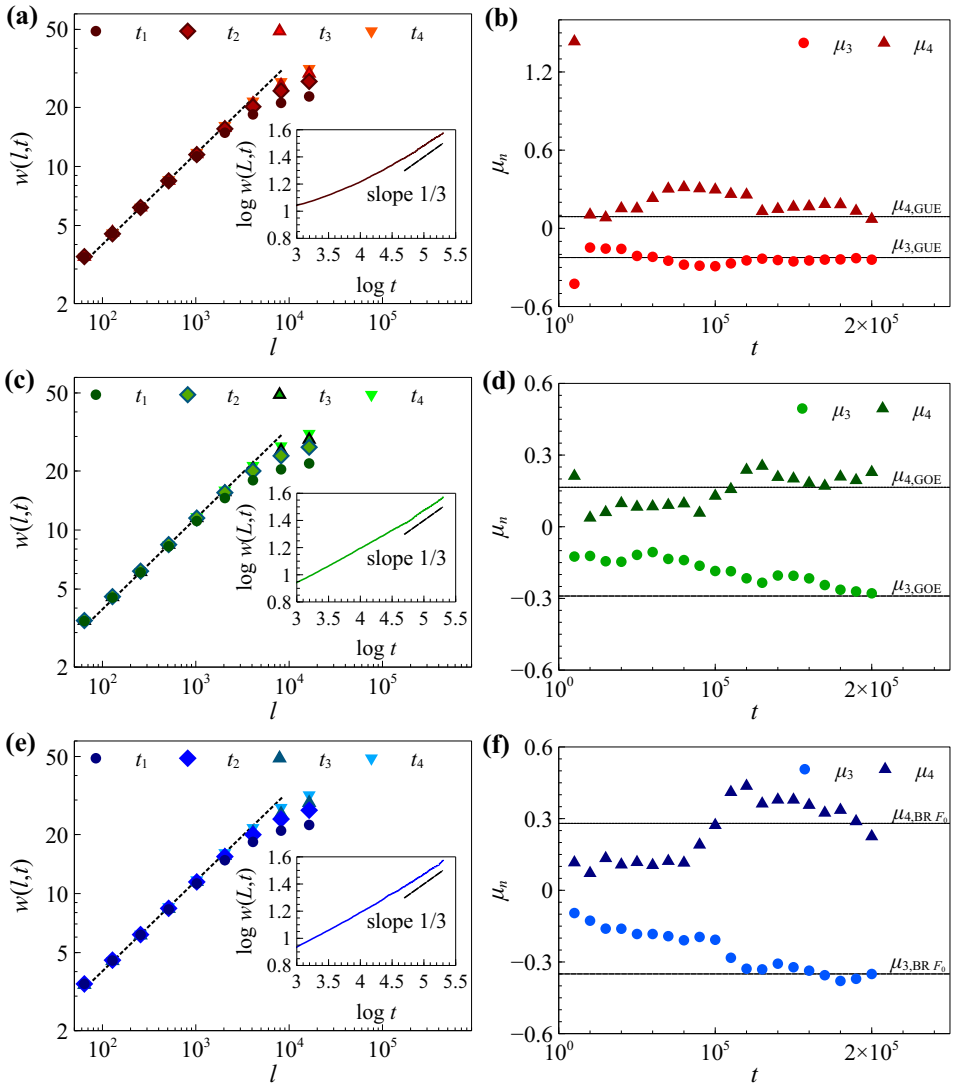

Figure 7.3: (Color online) Family-Vicsek scaling [94]: (a), (c), and (e) show, for IC1-IC3, respectively, plots of $w(l,t)$ versus l, for $l \ll L$, and $w(L,t)$ versus t (in the insets); $t_1 = 5\times10^4$, $t_2 = 10^5$, $t_3 = 1.5\times10^5$, and $t_4 = 2\times10^5$. The dotted lines are log-log fits for $w(l,t) = Al^\alpha$, with $\alpha = 0.46 \pm 0.07$ for IC1-IC3. In (b), (d), and (f) we plot, for IC1-IC3, respectively, the skewness μ_3 and the kurtosis μ_4 (see text) versus the time t; black lines indicate their large-t values for TW-GUE, TW-GOE, and BR F_0 PDFs in (b), (d), and (f). (See Appendix B for similar plots for IC4-IC6.)

Our results for two-point height correlation functions are consistent with those of earlier investigations [115, 202] of the statistical properties of the spatiotemporally chaotic state of the 1D

KS PDE: We show, e.g., the equal-time compensated spectrum $k^2E(k) = \langle L\tilde{h}(k,t)\tilde{h}^*(k,t)\rangle_t$, where $\langle\cdot\rangle_t$ is the time average, $\tilde{h}(k,t)$ is the spatial Fourier transform of $h(x,t)$, and k is the wavenumber, in Figure B.1 of Appendix B. In addition, we calculate the time-dependent, two-point correlation function $S(k,\delta t) = \langle k^2\tilde{h}(k,t_0)\tilde{h}^*(k,t_0+\delta t)\rangle_{t_0}$ in Figure B.4, for the IC3 initial condition. We find that the imaginary part of $S(k,\delta t)$ fluctuates around zero and its magnitude is much smaller than that of its real part, which we plot in Figure 7.2. Our data are consistent with the scaling form of $S(k,\delta t)$ (orange curve in Figure 7.2), which has been obtained analytically by Prähofer and Spohn [174] for the 1D KPZ SPDE; this comparison of $S(k,\delta t)$ for the 1D KS and 1D KPZ equations has not been made hitherto.

The scaling properties of the interface width $w(L,t)$ distinguish different universality classes in interface-growth models;

$$w(l,t) = \left(\langle[\Delta_l h(x,t)]^2\rangle_{x,l}\right)^{1/2}, \tag{7.2.3}$$

with $\Delta_l h(x,t) = h(x,t) - h(x,0) - \langle h(x,t) - h(x,0)\rangle_{x,l}$ and $\langle\cdot\rangle_{x,l}$ the spatial average over a region of spatial extent l. For $t \gg 1$ in the 1D KPZ equation, $w(L,t) \sim t^{\beta}$. Before crossover occurs in systems with $L > L_c$, the exponent β assumes the value $\beta_{\rm EW} = 1/4$, which is the Edwards-Wilkinson (EW) result [89, 113] for the linear SPDE with $\lambda = 0$ in Equation (7.2.2); finally, β assumes the KPZ value $\beta_{\rm KPZ} = 1/3$ in the NESS (for $t > t_c$). Moreover, the growing KPZ surface involves the length scale $\mathcal{L}(t) \sim t^{1/z}$, where the dynamic exponent $z = 3/2$; and the width $w(l,t) \sim l^{\alpha}$, for $l \ll \mathcal{L}(t)$, with $\alpha = 1/2$ [208]. We find from our DNSs of the 1D KS equation that these Family-Vicsek scaling [94] forms are indeed satisfied as we show in Figures 7.3 (a), (c), and (e) for IC1-IC3 (see Appendix B for IC4-IC6).

We define

$$\mu_n = \langle(\Delta_L h(x,t))^n\rangle / \langle(\Delta_L h(x,t))^2\rangle^{n/2} - 3\delta_{n,4}; \tag{7.2.4}$$

for $n = 3$ ($n = 4$), μ_n is the skewness (kurtosis); we plot μ_3 and μ_4 versus time t in the right panel of Figure 7.3; for each initial condition, IC1-IC6, we average these quantities for 100 surfaces, over a time interval of 10^4, and five independent DNS runs; i.e., our overall sample size is $\simeq 5 \times 10^8$ data points. [For our 1D KS, $\mu_3 < 0$ because of the sign of the nonlinear term in Equation (7.2.1); we ignore the sign of μ_3 for it can be reversed by the transformation $h(x,t) \to -h(x,t)$.] In addition, we calculate the probability distribution function (PDF) $\mathrm{P}(\chi)$ of the shifted and rescaled fluctuations, namely, $\chi = (h(x,t) - v_\infty t)/(\Gamma t)^{1/3}$, when both μ_3 and μ_4 are close to their standard values for the relevant TW or BR F_0 PDFs; for IC2, e.g., we compute $\mathrm{P}(\chi)$ when we have $\mu_3 \simeq 0.27$ and $\mu_4 \simeq 0.19$, which are close to the standard values $\mu_{3,\rm GOE} \simeq 0.29$ and $\mu_{4,\rm GOE} \simeq 0.16$, respectively.

For IC1, IC2, IC3, and IC4 we compare, on semilog plots, the PDFs with TW-GUE, TW-GOE, BR F_0, and $(F_{\rm GOE})^2$ [62] in Figures 7.1 (d), (h), (l), and (p), respectively. For ease of comparison, we show in Figure 7.4 that the PDFs we obtain from our DNSs of the 1D KS Equation (7.2.1) are very close to the TW-GUE, TW-GOE, and BR F_0 PDFs over *at least three orders of magnitude*. Stricly speaking, we must collect data only from those two points ($x = L/4, 3L/4$) at which the two different type of height profiles meet in cases IC4, IC5 and

IC6. However, this leads to inadequate statistics. Therefore, the PDFs of χ for IC4-6, which we show in Figures 7.1 (p), (t), and (x), have been computed by using data from the regions $[7L/32, 9L/32]$ and $[23L/32, 25L/32]$; we see that this averaging procedure already leads to PDFs (Figures 7.1 (p), (t) and (x)) that are distinctly different from TW-GUE, TW-GOE, and BR F_0 distributions.

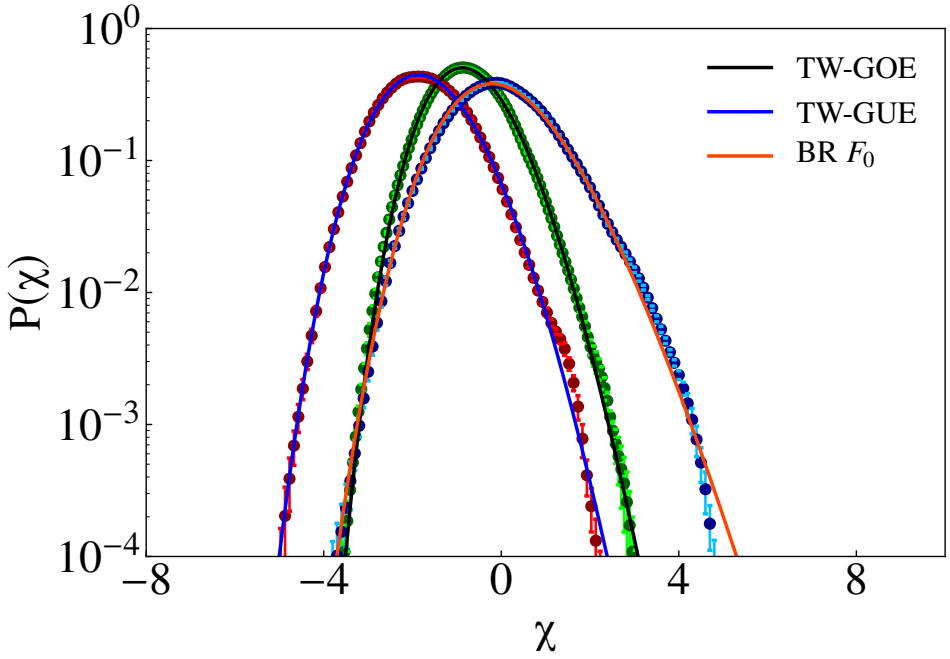

Figure 7.4: (Color online) Semilog plots of the PDFs P(χ) from our DNSs for IC1, IC2, and IC3; we compare these with the Tracy-Widom distributions, TW-GUE and TW-GOE, and the Baik-Rains distributions (BR F_0).

The TW distributions, for IC1 and IC2 initial conditions in the 1D KPZ equation, have been studied in the context of $N \times N$ GOE ($\beta = 1$) and GUE ($\beta = 2$) random matrices. The largest eigenvalue (after scaling with N) Λ of such random matrices is

$$\Lambda = \sqrt{2} + \frac{1}{\sqrt{2}} N^{-2/3} \chi_\beta \,, \tag{7.2.5}$$

where χ_β has the PDF [156]

$$\mathrm{P}(\Lambda, N) \approx \begin{cases} \exp[-\beta N^2 \phi_-(\Lambda)], & \Lambda < \sqrt{2}, |\Lambda - \sqrt{2}| \sim O(1), \\ \sqrt{2} N^{2/3} \mathrm{P}_{\mathrm{TW},\beta}(\chi_\beta), & |\Lambda - \sqrt{2}| \sim O(N^{-2/3}), \\ \exp[-\beta N \phi_+(\Lambda)], & \Lambda > \sqrt{2}, |\Lambda - \sqrt{2}| \sim O(1), \end{cases} \tag{7.2.6}$$

$\mathrm{P}_{\mathrm{TW},\beta}(\chi_\beta)$ denotes TW distributions, and the right and left large-deviation functions (LDFs)

$\phi_+(\Lambda)$ and $\phi_-(\Lambda)$, respectively, display the following asymptotic behaviors:

$$\begin{aligned} \phi_-(\Lambda) &\approx \frac{1}{6\sqrt{2}}(\sqrt{2}-\Lambda)^3\,, \quad \Lambda \to -\infty; \\ \phi_+(\Lambda) &\approx \frac{2^{7/4}}{3}(\Lambda-\sqrt{2})^{3/2}\,, \quad \Lambda \to +\infty. \end{aligned} \tag{7.2.7}$$

The LDFs, which yield the probabilities of atypically large fluctuations, match smoothly with the tails of $\mathrm{P}_{\mathrm{TW},\beta}(\chi_\beta)$. Because of different behaviors of the tails of $\mathrm{P}(\Lambda, N)$, a third-order transition [156] can be associated with Λ at $\Lambda_c = \sqrt{2}$ by defining the *free energy* $\propto \ln F_\beta(\Lambda, N)$, $F_\beta(\Lambda, N)$ being the cumulative density function (CDF) for Λ, for we have [156]

$$\lim_{N\to\infty} -\frac{1}{N^2}\ln F_\beta(\Lambda, N) = \begin{cases} \phi_-(\Lambda), & \Lambda < \sqrt{2}, \\ 0, & \Lambda > \sqrt{2}. \end{cases} \tag{7.2.8}$$

Similarly, we define, for the KS initial conditions IC1 and IC2, the free-energy function $\mathcal{F}(\overline{h})$, for $t, L \to \infty$, as follows:

$$\mathcal{F}(\overline{h}) = \lim_{t,L\to\infty} -\frac{1}{t^2}\ln F(\chi, t)\,, \tag{7.2.9}$$

where $\overline{h} = h(x,t)/t$ and $F(\chi, t)$ is the CDF for χ at time t. Therefore, for IC1 and IC2, we should obtain a third-order phase transition for $\overline{h}$ at the critical value $\overline{h}_c = v_\infty$; an explicit demonstration requires much better statistics for $\mathrm{P}(\chi)$ than is possible with our DNS.

7.3 Discussion

We have shown, by extensive pseudospectral DNSs of the 1D KS deterministic PDE, that the statistical properties of its spatiotemporally chaotic NESS are in the 1D KPZ universality class. This is not limited, merely, to the power-law forms of simple correlation functions and the width of the interface. It includes, in addition, (a) the complete scaling form for the two-point time-dependent correlation function $S(k, \delta t)$ (Figure 7.2), (b) the skewness and kurtosis shown in Figure 7.2, and (c) most important of all, the unversal limit distributions in Figure 7.1, obtained in "the 2^{nd} KPZ Revolution" [112]. Such results have not been obtained hitherto for a spatiotemporally chaotic NESS of any deterministic PDE. We conjecture that similar conclusions should ensue for the phase-chaos regime of the 1D Complex-Ginzburg-Landau equation [108]. Such studies are also being pursued for the 1D Calogero-Moser model [9].

Chapter 8

The characterization of decay in the unforced 1D Burgers equation

8.1 Introduction

The Burgers equation is studied in the context of many physical phenomena. Some instances include fluid mechanics [30], turbulence [49, 50], nonlinear acoustics [95], interstellar dynamics [131], modelling of atmospheric frontogenesis [38, 45], energy spectrum of fronts [11], adhesion model for cosmological structures [140, 109, 195], as well as modelling stellar and interstellar jet flows [179, 139]. The Burgers equation is useful as a simple model in which we can study the decay of Burgers turbulence (this is often the first step in understanding similar decay of homogeneous, isotropic fluid turbulence), a problem of fundamental importance [93, 159, 141, 142]. For a quick overview, see [110, 196, 74, 5].

Single-power-law with an exponent n along with a large cutoff wavenumber (see the next section) as the initial spectrum was considered in [110]. We first consider two typical cases studied in [110] and verify that our numerical results agree with the results obtained there. Then we consider other types of initial energy spectra $E(k)$ with (I) a sharp Gaussian peak; (II) combinations of two spectral ranges with different power laws as the initial spectrum; (III) combinations of four different power laws in the initial spectrum. For each of these cases, we compute the total energy with time. We consider four choices for the case (II) and two for the case (III). For each of these cases, we compute the evolution of the energy spectrum, the decay of the total energy with time, and the growth of the integral length scale as a function of time t. This chapter is organized as follows. The Burgers partial differential equation (PDE) is discussed in Section 8.2. We present our results in Section 8.3.

8.2 The Burgers model and methods

The one-dimensional (1D) viscous Burgers PDE is given by

$$\partial_t u + u\partial_x u = \nu \partial_{xx} u \,, \tag{8.2.1}$$

where $u(x,t)$ is the velocity field defined on the periodical interval $[0, L_s]$ with $\nu \in \mathbb{R}_+$. We consider the vanishing-kinematic-viscosity limit $\nu \to 0^+$. We can write this equation in terms of the potential $\psi(x,t)$ that is related to the velocity field as

$$u(x,t) = -\partial_x \psi(x,t) \ . \tag{8.2.2}$$

The equation then reads

$$\partial_t \psi = \frac{1}{2}(\partial_x \psi)^2 + \nu \partial_{xx} \psi, \qquad \nu \to 0^+. \tag{8.2.3}$$

It is well-known that the 1D Burgers PDE is integrable. The exact solution (see Section 6.3) was studied by Hopf [116, 117] as well as by Cole [59] in the late 1940s .

The exact solution of the 1D *inviscid* Burgers PDE with the initial condition $\psi(x, t_0)$ is given by the Legendre transform (see Appendix C) in the limit of $\nu \to 0^+$:

$$\psi(x,t) = \max_a \left[\psi(a, t_0) - \frac{(x-a)^2}{2(t-t_0)} \right], \tag{8.2.4}$$

where $t > t_0$ (see [196, 167]). The transformation $\psi(a, t_0) \to \psi(x,t)$ is sometimes referred to as the *aperture transform* [167]. Let us denote by $a(x,t)$ the function that maps the point x at time t to the point a (at time t_0); this corresponds to the maximization in the RHS of (8.2.4). We refer to $a(x,t)$ as *inverse Lagrangian function*. The function $a(x,t)$ gives the (initial) position at time t_0 of a fluid particle that is at x at time t. Thus the velocity $u(x,t)$ is found to be [196, 167]

$$u(x,t) = u(a(x,t), t_0) = \frac{x - a(x,t)}{t - t_0}. \tag{8.2.5}$$

We refer to x as the Eulerian position (coordinate) and $a(x,t)$ as the Lagrangian position (coordinate).

In our simulations, we consider a random initial velocity profile $u(x,0)$ for which the Fourier modes $\widetilde{u}_k(0)$ for the wavenumber $k \geq 0$ take the form

$$\widetilde{u}_k(0) = \big(A\, \mathcal{E}(k)\big)^{1/2} \exp\big[-k^2/k_c^2\big]\, X_N^{(k)} \exp\Big[i X_U^{(k)}\Big], \tag{8.2.6}$$

where A is a positive constant, k_c is a cutoff wavenumber with $k_c \gg 1$; $X_N^{(k)}$ is a random variable distributed according to $\mathsf{N}(0,1)$ for all $k \geq 0$, where $\mathsf{N}(0,1)$ is the normal distribution with mean 0 and standard deviation 1; $X_U^{(k)}$ is a random variable distributed according to $\mathsf{U}(0, 2\pi)$, i.e. uniform distribution on $[0, 2\pi]$ for all $k \geq 0$. Then the initial (average) energy spectrum $E_0(k)$ is given by

$$E_0(k) = \Big\langle |\widetilde{u}_k(0)|^2 \Big\rangle_{X_N^{(k)}, X_U^{(k)}} = A\, \mathcal{E}(k) \exp\big[-k^2/k_c^2\big], \tag{8.2.7}$$

where $\langle \cdot \rangle_{X_N^{(k)}, X_U^{(k)}}$ is average over realizations. The energy spectrum $E(k,t)$ at time t is defined

as

$$E(k,t) := \left\langle |\widetilde{u}_k(t)|^2 \right\rangle_{X_N^{(k)}, X_U^{(k)}} . \tag{8.2.8}$$

Furthermore, we define the (average) energy $E(t)$ as

$$E(t) := \left\langle \int_{-\infty}^{\infty} \mathrm{d}k \, |\widetilde{u}_k(t)|^2 \right\rangle_{X_N^{(k)}, X_U^{(k)}} , \tag{8.2.9}$$

and integral length scale as

$$L(t) := \frac{1}{E(t)} \left\langle \int_{-\infty}^{\infty} \mathrm{d}k \, k^{-1} \, |\widetilde{u}_k(t)|^2 \right\rangle_{X_N^{(k)}, X_U^{(k)}} . \tag{8.2.10}$$

The single-power-law case

$$\mathcal{E}(k) = |k|^n , \tag{8.2.11}$$

where the exponent n satisfies $-1 < n < 2$, was studied by Gurbatov, *et al.* [110] in details. We recall here that, for $-1 < n < 1$, the energy decay is self-similar with

$$E(t) \propto t^{e_E} , \qquad \text{where} \quad e_E = \frac{-2(n+1)}{n+3} . \tag{8.2.12}$$

The integral length scale $L(t)$ increases with time as

$$L(t) \propto t^{e_I} , \qquad \text{where} \quad e_I = \frac{2}{n+3} . \tag{8.2.13}$$

The proof for the energy decay [104] follows from noting the scaling properties of the velocity $u(x,t)$ [196]:

$$u(x,t) \overset{\text{law}}{=} t^{-\frac{n+1}{n+3}} u(x t^{-\frac{2}{n+3}}, 1), \tag{8.2.14}$$

where " $\overset{\text{law}}{=}$ " means both the RHS and the LHS have same the same probability distributions. Thus, the second moments of the RHS and LHS are related as

$$\left\langle u^2(x,t) \right\rangle_{X_N^{(k)}, X_U^{(k)}} = t^{-\frac{2(n+1)}{n+3}} \left\langle u^2(x t^{-\frac{2}{n+3}}, 1) \right\rangle_{X_N^{(k)}, X_U^{(k)}} . \tag{8.2.15}$$

First, we note that the energy $E(t)$ written in terms of the velocity $u(x,t)$ is given by

$$E(t) = \left\langle \int_0^{L_s} \mathrm{d}x \, u^2(x,t) \right\rangle_{X_N^{(k)}, X_U^{(k)}} = L_s \left\langle u^2(x,t) \right\rangle_{X_N^{(k)}, X_U^{(k)}} , \tag{8.2.16}$$

where L_s is the system size, and x is any point in $[0, L_s]$. Also, we note that

$$\begin{aligned}\left\langle \int_0^{L_s} \mathrm{d}x\, u^2(xt^{-\frac{2}{n+3}}, 1)\right\rangle_{X_N^{(k)}, X_U^{(k)}} &= \left\langle t^{\frac{2}{n+3}} \int_0^{L_s t^{-\frac{2}{n+3}}} \mathrm{d}\left(xt^{-\frac{2}{n+3}}\right)\, u^2(xt^{-\frac{2}{n+3}}, 1)\right\rangle_{X_N^{(k)}, X_U^{(k)}} \\ &= t^{\frac{2}{n+3}} \left\langle \int_0^{L_s t^{-\frac{2}{n+3}}} \mathrm{d}y\, u^2(y, 1)\right\rangle_{X_N^{(k)}, X_U^{(k)}} \\ &= L_s \left\langle u^2(y, 1)\right\rangle_{X_N^{(k)}, X_U^{(k)}},\end{aligned} \tag{8.2.17}$$

where y is any point in $[0, L_s t^{-\frac{2}{n+3}}]$. We expect $\left\langle u^2(x, 1)\right\rangle_{X_N^{(k)}, X_U^{(k)}} = \left\langle u^2(y, 1)\right\rangle_{X_N^{(k)}, X_U^{(k)}}$ for all $x, y \in [0, L_s]$ because of averaging over $X_N^{(k)}$ and $X_U^{(k)}$ (for all k). Thus, we have

$$E(t) = E(1)t^{-\frac{2(n+1)}{n+3}}. \tag{8.2.18}$$

In [110], $L(t)$ was suggested to be related to $E(t)$

$$\frac{\mathrm{d}}{\mathrm{d}t}L(t) = E(t)^{\frac{1}{2}}. \tag{8.2.19}$$

Then, $L(t)$ becomes

$$L(t) = \frac{1}{2}(n+3)E(0)^{\frac{1}{2}}t^{\frac{2}{n+3}} + L(0). \tag{8.2.20}$$

For $1 < n < 2$, the time-dependences of $E(t)$ and $L(t)$ are suggested to have the log-corrected Kida forms [110]:

$$\begin{aligned}E(t) &\sim t^{-1}\sigma_\psi \ln^{-1/2}(t/t_{nl}), \\ L(t) &\sim t^{1/2}(\sigma_\psi)^{1/2} \ln^{-1/4}(t/t_{nl}),\end{aligned} \tag{8.2.21}$$

where the constants σ_ψ and t_{nl} are given by

$$\sigma_\psi^2 = \left\langle \int_{-\infty}^{\infty} \mathrm{d}k\, k^{-2}\, |\widetilde{u}_k(0)|^2\right\rangle_{X_N^{(k)}, X_U^{(k)}}, \qquad t_{nl} = \frac{\sigma_\psi}{E_0}, \tag{8.2.22}$$

with

$$E_0 = \int_{-\infty}^{\infty} \mathrm{d}k\, E_0(k). \tag{8.2.23}$$

In this paramater range, we observe the *Gurbatov phenomenon* [110], which we define as follows. There is a non-empty time interval I_G such that there exist for all $t \in I_G$ some wavenumber $k_t > 0$ satisfying (a) $E(k_t, t) > E_0(k_t)$, and (b) $\partial_k E(k, t) < 0$ for all $k > k_t$.

Shocks appear in the velocity profile with time evolution. At the Eulerian position of the shock

x_* at time t, we define the *Lagrangian shock interval* [167] as

$$\Delta a(x) = \lim_{x \to x_*^+} a(x,t) - \lim_{x \to x_*^-} a(x,t) \ . \tag{8.2.24}$$

We compute the unnormalized histogram $N(\Delta a(x))$ of the Lagrangian shock intervals.

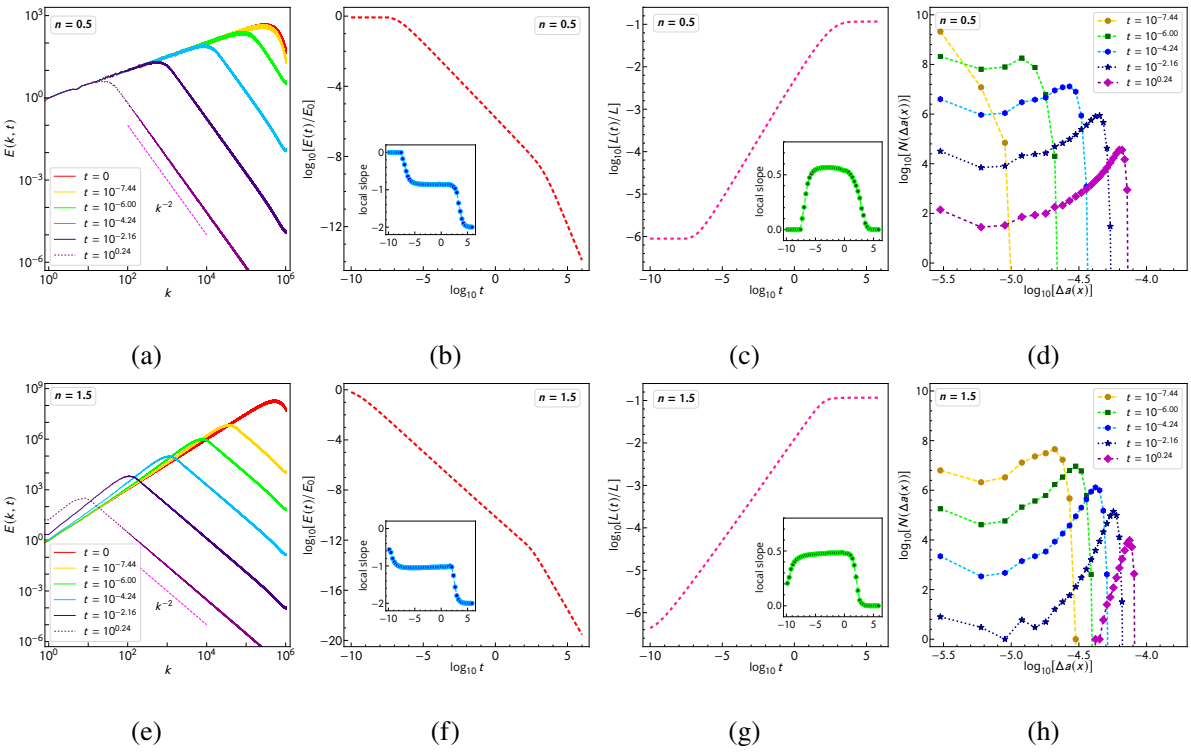

Figure 8.1: Plots of the evolution of the energy spectrum, the energy decay, the growth of the integral length scale, and the evolution of the histogram of the shock strengths, for the single-power law case. We plot $E(k,t)$ vs k on logarithmic scales for six different times for $n = 0.5$ in (a) and $n = 1.5$ in (e), $\log_{10} E(t)$ vs $\log_{10} t$ for $n = 0.5$ in (b) and $n = 1.5$ in (f), $\log_{10} L(t)$ vs $\log_{10} t$ for $n = 0.5$ in (c) and $n = 1.5$ in (g), and $\log_{10}[N(\Delta a(x))]$ vs $\log_{10}[\Delta a(x)]$ for $n = 0.5$ in (d) and $n = 1.5$ in (h). We show the relevant local slopes in the insets in (b), (c), (f), and (g).

8.3 Decay of the energy in the 1D inviscid Burgers equation

We present our results in the this section case by case.

8.3.1 Case 0: Single power law with $-1 < n < 2$

We have considered the single power laws for $n = 0.5$ and $n = 1.5$ in our numerical simulations. Our results for the energy spectrum $E(k,t)$, the decay of energy $E(t)$, and the growth of the integral length scale $L(t)$ are presented in Figures 1(a)-(f). We observe the following log-log behaviours:

- The equations (8.2.12) and (8.2.13) for the energy decay and the integral length scale respectively are satisfied in the case $n = 0.5$ as observed in Figures 8.1(b) and (c); note that $E(k,t)$ remains bounded above by $E_0(k)$ for all time $t > 0$, i.e. the spectrum at time $t > 0$ does not rise above the initial spectrum $k^{0.5}$ in any spectral region as shown in Figure 8.1(a) (non-Gurbatov).
- We observe the Gurbatov phenomenon for $n = 1.5$; $E(k,t)$ rises above $E_0(k)$ in some part of the spectral range for some $t > 0$ with the energy decay roughly following a t^{-1} law and integral length scale following a $t^{1/2}$ behaviour approximately. The results are shown in Figures 8.1(e)-(g). Given this simulation data, it is not easy to find the log-correction for $E(t)$ and $L(t)$.

The evolution of $N(\Delta a(x))$, the histogram for the Lagrangian shock intervals, shows different types of behaviour in these two cases as observed in Figures 8.1(d) and (h). For example, these figures show that, at time $t = 10^{0.24}$, only the larger shocks survive in the system for $n = 1.5$ in comparison to the case of $n = 0.5$.

8.3.2 Case I: Gaussian peak

We next consider a sharp Gaussian peak in the initial spectrum. For this, we consider $\mathcal{E}(k) = \exp\left[-(k-k_c)^2/2k_c + 2k^2/k_c^2\right]$, and $1 \ll k_c \ll k_m$, where k_m is the maximum wavenumber. In our simulation, k_m equals $(N/2-1)$, with system size $L_s = 2\pi$ and number of gridpoints $N = 2^{21}$. We can identify two prominent time intervals each being associated with two distinct regimes of the decay of energy, with an intermediate regime between these two. At the beginning of the energy decay, we observe that a few flat peaks appear for $k < k_c$ whereas several sharp peaks appear for $k > k_c$ and the initial sharp peak at k_c persists. Let us denote by $k_f(t)$ the wavenumber of the flat peak for which $E(k,t)$ is the highest in the spectral range $k < k_c$. We describe the time regimes below using peaks at k_c and $k_f(t)$:

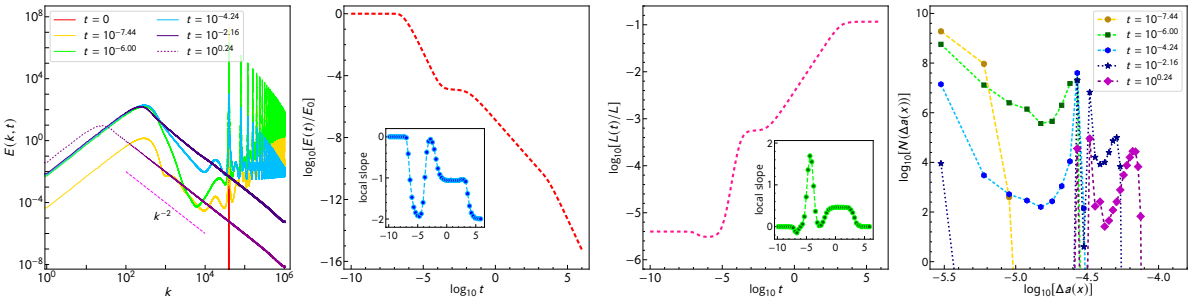

(a) (b) (c) (d)

Figure 8.2: Plots of the evolution of the energy spectrum, the energy decay, the growth of the integral length scale, and the evolution of the histogram of the shock strengths, for a Gaussian initial spectrum. We plot (a) $E(k,t)$ vs k on logarithmic scale for six different times, (b) $\log_{10} E(t)$ vs $\log_{10} t$, (c) $\log_{10} L(t)$ vs $\log_{10} t$, and (d) $\log_{10}[N(\Delta a(x))]$ vs $\log_{10} \Delta a(x)$ at different times. We show the local slope in the insets in (b) and (c).

- The first regime of energy decay starts roughly at around $t \simeq 10^{-7.5}$ in our simulations.

Initially, for very small wavenumbers, $k \lesssim k_c^{1/2}$, we observe a spectral range where the spectrum approximately behaves as $c(t)k^2$ with $k_f(t) \simeq k_c^{1/2}$; $k_f(t)$ remain fixed in this regime. Heights of the peaks, which appear at $k > k_c$, are less than that of the peak at k_c. $E(k,t)$ for $k \geq k_c$ decreases monotonically in this time regime. $E(k,t)$ for $k_f < k < k_c$ increases with time with gradual smoothening of other flat peaks in this spectral range; the overall behaviour of this intermediate spectral range approaches a k^{-2} form for large times. For $k < k_f$, $E(k,0)$ increases until $c(t) \simeq 1/k_c$. Upto the time $t \simeq 10^{-4.0}$, the energy decay is dominated by the decay of the original peak at k_c as well as other sharp peaks formed at higher wavenumbers in the beginning of this decay regime. During this regime, the decay occurs very sharply. The local slope goes to $\simeq -2.0$ as shown in the inset of Figure 8.2(b). Also we note that the integral length scale decreases initially within a brief time-interval (see Figure 8.2(c)) and then starts to grow. These observations are supported by the plots in Figures 8.3 and 8.4.

- Beyond the first regime, the energy decay undergoes a crossover which is observed in our simulations for the time interval $(10^{-4.0}, 10^{-2.0})$. $E(k,t)$ at $k = k_f(t)$ becomes comparable to $E(k_c,t)$, and eventually becomes poised to dominate the energy decay. $k_f(t)$ remains fixed, and the spectral character remains unaltered for $k < k_f(t)$. The sharp peaks in the range $k > k_c$ decays to the extent that the overall spectral character of the spectrum here falls off as $\sim k^{-2}$. The spectral range $k_f(t) < k < k_c$ adjusts such that the whole spectral range beyond $k_f(t)$ follows a $\sim k^{-2}$ form by the end of the crossover (see 8.5). Both the changes in the energy decay and integral length scale are very small during this crossover as observed in Figures 8.2(b) and (c) respectively.

- Finally, we have another decay regime which spans over the time-interval $[10^{-2.0}, 10^{3.5}]$. when there are only two spectral ranges - low wavenumber range with k^2-dependence for $k < k_f(t)$ and high wavenumber range with $\sim k^{-2}$-dependence for $k > k_f(t)$. The peak position $k_f(t)$ is now a decreasing function of time. The energy decay have same characteristics for a single power law with $n = 2$. The energy decay exponent is again nearly -1 whereas the exponent for integral length-scale is $\simeq 0.5$ (see Figures 8.2(b) and (c)). In this regime, mostly the shocks with large Lagrangian shock intervals survive. This is supported by the histogram of the Lagrangian shock intervals shown in Figure 8.2(d).

In summary, we note that $E(t)$ decays fast as $\sim t^{-2}$ in the first decay regime, then slows down as the energy decay crosses over to a regime where $E(t)$ decays as $\sim t^{-1}$; finally $E(t)$ decays as $\sim t^{-2}$.

8.3.3 Case II: Composite two-range initial energy spectrum

Now we consider the cases where there are two spectral ranges with different power laws. We assume following functional form for the initial spectrum

$$E_0(k) = \begin{cases} A_1 \mathcal{E}_1(k) & \text{for } k < k_1 \,, \\ A_2 \mathcal{E}_2(k) & \text{for } k_1 \leq k < k_1^2 \,, \\ A_3 \mathcal{E}_2(k) \exp\left[-2k^2/k_c^2\right] & \text{for } k \geq k_1^2 \,, \end{cases} \tag{8.3.1}$$

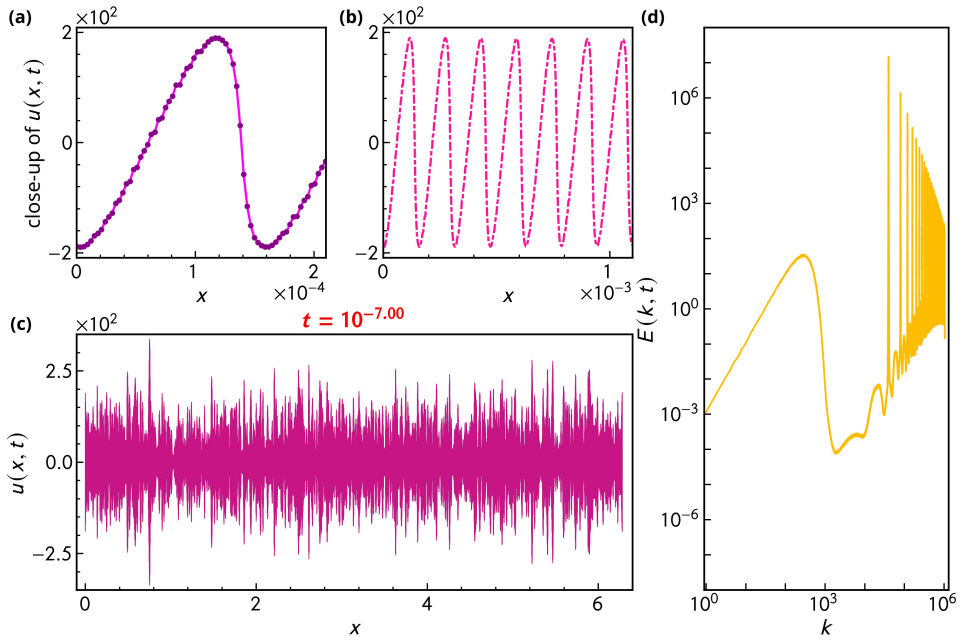

Figure 8.3: Snapshot of the system at $t = 10^{-7}$ showing the spatiotemporal evolution of the velocity profiles for the case I. We plot $u(x,t)$ versus x for (a) $x \in [0, 2.1 \times 10^{-4}]$, (b) $x \in [0, 1.1 \times 10^{-}]$, and (c) $x \in [0, 2\pi]$; we show corresponding $E(k,t)$ versus k in (d).

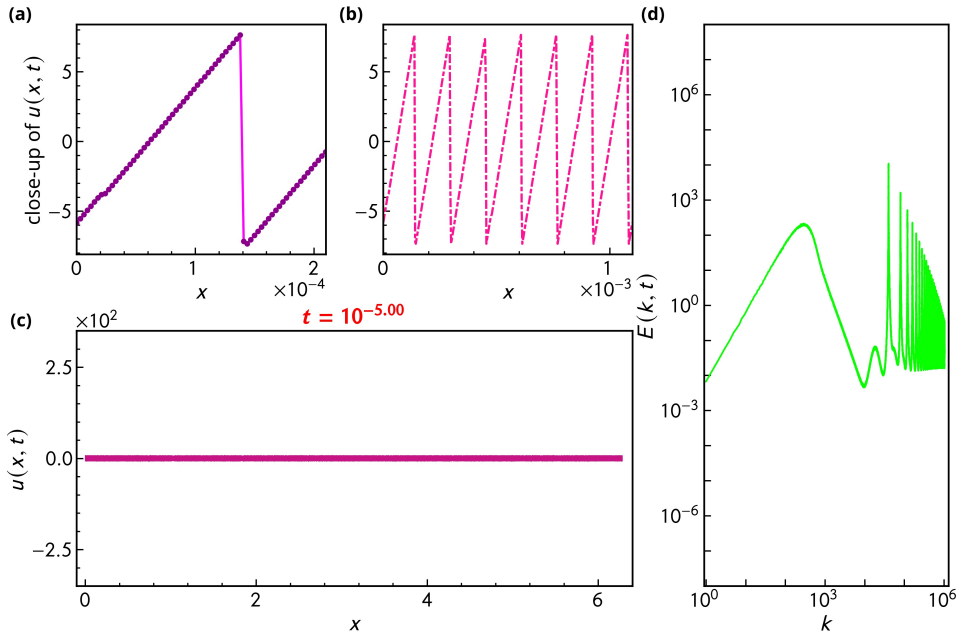

Figure 8.4: Snapshot of the system at $t = 10^{-5}$ showing the spatiotemporal evolution of the velocity profiles for the case I. We plot $u(x,t)$ versus x for (a) $x \in [0, 2.1 \times 10^{-4}]$, (b) $x \in [0, 1.1 \times 10^{-}]$, and (c) $x \in [0, 2\pi]$; we show corresponding $E(k,t)$ versus k in (d). A ramp and shock structure is clearly visible in the zoomed velocity profiles of $u(x,t)$.

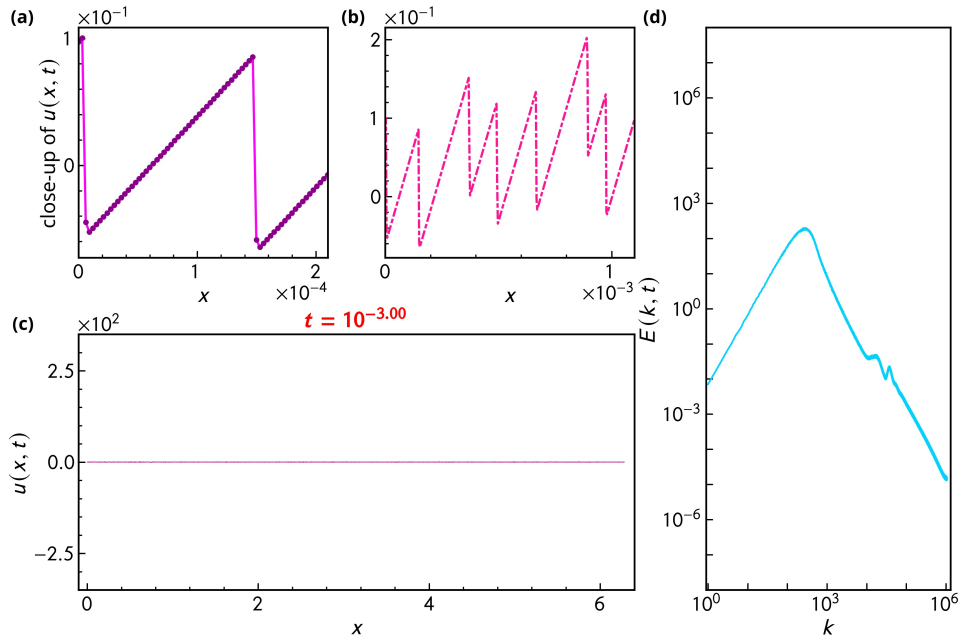

Figure 8.5: Snapshot of the system at $t = 10^{-3}$ showing the spatiotemporal evolution of the velocity profiles for the case I. We plot $u(x,t)$ versus x for (a) $x \in [0, 2.1 \times 10^{-4}]$, (b) $x \in [0, 1.1 \times 10^{-}]$, and (c) $x \in [0, 2\pi]$; we show corresponding $E(k,t)$ versus k in (d). Shocks are clearly visible in the zoomed velocity profiles of $u(x,t)$.

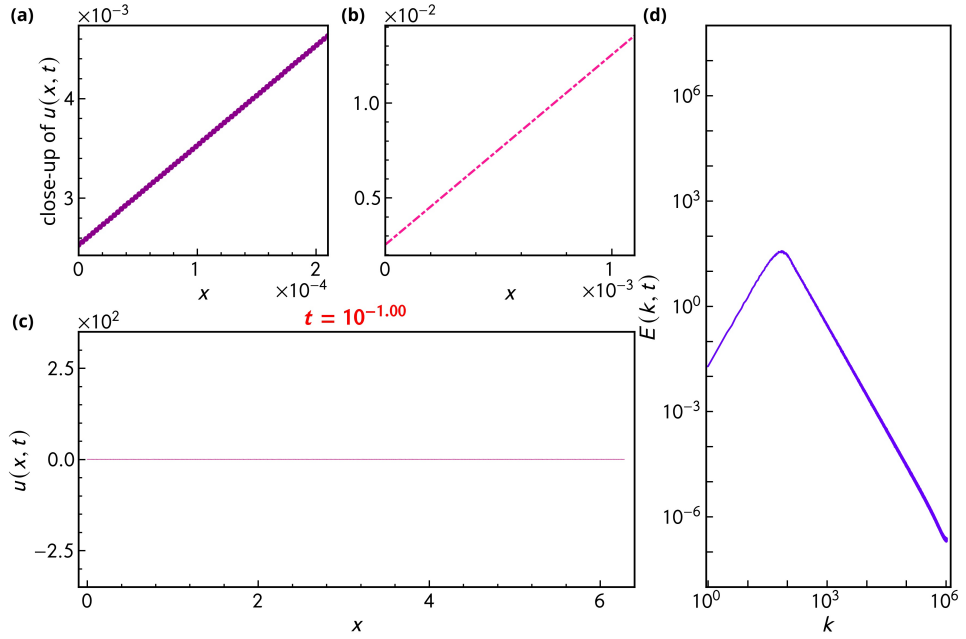

Figure 8.6: Snapshot of the system at $t = 10^{-7}$ showing the spatiotemporal evolution of the velocity profiles for the case I. We plot $u(x,t)$ versus x for (a) $x \in [0, 2.1 \times 10^{-4}]$, (b) $x \in [0, 1.1 \times 10^{-}]$, and (c) $x \in [0, 2\pi]$; we show corresponding $E(k,t)$ versus k in (d).

The constants A_1, A_2, and A_3 are chosen such that $E_0(k)$ is continuous. The function $\mathcal{E}_i(k)$ is given by

$$\mathcal{E}_i(k) = k^{n_i}. \tag{8.3.2}$$

Let us refer to the initial spectrum of the case II with the 2-tuple $\overline{n} = (n_1, n_2)$. We consider four subcases as follows:

IIa $\overline{n} = (0.25, 0.75)$,

IIb $\overline{n} = (0.5, 1.5)$,

IIc $\overline{n} = (1.5, 0.5)$,

IId $\overline{n} = (1.25, 1.75)$.

Let us describe our simulation results for the case IIa first in details. Then we briefly mention the other cases. We remark here that in some of these cases the exponents are not very clear, especially for $L(t)$ given the resolution in our simulations.

8.3.3.1 Case IIa

The spectrum at time $t > 0$ has one peak. We denote the peak position by $k_p(t)$. Since this is the simplest case, let us describe the behaviour of the spectrum using detailed mathematical expressions. The spectrum at time t is given by

$$E(k,t) = \begin{cases} E_0(k) & \text{for } k < k'(t) < k_p(t)\ , \\ J(k,t) & \text{for } k'(t) \le k \le k''(t)\ , \\ J(k''(t),t)(k''(t)/k)^2 & \text{for } k > k''(t) > k_p(t)\ . \end{cases} \tag{8.3.3}$$

The function $J(k,t)$ is defined on the interval $[k'(t), k''(t)]$. $J(k,t)$ describes smooth portion of the continuous part of the spectrum that includes the peak at $k_p(t)$. The evolution of $E(k,t)$ is shown in Figure 8.7(a).

The energy decay and the growth of the integral length scale clearly show two time regimes. $E(k,t)$ decays as $\sim t^{0.9}$ (resp. $\sim t^{0.8}$) respectively for $t \in [10^{-7}, 10^{-2}]$ (resp. $t \in [10^{-2}, 10^{2}]$). $L(t)$ grows with an exponent greater than 0.5 throughout these two time-intervals. The variation in the local slopes are shown insets of the plots of $E(t)$ vs t and $L(t)$ vs t in Figure 8.7(b) and (c) respectively. The exponents for the energy decay, $\simeq -0.9$ and $\simeq -0.8$, compare well with the values -0.77 and 0.93 respectively, which are computed using the formula for the single-power-law case in (8.2.12) and taking into consideration the peak position $k_p(t)$. The value of the exponent for $L(t)$ is not very clear. The histogram for shock intervals evolves as shown in Figure 8.7(d).

8.3.3.2 Case IIb

In this case too, there is exactly one peak at $k_p(t)$. Depending on $k_p(t)$, the spectrum has different behaviour as observed in 8.7(e). When $k_1 < k_p(t) < k_1^2$, $E(k,t)$ is same as $E_0(k)$ for some k' with $k < k' < k_1$. Also, there is a spectral interval $k'' < k < k'''$ with $k' < k''$ and

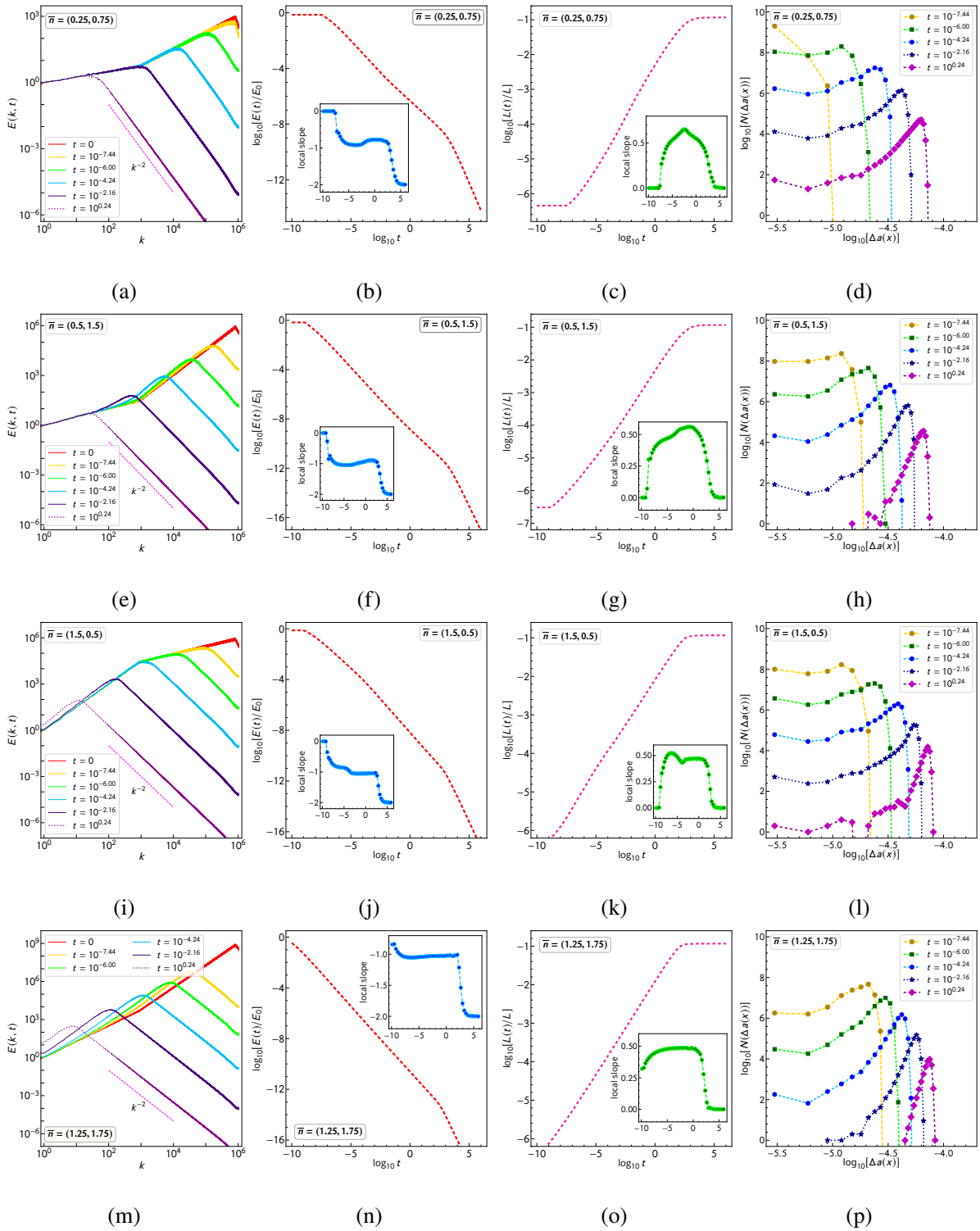

Figure 8.7: Plots of the evolution of the energy spectrum, the energy decay, the growth of the integral length scale, and the evolution of the histogram of the shock strengths, for composite initial spectrum with two power laws. We show plots of $E(k,t)$ vs k on logarithmic scale for six different times for cases IIa in (a), IIb in (e), IIc in (i), and IId in (m); plots of $\log_{10} E(t)$ vs $\log_{10} t$ for cases IIa in (b), IIb in (f), IIc in (j), and IId in (n); plots of $\log_{10} L(t)$ vs $\log_{10} t$ for cases IIa in (c), IIb in (g), IIc in (k), and IId in (o); plots of $\log_{10}[N(\Delta a(x))]$ vs $\log_{10} \Delta a(x)$ for cases IIa in (d), IIb in (h), IIc in (l), IId in (p). We show the relevant local slopes in the insets in (b), (c), (f), (g), (j), (k), (n) and (o).

$k''' < k_p(t)$, where $E(k,t) \sim k^2$ with $E(k,t) > E_0(k)$. A continuous curve bridges these two spectral regions. This is reminiscent of the Gurbatov phenomenon. When $k_p(t) < k_1$, i.e. in the low wavenumber region, the peak height diminishes with time till the second spectral range where the spectrum was proportional to k^2 is vanishes. Eventually, the spectrum becomes such that $E(k,t) \leq E_0(t)$ for all k. Thus the memory of the initial spectral range with $n_2 = 1.5$ lingers in the system for some time.

The energy decay occurs in mainly two regimes. In our simulation, the first regime occurs approximately for $t \in [10^{-8}, 10^{-3}]$, whereas the second regime happens for $10^0 \lesssim t \lesssim 10^3$ with an itermediate transient decay. Though we observe $E(k,t) \sim t^{-1}$ in the first regime, the situation in the second regime is not very clear. Only towards the end of the second regime we observe that the energy decays as $\sim t^{-0.9}$ (see the inset in Figure 8.7(f)). The exponent for $L(t)$ is not clear (see Figure 8.7(g)). Figure 8.7(h) shows the evolution of the histogram for the shock intervals.

8.3.3.3 Case IIc

There is a single peak at $k_p(t)$ in the spectrum just as in the case IIb. Again the energy decay takes place in two regimes. However, this case appears to be simpler as observed in the plot of the evolution of $E(k,t)$ in Figure 8.7(i). When $k_1 < k_p(t) < k_1^2$ the decay is exactly like the single power law case with $n = 0.5$. The exponent for energy decay is approximately -0.9. But, for $k_p(t) < k_1$, we observe the Gurbatov phenomenon, i.e. the behaviour resembles the single power law case $n = 1.5$. The reader is referred to the Figures 8.7(j) and (k) for the relevant plots. The histograms for the Lagrangian shock intervals is shown in Figure 8.7(l).

8.3.3.4 Case IId

The evolution of $E(k,t)$ exhibits the Gurbatov phenomenon (Figure 8.7(m)). The exponents for energy decay and integral length scale growth are same as for $1 < n < 2$ in the the single power law case. The exponents for the decay of the energy decay and the growth of the integral length scale are roughly -1.0 and 0.5 (as observed in Figures 8.7(n) and (o)). The evolution histogram for the Lagrangian shock intervals shown in Figure 8.7(p) looks different from the those for IIa-c.

8.3.4 Case III: Composite four-range initial energy spectrum

The initial spectrum involving four main spectral ranges with power law dependence is given by

$$E_0(k) = \begin{cases} A_1\mathcal{E}_1(k) & \text{for } k < k_1\,, \\ A_2\mathcal{E}_2(k) & \text{for } k_1 \leq k < k_1^2\,, \\ A_3\mathcal{E}_3(k) & \text{for } k_1^2 \leq k < k_1^3\,, \\ A_4\mathcal{E}_4(k) & \text{for } k_1^3 \leq k < k_1^4\,, \\ A_5\mathcal{E}_4(k)\exp\left[-2k^2/k_c^2\right] & \text{for } k \geq k_1^4\,, \end{cases} \tag{8.3.4}$$

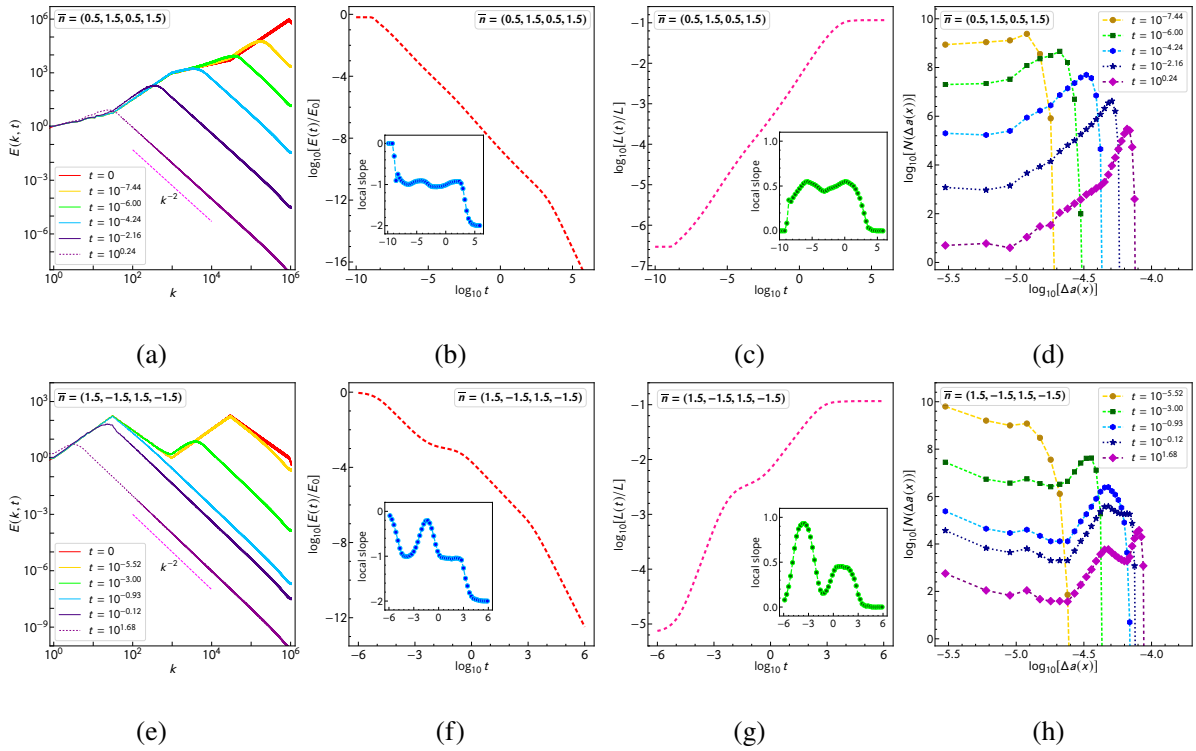

Figure 8.8: Plots of the evolution of the energy spectrum, the energy decay, the growth of the integral length scale, and the evolution of the histogram of the shock strengths, for composite initial spectra with four power laws. We show plots of $E(k,t)$ vs k on logarithmic scales for six different times for cases IIIa in (a) and IIIb in (e); plots of $\log_{10} E(t)$ vs $\log_{10} t$ for cases IIIa in (b), and IIIb in (f); plots of $\log_{10} L(t)$ vs $\log_{10} t$ for cases IIIa in (c) and IIIb in (g); plots of $\log_{10}[N(\Delta a(x))]$ vs $\log_{10} \Delta a(x)$ for cases IIIa in (d), and IIIb in (h). We show the relevant local slopes in the insets in (b), (c), (f), and (g).

where $\mathcal{E}_i$ is a power law with exponent n_i as in (8.3.2). Let us refer to this type of initial conditions with the 4-tuple $\overline{n} = (n_1, n_2, n_3, n_4)$. We consider the following two choices

IIIa $\overline{n} = (0.5, 1.5, 0.5, 1.5)$

IIIb $\overline{n} = (1.5, -1.5, 1.5, -1.5)$

We describe our results case by case below. The exponents for the decay of the energy decay and the growth of the integral length scale are not very clear in some of the temporal ranges for these cases.

8.3.4.1 Case IIIa

The changes in the spectrum are similar to those in IIb. In fact, the first two and the last two spectral ranges can be considered independently, in light of the discussion for case IIb. There is only one peak, the position of which is again denoted by $k_p(t)$. When the changes appear in the last two spectral ranges, there is no visible change in the first two spectral ranges (see Figure 8.8(a)). Only when the peak approach the second spectral range, visible changes begin to appear in the first spectral range as well. Thus the exponent for the energy decay and the growth of the integral length scale fluctuate around -1.0 and 0.5 respectively (see the plots in Figure 8.8(b)-(c)).

8.3.4.2 Case IIIb

We consider at time t the peak in the spectrum at $k_p(t)$. When $k_p(t)$ is in the first and the third spectral ranges ((8.3.4)), we observe phenomena which resemble the Gurbatov phenomenon. The local slope corresponding to the exponent for the energy decay is nearly -1.0 (see Figure 8.8(f)). The exponent for the growth of the integral length scale remains constant at approximately 0.5 only when $k_p(t)$ is in the first spectral range (see Figure 8.8(g)). When the peak is in the third spectral range, the exponent rises close to the value 1 (see the inset in Figure 8.8(g)). We also observe a short period of slowing down of the energy decay and integral-length scale-growth when $k_p(t)$ passes through the junction of the second and the third spectral range.

8.4 Conclusion

In conclusion, we have considered different types of initial spectra in cases I-III where the energy decay can have complicated dependences on time t in different temporal ranges. By carrying out this study, we have gone beyond the results for simple spectral ranges, presented in Gurbatov, *et al.* For similar studies on the Navier-Stokes turbulence, the reader is referred to [159] which treats this decay using closure theory, and numerical studies involving direct numerical simulations [158].

Appendices

Appendix A

The semipermeable TASEP and ASEP

We review the semipermeable TASEP [22] using the original terminology, but with the notation of the mTASEP. Let us recall first the model here. The semipermeable TASEP is defined on an open, one-dimensional lattice of size L. It involves three species, denoted with $1, 0$ and $\overline{1}$. The 1's are positive charges, the 0's are thought of as vacancies, and $\overline{1}$'s are negative charges. In the bulk, these species follow totally asymmetric hopping rules with rates

$$\begin{cases} 10 \to 01 & \text{with rate 1,} \\ 1\overline{1} \to \overline{1}1 & \text{with rate 1,} \\ 0\overline{1} \to \overline{1}0 & \text{with rate 1.} \end{cases}$$

An the left boundary, the negative charges can be replaced with the positive charges

$$\overline{1} \to 1 \quad \text{with rate } \alpha. \tag{A.0.1}$$

The positive charges can be replaced with the negative charges on the right boundary with rate

$$1 \to \overline{1} \quad \text{with rate } \beta. \tag{A.0.2}$$

The semipermeable TASEP was originally conceived as a model of first-class particles (1's), second-class particles (0's) and vacancies ($\overline{1}$'s) where both particles hop only to the right, and where first-class particles overtake second-class ones. In addition, 0's are constrained to remain in the system. This model then corresponds to the mTASEP with $r = 1$. We consider the large-size limit of the semipermeable TASEP so that the ratio of the number of 0's to the size of the system approaches a fixed constant, θ_0. The phase diagram is thus determined by three parameters: α, β and θ_0.

The phase diagram of the semipermeable TASEP was understood using two important concepts. The first was a *current-density relation*, which was derived assuming the typical configuration in the stationary distribution has uniform regions of a given density. This showed that either $\rho_1 = \rho_{\overline{1}}$ or $\rho_1 = 1 - \rho_{\overline{1}}$ in the bulk. The second was a *colouring argument* which said the following. If one could not distinguish between 0's and $\overline{1}$'s, then the dynamics were the same as the original TASEP in the bulk between 1's and these two. A similar argument was made

if one could not distinguish between 1's and 0's. Although these identifications fail at the boundaries, this argument gives the correct physical picture. These two ideas led to the notion of a *fat shock*, a macroscopic region in which all the second class particles are present. The width of the fat shock was then determined by the number of confined 0's.

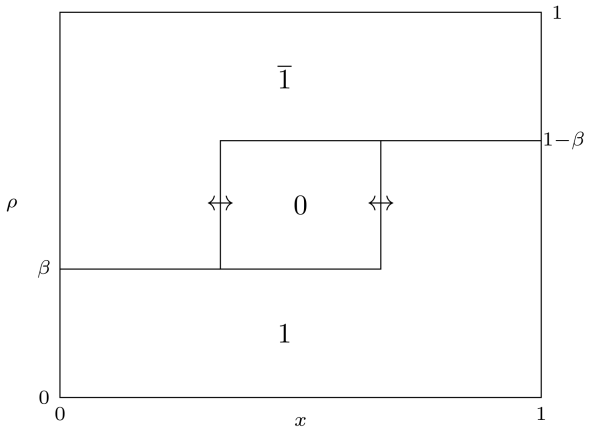

Figure A.1: Instantaneous picture of the fat shock in the $\mathbb{1} - \overline{\mathbb{1}}$ boundary in the semipermeable TASEP. Each connected region is labelled with the species of a particle and the height of a region at a given location represents the density of that species at that point.

An illustration of the fat shock is given in Figure A.1. The regions separating $\overline{1} - 0$ and $0 - 1$ execute synchronized random walks so that the width of the fat shock is fixed. In various regions of the phase diagram, the fat shock has either negative, positive, or zero drift.

Phase	Densities			Current of 1's
	ρ_1	ρ_0	$\rho_{\overline{1}}$	
$\mathbb{0}$ = C $b, \zeta_0 < a$	$(1-\theta_0)/2$	θ_0	$(1-\theta_0)/2$	$(1-\theta_0^2)/4$
$\overline{\mathbb{1}}$ = A $b, \zeta_0 < a$	$f(a)$	$\begin{cases} 0 & x < x_0 \\ (1-2f(a)) & x > x_0 \end{cases}$	$\begin{cases} 1-f(a) & x < x_0 \\ f(a) & x > x_0 \end{cases}$	$(1-q)f(a)(1-f(a))$
$\mathbb{1}$ = B $a, \zeta_0 < b$	$\begin{cases} f(b) & x < x_1 \\ 1-f(b) & x > x_1 \end{cases}$	$\begin{cases} 1-2f(b) & x < x_1 \\ 0 & x > x_1 \end{cases}$	$f(b)$	$(1-q)f(b)(1-f(b))$
A-B boundary $\zeta_0 < a = b$	$\begin{cases} f(a) & x < x_1 \\ \text{linear} & x > x_1 \end{cases}$	$\begin{cases} 1-2f(a) & x < x_1 \\ & \text{or } x > x_0 \\ \text{linear} & \text{otherwise} \end{cases}$	$\begin{cases} \text{linear} & x < x_0 \\ f(a) & x > x_0 \end{cases}$	$(1-q)f(a)(1-f(a))$

Table A.1: Densities and currents of the semipermeable ASEP. We have used the notation θ_0 for the fixed fraction of 0's, and set $\zeta_0 = (1+\theta_0)/(1-\theta_0)$, $x_0 = 1 - \theta_0(a+1)/(a-1)$ and $x_1 = \theta_0(b+1)/(b-1)$.

Since 0's are confined to the lattice, their average current vanishes. Because of particle conservation, the current of 1's to the right is the same as that of $\overline{1}$'s to the left. We will thus describe only the former, denoted J_1. In region $\mathbb{0}$ = C, the fat shock permeates the system and

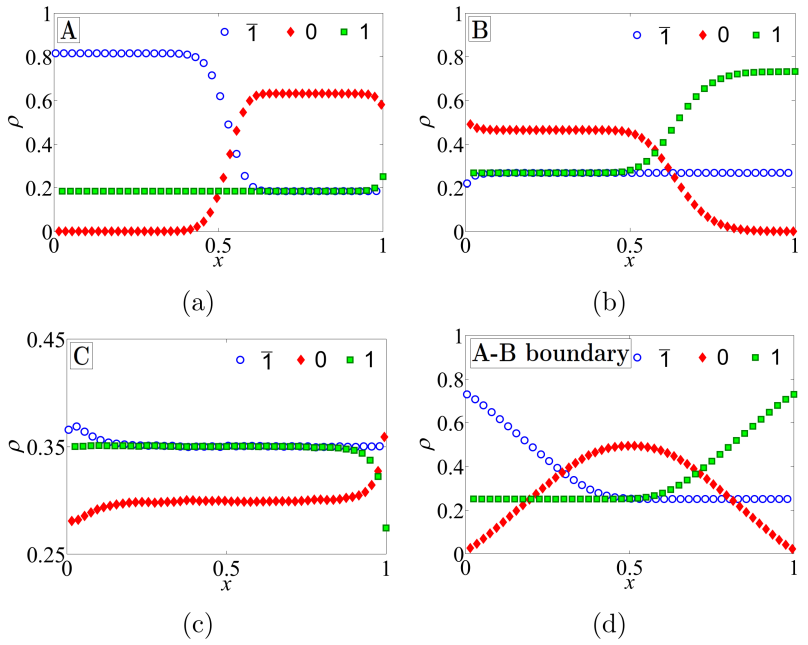

Figure A.2: Plots of the densities of particles 1 (green squares), 0 (red diamonds), and 1 (blue circles), versus the scaled position $x = m/n$ for the $r = 1$ semipermeable ASEP with $n = 200$; $\theta_0 = 0.3$ and $\theta_1 = 0.7$ in the regions (a) A ($\alpha = 0.19, \beta = 0.78, \gamma = 0.41, \delta = 0.63, q = 0.47$), (b) B ($\alpha = 0.89, \beta = 0.34, \gamma = 0.43, \delta = 0.63, q = 0.59$), (c) C ($\alpha = 0.84, \beta = 0.89, \gamma = 0.61, \delta = 0.43, q = 0.59$), and the (d) A-B boundary ($\alpha = \beta = 0.34, \gamma = \delta = 0.63, q = 0.52$).

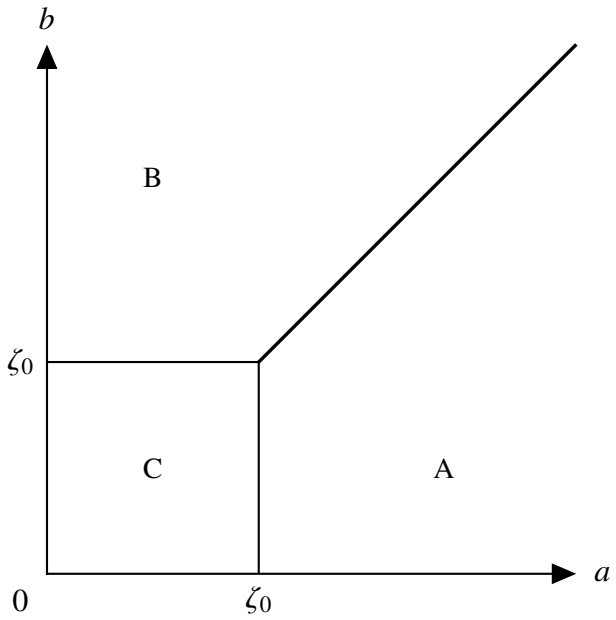

Figure A.3: Stationary phase diagram of the semipermeable ASEP. The parameter ζ_0 depends on the density of species 0, θ_0 which is a fixed parameter in this system as $\zeta_0 = (1+\theta_0)/(1-\theta_0)$.

thus, all densities are constant. The density of 1's and $\overline{1}$'s is $\rho_1 = \rho_{\overline{1}} = (1 - \theta_0)/2$ and their current is $J_1 = (1 - \theta_0^2)/4$. In region $\overline{\mathbb{1}}$ = A, the fat shock is pinned on the right, the density of 1's is $\rho_1 = \alpha$ throughout and the current is $J_1 = \alpha(1 - \alpha)$. In region $\mathbb{1}$ = B, the fat shock is pinned on the left, the density of 1's is $\rho_{\overline{1}} = \beta$ throughout and the current is $J_1 = \beta(1 - \beta)$. On the $\mathbb{1} - \overline{\mathbb{1}}$ boundary, the two ends of the shock perform synchronized oscillations so as to keep the width fixed. In all regions, the width is governed by the fraction θ_0, which is fixed.

Although the existence of the fat shock was proved rigorously only for the semipermeable TASEP [22], the calculations of the density and current for the semipermeable ASEP in [211] strongly suggest that they exist in the latter. The simulations in Figure A.2 attest to this hypothesis. The formulas for the densities and currents in the semipermeable ASEP are summarized in Table A.1. The phase diagram is shown in Figure A.3.

Appendix B

Supplemental Information for KSE

B.1 The compensated spectrum

We show the equal-time compensated spectrum $k^2E(k) = \langle L\tilde{h}(k,t)\tilde{h}^*(k,t)\rangle_t$, where $\langle\cdot\rangle_t$ is the time average and $\tilde{h}(k,t)$ is the spatial Fourier transform of $h(x,t)$ and k is the wave number, in Figure B.1. The compensated spectrum $k^2E(k)$ that we present in Figure B.1 covers a much larger range of wave numbers than in earlier simulations [115, 202].

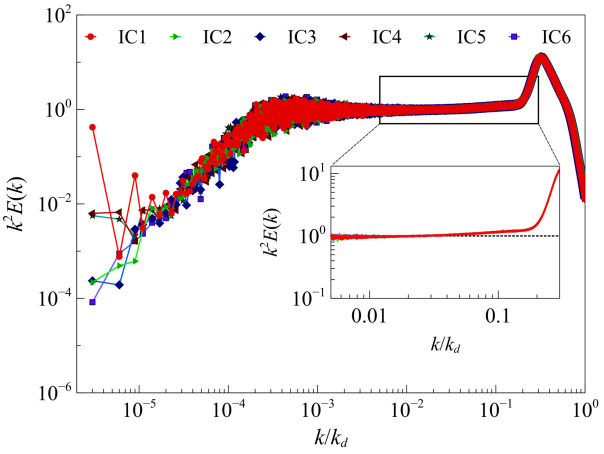

Figure B.1: (Color online) Log-log plots of the compensated spectrum $k^2E(k)$ versus k/k_d for the six different initial conditions IC1-IC6 (see Figure (1) of the main text). We zoom into the region $\delta k/k_d = [0.005, 0.3]$, where the curves appear flat, and show, in the inset, how our data compare with the line $k^2E(k) = 1$. Here, $k_d = \pi\lfloor L/3\rfloor/L$ is the value of the maximum wave number after dealiasing and the system size $L = 2^{20}$.

B.2 Computation of the parameters v_∞ , Γ, and β

We compute the model-dependent parameters v_∞ and Γ (see Equation (1) in the main paper) from our DNS data as follows. By choosing two Kuramoto-Sivashinsky (KS) surfaces at two

different times with $\delta t = 100$, we compute $\delta\langle h(x,t)\rangle_L/\delta t$, where $\langle\cdot\rangle_L$ is the spatial average over our simulation domain; we plot it versus time t in Figure B.2 (a); the $t \to \infty$ limit yields $v_\infty \simeq -0.86$.

The exponent β appears in the Family-Vicsek scaling form:

$$w(L,t) \sim t^{\beta}, \text{ for } t \to \infty, \tag{B.2.1}$$

where $w(L,t)$ is the width (see the main paper). To compute β we plot $\log w(L,t)$ for IC2 (the flat initial condition) against $\log t$ in Figure B.2 (b); a linear fit yields the exponent $\beta \simeq 0.32$, which is close to the KPZ value $\beta_{\rm KPZ} = 1/3$.

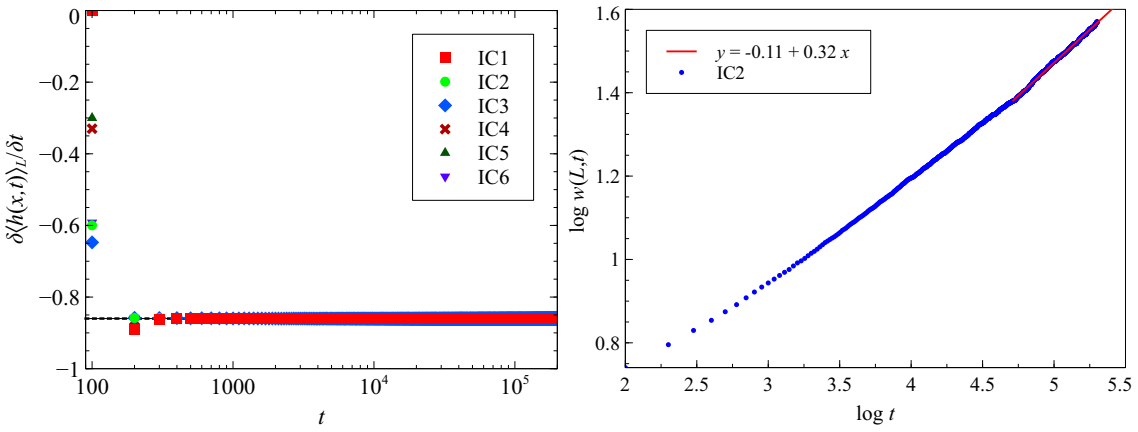

(a) (b)

Figure B.2: (Color online) Plot of $\langle\delta h(x,t)\rangle_L/\delta t$ versus t in (a). In (b), we display $\log w(L,t)$ versus $\log t$.

In order to find the constant Γ, we compute $\Sigma(t)$, the variance of $(h(x,t) - v_\infty t)/t^{\beta_{\rm KPZ}}$, and plot it versus t (see the log-log plot in Figure B.3). For $t \gg 1$, we have $\Sigma(t) \to \Gamma^{2/3}\mathrm{Var}(\chi_\beta)$, where $\mathrm{Var}(\chi_\beta)$ is the variance of the random variable χ_β with $\beta = 1$ for IC2 and $\beta = 2$ for IC1. Given that the variances of the PDFs of χ_1 and χ_2 are, respectively, $\simeq 0.638$ and $\simeq 0.813$ (see Ref. [173]), we compute $\Gamma \simeq 0.358$ and $\Gamma \simeq 0.496$ for IC1 and IC2, respectively.

B.3 Family-Vicsek scaling and the skewness and kurtosis for IC4-IC6

In Figs. (B.4) (a)-(c) we show Family-Vicsek scaling for the initial conditions IC4-IC6. In Figs. (B.4) (d)-(f) we plot the skewness and kurtosis for these initial conditions. Stricly speaking, we must collect data only from those two points ($x = L/4, 3L/4$) at which the two different type of height profiles meet in cases IC4, IC5, and IC6. However, this leads to inadequate statistics. Therefore, the skewness and kurtosis are computed by using data from the regions $[7L/32, 9L/32]$ and $[23L/32, 25L/32]$.

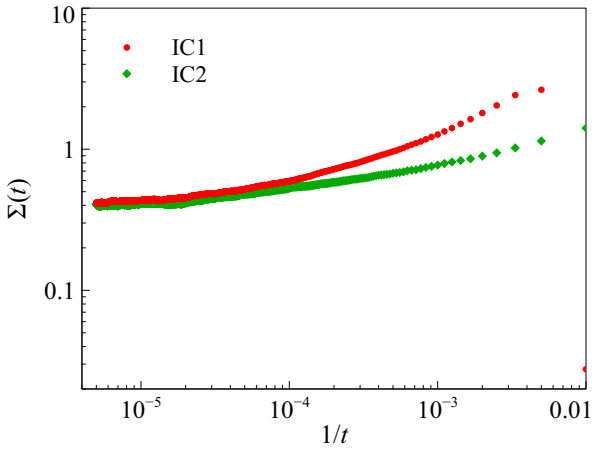

Figure B.3: (Color online) Log-log plots of $\Sigma(t)$ versus t for IC1 and IC2.

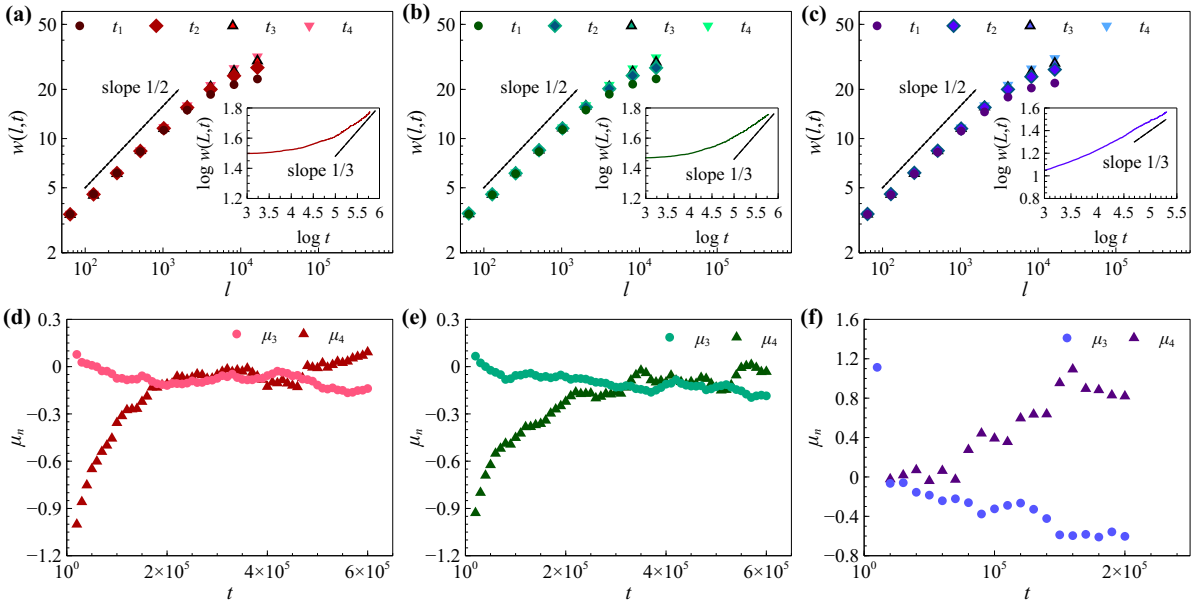

Figure B.4: (Color online) Plots of Family-Vicsek scaling in (a)-(c), and the skewness and kurtosis in (d)-(f) for IC4-IC6, respectively.

B.4 Simulation details

We have used the exponential time-differencing fourth-order Runge-Kutta method (ETDRK4) [64, 130] for time marching in our direct numerical simulation (DNS) for the 1D KS equation. The whole simulation is programmed in CUDA C, by using the in-built *Fast Fourier Transform* in CUDA to switch back and forth between Fourier and real space in our pseudospectral DNS. Moreover, the $2/3$ dealiasing rule is incorporated to avoid aliasing errors. The parameters for our DNSs are given in Table B.1.

L	N	δx	δt	t_{max}
2^{20}	2^{20}	1	0.01	$2 - 6 \times 10^5$

Table B.1: DNS parameters: L is the system size, N is the number of collocation points, $\delta x = L/N$, δt is the time step, and t_{max} is the maximum time for which we run our DNS.

The evolution of $h(x,t)$ for the six initial conditions IC1-IC6 is captured in the videos that are available at the URLs provided below:

- IC1 : `https://drive.google.com/open?id=1CPqNxda1GbntAmgHDydg3xzDRsqycxrr`
- IC2 : `https://drive.google.com/open?id=1iL154onInbzeCTzjmRJgZ-osgf6TuhcN`
- IC3 : `https://drive.google.com/open?id=1xRcXlFrETj1VqUYC5fYXeZ9s0oORw-V4`
- IC4 : `https://drive.google.com/open?id=1RULXEHa-gz4i8vGKNzH2Q54wQo4GTemw`
- IC5 : `https://drive.google.com/open?id=14rmSiAmzhBFSQ84HNj_9MOn7U_MWzzyC`
- IC6 : `https://drive.google.com/open?id=131uJ5mBO8DCifAUovsr4i3FHN4Zh7758`

B.5 Numerical scheme for DNS for KS equation

We have implemented the exponential time differencing method with Runge-Kutta scheme of the fourth order (or ETDRK4 in short) in our CUDA C code. The method is suited to stiff partial differential equations of the form

$$\partial_t u = cu + F(u,t), \tag{B.5.1}$$

where c is a constant, and $F(u,t)$ is the non-linearity. Let the numerical approximation for $u(t)$ be denoted by u_n at time $t_n = nh$, where h is the time step. Given that u_n is known, then u_{n+1} is exactly given by

$$u_{n+1} = u_n e^{ch} + e^{ch} \int_0^h e^{-c\tau} F(u(t_n + \tau), t_n + \tau) d\tau. \tag{B.5.2}$$

This formula is the basis for exponential time differencing methods. Using an approximation for the integral, a fourth order Runge-Kutta scheme was derived in [64]. The scheme is given

by the formulae given below.

$$
\begin{aligned}
A_n &= u_n e^{ch/2} + Q_1 F(u_n, t_n), && \text{(B.5.3)}\\
B_n &= u_n e^{ch/2} + Q_1 F(A_n, t_n + h/2), && \text{(B.5.4)}\\
C_n &= A_n e^{ch/2} + Q_1 [2F(B_n, t_n + h/2) - F(u_n, t_n))], && \text{(B.5.5)}\\
u_{n+1} &= u_n e^{ch} + Q_2 F(u_n, t_n) + 2Q_3 \big(F(A_n, t_n + h/2) + F(B_n, t_n + h/2)\big) && \text{(B.5.6)}\\
&\quad + Q_4 F(C_n, t_n + h),
\end{aligned}
$$

where the coefficients Q_1, Q_2, Q_3 and Q_4 are the following

$$
\begin{aligned}
Q_1 &= \frac{h}{z}(e^{z/2} - 1), && \text{(B.5.7)}\\
Q_2 &= \frac{h}{z^3}[e^z(z^2 - 3z + 4) - z - 4], && \text{(B.5.8)}\\
Q_3 &= \frac{h}{z^3}[e^z(z - 2) + z + 2], && \text{(B.5.9)}\\
Q_4 &= \frac{h}{z^3}[e^z(4 - z) - z^2 - 3z - 4], \quad \text{with } z = ch. && \text{(B.5.10)}
\end{aligned}
$$

The KS equation is cast into the form as in (B.5.2) when we take the Fourier transform. Then the constant c equals $(k^2 - k^4)$, and the non-linearity function is given by

$$
F(u, t) = \mathcal{F}\left[-0.5u_x^2\right] , \qquad \text{(B.5.11)}
$$

where $\mathcal{F}[\cdot]$ is the Fourier transform.

Appendix C

Fast Legendre transform for 1D Burgers equation

We provide the details about the solution of the 1D Burgers equation in terms of the fast Legendre transform (FLT) on a discrete space interval. We explain very briefly the algorithm in 1D for periodic boundary condition (PBC). More details can be found in [167].

As mentioned in Chapter 8, we fix the number of grid-points N to be 2^{21}, and the system size to be $L = 2\pi$. Let us describe the method for general N with PBC.

The goal is to maximize the RHS in (8.2.4) for each of the N gridpoints for jumping ahead to time t from time t_0. Naively, we have to check the maximization at each and every gridpoint for evaluating the potential at time t at the gridpoint under consideration. Thus the search operation is of order $O(N^2)$. Let us, only for our purpose of describing the algorithm here, think of $n \geq 0$ as the position of the nth gridpoint obtained by dividing the periodic interval equally into N intervals of size L/N.

The FLT algorithm takes advantage of the following relation for the inverse Lagrangian function:

$$\big(a(m) - a(n)\big)(m - n) \geq 0 \,, \qquad m, n \in [0, N[\tag{C.0.1}$$

i.e. $a(n)$ is a monotonous function of n. Because of PBC, we shall assume $a(n+N) = a(n)+N$. Now we find $a(n)$ for each and every n, but follow a different order to visit the gridpoints for the maximization instead of visiting them in the increasing order of n. First, we visit the point $n = 0$, and find $a(0)$ by searching in the interval $[-N/2, N/2[$. Also, we set $a(N) = a(0) + N$. Then we divide the interval $[0, N]$ into two sub-intervals of equal length: $[0, N/2]$ and $[N/2, N]$. Now we visit the gridpoint $N/2$ which is at the boundary of these sub-intervals, and search for $a(N/2)$ within the interval $[a(0), a(N)]$. This is enough because the inequality

$$a(0) \leq a(N/2) \leq a(N) \,, \tag{C.0.2}$$

is satisfied due to (C.0.1).

After computing $a(N/2)$ we sub-divide the interval $[0, N/2]$ into two equal sub-intervals of length $N/4$, and compute $a(N/4)$ that lies in the interval $[a(0), a(N/2)]$. Similarly, we

continue the sub-division process until we reach $n = 1$ and compute $a(1)$. Till this time, we have the knowledge of $a(0), a(1), a(2), a(4), \ldots, a(N/2), a(N)$. So, in the interval $[0, 2]$, there are no more points where $a(n)$ has not been computed yet. Thus we move to the interval $[2, 4]$ and apply the sub-division process. The next interval is $[4, 8]$ where we advance via the application of sub-division mechanism. Carrying on in this way, we can determine $a(n)$ for every $n \in [N]$.

The way the gridpoints are visited is referred to as *in-order* visiting. The required number of operations for the Legendre transform is now reduced to $O(N \log_2 N)$. An example for $n = 16$ can be found in [167].

Bibliography

[1] *Marco (2020). Approximation for the Tracy-Widom laws, MATLAB Central File Exchange*. URL https://www.mathworks.com/matlabcentral/fileexchange/44711-approximation-for-the-tracy-widom-laws.

[2] *Turbulence and predictability in geophysical fluid dynamics and climate dynamics*, Proceedings of the International School of Physics "Enrico Fermi" ; course 88, 1985. Amsterdam; New York : North-Holland.

[3] *The Kuramoto-Sivashinsky equation: A caricature of hydrodynamic turbulence?*, volume 230 of *Lecture Notes in Physics*, 1985. Springer-Verlag Berlin Heidelberg.

[4] Exact solution of a partially asymmetric exclusion model using a deformed oscillator algebra. *Journal of Physics A: Mathematical and General*, 33(12):2313, 2000. URL http://stacks.iop.org/0305-4470/33/i=12/a=301.

[5] On the decay of isotropic turbulence. *Journal of Fluid Mechanics*, 564:455–475, 2006. doi: 10.1017/S0022112006001625.

[6] F.D.A. Aarão Reis. Roughness fluctuations, roughness exponents and the universality class of ballistic deposition. *Physica A: Statistical Mechanics and its Applications*, 364:190 – 196, 2006. ISSN 0378-4371. doi: https://doi.org/10.1016/j.physa.2005.09.052. URL http://www.sciencedirect.com/science/article/pii/S0378437105010137.

[7] L Ts Adzhemyan, N V Antonov, and A N Vasiliev. Quantum field renormalization group in the theory of fully developed turbulence. *Physics-Uspekhi*, 39(12):1193–1219, dec 1996. doi: 10.1070/pu1996v039n12abeh000183. URL https://doi.org/10.1070%2Fpu1996v039n12abeh000183.

[8] L. Ts Adzhemyan, N. V. Antonov, and A. N. Vasiliev. *Field Theoretic Renormalization Group in Fully Developed Turbulence*. Gordon and Breach Science Publishers, 1999.

[9] Sanaa Agarwal, Manas Kulkarni, and Abhishek Dhar. Some connections between the classical calogero–moser model and the log-gas. *Journal of Statistical Physics*, 176(6):1463–1479, Sep 2019. ISSN 1572-9613. doi: 10.1007/s10955-019-02349-6. URL https://doi.org/10.1007/s10955-019-02349-6.

[10] Yashar Aghababaie, Gautam I. Menon, and Michael Plischke. Universal properties of interacting brownian motors. *Phys. Rev. E*, 59:2578–2586, Mar 1999. doi: 10.

1103/PhysRevE.59.2578. URL https://link.aps.org/doi/10.1103/PhysRevE.59.2578.

[11] D. G. Andrews and B. J. Hoskins. Energy Spectra Predicted by Semi-Geostrophic Theories of Frontogenesis. *Journal of the Atmospheric Sciences*, 35(3):509–512, 03 1978. ISSN 0022–4928. doi: 10.1175/1520-0469(1978)035<0509:ESPBSG>2.0.CO;2. URL https://doi.org/10.1175/1520-0469(1978)035<0509:ESPBSG>2.0.CO;2.

[12] Igor S. Aranson and Lorenz Kramer. The world of the complex Ginzburg-Landau equation. *Rev. Mod. Phys.*, 74:99–143, Feb 2002. doi: 10.1103/RevModPhys.74.99. URL https://link.aps.org/doi/10.1103/RevModPhys.74.99.

[13] Chikashi Arita. Phase transitions in the two-species totally asymmetric exclusion process with open boundaries. *Journal of Statistical Mechanics: Theory and Experiment*, 2006(12):P12008, 2006. URL http://stacks.iop.org/1742-5468/2006/i=12/a=P12008.

[14] Chikashi Arita. Exact analysis of two-species totally asymmetric exclusion process with open boundary condition. *Journal of the Physical Society of Japan*, 75(6):065003, 2006. doi: 10.1143/JPSJ.75.065003. URL https://doi.org/10.1143/JPSJ.75.065003.

[15] Chikashi Arita, Arvind Ayyer, Kirone Mallick, and Sylvain Prolhac. Recursive structures in the multispecies TASEP. *Journal of Physics A: Mathematical and Theoretical*, 44 (33):335004, jul 2011. doi: 10.1088/1751-8113/44/33/335004. URL https://doi.org/10.1088%2F1751-8113%2F44%2F33%2F335004.

[16] Chikashi Arita, Arvind Ayyer, Kirone Mallick, and Sylvain Prolhac. Generalized matrix ansatz in the multispecies exclusion process—the partially asymmetric case. *Journal of Physics A: Mathematical and Theoretical*, 45(19):195001, apr 2012. doi: 10.1088/1751-8113/45/19/195001. URL https://doi.org/10.1088%2F1751-8113%2F45%2F19%2F195001.

[17] Chikashi Arita, Julien Cividini, and Cécile Appert-Rolland. Two dimensional outflows for cellular automata with shuffle updates. *Journal of Statistical Mechanics: Theory and Experiment*, 2015(10):P10019, oct 2015. doi: 10.1088/1742-5468/2015/10/p10019. URL https://doi.org/10.1088%2F1742-5468%2F2015%2F10%2Fp10019.

[18] Peter F. Arndt, Thomas Heinzel, and Vladimir Rittenberg. First-order phase transitions in one-dimensional steady states. *Journal of Statistical Physics*, 90:783–815, 1998. doi: 10.1023/A:1023229004414. URL https://doi.org/10.1023/A:1023229004414.

[19] Peter F. Arndt, Thomas Heinzel, and Vladimir Rittenberg. Spontaneous breaking of translational invariance and spatial condensation in stationary states on a ring. i. the neutral system. *Journal of Statistical Physics*, 97:1–65, 1999. doi: 10.1023/A:1004670916674. URL https://doi.org/10.1023/A:1004670916674.

[20] Arvind Ayyer and Svante Linusson. Correlations in the multispecies TASEP and a conjecture by lam. *Trans. Amer. Math. Soc.*, 369(2):1097–1125, 2017. doi: https://doi.org/10.1090/tran/6806.

[21] Arvind Ayyer and Dipankar Roy. The exact phase diagram for a class of open multispecies asymmetric exclusion processes. *Scientific Reports*, 7:13555–, Oct 2017. doi: 10.1038/s41598-017-12768-8. URL https://doi.org/10.1038/s41598-017-12768-8.

[22] Arvind Ayyer, Joel L. Lebowitz, and Eugene R. Speer. On the two species asymmetric exclusion process with semi-permeable boundaries. *Journal of Statistical Physics*, 135 (5):1009–1037, Jun 2009. doi: 10.1007/s10955-009-9724-2. URL https://doi.org/10.1007/s10955-009-9724-2.

[23] Arvind Ayyer, Joel L. Lebowitz, and Eugene R. Speer. On some classes of open two-species exclusion processes. *Markov Processes And Related Fields*, 18:157–176, 2012.

[24] Arvind Ayyer, Caley Finn, and Dipankar Roy. Matrix product solution of a left-permeable two-species asymmetric exclusion process. *Phys. Rev. E*, 97:012151, Jan 2018. doi: 10.1103/PhysRevE.97.012151. URL https://link.aps.org/doi/10.1103/PhysRevE.97.012151.

[25] Arvind Ayyer, Caley Finn, and Dipankar Roy. The phase diagram for a multispecies left-permeable asymmetric exclusion process. *Journal of Statistical Physics*, Nov 2018. ISSN 1572-9613. doi: 10.1007/s10955-018-2183-x. URL https://doi.org/10.1007/s10955-018-2183-x.

[26] A. J. Babchin, A. L. Frenkel, B. G. Levich, and G. I. Sivashinsky. Nonlinear saturation of Rayleigh–Taylor instability in thin films. *The Physics of Fluids*, 26(11):3159–3161, 1983. doi: 10.1063/1.864083. URL https://aip.scitation.org/doi/abs/10.1063/1.864083.

[27] Jinho Baik and Eric M. Rains. Limiting distributions for a polynuclear growth model with external sources. *Journal of Statistical Physics*, 100(3):523–541, Aug 2000. ISSN 1572-9613. doi: 10.1023/A:1018615306992. URL https://doi.org/10.1023/A:1018615306992.

[28] Jinho Baik, Percy Deift, and Kurt Johansson. On the distribution of the length of the longest increasing subsequence of random permutations. *Journal of the American Mathematical Society*, 12(4):1119–1178, June 1999. doi: https://doi.org/10.1090/S0894-0347-99-00307-0. URL https://doi.org/10.1090/S0894-0347-99-00307-0.

[29] G. K. Batchelor. *An Introduction to Fluid Dynamics*. Cambridge Mathematical Library. Cambridge University Press, 2000. doi: 10.1017/CBO9780511800955.

[30] Harry Bateman. Some recent researches on the motion of fluids. *Monthly Weather Review*, 43(4):163–170, 04 1915. ISSN 0027-0644. doi: 10.1175/1520-0493(1915)43<163:SRROTM>2.0.CO;2. URL https://doi.org/10.1175/1520-0493(1915)43<163:SRROTM>2.0.CO;2.

[31] R. Benzi and U. Frisch. Turbulence. *Scholarpedia*, 5(3):3439, 2010. doi: 10.4249/scholarpedia.3439.

[32] R Benzi, G Paladin, G Parisi, and A Vulpiani. On the multifractal nature of fully developed turbulence and chaotic systems. *Journal of Physics A: Mathematical and*

General, 17(18):3521–3531, dec 1984. doi: 10.1088/0305-4470/17/18/021. URL https://doi.org/10.1088%2F0305-4470%2F17%2F18%2F021.

[33] L. Bertini, A. De Sole, D. Gabrielli, G. Jona-Lasinio, and C. Landim. Current fluctuations in stochastic lattice gases. *Phys. Rev. Lett.*, 94:030601, Jan 2005. doi: 10.1103/PhysRevLett.94.030601. URL https://link.aps.org/doi/10.1103/PhysRevLett.94.030601.

[34] J K Bhattacharjee. Randomly stirred fluids, mode coupling theories and the turbulent prandtl number. *Journal of Physics A: Mathematical and General*, 21(10):L551–L554, may 1988. doi: 10.1088/0305-4470/21/10/003. URL https://doi.org/10.1088%2F0305-4470%2F21%2F10%2F003.

[35] L Biferale, M Cencini, A S Lanotte, M Sbragaglia, and F Toschi. Anomalous scaling and universality in hydrodynamic systems with power-law forcing. *New Journal of Physics*, 6:37–37, mar 2004. doi: 10.1088/1367-2630/6/1/037. URL https://doi.org/10.1088%2F1367-2630%2F6%2F1%2F037.

[36] Benjamin J. Binder and Kerry A. Landman. Exclusion processes on a growing domain. *Journal of Theoretical Biology*, 259(3):541 – 551, 2009. ISSN 0022-5193. doi: https://doi.org/10.1016/j.jtbi.2009.04.025. URL http://www.sciencedirect.com/science/article/pii/S002251930900191X.

[37] Anders Björner and Brenti Francesco. Combinatorics of Coxeter Groups. *Graduate Texts in Mathematics*, 230(0072-5285):366, 2005. doi: 10.1007/3-540-27596-7. URL https://www.springer.com/gp/book/9783540442387.

[38] William Blumen. A comparison between the hoskins-bretherton model of frontogenesis and the analysis of an intense surface frontal zone. *Journal of the Atmospheric Sciences*, 37(1):64–77, 01 1980. ISSN 0022–4928. doi: 10.1175/1520-0469(1980)037<0064:ACBTHB>2.0.CO;2. URL https://doi.org/10.1175/1520-0469(1980)037<0064:ACBTHB>2.0.CO;2.

[39] R. A. Blythe and M. R. Evans. Lee-yang zeros and phase transitions in nonequilibrium steady states. *Phys. Rev. Lett.*, 89:080601, Aug 2002. doi: 10.1103/PhysRevLett.89.080601. URL https://link.aps.org/doi/10.1103/PhysRevLett.89.080601.

[40] R A Blythe and M R Evans. Nonequilibrium steady states of matrix-product form: a solver's guide. *Journal of Physics A: Mathematical and Theoretical*, 40(46):R333, 2007. URL http://stacks.iop.org/1751-8121/40/i=46/a=R01.

[41] T. Bodineau and B. Derrida. Current fluctuations in nonequilibrium diffusive systems: An additivity principle. *Phys. Rev. Lett.*, 92:180601, May 2004. doi: 10.1103/PhysRevLett.92.180601. URL https://link.aps.org/doi/10.1103/PhysRevLett.92.180601.

[42] Bruce M. Boghosian, Carson C. Chow, and Terence Hwa. Hydrodynamics of the kuramoto-sivashinsky equation in two dimensions. *Phys. Rev. Lett.*, 83:5262–5265, Dec 1999. doi: 10.1103/PhysRevLett.83.5262. URL https://link.aps.org/doi/10.1103/PhysRevLett.83.5262.

[43] Folkmar Bornemann. On the numerical evaluation of fredholm determinants. *Mathematics of Computation*, 79:871–915, 2010. doi: https://doi.org/10.1090/S0025-5718-09-02280-7. URL https://doi.org/10.1090/S0025-5718-09-02280-7.

[44] Alexei Borodin, Patrik L. Ferrari, and Tomohiro Sasamoto. Transition between airy1 and airy2 processes and tasep fluctuations. *Communications on Pure and Applied Mathematics*, 61(11):1603–1629, 2008. doi: 10.1002/cpa.20234. URL https://onlinelibrary.wiley.com/doi/abs/10.1002/cpa.20234.

[45] John P. Boyd. The energy spectrum of fronts: Time evolution of shocks in Burgers' equation. *Journal of the Atmospheric Sciences*, 49(2):128–139, 01 1992. ISSN 0022-4928. doi: 10.1175/1520-0469(1992)049<0128:TESOFT>2.0.CO;2. URL https://doi.org/10.1175/1520-0469(1992)049<0128:TESOFT>2.0.CO;2.

[46] D. Bressoud. A Simple Proof of Mehler's Formula for q-Hermite Polynomials. *Indiana Univ. Math. J.*, 29:577–580, 1980. ISSN 0022-2518.

[47] Maria Bruna and S. Jonathan Chapman. Diffusion of multiple species with excluded-volume effects. *The Journal of Chemical Physics*, 137(20):204116, 2012. doi: 10.1063/1.4767058. URL https://doi.org/10.1063/1.4767058.

[48] R. Bundschuh. Asymmetric exclusion process and extremal statistics of random sequences. *Phys. Rev. E*, 65:031911, Mar 2002. doi: 10.1103/PhysRevE.65.031911. URL https://link.aps.org/doi/10.1103/PhysRevE.65.031911.

[49] J.M. Burgers. A Mathematical Model Illustrating the Theory of Turbulence. 1:171 – 199, 1948. ISSN 0065-2156. doi: https://doi.org/10.1016/S0065-2156(08)70100-5. URL http://www.sciencedirect.com/science/article/pii/S0065215608701005.

[50] J.M. Burgers. The Nonlinear Diffusion Equation. 1974. doi: 10.1007/978-94-010-1745-9. URL https://www.springer.com/gp/book/9789027704948.

[51] Pasquale Calabrese and Pierre Le Doussal. Exact solution for the kardar-parisi-zhang equation with flat initial conditions. *Phys. Rev. Lett.*, 106:250603, Jun 2011. doi: 10.1103/PhysRevLett.106.250603. URL https://link.aps.org/doi/10.1103/PhysRevLett.106.250603.

[52] Luigi Cantini. Asymmetric simple exclusion process with open boundaries and koornwinder polynomials. *Annales Henri Poincaré*, 18(4):1121–1151, Apr 2017. ISSN 1424-0661. doi: 10.1007/s00023-016-0540-3. URL https://doi.org/10.1007/s00023-016-0540-3.

[53] Luigi Cantini, Alexandr Garbali, Jan de Gier, and Michael Wheeler. Koornwinder polynomials and the stationary multi-species asymmetric exclusion process with open boundaries. *Journal of Physics A: Mathematical and Theoretical*, 49(44):444002, 2016. URL http://stacks.iop.org/1751-8121/49/i=44/a=444002.

[54] C. Canuto and A. Quarteroni. Spectral and pseudo-spectral methods for parabolic problems with non periodic boundary conditions. *CALCOLO*, 18(3):197–217, Sep 1981. ISSN 1126-5434. doi: 10.1007/BF02576357. URL https://doi.org/10.1007/BF02576357.

[55] C. Canuto, M. Y. Hussaini, A. Quarteroni, and T. A. Zang. *Spectral Methods*. Springer-Verlag Berlin Heidelberg, 2006. doi: 10.1007/978-3-540-30726-6.

[56] Liang-Heng Chen and Hsueh-Chia Chang. Nonlinear waves on liquid film surfaces—ii. bifurcation analyses of the long-wave equation. *Chemical Engineering Science*, 41(10):2477 – 2486, 1986. ISSN 0009-2509. doi: https://doi.org/10.1016/0009-2509(86)80033-1. URL http://www.sciencedirect.com/science/article/pii/0009250986800331.

[57] Tom Chou and Detlef Lohse. Entropy-driven pumping in zeolites and biological channels. *Phys. Rev. Lett.*, 82:3552–3555, Apr 1999. doi: 10.1103/PhysRevLett.82.3552. URL https://link.aps.org/doi/10.1103/PhysRevLett.82.3552.

[58] Debashish Chowdhury, Ludger Santen, and Andreas Schadschneider. Statistical physics of vehicular traffic and some related systems. *Physics Reports*, 329(4):199–329, 2000. ISSN 0370–1573. doi: https://doi.org/10.1016/S0370-1573(99)00117-9. URL http://www.sciencedirect.com/science/article/pii/S0370157399001179.

[59] Julian D. Cole. On a quasi-linear parabolic equation occurring in aerodynamics. *Quarterly of Applied Mathematics*, 9:225–236, 1951. doi: https://doi.org/10.1090/qam/42889. URL https://doi.org/10.1090/qam/42889.

[60] P. Collet, J.-P. Eckmann, H. Epstein, and J. Stubbe. A global attracting set for the kuramoto-sivashinsky equation. *Communications in Mathematical Physics*, 152(1):203 – 214, 1993. ISSN 1432-0916. doi: https://doi.org/10.1007/BF02097064. URL https://link.springer.com/article/10.1007%2FBF02097064?LI=true.

[61] R Conte and M Musette. Painleve analysis and backlund transformation in the kuramoto-sivashinsky equation. *Journal of Physics A: Mathematical and General*, 22(2):169, 1989. URL http://stacks.iop.org/0305-4470/22/i=2/a=006.

[62] Ivan Corwin. The Kardar-Parisi-Zhang Equation and Universality Class. *Random Matrices: Theory and Applications*, 01(01):1130001, 2012. doi: 10.1142/S2010326311300014. URL https://www.worldscientific.com/doi/abs/10.1142/S2010326311300014.

[63] Ivan Corwin, Patrik L. Ferrari, and Sandrine Péché. Limit processes for tasep with shocks and rarefaction fans. *Journal of Statistical Physics*, 140(2):232–267, Jul 2010. ISSN 1572-9613. doi: 10.1007/s10955-010-9995-7. URL https://doi.org/10.1007/s10955-010-9995-7.

[64] S.M. Cox and P.C. Matthews. Exponential time differencing for stiff systems. *Journal of Computational Physics*, 176(2):430 – 455, 2002. ISSN 0021-9991. doi: https://doi.org/10.1006/jcph.2002.6995. URL http://www.sciencedirect.com/science/article/pii/S0021999102969950.

[65] N Crampe, E Ragoucy, and M Vanicat. Integrable approach to simple exclusion processes with boundaries. review and progress. *Journal of Statistical Mechanics: Theory and Experiment*, 2014(11):P11032, nov 2014. doi: 10.1088/1742-5468/2014/11/p11032. URL https://doi.org/10.1088%2F1742-5468%2F2014%2F11%2Fp11032.

[66] N Crampe, K Mallick, E Ragoucy, and M Vanicat. Open two-species exclusion processes with integrable boundaries. *Journal of Physics A: Mathematical and Theoretical*, 48 (17):175002, apr 2015. doi: 10.1088/1751-8113/48/17/175002. URL https://doi.org/10.1088%2F1751-8113%2F48%2F17%2F175002.

[67] N Crampe, M R Evans, K Mallick, E Ragoucy, and M Vanicat. Matrix product solution to a 2-species TASEP with open integrable boundaries. *Journal of Physics A: Mathematical and Theoretical*, 49(47):475001, oct 2016. doi: 10.1088/1751-8113/49/47/475001. URL https://doi.org/10.1088%2F1751-8113%2F49%2F47%2F475001.

[68] N Crampe, M R Evans, K Mallick, E Ragoucy, and M Vanicat. Matrix product solution to a 2-species TASEP with open integrable boundaries. *Journal of Physics A: Mathematical and Theoretical*, 49(47):475001, 2016. URL http://stacks.iop.org/1751-8121/49/i=47/a=475001.

[69] N Crampe, C Finn, E Ragoucy, and M Vanicat. Integrable boundary conditions for multi-species ASEP. *Journal of Physics A: Mathematical and Theoretical*, 49(37): 375201, 2016. URL http://stacks.iop.org/1751-8121/49/i=37/a=375201.

[70] M. C. Cross and P. C. Hohenberg. Pattern formation outside of equilibrium. *Rev. Mod. Phys.*, 65:851–1112, Jul 1993. doi: 10.1103/RevModPhys.65.851. URL https://link.aps.org/doi/10.1103/RevModPhys.65.851.

[71] Michael Cross and Henry Greenside. *Pattern Formation and Dynamics in Nonequilibrium Systems*. Cambridge University Press, 2009. doi: 10.1017/CBO9780511627200.

[72] Jan de Gier and Fabian H. L. Essler. Bethe ansatz solution of the asymmetric exclusion process with open boundaries. *Phys. Rev. Lett.*, 95:240601, Dec 2005. doi: 10.1103/PhysRevLett.95.240601. URL https://link.aps.org/doi/10.1103/PhysRevLett.95.240601.

[73] Jan de Gier, Caley Finn, and Mark Sorrell. The relaxation rate of the reverse-biased asymmetric exclusion process. *Journal of Physics A: Mathematical and Theoretical*, 44 (40):405002, sep 2011. doi: 10.1088/1751-8113/44/40/405002. URL https://doi.org/10.1088%2F1751-8113%2F44%2F40%2F405002.

[74] Theodore de Karman and Leslie Howarth. On the statistical theory of isotropic turbulence. *Proceedings of the Royal Society of London. Series A - Mathematical and Physical Sciences*, 164(917):192–215, 1938. doi: 10.1098/rspa.1938.0013. URL https://royalsocietypublishing.org/doi/abs/10.1098/rspa.1938.0013.

[75] C. DeDominicis and P. C. Martin. Energy spectra of certain randomly-stirred fluids. *Phys. Rev. A*, 19:419–422, Jan 1979. doi: 10.1103/PhysRevA.19.419. URL https://link.aps.org/doi/10.1103/PhysRevA.19.419.

[76] B. Derrida and C. Appert. Universal Large–Deviation Function of the Kardar–Parisi–Zhang Equation in One Dimension. *Journal of Statistical Physics*, 94:1–30, Jan 1999. doi: 10.1023/A:1004599526997. URL https://doi.org/10.1023/A:1004599526997.

[77] B Derrida and K Mallick. Exact diffusion constant for the one-dimensional partially asymmetric exclusion model. *Journal of Physics A: Mathematical and General*, 30(4): 1031–1046, Feb 1997. doi: 10.1088/0305-4470/30/4/007. URL https://doi.org/10.1088%2F0305-4470%2F30%2F4%2F007.

[78] B. Derrida, E. Domany, and D. Mukamel. An exact solution of a one-dimensional asymmetric exclusion model with open boundaries. *J. Stat. Phys.*, 69(3-4):667–687, 1992. ISSN 0022-4715. doi: 10.1007/BF01050430.

[79] B Derrida, M R Evans, V Hakim, and V Pasquier. Exact solution of a 1d asymmetric exclusion model using a matrix formulation. *Journal of Physics A: Mathematical and General*, 26(7):1493, 1993. URL http://stacks.iop.org/0305-4470/26/i=7/a=011.

[80] B. Derrida, S. A. Janowsky, J. L. Lebowitz, and E. R. Speer. Exact solution of the totally asymmetric simple exclusion process: Shock profiles. *Journal of Statistical Physics*, 73: 813–842, dec 1993. doi: 10.1007/BF01052811. URL https://doi.org/10.1007/BF01052811.

[81] B Derrida, S. A Janowsky, J. L Lebowitz, and E. R Speer. Microscopic-shock profiles: Exact solution of a non-equilibrium system. *Europhysics Letters (EPL)*, 22(9):651–656, jun 1993. doi: 10.1209/0295-5075/22/9/003. URL https://doi.org/10.1209%2F0295-5075%2F22%2F9%2F003.

[82] B. Derrida, M. R. Evans, and K. Mallick. Exact diffusion constant of a one-dimensional asymmetric exclusion model with open boundaries. *Journal of Statistical Physics*, 79 (5):833–874, Jun 1995. ISSN 1572-9613. doi: 10.1007/BF02181206. URL https://doi.org/10.1007/BF02181206.

[83] B. Derrida, J. L. Lebowitz, and E. R. Speer. Shock profiles for the asymmetric simple exclusion process in one dimension. *Journal of Statistical Physics*, 89:135–167, oct 1997. doi: 10.1007/BF02770758. URL https://doi.org/10.1007/BF02770758.

[84] B. Derrida, J. L. Lebowitz, and E. R. Speer. Exact free energy functional for a driven diffusive open stationary nonequilibrium system. *Phys. Rev. Lett.*, 89:030601, Jun 2002. doi: 10.1103/PhysRevLett.89.030601. URL https://link.aps.org/doi/10.1103/PhysRevLett.89.030601.

[85] B. Derrida, C. Enaud, and J. L. Lebowitz. The asymmetric exclusion process and brownian excursions. *Journal of Statistical Physics*, 115:365–382, Apr 2004. doi: 10.1023/B:JOSS.0000019833.35328.b4. URL https://doi.org/10.1023/B:JOSS.0000019833.35328.b4.

[86] B. Derrida, C. Enaud, C. Landim, and S. Olla. Fluctuations in the weakly asymmetric exclusion process with open boundary conditions. *Journal of Statistical Physics*, 118:

795–811, Mar 2005. doi: 10.1007/s10955-004-1989-x. URL https://doi.org/10.1007/s10955-004-1989-x.

[87] Bernard Derrida and Joel L. Lebowitz. Exact large deviation function in the asymmetric exclusion process. *Phys. Rev. Lett.*, 80:209–213, Jan 1998. doi: 10.1103/PhysRevLett.80.209. URL https://link.aps.org/doi/10.1103/PhysRevLett.80.209.

[88] S. F. Edwards. The statistical dynamics of homogeneous turbulence. *Journal of Fluid Mechanics*, 18(2):239–273, 1964. doi: 10.1017/S0022112064000180.

[89] Samuel Frederick Edwards and DR Wilkinson. The surface statistics of a granular aggregate. *Proceedings of the Royal Society of London. A. Mathematical and Physical Sciences*, 381(1780):17–31, 1982.

[90] Fabian H L Essler and Vladimir Rittenberg. Representations of the quadratic algebra and partially asymmetric diffusion with open boundaries. *Journal of Physics A: Mathematical and General*, 29(13):3375–3407, Jul 1996. doi: 10.1088/0305-4470/29/13/013. URL https://doi.org/10.1088%2F0305-4470%2F29%2F13%2F013.

[91] M. R. Evans, D. P. Foster, C. Godrèche, and D. Mukamel. Asymmetric exclusion model with two species: Spontaneous symmetry breaking. *Journal of Statistical Physics*, 80 (1):69–102, Jul 1995. ISSN 1572–9613. doi: 10.1007/BF02178354. URL https://doi.org/10.1007/BF02178354.

[92] Martin R. Evans, Pablo A. Ferrari, and Kirone Mallick. Matrix representation of the stationary measure for the multispecies TASEP. *Journal of Statistical Physics*, 135 (2):217–239, apr 2009. ISSN 1572-9613. doi: 10.1007/s10955-009-9696-2. URL https://doi.org/10.1007/s10955-009-9696-2.

[93] Gregory L. Eyink and David J. Thomson. Free decay of turbulence and breakdown of self-similarity. *Physics of Fluids*, 12(3):477–479, 2000. doi: 10.1063/1.870279. URL https://doi.org/10.1063/1.870279.

[94] F Family and T Vicsek. Scaling of the active zone in the eden process on percolation networks and the ballistic deposition model. *Journal of Physics A: Mathematical and General*, 18(2):L75, 1985. URL http://stacks.iop.org/0305-4470/18/i=2/a=005.

[95] Francis Hugh Fenlon. On the performance of a dual frequency parametric source via matched asymptotic solutions of burgers' equation. *The Journal of the Acoustical Society of America*, 55(1):35–46, 1974. doi: 10.1121/1.1919473. URL https://doi.org/10.1121/1.1919473.

[96] Pablo A. Ferrari and J. B. Martin. Multi-class processes, dual points and M/M/1 queues. *Markov Process. Related Fields*, 12(2):175–201, 2006.

[97] Pablo A. Ferrari and James B. Martin. Stationary distributions of multi-type totally asymmetric exclusion processes. *The Annals of Probability*, 35(3):807–832, 05 2007. doi: 10.1214/009117906000000944. URL https://doi.org/10.1214/009117906000000944.

[98] P. C. Fife. *Mathematical Aspects of Reacting and Diffusing Systems*. Springer-Verlag Berlin Heidelberg, 1979. doi: 10.1007/978-3-642-93111-6.

[99] Dieter Forster, David R. Nelson, and Michael J. Stephen. Large-distance and long-time properties of a randomly stirred fluid. *Phys. Rev. A*, 16:732–749, Aug 1977. doi: 10.1103/PhysRevA.16.732. URL https://link.aps.org/doi/10.1103/PhysRevA.16.732.

[100] M E Fouladvand and F Jafarpour. Multi-species asymmetric exclusion process in ordered sequential update. *Journal of Physics A: Mathematical and General*, 32(32):5845–5867, Jul 1999. doi: 10.1088/0305-4470/32/32/301. URL https://doi.org/10.1088%2F0305-4470%2F32%2F32%2F301.

[101] J. D. Fournier and U. Frisch. Remarks on the renormalization group in statistical fluid dynamics. *Phys. Rev. A*, 28:1000–1002, Aug 1983. doi: 10.1103/PhysRevA.28.1000. URL https://link.aps.org/doi/10.1103/PhysRevA.28.1000.

[102] U. Frisch. *Turbulence: The Legacy of A.N. Kolmogorov*. Cambridge University Press, 1995.

[103] Uriel Frisch. *Turbulence: The Legacy of A. N. Kolmogorov*. Cambridge University Press, 1995. doi: 10.1017/CBO9781139170666.

[104] Uriel Frisch. Private communication. 2020.

[105] George Gasper and Mizan Rahman. *Basic Hypergeometric Series*. Encyclopedia of Mathematics and its Applications. Cambridge University Press, 2 edition, 2004. doi: 10.1017/CBO9780511526251.

[106] Achille Giacometti and Maurice Rossi. Pseudospectral approach to inverse problems in interface dynamics. *Phys. Rev. E*, 63:046102, Mar 2001. doi: 10.1103/PhysRevE.63.046102. URL https://link.aps.org/doi/10.1103/PhysRevE.63.046102.

[107] Lorenzo Giada, Achille Giacometti, and Maurice Rossi. Pseudospectral method for the kardar-parisi-zhang equation. *Phys. Rev. E*, 65:036134, Mar 2002. doi: 10.1103/PhysRevE.65.036134. URL https://link.aps.org/doi/10.1103/PhysRevE.65.036134.

[108] G. Grinstein, C. Jayaprakash, and R. Pandit. Conjectures about phase turbulence in the complex ginzburg-landau equation. *Physica D: Nonlinear Phenomena*, 90(1):96 – 106, 1996. ISSN 0167-2789. doi: https://doi.org/10.1016/0167-2789(95)00036-4. URL http://www.sciencedirect.com/science/article/pii/0167278995000364.

[109] S. N. Gurbatov, A. I. Saichev, and S. F. Shandarin. The large-scale structure of the universe in the frame of the model equation of non-linear diffusion. *Monthly Notices of the Royal Astronomical Society*, 236(2):385–402, 01 1989. ISSN 0035-8711. doi: 10.1093/mnras/236.2.385. URL https://doi.org/10.1093/mnras/236.2.385.

[110] S. N. Gurbatov, S. I. Simdyankin, E. Aurell, U. Frisch, and G. Tóth. On the decay of burgers turbulence. *Journal of Fluid Mechanics*, 344:339–374, 1997. doi: 10.1017/S0022112097006241.

[111] Timothy Halpin-Healy and Yuexia Lin. Universal aspects of curved, flat, and stationary-state Kardar-Parisi-Zhang statistics. *Phys. Rev. E*, 89:010103, Jan 2014. doi: 10.1103/PhysRevE.89.010103. URL https://link.aps.org/doi/10.1103/PhysRevE.89.010103.

[112] Timothy Halpin-Healy and Kazumasa A. Takeuchi. A KPZ Cocktail-Shaken, not Stirred... *Journal of Statistical Physics*, 160:794–814, aug 2015. doi: 10.1007/s10955-015-1282-1. URL https://doi.org/10.1007/s10955-015-1282-1.

[113] Timothy Halpin-Healy and Yi-Cheng Zhang. Kinetic roughening phenomena, stochastic growth, directed polymers and all that. aspects of multidisciplinary statistical mechanics. *Physics Reports*, 254(4):215 – 414, 1995. ISSN 0370-1573. doi: https://doi.org/10.1016/0370-1573(94)00087-J. URL http://www.sciencedirect.com/science/article/pii/037015739400087J.

[114] F. Hayot, C. Jayaprakash, and Ch. Josserand. Long-wavelength properties of the Kuramoto-Sivashinsky equation. *Phys. Rev. E*, 47:911–915, Feb 1993. doi: 10.1103/PhysRevE.47.911. URL https://link.aps.org/doi/10.1103/PhysRevE.47.911.

[115] F. Hayot, C. Jayaprakash, and Ch. Josserand. Long-wavelength properties of the kuramoto-sivashinsky equation. *Phys. Rev. E*, 47:911–915, Feb 1993. doi: 10.1103/PhysRevE.47.911. URL https://link.aps.org/doi/10.1103/PhysRevE.47.911.

[116] Eberhard Hopf. A mathematical example displaying features of turbulence. *Communications on Pure and Applied Mathematics*, 1(4):303–322, 1948. doi: 10.1002/cpa.3160010401. URL https://onlinelibrary.wiley.com/doi/abs/10.1002/cpa.3160010401.

[117] Eberhard Hopf. The partial differential equation $u_t+uu_x = \mu_{xx}$. *Communications on Pure and Applied Mathematics*, 3(3):201–230, 1950. doi: 10.1002/cpa.3160030302. URL https://onlinelibrary.wiley.com/doi/abs/10.1002/cpa.3160030302.

[118] Yosyp A. Humenyuk, Miroslav Kotrla, Karel Netočný, and František Slanina. Separation of dense colloidal suspensions in narrow channels: A stochastic model. *Phys. Rev. E*, 101:032608, Mar 2020. doi: 10.1103/PhysRevE.101.032608. URL https://link.aps.org/doi/10.1103/PhysRevE.101.032608.

[119] James M. Hyman and Basil Nicolaenko. The Kuramoto-Sivashinsky equation: A bridge between PDE's and dynamical systems. *Physica D: Nonlinear Phenomena*, 18(1):113 – 126, 1986. ISSN 0167-2789. doi: https://doi.org/10.1016/0167-2789(86)90166-1. URL http://www.sciencedirect.com/science/article/pii/0167278986901661.

[120] James M. Hyman and Basil Nicolaenko. The kuramoto-sivashinsky equation: A bridge between pde's and dynamical systems. *Physica D: Nonlinear Phenomena*, 18(1):113 – 126, 1986. ISSN 0167-2789. doi: https://doi.org/10.1016/0167-2789(86)90166-1. URL http://www.sciencedirect.com/science/article/pii/0167278986901661.

[121] James M. Hyman, Basil Nicolaenko, and Stéphane Zaleski. Order and complex-

ity in the Kuramoto-Sivashinsky model of weakly turbulent interfaces. *Physica D: Nonlinear Phenomena*, 23(1):265 – 292, 1986. ISSN 0167-2789. doi: https://doi.org/10.1016/0167-2789(86)90136-3. URL http://www.sciencedirect.com/science/article/pii/0167278986901363.

[122] Takashi Imamura and Tomohiro Sasamoto. Exact Solution for the Stationary Kardar-Parisi-Zhang Equation. *Phys. Rev. Lett.*, 108:190603, May 2012. doi: 10.1103/PhysRevLett.108.190603. URL https://link.aps.org/doi/10.1103/PhysRevLett.108.190603.

[123] Ernst Ising. Beitrag zur Theorie des Ferromagnetismus. *Zeitschrift fur Physik*, 31(1): 253–258, feb 1925. doi: 10.1007/BF02980577.

[124] C. Jayaprakash, F. Hayot, and Rahul Pandit. Universal properties of the two-dimensional kuramoto-sivashinsky equation. *Phys. Rev. Lett.*, 71:12–15, Jul 1993. doi: 10.1103/PhysRevLett.71.12. URL https://link.aps.org/doi/10.1103/PhysRevLett.71.12.

[125] Kurt Johansson. Shape fluctuations and random matrices. *Communications in Mathematical Physics*, 209:437–476, 2000. doi: 10.1007/s002200050027. URL https://doi.org/10.1007/s002200050027.

[126] M.S. Jolly, I.G. Kevrekidis, and E.S. Titi. Approximate inertial manifolds for the Kuramoto-Sivashinsky equation: Analysis and computations. *Physica D: Nonlinear Phenomena*, 44(1):38 – 60, 1990. ISSN 0167-2789. doi: https://doi.org/10.1016/0167-2789(90)90046-R. URL http://www.sciencedirect.com/science/article/pii/016727899090046R.

[127] A. Kalogirou, E. E. Keaveny, and D. T. Papageorgiou. An in-depth numerical study of the two-dimensional Kuramoto-Sivashinsky equation. *Proceedings of the Royal Society A: Mathematical, Physical and Engineering Sciences*, 471(2179):20140932, 2015. doi: 10.1098/rspa.2014.0932. URL https://royalsocietypublishing.org/doi/abs/10.1098/rspa.2014.0932.

[128] Mehran Kardar, Giorgio Parisi, and Yi-Cheng Zhang. Dynamic scaling of growing interfaces. *Phys. Rev. Lett.*, 56:889–892, Mar 1986. doi: 10.1103/PhysRevLett.56.889. URL https://link.aps.org/doi/10.1103/PhysRevLett.56.889.

[129] V. Karimipour. Multispecies asymmetric simple exclusion process and its relation to traffic flow. *Phys. Rev. E*, 59:205–212, Jan 1999. doi: 10.1103/PhysRevE.59.205. URL https://link.aps.org/doi/10.1103/PhysRevE.59.205.

[130] Aly-Khan Kassam and Lloyd N. Trefethen. Fourth-order time-stepping for stiff pdes. *SIAM Journal on Scientific Computing*, 26(4):1214–1233, 2005. doi: 10.1137/S1064827502410633. URL https://doi.org/10.1137/S1064827502410633.

[131] J. I. Katz and M.L. Green. A burgers model of interstellar dynamics. *Astron. Astrophys.*, 161:139–141, jun 1986.

[132] Sheldon Katz, Joel L. Lebowitz, and Herbert Spohn. Nonequilibrium steady states of stochastic lattice gas models of fast ionic conductors. *Journal of Statistical Physics*, 34:

497–537, feb 1984. doi: 10.1007/BF01018556. URL https://doi.org/10.1007/BF01018556.

[133] Eytan Katzav and Moshe Schwartz. What is the connection between ballistic deposition and the kardar-parisi-zhang equation? *Phys. Rev. E*, 70:061608, Dec 2004. doi: 10.1103/PhysRevE.70.061608. URL https://link.aps.org/doi/10.1103/PhysRevE.70.061608.

[134] Ioannis G. Kevrekidis, Basil Nicolaenko, and James C. Scovel. Back in the saddle again: A computer assisted study of the kuramoto–sivashinsky equation. *SIAM Journal on Applied Mathematics*, 50(3):760–790, 1990. doi: 10.1137/0150045. URL https://doi.org/10.1137/0150045.

[135] M. Khorrami and V. Karimipour. Exact determination of the phase structure of a multi-species asymmetric exclusion process. *Journal of Statistical Physics*, 100(5):999–1030, Sep 2000. ISSN 1572-9613. doi: 10.1023/A:1018758907902. URL https://doi.org/10.1023/A:1018758907902.

[136] Stefan Klumpp and Reinhard Lipowsky. Traffic of molecular motors through tube-like compartments. *Journal of Statistical Physics*, 113:233–268, Oct 2003. doi: 10.1023/A:1025778922620. URL https://doi.org/10.1023/A:1025778922620.

[137] Stefan Klumpp and Reinhard Lipowsky. Traffic of molecular motors through tube-like compartments. *Journal of Statistical Physics*, 113:233–268, oct 2003. doi: 10.1023/A:1025778922620. URL https://doi.org/10.1023/A:1025778922620.

[138] R. Koekoek, P. Lesky, and R. Swarttouw. *Hypergeometric Orthogonal Polynomials and Their q-Analogues*. Springer-Verlag, Berlin, Heidelberg, 2010.

[139] Lev Kofman and A. C. Raga. Modeling structures of knots in jet flows with the burgers equation. *The Astrophysical Journal*, 390:359, may 1992. doi: 10.1086/171287.

[140] Lev A. Kofman and Sergey F. Shandarin. Theory of adhesion for the large-scale structure of the universe. *Nature*, 334:129–131, jul 1988. doi: https://doi.org/10.1038/334129a0. URL https://doi.org/10.1038/334129a0.

[141] A. N. Kolmogorov. The Local Structure of Turbulence in Incompressible Viscous Fluid for Very Large Reynolds' Numbers. *Dokl. Akad. Nauk SSSR*, 30:301–305, 1941.

[142] A. N. Kolmogorov. On degeneration of isotropic turbulence in an incompressible viscous liquid. *Dokl. Akad. Nauk SSSR*, 31:538–540, 1941.

[143] Anatoly B Kolomeisky, Gunter M Schütz, Eugene B Kolomeisky, and Joseph P Straley. Phase diagram of one-dimensional driven lattice gases with open boundaries. *Journal of Physics A: Mathematical and General*, 31(33):6911–6919, aug 1998. doi: 10.1088/0305-4470/31/33/003. URL https://doi.org/10.1088%2F0305-4470%2F31%2F33%2F003.

[144] Robert H. Kraichnan. Lagrangian-History Statistical Theory for Burgers' Equation. *The Physics of Fluids*, 11:265–277, 1968. doi: 10.1063/1.1691900. URL https://aip.scitation.org/doi/full/10.1063/1.1691900.

[145] Joachim Krug. Boundary-induced phase transitions in driven diffusive systems. *Phys. Rev. Lett.*, 67:1882–1885, 1991. doi: 10.1103/PhysRevLett.67.1882.

[146] Yoshiki Kuramoto. Diffusion–Induced Chaos in Reaction Systems. *Progress of Theoretical Physics Supplement*, 64:346–367, 02 1978. ISSN 0375-9687. doi: 10.1143/PTPS.64.346. URL https://doi.org/10.1143/PTPS.64.346.

[147] Yoshiki Kuramoto and Toshio Tsuzuki. On the Formation of Dissipative Structures in Reaction-Diffusion Systems: Reductive Perturbation Approach. *Progress of Theoretical Physics*, 54(3):687–699, 09 1975. ISSN 0033–068X. doi: 10.1143/PTP.54.687. URL https://doi.org/10.1143/PTP.54.687.

[148] Yoshiki Kuramoto and Toshio Tsuzuki. Persistent propagation of concentration waves in dissipative media far from thermal equilibrium. *Progress of Theoretical Physics*, 55 (2):356–369, 1976. doi: 10.1143/PTP.55.356. URL http://dx.doi.org/10.1143/PTP.55.356.

[149] Yoshiki Kuramoto and Toshio Tsuzuki. Persistent propagation of concentration waves in dissipative media far from thermal equilibrium. *Progress of Theoretical Physics*, 55 (2):356–369, 1976. doi: 10.1143/PTP.55.356. URL http://dx.doi.org/10.1143/PTP.55.356.

[150] Alexandre Lazarescu and Kirone Mallick. An exact formula for the statistics of the current in the TASEP with open boundaries. *Journal of Physics A: Mathematical and Theoretical*, 44(31):315001, jul 2011. doi: 10.1088/1751-8113/44/31/315001. URL https://doi.org/10.1088%2F1751-8113%2F44%2F31%2F315001.

[151] H-W Lee, V Popkov, and D Kim. Two-way traffic flow: Exactly solvable model of traffic jam. *Journal of Physics A: Mathematical and General*, 30(24):8497–8513, dec 1997. doi: 10.1088/0305-4470/30/24/014. URL https://doi.org/10.1088%2F0305-4470%2F30%2F24%2F014.

[152] Marcel Lesieur. *Turbulence in Fluids*. Springer Netherlands, 2008. doi: 10.1007/978-1-4020-6435-7.

[153] David A. Levin, Yuval Peres, and Elizabeth L. Wilmer. *Markov chains and mixing times*. American Mathematical Society, Providence, RI, 2009.

[154] Carolyn T. MacDonald and Julian H. Gibbs. Concerning the kinetics of polypeptide synthesis on polyribosomes. *Biopolymers*, 7(5):707–725, 1969. doi: 10.1002/bip.1969.360070508. URL https://onlinelibrary.wiley.com/doi/abs/10.1002/bip.1969.360070508.

[155] Carolyn T. MacDonald, Julian H. Gibbs, and Allen C. Pipkin. Kinetics of biopolymerization on nucleic acid templates. *Biopolymers*, 6(1):1–25, 1968. doi: 10.1002/bip.1968.360060102. URL https://onlinelibrary.wiley.com/doi/abs/10.1002/bip.1968.360060102.

[156] Satya N Majumdar and Grégory Schehr. Top eigenvalue of a random matrix: large deviations and third order phase transition. *Journal of Statistical Mechanics: Theory and*

Experiment, 2014(1):P01012, 2014. URL http://stacks.iop.org/1742-5468/2014/i=1/a=P01012.

[157] K Mallick and S Sandow. Finite-dimensional representations of the quadratic algebra: Applications to the exclusion process. *J. Phys. A: Math. Gen.*, 30:4513, 1997. doi: 10.1088/0305-4470/30/13/008.

[158] Takeshi Matsumoto, et al. In preparation. 2020.

[159] Marcello Meldi and Pierre Sagaut. On non-self-similar regimes in homogeneous isotropic turbulence decay. *Journal of Fluid Mechanics*, 711:364–393, 2012. doi: 10.1017/jfm.2012.396.

[160] Charles Meneveau and K. R. Sreenivasan. The multifractal nature of turbulent energy dissipation. *Journal of Fluid Mechanics*, 224:429–484, 1991. doi: 10.1017/S0022112091001830.

[161] D.M. Michelson and G.I. Sivashinsky. Nonlinear analysis of hydrodynamic instability in laminar flames–ii. numerical experiments. *Acta Astronautica*, 4(11):1207 – 1221, 1977. ISSN 0094–5765. doi: https://doi.org/10.1016/0094-5765(77)90097-2. URL http://www.sciencedirect.com/science/article/pii/0094576577900972.

[162] Chung-Yu Mou and Peter B. Weichman. Multicomponent turbulence, the spherical limit, and non-kolmogorov spectra. *Phys. Rev. E*, 52:3738–3796, Oct 1995. doi: 10.1103/PhysRevE.52.3738. URL https://link.aps.org/doi/10.1103/PhysRevE.52.3738.

[163] M. Myllys, J. Maunuksela, M. J. Alava, T. Ala-Nissila, and J. Timonen. Scaling and noise in slow combustion of paper. *Phys. Rev. Lett.*, 84:1946–1949, Feb 2000. doi: 10.1103/PhysRevLett.84.1946. URL https://link.aps.org/doi/10.1103/PhysRevLett.84.1946.

[164] M. Myllys, J. Maunuksela, M. Alava, T. Ala-Nissila, J. Merikoski, and J. Timonen. Kinetic roughening in slow combustion of paper. *Phys. Rev. E*, 64:036101, Aug 2001. doi: 10.1103/PhysRevE.64.036101. URL https://link.aps.org/doi/10.1103/PhysRevE.64.036101.

[165] Takashi Nagatani. From ballistic deposition to the kardar-parisi-zhang equation through a limiting procedure. *Phys. Rev. E*, 58:700–703, Jul 1998. doi: 10.1103/PhysRevE.58.700. URL https://link.aps.org/doi/10.1103/PhysRevE.58.700.

[166] B. Nicolaenko, B. Scheurer, and R. Temam. Some global dynamical properties of the Kuramoto-Sivashinsky equations: Nonlinear stability and attractors. *Physica D: Nonlinear Phenomena*, 16(2):155 – 183, 1985. ISSN 0167-2789. doi: https://doi.org/10.1016/0167-2789(85)90056-9. URL http://www.sciencedirect.com/science/article/pii/0167278985900569.

[167] A. Noullez and M. Vergassola. A fast legendre transform algorithm and applications to the adhesion model. *Journal of Scientific Computing*, 9, 1994. doi: 10.1007/BF01575032. URL https://doi.org/10.1007/BF01575032.

[168] Lars Onsager. Crystal statistics. i. a two-dimensional model with an order-disorder transition. *Phys. Rev.*, 65:117–149, Feb 1944. doi: 10.1103/PhysRev.65.117. URL https://link.aps.org/doi/10.1103/PhysRev.65.117.

[169] Shalin Parekh. The kpz limit of asep with boundary. *Communications in Mathematical Physics*, 365:569–649, Aug 2018. doi: 10.1103/PhysRevE.98.022405. URL 10.1007/s00220-018-3258-x.

[170] Catherine J. Penington, Barry D. Hughes, and Kerry A. Landman. Building macroscale models from microscale probabilistic models: A general probabilistic approach for nonlinear diffusion and multispecies phenomena. *Phys. Rev. E*, 84:041120, Oct 2011. doi: 10.1103/PhysRevE.84.041120. URL https://link.aps.org/doi/10.1103/PhysRevE.84.041120.

[171] Y. Pomeau, A. Pumir, and P. Pelce. Intrinsic stochasticity with many degrees of freedom. *Journal of Statistical Physics*, 37:39–49, oct 1984. doi: https://doi.org/10.1007/BF01012904. URL 10.1007/BF01012904.

[172] Vladislav Popkov and Gunter M. Schütz. Shocks and Excitation Dynamics in a Driven Diffusive Two-Channel System. *Journal of Statistical Physics*, 112:523–540, aug 2003. doi: 10.1023/A:1023819807616. URL https://doi.org/10.1023/A:1023819807616.

[173] Michael Prähofer and Herbert Spohn. Universal distributions for growth processes in 1 + 1 dimensions and random matrices. *Phys. Rev. Lett.*, 84:4882–4885, May 2000. doi: 10.1103/PhysRevLett.84.4882. URL https://link.aps.org/doi/10.1103/PhysRevLett.84.4882.

[174] Michael Prähofer and Herbert Spohn. Exact scaling functions for one-dimensional stationary kpz growth. *Journal of Statistical Physics*, 115(1):255–279, Apr 2004. ISSN 1572-9613. doi: 10.1023/B:JOSS.0000019810.21828.fc. URL https://doi.org/10.1023/B:JOSS.0000019810.21828.fc.

[175] A Proeme, R A Blythe, and M R Evans. Dynamical transition in the open-boundary totally asymmetric exclusion process. *Journal of Physics A: Mathematical and Theoretical*, 44(3):035003, dec 2010. doi: 10.1088/1751-8113/44/3/035003. URL https://doi.org/10.1088%2F1751-8113%2F44%2F3%2F035003.

[176] S Prolhac, M R Evans, and K Mallick. The matrix product solution of the multispecies partially asymmetric exclusion process. *Journal of Physics A: Mathematical and Theoretical*, 42(16):165004, 2009. URL http://stacks.iop.org/1751-8121/42/i=16/a=165004.

[177] A. Pumir, P. Manneville, and Y. Pomeau. On solitary waves running down an inclined plane. *Journal of Fluid Mechanics*, 135:27–50, 1983. doi: 10.1017/S0022112083002943.

[178] Jeremy Quastel and Herbert Spohn. The one-dimensional kpz equation and its universality class. *Journal of Statistical Physics*, 160(4):965–984, Aug 2015. ISSN

1572-9613. doi: 10.1007/s10955-015-1250-9. URL https://doi.org/10.1007/s10955-015-1250-9.

[179] A. C. Raga, J. Canto, L. Binette, and N. Calvet. Stellar jets with intrinsically variable sources. *The Astrophysical Journal*, 364:601, dec 1990. doi: 10.1086/169443.

[180] N. Rajewsky, L. Santen, A. Schadschneider, and M. Schreckenberg. The asymmetric exclusion process: Comparison of update procedures. *Journal of Statistical Physics*, 92(1572-9613):151–194, Jul 1998. doi: 10.1023/A:1023047703307. URL https://doi.org/10.1023/A:1023047703307.

[181] C. Ruyer-Quil and P. Manneville. Modeling film flows down inclined planes. *The European Physical Journal B - Condensed Matter and Complex Systems*, 6:277–292, nov 1998. doi: 10.1007/s100510050550. URL https://doi.org/10.1007/s100510050550.

[182] C. Ruyer-Quil and P. Manneville. Modeling film flows down inclined planes. *The European Physical Journal B - Condensed Matter and Complex Systems*, 6(2):277–292, Nov 1998. ISSN 1434-6036. doi: 10.1007/s100510050550. URL https://doi.org/10.1007/s100510050550.

[183] Abbas Ali Saberi, Hor Dashti-Naserabadi, and Joachim Krug. Competing universalities in kardar-parisi-zhang growth models. *Phys. Rev. Lett.*, 122:040605, Jan 2019. doi: 10.1103/PhysRevLett.122.040605. URL https://link.aps.org/doi/10.1103/PhysRevLett.122.040605.

[184] Anirban Sain, Manu, and Rahul Pandit. Turbulence and Multiscaling in the Randomly Forced Navier-Stokes Equation. *Phys. Rev. Lett.*, 81:4377–4380, Nov 1998. doi: 10.1103/PhysRevLett.81.4377. URL https://link.aps.org/doi/10.1103/PhysRevLett.81.4377.

[185] Sven Sandow. Partially asymmetric exclusion process with open boundaries. *Phys. Rev. E*, 50:2660–2667, Oct 1994. doi: 10.1103/PhysRevE.50.2660. URL https://link.aps.org/doi/10.1103/PhysRevE.50.2660.

[186] Silvia N. Santalla and Silvio C. Ferreira. Eden model with nonlocal growth rules and kinetic roughening in biological systems. *Phys. Rev. E*, 98:022405, Aug 2018. doi: 10.1103/PhysRevE.98.022405. URL https://link.aps.org/doi/10.1103/PhysRevE.98.022405.

[187] Tomohiro Sasamoto. One-dimensional partially asymmetric simple exclusion process with open boundaries: orthogonal polynomials approach. *Journal of Physics A: Mathematical and General*, 32(41):7109–7131, sep 1999. doi: 10.1088/0305-4470/32/41/306. URL https://doi.org/10.1088%2F0305-4470%2F32%2F41%2F306.

[188] Tomohiro Sasamoto. Density profile of the one-dimensional partially asymmetric simple exclusion process with open boundaries. *Journal of the Physical Society of Japan*, 69(4):1055–1067, 2000. doi: 10.1143/JPSJ.69.1055. URL https://doi.org/10.1143/JPSJ.69.1055.

[189] Tomohiro Sasamoto and Herbert Spohn. One-dimensional kardar-parisi-zhang equation: An exact solution and its universality. *Phys. Rev. Lett.*, 104:230602, Jun 2010. doi: 10.1103/PhysRevLett.104.230602. URL https://link.aps.org/doi/10.1103/PhysRevLett.104.230602.

[190] A Schadschneider and M Schreckenberg. Cellular automation models and traffic flow. *Journal of Physics A: Mathematical and General*, 26(15):L679–L683, Aug 1993. doi: 10.1088/0305-4470/26/15/011. URL https://doi.org/10.1088%2F0305-4470%2F26%2F15%2F011.

[191] Andreas Schadschneider. Statistical physics of traffic flow. *Physica A: Statistical Mechanics and its Applications*, 285(1):101 – 120, 2000. ISSN 0378-4371. doi: https://doi.org/10.1016/S0378-4371(00)00274-0. URL http://www.sciencedirect.com/science/article/pii/S0378437100002740.

[192] Andreas Schadschneider. Traffic flow: a statistical physics point of view. *Physica A: Statistical Mechanics and its Applications*, 313(1):153–187, 2002. ISSN 0378-4371. doi: https://doi.org/10.1016/S0378-4371(02)01036-1. URL http://www.sciencedirect.com/science/article/pii/S0378437102010361. Fundamental Problems in Statistical Physics.

[193] G. Schütz and E. Domany. Phase transitions in an exactly soluble one-dimensional exclusion process. *Journal of Statistical Physics*, 72(1):277–296, Jul 1993. ISSN 1572-9613. doi: 10.1007/BF01048050. URL https://doi.org/10.1007/BF01048050.

[194] Gunter M. Schütz. Exactly solvable models for many-body systems far from equilibrium. *Phase Transitions and Critical Phenomena*, 19:1–251, Sep 2000. URL https://www.elsevier.com/books/phase-transitions-and-critical-phenomena/domb/978-0-12-220319-0.

[195] S. F. Shandarin and Ya. B. Zeldovich. The large-scale structure of the universe: Turbulence, intermittency, structures in a self-gravitating medium. *Rev. Mod. Phys.*, 61:185–220, Apr 1989. doi: 10.1103/RevModPhys.61.185. URL https://link.aps.org/doi/10.1103/RevModPhys.61.185.

[196] Zhen-Su She, Erik Aurell, and Uriel Frisch. The inviscid burgers equation with initial data of brownian type. *Comm. Math. Phys.*, 148(3):623–641, 1992. URL https://projecteuclid.org:443/euclid.cmp/1104251047.

[197] Shlang, T. and Sivashinsky, G.I. Irregular flow of a liquid film down a vertical column. *J. Phys. France*, 43(3):459–466, 1982. doi: 10.1051/jphys:01982004303045900. URL https://doi.org/10.1051/jphys:01982004303045900.

[198] Matthew J. Simpson, Kerry A. Landman, and Barry D. Hughes. Multi-species simple exclusion processes. *Physica A: Statistical Mechanics and its Applications*, 388(4):399 – 406, 2009. ISSN 0378-4371. doi: https://doi.org/10.1016/j.physa.2008.10.038. URL http://www.sciencedirect.com/science/article/pii/S0378437108008935.

[199] G. I. Sivashinsky. On flame propagation under conditions of stoichiometry. *SIAM*

Journal on Applied Mathematics, 39(1):67–82, 1980. doi: 10.1137/0139007. URL https://doi.org/10.1137/0139007.

[200] G. I. Sivashinsky and D. M. Michelson. On Irregular Wavy Flow of a Liquid Film Down a Vertical Plane. *Progress of Theoretical Physics*, 63(6):2112–2114, 06 1980. ISSN 0033-068X. doi: 10.1143/PTP.63.2112. URL https://doi.org/10.1143/PTP.63.2112.

[201] G.I. Sivashinsky. Nonlinear analysis of hydrodynamic instability in laminar flames–i. derivation of basic equations. *Acta Astronautica*, 4(11):1177 – 1206, 1977. ISSN 0094-5765. doi: https://doi.org/10.1016/0094-5765(77)90096-0. URL http://www.sciencedirect.com/science/article/pii/0094576577900960.

[202] K. Sneppen, J. Krug, M. H. Jensen, C. Jayaprakash, and T. Bohr. Dynamic scaling and crossover analysis for the Kuramoto-Sivashinsky equation. *Phys. Rev. A*, 46:R7351–R7354, Dec 1992. doi: 10.1103/PhysRevA.46.R7351. URL https://link.aps.org/doi/10.1103/PhysRevA.46.R7351.

[203] Frank Spitzer. Interaction of markov processes. *Advances in Mathematics*, 5:246–290, 1970. ISSN 0001-8708. doi: https://doi.org/10.1016/0001-8708(70)90034-4. URL http://www.sciencedirect.com/science/article/pii/0001870870900344.

[204] Kazumasa A Takeuchi. Statistics of circular interface fluctuations in an off-lattice eden model. *Journal of Statistical Mechanics: Theory and Experiment*, 2012(05):P05007, may 2012. doi: 10.1088/1742-5468/2012/05/p05007. URL https://doi.org/10.1088%2F1742-5468%2F2012%2F05%2Fp05007.

[205] Kazumasa A. Takeuchi. Crossover from Growing to Stationary Interfaces in the Kardar-Parisi-Zhang Class. *Phys. Rev. Lett.*, 110:210604, May 2013. doi: 10.1103/PhysRevLett.110.210604. URL https://link.aps.org/doi/10.1103/PhysRevLett.110.210604.

[206] Kazumasa A. Takeuchi. An appetizer to modern developments on the Kardar-Parisi-Zhang universality class. *Physica A: Statistical Mechanics and its Applications*, 504:77 – 105, 2018. ISSN 0378-4371. doi: https://doi.org/10.1016/j.physa.2018.03.009. URL http://www.sciencedirect.com/science/article/pii/S0378437118303170. Lecture Notes of the 14th International Summer School on Fundamental Problems in Statistical Physics.

[207] Kazumasa A. Takeuchi and Masaki Sano. Evidence for Geometry-Dependent Universal Fluctuations of the Kardar-Parisi-Zhang Interfaces in Liquid-Crystal Turbulence. *Journal of Statistical Physics*, 147(5):853–890, Jun 2012. ISSN 1572-9613. doi: 10.1007/s10955-012-0503-0. URL https://doi.org/10.1007/s10955-012-0503-0.

[208] Kazumasa A. Takeuchi, Masaki Sano, Tomohiro Sasamoto, and Herbert Spohn. Growing interfaces uncover universal fluctuations behind scale invariance. *Scientific Reports*, 1 (34), Nov 2011. doi: 10.1038/srep00034. URL http://dx.doi.org/10.1038/srep00034.

[209] Craig A. Tracy and Harold Widom. Level-spacing distributions and the airy kernel.

Communications in Mathematical Physics, 159(1):151–174, Jan 1994. ISSN 1432-0916. doi: 10.1007/BF02100489. URL https://doi.org/10.1007/BF02100489.

[210] L. N. Trefethen. *Spectral Methods in MATLAB*. SIAM, Philadelphia, 2000. URL https://people.maths.ox.ac.uk/trefethen/spectral.html.

[211] Masaru Uchiyama. Two-species asymmetric simple exclusion process with open boundaries. *Chaos, Solitons and Fractals*, 35(2):398–407, 2008. ISSN 0960-0779. doi: https://doi.org/10.1016/j.chaos.2006.05.013. URL http://www.sciencedirect.com/science/article/pii/S096007790600470X.

[212] Masaru Uchiyama, Tomohiro Sasamoto, and Miki Wadati. Asymmetric simple exclusion process with open boundaries and Askey–Wilson polynomials. *Journal of Physics A: Mathematical and General*, 37(18):4985, 2004. URL http://stacks.iop.org/0305-4470/37/i=18/a=006.

[213] M. Vergassola, B. Dubrulle, U. Frisch, and A. Noullez. Burgers' equation, Devil's staircases and the mass distribution for large-scale structures. *Astron. Astrophys.*, 289: 325–356, sep 1994.

[214] Mahendra K. Verma. Intermittency exponents and energy spectrum of the Burgers and KPZ equations with correlated noise. *Physica A: Statistical Mechanics and its Applications*, 277(3):359 – 388, 2000. ISSN 0378-4371. doi: https://doi.org/10.1016/S0378-4371(99)00544-0. URL http://www.sciencedirect.com/science/article/pii/S0378437199005440.

[215] V. Yakhot. Large-scale properties of unstable systems governed by the kuramoto-sivashinksi equation. *Phys. Rev. A*, 24:642–644, Jul 1981. doi: 10.1103/PhysRevA.24.642. URL https://link.aps.org/doi/10.1103/PhysRevA.24.642.

[216] Victor Yakhot and Steven A. Orszag. Renormalization group analysis of turbulence. i. basic theory. *Journal of Scientific Computing*, 1(1):3–51, Mar 1986. ISSN 1573-7691. doi: 10.1007/BF01061452. URL https://doi.org/10.1007/BF01061452.